QUANTITATIVE WHOLE BODY IMAGING AT HIGH FIELD

Eleanor F. Cox, MSci.

Thesis submitted to the University of Nottingham
for the degree of Doctor of Philosophy

April 2009

TABLE OF CONTENTS

ABSTRACT

In this thesis methods of accurately and reproducibly measuring intestinal content and transverse relaxation to study the fate of food in the gastrointestinal tract are reported. In addition to this a technique for measuring relaxation parameters in the brain at ultra-high field is also investigated.

Several methods can be used when quantifying the fate of food through the gastrointestinal tract; there are many factors that can be measured using MRI and these are discussed along with other non-MRI techniques. In this work a method for quantifying small bowel water content (SBWC) is optimised and validated for use at 3.0 T and a technique for measuring T_2 in the abdomen is developed and optimised called T_2-prepared balanced turbo field echo (T_2-prep bTFE). These two methods are then used, in conjunction with other established MRI techniques, to study the fate of food in the gastrointestinal tract from the stomach all the way through to the colon.

A hybrid gradient echo-spin echo (GESSE) sequence is also investigated and optimised for measuring T_2 and T_2* simultaneously in the brain at 7.0 T. This sequence is also proved to have applications in the liver at lower field strengths. The GESSE sequence is used to measure the first T_2 values in deep grey structures in the brain at 7.0 T. In this work cross-field (1.5, 3.0 and 7.0 T) variations in T_2 are studied. Also differences in T_2 and T_2* are measured in the brain to determine variations between white matter tracts and to ascertain any effects of Parkinson's disease on deep grey matter structures.

ACKNOWLEDGEMENTS

Firstly, I would like to thank my supervisor Prof. Penny Gowland for her invaluable help and guidance during the last 3 and a half years. I also have to say a big thank you to Dr. Caroline Hoad and Dr. Luca Marciani for their continuous assistance and support. Also, thanks to Prof. Robin Spiller, Prof. Dorothee Auer, Dr. Andrew Peters Dr. Jeff Wright, Mrs. Debbie Bush and Mrs. Sue Pritchard for their expertise and assistance with experiments. I must acknowledge all my volunteers that have agreed to go in the scanner and those that allowed me to feed them some less than appetizing meals!

Next I would like to thank all my colleagues at the SPMMRC, in particular to Karen, Mary, Claire, Johanna, Lesley, Nicki, Nic, Matt and Alex for being great friends, for listening to me when I moan and giving me encouragement when I needed it, and also to Jim for entertaining us every lunchtime with the quiz - I'm not sure how we used to survive without the quiz!

I must thank all my friends who have supported me and kept me sane: Liz, James, Emily, Andrew, David, Julia and Chris. Thanks for listening and pretending to understand what it was all about!

Without the support of my family I would not have been able to make it this far, so a big thank you Mum, Dad, Michael and Gran for everything. Finally, I have to thank Duncan who has been my rock over the past few months, providing me with a lot of encouragement, numerous cups of tea and introducing me to the wildlife at the lake.

CHAPTER 1

INTRODUCTION

1.1 INTRODUCTION

The work contained in this thesis began late in the summer of 2005 and was carried out at the Sir Peter Mansfield Magnetic Resonance Centre at the University of Nottingham. Focus was placed on developing techniques for quantitative whole body imaging within the abdomen and brain. The original aim was to develop techniques to measure small bowel water content and quantify changes in stomach and colon contents in order to investigate the fate of food within the gastrointestinal tract at 3.0 T, but with the arrival of the 7.0 T this prompted testing of the 3.0 T sequences at ultra-high field and development of further sequences for use in the brain at 7.0 T. A thesis overview is given in section 1.3. The University of Nottingham has an illustrious history in MRI and the following section describes the history of MRI in Nottingham with the key research outcomes.

1.2 MRI IN NOTTINGHAM

In 1973, Peter Mansfield, a British physicist, published the first paper from Nottingham on MRI [1]. Around the same time an American chemist, Paul Lauterbur, was also publishing the first developments made on MRI on the other side of the Atlantic [2]. Several developments were made in Nottingham in the following years including slice selection [3], echo planar imaging [4], actively shielded gradients [5] and echo volumar imaging [6].

In 1991, the Magnetic Resonance Centre, a purpose built annex of the School of Physics and Astronomy, was opened. The first scanners to be installed were in-house custom built 0.5 T and 3.0 T whole body scanners. This lead to

publications of high speed imaging at 3.0 T [7], acoustically shielded gradients [8], event related functional MRI [9], fetal functional MRI [10] and gastrointestinal imaging [11-13].

In 2003, Peter Mansfield was jointly awarded the Nobel Prize for medicine with Paul Lauterbur '*for their discoveries concerning magnetic resonance imaging*' (www.nobelprize.org). With a new extension, the Magnetic Resonance Centre was renamed to acknowledge this achievement and is now known as the Sir Peter Mansfield Magnetic Resonance Centre. The original 0.5 T scanner has since been replaced by a commercial Philips Achieva whole body 3.0 T scanner and in 2006, a research Philips 7.0 T scanner was also installed. Scanning at ultra-high field is particularly challenging and the learning process continues.

1.3 THESIS OVERVIEW

The overall aim of this work was to develop MRI techniques that allow quantitative analysis of the whole body, particularly in the gastrointestinal tract.

Chapter 2 contains background theory including basic principles of nuclear magnetic resonance and the concepts of imaging using magnetic resonance. It also describes the instrumentation required for magnetic resonance imaging and the attention to safety that is required. Chapter 3 is an extensive review of methods for measuring T_2 and their advantages and disadvantages.

Chapter 4 describes the work which validates a non-invasive method for measuring small bowel water content at 3.0 T. Chapter 5 introduces the T_2-prepared balanced turbo field echo sequence which is used to measure T_2 and is particularly applicable in the abdomen. The sequence is validated and optimised before obtaining T_2 values for several abdominal tissues. Chapter 6 combines the methods described in chapters 4 and 5 to investigate the fate of

food in the gastrointestinal tract. The effects of alginate beads and meal composition are studied.

Chapter 7 presents a second sequence for measuring T_2, which is also capable of measuring T_2* simultaneously: a hybrid gradient echo-spin echo sequence. It is validated, optimised and used to obtain the first T_2 measurements of the brain at 7.0 T. Cross-field variations in T_2, the effects of Parkinson's disease on deep grey matter T_2s and the correlation between relaxation and axonal structure in white matter tracts are all investigated.

Chapter 8 summarises the results from chapters 4 to 7 and draws general conclusions about this work.

1.4 References

1. Mansfield, P. and P.K. Grannell, *NMR 'diffraction' in solids?* J. Phys. C: Solid State Phys., 1973. **6**: p. L422-L426.
2. Lauterbur, P.C., *Image Formation by Induced Local Interactions: Examples Employing Nuclear Magnetic Resonance.* Nature, 1973. **242**: p. 190-191.
3. Garroway, A.N., P.K. Grannell, and P. Mansfield, *Image formation in NMR by a selective irradiative process.* J. Phys. C - Solid state phys, 1974. **7**: p. L457-L562.
4. Mansfield, P., *Multi-planar image formation using NMR spin echoes.* J. Phys. C: Solid State Phys., 1977. **10**: p. L55-L58.
5. Mansfield, P. and B. Chapman, *Active magnetic screening of coils for static and time-dependent magnetic field generation in NMR imaging.* J. Phys. E: Sci. Instrum., 1986. **19**: p. 540-545.
6. Mansfield, P., A.M. Howseman, and R.J. Ordidge, *Volumar imaging using NMR spin echoes - echo-volumar imaging (EVI) at 0.1-T.* J. Phys. E - Sci. Instr., 1989. **22**(5): p. 324-330.

7. Mansfield, P., R. Coxon, and P. Glover, *Echo-Planar Imaging of the Brain at 3.0 T: First Normal Volunteer Results.* JCAT, 1994. **18**(3): p. 339-343.
8. P.Mansfield, P. Glover, and R. Bowtell, *Active acoustic screening: design principles for quiet gradient coils in MRI.* Meas. Sci. Tech., 1994. **5**: p. 1021-1025.
9. Humberstone, M., et al., *Functional Magnetic Resonance Imaging of Single Motor Events Reveals Human Presupplementary Motor Area.* Ann. Neurol., 1997. **42**: p. 632-637.
10. Hykin, J., et al., *Fetal brain activity demonstrated by functional magnetic resonance imaging.* Lancet, 1999. **354**: p. 645-646.
11. Stehling, M.K., et al., *Gastrointestinal Tract: Dynamic MR Studies with Echo-Planar Imaging.* Radiology, 1989. **171**: p. 41-46.
12. Evans, D.F., et al., *Prolonged monitoring of the upper gastrointestinal tract using echo planar magnetic resonance imaging.* Gut, 1993. **34**: p. 848-852.
13. Hykin, J., et al., *Measurement of GI water content using EPI at 0.5 tesla.* MAGMA, 1994. **2**: p. 471-473.

CHAPTER 2

NUCLEAR MAGNETIC RESONANCE THEORY

2.1 INTRODUCTION

This chapter will introduce the theory of nuclear magnetic resonance and the principles and instrumentation behind magnetic resonance imaging. The importance of safety and ethics will also be discussed.

2.2 NUCLEAR MAGNETIC RESONANCE

2.2.1 Background

Nuclear magnetic resonance (NMR) is performed on the nuclei of atoms which comprise matter. The atoms contain electrons and a nucleus containing protons and neutrons. The nucleus has three important fundamental physical properties: mass, electronic charge and spin. It is the subtle interactions of charge and spin within some nuclei which allows molecular exploration using NMR.

2.2.2 Fundamentals of spin

Spin is a form of angular momentum and is an intrinsic property of atomic nuclei. Classically, the angular momentum of a moving object about any point is the vector product of the position vector of the object and its translational momentum $\mathbf{L} = \mathbf{r} \times \mathbf{p}$; it is a conserved quantity. The total angular momentum of a nucleus is determined by the intrinsic spin quantum number I and all elementary particles have an intrinsic spin quantum number of either integral or half-integral values of I. When nuclei consist of multiple particles, their spins combine to give a net spin for the nucleus which is 0 or

an integer multiple of ½. Table 2-1 gives a selection of nuclear isotopes and their properties.

Isotope	Nuclear Spin	Natural Abundance (%)	Gyromagnetic ratio (MHz T^{-1})
^{1}H	½	~100	267.522
^{2}H	1	0.015	41.066
^{3}H	½	0	285.349
^{13}C	½	1.1	67.283
^{14}N	1	99.6	19.338
^{15}N	½	0.37	-27.126
^{17}O	5/2	0.04	-36.281
^{19}F	½	~100	251.815
^{23}Na	3/2	~100	70.808
^{31}P	½	~100	108.394

Table 2-1: Some nuclear isotopes and their properties [1].

In non-relativistic quantum mechanics, the spin angular momentum vector ***P*** of a nucleus with spin quantum number *I* is

$$P = \hbar\sqrt{I(I+1)} = |\mathbf{P}| \qquad \textbf{[2-1]}$$

where $\hbar$ is $h/2\pi$ and h is Plank's constant. Nuclei with spin state I have $2I+1$ sub-levels. These are degenerate in the absence of an external magnetic or electric field, but in the presence of a static magnetic field these sub-levels have different energies. The quantum number m_I defines the allowed orientations, or magnetic spin states, of the nucleus when a magnetic field is applied; it is sometimes called the *azimuthal* quantum number. For an integer I, $m_I = I, (I\text{-}1), (I\text{-}2), \ldots, 0, \ldots, -I$ and for a ½ integral I, $m_I = I, (I\text{-}1), (I\text{-}2), \ldots,$ ½, -½, …, $-I$. If the magnetic field is along the z direction, it defines a direction to the spin system and it is the z component of the spin angular momentum which is quantised by the number m_I according to

$$P_z = \hbar m_I \qquad \textbf{[2-2]}$$

Figure 2-1 illustrates the relationship between these quantities for $I = ½$.

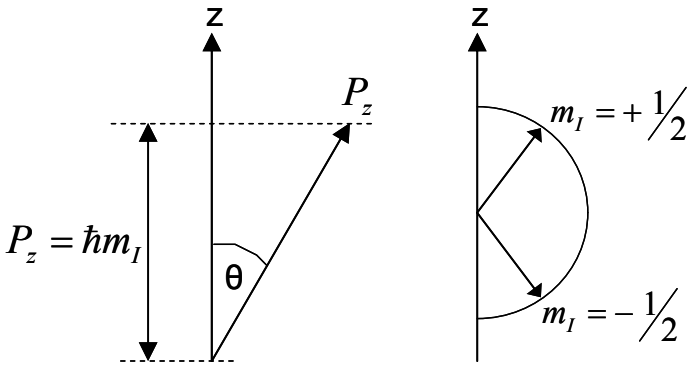

Figure 2-1: Quantisation of the orientation of the spin angular momentum vector

2.2.3 Magnetism

In NMR, many phenomena are studied only at the level of multiple interacting spins (bulk magnetisation), so a simpler classical description can be used. The magnetic moment of a nucleus **μ** is a vector quantity parallel to the associated spin angular momentum **P**:

$$\boldsymbol{\mu} = \gamma \mathbf{P} \qquad \textbf{[2-3]}$$

where γ is the gyromagnetic ratio. Each nucleus has its own value of the gyromagnetic ratio (Table 2-1).

There are three sources of magnetisation: circulation of molecular electric currents, magnetic moment of electrons and magnetic moment of atomic nuclei. Generally, the nuclear contribution is far smaller than the electronic contributions.

Classically, the energy E of a magnetic moment placed in a magnetic field **B** is

$$E = -\boldsymbol{\mu} \cdot \mathbf{B} \qquad \textbf{[2-4]}$$

The negative sign indicates that the energy is lowest when **μ** is parallel to **B**. The energy depends on the magnetic quantum state of the nucleus, the strength of the magnetic field and the particular type of nucleus (gyromagnetic ratio, γ). For a spin-½ nucleus, there are two allowed energy states separated by $\Delta E = \hbar\gamma B_z$. This separation is known as the Zeeman splitting (Figure 2-2).

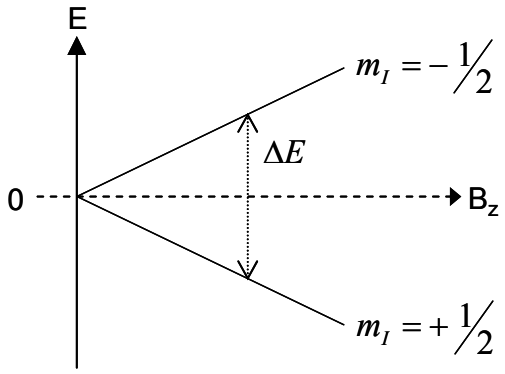

Figure 2-2: Illustration of the Zeeman splitting of energy levels due to the presence of an applied magnetic field

Spectroscopy involves the application of an electromagnetic field to induce a change in the quantum state of the system. In the presence of a magnetic field, the nuclear spin state can be changed by either absorption or stimulated emission of electromagnetic photons with energy that matches the Zeeman splitting ΔE (Figure 2-2). The photon frequency ν required to induce the transition can be calculated by rearranging equation 2-5 to obtain a value of ν (equation 2-6).

$$\Delta E = \hbar\gamma B_z = h\nu \qquad \textbf{[2-5]}$$

$$\nu = \frac{\gamma B_z}{2\pi} \qquad \textbf{[2-6]}$$

Different photon frequencies will be required for different nuclei to induce transitions in the same magnetic field due to the characteristic gyromagnetic ratio of the particular nuclei. For protons in an applied magnetic field of 1.0

T, ν = 42.58 MHz (since $\gamma \sim 267.5$ MHz T^{-1}) which is in the radiofrequency region of the electromagnetic spectrum.

Classically, for a net magnetic moment $\boldsymbol{\mu}$ in a static magnetic field **B**, of arbitrary strength, orientation and time-dependence, a torque **T** will be experienced. The response to the torque is limited by the fact that inherent to $\boldsymbol{\mu}$ is a spin vector **P** and the total angular momentum must be conserved. Under these conditions, the equation of motion of $\boldsymbol{\mu}$ is obtained from Newton's Second Law for rotational motion:

$$\mathbf{T} = \frac{d\mathbf{P}}{dt} = \boldsymbol{\mu} \times \mathbf{B} \qquad \textbf{[2-7]}$$

but since $\boldsymbol{\mu} = \gamma \mathbf{P}$ this becomes:

$$\frac{d\boldsymbol{\mu}}{dt} = \gamma\, \boldsymbol{\mu} \times \mathbf{B} \qquad \textbf{[2-8]}$$

This indicates that at any instant in time, the rate of change of $\boldsymbol{\mu}$ is perpendicular to both $\boldsymbol{\mu}$ and **B**. So far, **B** has not been specified as being static, uniform or time-dependent; if it was stationary, uniform and directed along the *z* axis then

$$\mathbf{B} = B_z \mathbf{k} \qquad \textbf{[2-9]}$$

If $\boldsymbol{\mu}$ is written in terms of its components:

$$\boldsymbol{\mu} = \mu_x \mathbf{i} + \mu_y \mathbf{j} + \mu_z \mathbf{k} \qquad \textbf{[2-10]}$$

Equation 2-8 can also be separated into its components:

$$\frac{d\mu_x}{dt} = \gamma \mu_y B_z \;\; ; \;\; \frac{d\mu_y}{dt} = -\gamma \mu_x B_z \;\; ; \;\; \frac{d\mu_z}{dt} = 0 \qquad \textbf{[2-11]}$$

The solutions to these equations are given by

$$\mu_x(t) = \mu_x(0)\cos(\gamma B_z t) + \mu_y(0)\sin(\gamma B_z t)$$
$$\mu_y(t) = -\mu_x(0)\sin(\gamma B_z t) + \mu_y(0)\cos(\gamma B_z t) \qquad \textbf{[2-12]}$$
$$\mu_z(t) = \mu_z(0)$$

The motion of the magnetic moment described by equation 2-12 is termed precession and is illustrated in Figure 2-3. It can be seen that the *z* component of **μ** remains constant, whilst the tip of the transverse magnetisation vector follows a circular trajectory with an angular frequency $\omega_L = \gamma B_z$. The magnetic moment is precessing around the direction of the magnetic field and traces out a cone as a function of time.

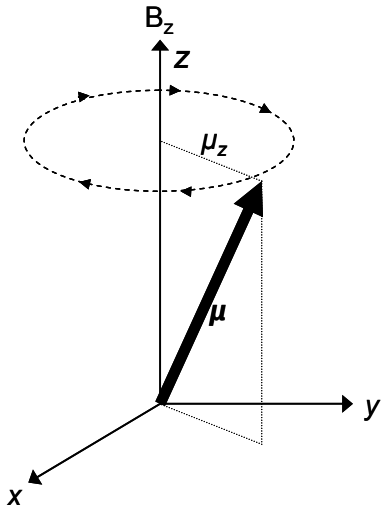

Figure 2-3: Illustration of the precessional cone of the magnetic moment.

The magnetic moment of a nucleus points either in the same direction to the spin polarisation for nuclei with $\gamma > 0$, or in the opposite direction to the spin polarisation for nuclei with $\gamma < 0$. In the absence of a magnetic field, the magnetic moments are distributed isotropically and the sample is in equilibrium. When a magnetic field is applied to the sample, the magnetic moments experience an aligning torque. This interacts with their spin to cause them to precess about the magnetic field, minimising the magnetic energy. The angle of the cone depends on the initial spin polarisation and coherence. Spins behave in this way because they have angular momentum as well as a

magnetic moment and this resulting behaviour is determined by the gyroscope effect. If the spin is rotating with its axis exactly vertical then the motion of the spin is stable. However, if the spin is not exactly vertical, then a torque **T** is applied:

$$\mathbf{T} = \frac{d\mathbf{L}}{dt} = \frac{d(I\boldsymbol{\omega})}{dt} = I\boldsymbol{\alpha} \qquad \textbf{[2-13]}$$

where **L** is the angular momentum, I is the moment of inertia, **ω** is the angular velocity and **α** is the angular acceleration. The torque is applied perpendicular to the axis of rotation and also perpendicular to the angular momentum; this results in a rotation about an axis perpendicular to both of these. The angular velocity of precession $\boldsymbol{\Omega_p}$ is related to torque and angular momentum by:

$$\mathbf{T} = \boldsymbol{\Omega}_p \times \mathbf{L} \qquad \textbf{[2-14]}$$

and the angular rate of precession is defined as:

$$\omega_0 = \gamma B_0 \qquad \textbf{[2-15]}$$

The corresponding frequency is called the Larmor frequency:

$$\nu_L = \frac{\omega_L}{2\pi} = \frac{\gamma B_z}{2\pi} \qquad \textbf{[2-16]}$$

This is the natural precession frequency of the classical magnetic moment and is identical to the frequency of photons required to drive transitions between the magnetic energy levels of a spin-½ nucleus (equation 2-6). The Larmor frequency has a defined sign indicating the sense of the spin precession; most nuclei have a positive γ resulting in a negative Larmor frequency and clockwise precession. Nuclei that have a negative γ (such as ^{15}N and ^{29}Si) precess anti-clockwise; the electron also has a negative γ.

Nuclear spins interact with electromagnetic photons to induce changes in the spin state; these transitions are driven by magnetic dipoles. Equation 2-9 described a stationary magnetic field, but if an oscillating and therefore time-

dependent magnetic field $\mathbf{B}_1(t)$ is applied perpendicular to the z axis, then the total field is represented by two components:

$$\begin{aligned}\mathbf{B} &= B_z\mathbf{k} \\ \mathbf{B}_1(t) &= 2B_1\cos(\omega t)\mathbf{i}\end{aligned} \qquad \textbf{[2-17]}$$

Since $\mathbf{B}_1(t)$ is applied perpendicular to the *z* axis, it is linearly polarised along the *x* axis and can therefore be resolved into two circular components rotating at $\pm\omega$:

$$\begin{aligned}\mathbf{B}_a(t) &= B_1\left[\cos(\omega t)\mathbf{i} + \sin(\omega t)\mathbf{j}\right] \\ \mathbf{B}_c(t) &= B_1\left[\cos(\omega t)\mathbf{i} - \sin(\omega t)\mathbf{j}\right]\end{aligned} \qquad \textbf{[2-18]}$$

Here, $\mathbf{B}_c(t)$ represents the clockwise rotating component with angular frequency $-\omega$ and $\mathbf{B}_a(t)$ is the anti-clockwise rotating component with angular frequency $+\omega$. Figure 2-4 illustrates these two circulating polarised fields.

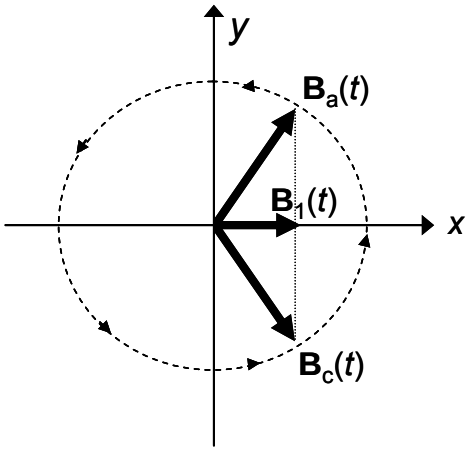

Figure 2-4: Two circulating polarised fields comprising of clockwise and anti-clockwise rotating components of the time-dependent magnetic field.

Taking this into account, the equation of motion of $\boldsymbol{\mu}$ (equation 2-8) becomes:

$$\frac{d\boldsymbol{\mu}}{dt} = \gamma\,\boldsymbol{\mu}\times\left[\mathbf{B} + \mathbf{B}_a(t) + \mathbf{B}_c(t)\right] \qquad \textbf{[2-19]}$$

The precessional motion due to the constant torque exerted by **B** is now perturbed by extra radiofrequency torques from $\mathbf{B}_a$ and $\mathbf{B}_c$. At normal RF field strengths, the effects of the torques from $\mathbf{B}_a$ and $\mathbf{B}_c$ are much weaker than **B**. However, if $\omega = \omega_{L,}$ that is if $\mathbf{B}_c$ is rotating at the same frequency as $\boldsymbol{\mu}$ is precessing, then the torque due to the RF field is consistently in the same direction and perturbs the motion of $\boldsymbol{\mu}$ dramatically. In this situation, the torque from $\mathbf{B}_a$ is insignificant and equation 2-19 becomes:

$$\frac{d\boldsymbol{\mu}}{dt} = \gamma\,\boldsymbol{\mu} \times \left[\mathbf{B} + \mathbf{B}_c(t)\right] \qquad \textbf{[2-20]}$$

The effect of this additional rotation is to increase the precessional angle as shown in Figure 2-5. For a classical magnetic moment a continuum of angles is available to the system, but for a quantum description this is not the case; for a spin-½ quantum system, only two orientations corresponding to μ_α and μ_β are available.

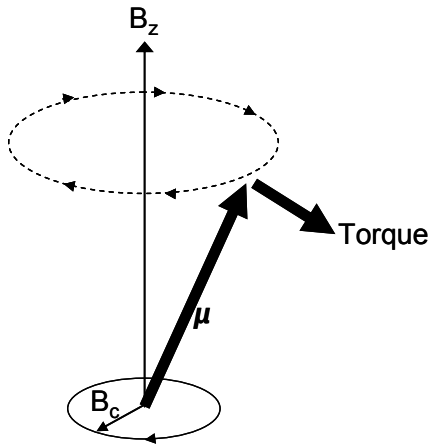

Figure 2-5: The torque due to the RF field is consistently in the same direction when a system is on resonance.

If the system deviates from resonance ($\omega = \omega_L$), the torque no longer acts in a consistent direction; the ability of the RF field to induce transitions progressively diminishes as ω moves further from ω_L.

In order to understand excitation (on- and off-resonance) the equations of motion of $\boldsymbol{\mu}$ can be solved by allowing ω to take an arbitrary value. If $\omega \approx \omega_L$

then $\mathbf{B}_a(t)$ is irrelevant since it is off-resonance and the equation of motion of $\boldsymbol{\mu}$ becomes:

$$\begin{aligned}\frac{d\boldsymbol{\mu}}{dt} &= \gamma\,\boldsymbol{\mu}\times\left[\mathbf{B}+\mathbf{B}_c(t)\right] \\ &= \gamma\,\boldsymbol{\mu}\times\left[B_z\mathbf{k}+B_1\left(\cos(\omega t)\mathbf{i}-\sin(\omega t)\mathbf{j}\right)\right]\end{aligned} \qquad \textbf{[2-21]}$$

The analysis of this general case can be simplified considerably by moving into the rotating frame of reference which rotates clockwise about the z axis at a frequency of $-\omega$.

In the rotating frame of reference, the time dependence of the $\mathbf{B}_1(t)$ is removed from the equations of motion of $\boldsymbol{\mu}$. The $\mathbf{B}_1$ field becomes:

$$\mathbf{B}_1(t) = B_1\mathbf{i}' \qquad \textbf{[2-22]}$$

and the magnetic moment vector becomes:

$$\boldsymbol{\mu} = \mu_{x'}\mathbf{i}' + \mu_{y'}\mathbf{j}' + \mu_z\mathbf{k} \qquad \textbf{[2-23]}$$

where ($\mathbf{i}'$, $\mathbf{j}'$, $\mathbf{k}$) are the unit vectors in the new axis system (x', y', z). In classical mechanics, the time derivative of a vector, $\mathbf{r}$, in the non-rotating frame of reference is $\left(\frac{d\mathbf{r}}{dt}\right)_{x,y,z}$ and this can be transformed into the rotating frame of reference:

$$\left(\frac{d\mathbf{r}}{dt}\right)_{x,y,z} = \boldsymbol{\omega}\times\mathbf{r} + \left(\frac{d\mathbf{r}}{dt}\right)_{x',y',z} \qquad \textbf{[2-24]}$$

where $\boldsymbol{\omega}(=-\omega\mathbf{k})$ is the angular velocity. By applying this transformation to equation 2-19, the equation of motion becomes:

$$\begin{aligned}\boldsymbol{\omega}\times\boldsymbol{\mu} + \left(\frac{d\boldsymbol{\mu}}{dt}\right)_{x',y',z} &= \gamma\boldsymbol{\mu}\times\left(\mathbf{B}+\mathbf{B}_1(t)\right) \\ &= \gamma\boldsymbol{\mu}\times\left(B_z\mathbf{k}+B_1\mathbf{i}'\right)\end{aligned} \qquad \textbf{[2-25]}$$

We can rearrange this to obtain the time derivative of the magnetic moment:

$$\left(\frac{d\boldsymbol{\mu}}{dt}\right)_{x',y',z} = \gamma\boldsymbol{\mu}\times\left(B_z\mathbf{k}+\frac{\boldsymbol{\omega}}{\gamma}+B_1\mathbf{i}'\right) = \gamma\boldsymbol{\mu}\times\left(\left(B_z-\frac{\omega}{\gamma}\right)\mathbf{k}+B_1\mathbf{i}'\right) \qquad \textbf{[2-26]}$$

If an effective magnetic field is defined as:

$$\mathbf{B}_{eff} = B_1\mathbf{i}'+\left(B_z-\frac{\omega}{\gamma}\right)\mathbf{k} \qquad \textbf{[2-27]}$$

Then equation 2-26 becomes:

$$\left(\frac{d\boldsymbol{\mu}}{dt}\right)_{x',y',z} = \boldsymbol{\mu}\times\gamma\mathbf{B}_{eff} \qquad \textbf{[2-28]}$$

This equation implies that the magnetic moment will precess about the axis of $\mathbf{B}_{eff}$ with frequency $\omega_{eff} = \gamma B_{eff}$ and this is illustrated in Figure 2-6. The effective field comprises of components in the x' and z direction so the effective field is in the $x'z$ plane.

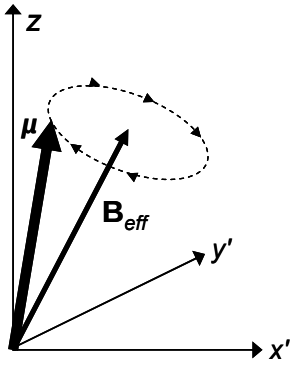

Figure 2-6: The magnetic moment μ precesses about the axis of the effective magnetic field B_{eff}.

The time dependence has been removed, but there has been an additional virtual field component $\boldsymbol{\omega}/\gamma$ introduced; for $\boldsymbol{\omega} = -\omega\mathbf{k}$, this virtual field $(-\omega/\gamma)\mathbf{k}$ is along the $-z$ direction and works against the effects of the static magnetic field **B**. The z component of the effective magnetic field (from equation 2-27) is referred to as the offset field since it measures the deviation of the RF carrier frequency from the resonance condition.

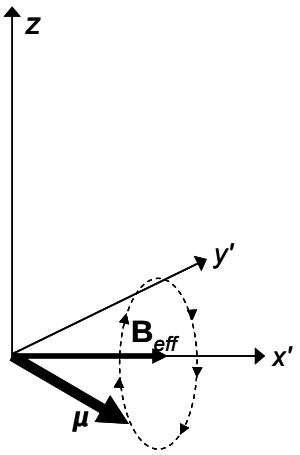

Figure 2-7: The magnetic moment μ precesses about the z axis when the $B_1(t)$ component of the effective magnetic field B_{eff} is zero.

If the RF field is on-resonance, the offset field along the z axis is zero and $\boldsymbol{\mu}$ precesses about the x' axis in the $y'z$ plane (Figure 2-7) at an angular frequency of $\omega = \gamma B_1$ since:

$$\mathbf{B}_{eff} = B_1\mathbf{i}' \qquad \textbf{[2-29]}$$

In a time t_w, $\boldsymbol{\mu}$ rotates through an angle θ:

$$\theta = \gamma B_1 t_w \qquad \textbf{[2-30]}$$

Therefore, if a RF pulse of duration t_w and frequency ω_L is applied to a system that is polarised in a plane perpendicular to the applied static magnetic field, $\boldsymbol{\mu}$ tips through an angle θ. This is often called the tip or flip angle and corresponds to inducing transitions between the α and β spin states of the

system; absorption and stimulated emission of the electromagnetic photons will be observed.

2.2.4 Bulk magnetisation

Real systems consist of an ensemble of varying nuclear spins and observed macroscopic quantities reflect the average response of the sample. The bulk magnetisation contains information about the individual magnetic moments and is described by the macroscopic magnetic moment vector **M**.

In the absence of a magnetic field, spins are uniformly distributed resulting in a net magnetisation **M** of zero. If a magnetic field is applied, spins execute Larmor precession and after a period of time later the system reaches thermal equilibrium. For a spin-½ system in thermal equilibrium, there are two possible spin states (low, α, and high, β, energy); the populations of the two states, N_α and N_β, are related by:

$$\frac{N_\beta}{N_\alpha} = \exp\left(-\frac{\hbar\gamma B_z}{k_B T}\right) = \exp\left(-\frac{\Delta E}{k_B T}\right) \qquad \textbf{[2-31]}$$

where T is temperature and k_B is the Boltzmann constant. It can be seen from this equation that the population ratio of the states is dependent on the magnetic field and the temperature of the sample. In thermal equilibrium, there is a higher population of spins in the α state ($m_I = +½$) than in the β state ($m_I = -½$) since the α state has the lowest energy; this results in a net magnetisation **M**. A value of **M** can be obtained by applying the high temperature approximation ($k_B T >> \Delta E$) so that equation 2-31 can be expanded as a power series, and approximated to:

$$\frac{N_\beta}{N_\alpha} \approx 1 - \frac{\hbar\gamma B_z}{k_B T} \qquad \textbf{[2-32]}$$

The population difference n can then be expressed as:

$$\begin{aligned} n &= N_\alpha - N_\beta \\ &= N_\alpha \frac{\hbar\gamma B_z}{k_B T} \\ &\cong \frac{N}{2}\frac{\hbar\gamma B_z}{k_B T} \end{aligned} \qquad \textbf{[2-33]}$$

where N_α can be approximated to $N/2$ (N = total number of spins) since the difference in the populations is very small (3 ppm). The magnitude of the net magnetisation **M** is the vector sum of the magnetic moments of the individual spins:

$$\left|\mathbf{M}\right| = M_0 = N_\alpha \mu_z^{(\alpha)} + N_\beta \mu_z^{(\beta)} \qquad \textbf{[2-34]}$$

Since $\mu_z^{(\alpha)} = -\mu_z^{(\beta)}$ and $\boldsymbol{\mu} = \gamma\mathbf{P} = \gamma\hbar m_I$, the magnitude of the net magnetisation for $m_I = ½$ becomes:

$$M_0 = n\frac{\hbar\gamma}{2} \qquad \textbf{[2-35]}$$

This is the Curie Law and can be written as:

$$\left|M\right| = M_0 = \frac{1}{4}N(\hbar\gamma)^2\frac{B_z}{k_B T} \qquad \textbf{[2-36]}$$

As long as the high temperature approximation is valid, the magnitude of the magnetisation vector is proportional to the applied magnetic field and inversely proportional to the temperature of the system.

The bulk magnetisation **M** obeys the same classical equation of motion as the case of the single spin earlier. The time derivative of **M** (torque) is therefore:

$$\frac{d\mathbf{M}}{dt} = \gamma\mathbf{M}\times\mathbf{B} \qquad \textbf{[2-37]}$$

and the description used for a single magnetic moment can be applied.

2.2.5 Relaxation

When a system is placed in a magnetic field all spins align with the direction of the field with a resulting magnetisation **M**, the spins in a system are in their lowest energy state and are therefore in thermal equilibrium:

$$M_z = M_0 \quad ; \quad M_x = M_y = 0 \qquad \textbf{[2-38]}$$

If, for example, a 90º RF pulse is applied along the *x* axis, the spins are excited and the magnetisation **M** is tipped away from the *z* axis and precesses in the *x*-*y* plane, such that $M_z = 0$ and M_x and M_y are both finite quantities. After the RF pulse has been applied, the spins must return to the lowest energy state to regain equilibrium; this process is termed spin relaxation. There are two processes of relaxation: longitudinal and transverse. In an ensemble of spins-½, there are two time constants for these relaxation processes: the longitudinal relaxation time constant (T_1) for equilibration of spin populations and the transverse relaxation time constant (T_2) for spin coherence decay. The processes that T_1 and T_2 are attributed to are independent, but $T_2 < T_1$.

2.2.5.1 T_1

Longitudinal relaxation, also called spin-lattice relaxation, is concerned with return of the spin system back to the Boltzmann distribution values ($M_z = M_0$) as the spins give the energy acquired from the RF pulse back to the surrounding lattice. Longitudinal relaxation varies between tissue types and depends on efficiency of energy transfer from the protons to the lattice. The most efficient energy transfer occurs when the natural motional frequency of the molecules containing magnetic moments (e.g. protons) is equal to the Larmor frequency.

Water and solid tissues do not transfer energy efficiently; the natural motional frequency is much greater than the Larmor frequency for water and less for

solid tissue. Both water and solid tissue both have long T_1 values, but water has a longer T_1 than solid tissue. Fat has hydrogen protons with almost the same natural motional frequency as the Larmor frequency; the efficiency of energy transfer is therefore high resulting in a decrease in T_1 compared with water or solid tissue. Since most of the water in the body is bound to hydrophilic macromolecules like protein, these bound molecules have a reduced motion and the natural motional frequencies of these molecules is closer to the Larmor frequency, resulting in a more efficient energy transfer and a shortening of T_1.

2.2.5.2 T_2

Transverse relaxation, also called spin-spin relaxation, is concerned with the spins dephasing. After a 90º RF pulse has been applied, all spins are initially brought into phase and are rotating at approximately the same frequency ω_0, but the spins will dephase over time. There are two mechanisms that cause this: intrinsic effects such as interactions between individual spins (spin-spin interactions) and external magnetic field inhomogeneities. Transverse relaxation varies due to varying interactions between hydrogen protons. If a tissue has a high water content, there are few spin-spin interactions among the protons due to the sparsity of these molecules and dephasing occurs at a slow rate (long T_2). However, if the tissue is more solid, there will be more spin-spin interactions due to the compact structure, and dephasing of the spins will occur faster (short T_2). Fat and proteinaceous materials show more dephasing than in water, but less than for a solid (intermediate T_2).

2.2.5.3 Spin interaction mechanisms

Spins that are near each other are affected by dipole-dipole interactions. This means that the magnitude and direction of the magnetic field exerted by one spin affects other spins in its vicinity. For example, one spin may experience the applied magnetic field B_0 but also a contribution from a small magnetic

field due to a neighbouring spin that is aligned with the applied field, resulting in a slightly higher magnetic field. Similarly, if a neighbouring spin was aligned against the B_0 field, then the spin would experience a slightly lower magnetic field. This results in inhomogeneities in the magnetic field strength experienced by the spins, causing them to dephase. However molecular motion means these effects vary with time in a random way, so the dephasing cannot be recovered.

For spins-½, the dominant mechanism of relaxation is due to dipole-dipole coupling between two nuclear spins in the same molecule. As the molecule tumbles, the magnitude and direction of the magnetic field, exerted by one spin on the other, changes. Another source of local fields is due to chemical shift anisotropy (CSA); molecular electron currents, induced by the external magnetic field cause local fields and as the molecules tumble, in a liquid, the direction and magnitude of these fields change too. These local fields, together with the large static field, result in a total field that fluctuates slightly in direction and magnitude as the molecules rotate. This subtle effect is however large enough to cause longitudinal relaxation.

The fluctuating transverse fields have the following properties:

$$\begin{aligned} \langle B_x(t) \rangle &= 0 \\ \langle B_x^2(t) \rangle &\neq 0 \end{aligned} \qquad \textbf{[2-39]}$$

That is to say that the mean fluctuating field is zero and the mean square fluctuating field is a finite value. The autocorrelation function G is used to describe how rapidly the field is fluctuating over a time τ:

$$G(\tau) = \langle B_x(t) B_x(t+\tau) \rangle \neq 0 \qquad \textbf{[2-40]}$$

A rapidly fluctuating field has an autocorrelation function that decays quickly with respect to τ, whereas a slowly fluctuating field has an autocorrelation function that decays much slower with respect to τ. If $\tau = 0$, then $G(\tau)$ is

simply equal to the mean square field $\langle B_x^2(t) \rangle$. The decay rate and form of the autocorrelation function is very important for spin relaxation. In general the autocorrelation function is large for small values of τ and small for large values of τ. It is therefore often assumed that the autocorrelation function follows an exponential form:

$$G(t) = \langle B_x^2 \rangle \exp\left(-\frac{\tau}{\tau_c}\right) \qquad \textbf{[2-41]}$$

The parameter τ_c is the correlation time of the fluctuations; rapid fluctuations have a small value of τ_c whereas slow fluctuations have a large value of τ_c. Qualitatively, the correlation time indicates the time passed before the random field changes sign. It is affected by temperature; τ_c is shortened with increased temperature since the increase in temperature results in increased molecular motion and vice versa. Therefore the relaxation parameters, T_1 and T_2, are dependent on temperature.

The spectral density $J(\omega)$ is defined as twice the Fourier transform of the autocorrelation function:

$$J(\omega) = 2\int_0^\infty G(\tau)\exp(i\omega\tau)d\tau \qquad \textbf{[2-42]}$$

If the transverse field fluctuates rapidly, then the correlation time is short and the spectral density function is broad; similarly if the transverse field fluctuates slowly, then the correlation time is long and the spectral density function is narrow. The area under the spectral density function is independent of τ_c and is twice the mean square amplitude of the fluctuating field ($2\langle B_x^2 \rangle$). The spectral density function can be normalised with respect to the area under the curve; this is termed the normalised spectral density:

$$j(\omega) = \frac{\tau_c}{1+\omega^2\tau_c^2} \qquad \textbf{[2-43]}$$

The Bloembergen-Purcell-Pound theory [2] uses the normalised spectral density to explain the correlation between relaxation and the state of the substance. T_1 and T_2 are related to the spectral density by:

$$\frac{1}{T_1} = \frac{3}{10} b^2 \{ j(\omega_0) + 4 j(2\omega_0) \}$$
$$\frac{1}{T_2} = \frac{3}{20} b^2 \{ 3 j(0) + 5 j(\omega_0) + 2 j(2\omega_0) \} \qquad \textbf{[2-44]}$$

where *b* is the dipole-dipole coupling constant given by:

$$b = -\frac{\mu_0}{4\pi} \frac{\hbar \gamma^2}{r^3} \qquad \textbf{[2-45]}$$

T_1 and T_2 are both related to the correlation time and therefore temperature dependant (Figure 2-8). This theory works well for pure substances, but not for the human body which is much more complicated.

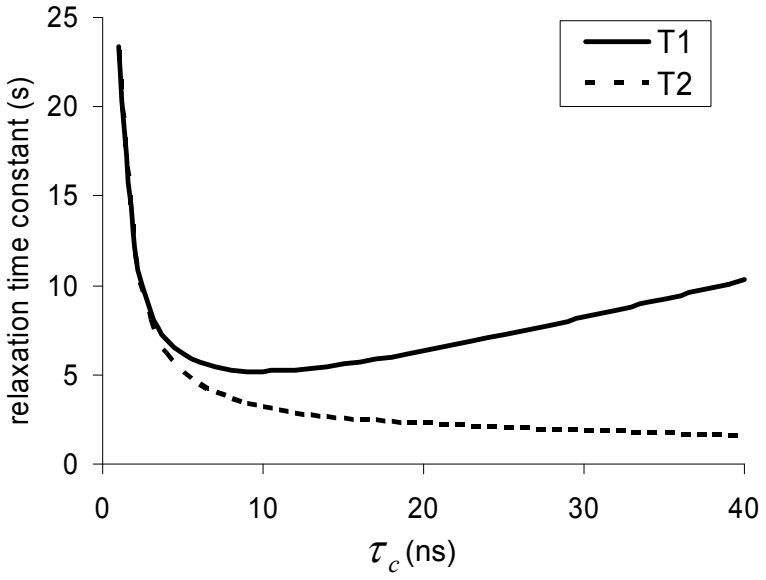

Figure 2-8: Variation of T_1 and T_2 with correlation time τ_c for intra-molecular dipole-dipole relaxation (calculated for two protons separated by 0.2 nm, in a field of 1.5 T).

In addition to the dipole-dipole interactions that cause small time-varying inhomogeneities in the magnetic field, the external field will never be

completely homogeneous. The result of this, is that once again, the spins in the system will not be experiencing exactly the same field strength and therefore transverse dephasing occurs. Dipole-dipole interactions and effects such as molecular diffusion around small field inhomogeneities forms the basis of T_2 contrast in BOLD (**b**lood **o**xygenation **l**evel-**d**ependent) MRI studies.

*2.2.5.4 T_2**

T_2 does not depend on the external magnetic field inhomogeneities and is sample dependent. Another relaxation time constant is required: T_2* is dependent on both the sample interactions and the external magnetic field inhomogeneities, so varies according to magnet uniformity. T_2* is dependent on T_2 decay:

$$\frac{1}{T_2 *} = \frac{1}{T_2} + \frac{1}{T_2'} \qquad \textbf{[2-46]}$$

In all cases, T_2 is measured smaller than T_2*, since no magnet is perfectly uniform. Figure 2-9 shows the decaying sinusoidal waveform that the receiver acquires. As the spins precess around the *z*-axis, they are continuously decaying in magnitude. The received signal is therefore an oscilating, decaying function called a free induction decay (FID) (Figure 2-9).

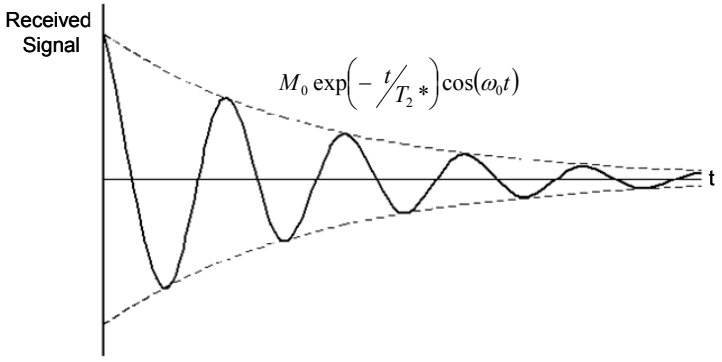

Figure 2-9: Free induction decay illustrating the effect of T_2*.

2.2.5.5 *Effect of relaxation*

The effect of relaxation can be incorporated into the classical equation of motion of **M** (equation 2-37) to give:

$$\frac{d\mathbf{M}}{dt} = \gamma \mathbf{M} \times \mathbf{B} - \frac{\left(M_z - M_0\right)}{T_1}\mathbf{k} - \frac{M_x}{T_2}\mathbf{i} - \frac{M_y}{T_2}\mathbf{j} \qquad \textbf{[2-47]}$$

where the applied magnetic field $\mathbf{B} = B_z\mathbf{k} + B_1(t)\mathbf{i}$. After the 90º RF pulse, the $B_1(t)$ component is zero and equation 2-47 can be split into individual vector components of the magnetisation **M**, known as the Bloch equations (after Felix Bloch):

$$\begin{aligned} \frac{dM_x}{dt} &= \gamma M_y B_z - \frac{M_x}{T_2} \\ \frac{dM_y}{dt} &= -\gamma M_x B_z - \frac{M_y}{T_2} \\ \frac{dM_z}{dt} &= -\frac{\left(M_z - M_0\right)}{T_1} \end{aligned} \qquad \textbf{[2-48]}$$

Figure 2-10 illustrates these equations graphically for a spin system that is initially tipped into the *x*-*y* plane.

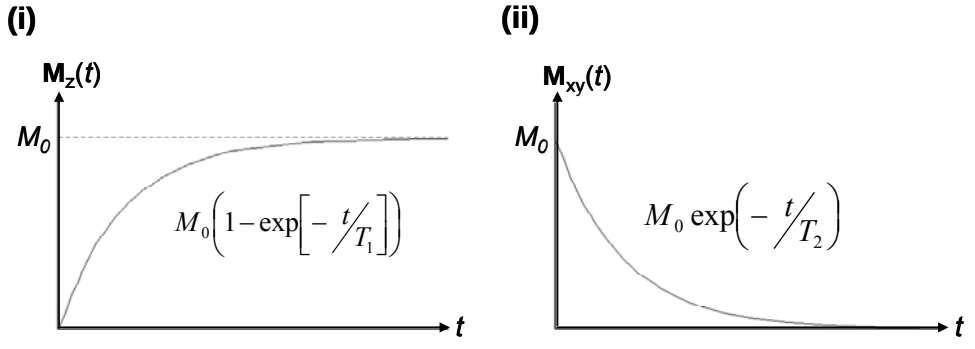

Figure 2-10: Relaxation of the (i) longitudinal and (ii) transverse magnetisation. The equations of the curves are found by solving the Bloch equations (2-48).

2.2.6 Relaxometry

2.2.6.1 Measuring T_2

The transverse relaxation time T_2 can be measured using a spin echo pulse sequence which refocuses the transverse magnetisation and removes the effects of magnetic field inhomogeneities.

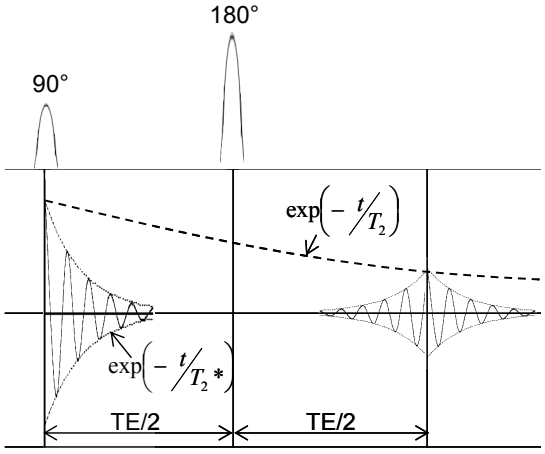

Figure 2-11: Spin echo sequence.

Figure 2-11 shows a spin echo sequence which eliminates the dephasing caused by non-uniformity of the magnetic field. The 90º RF pulse tips the magnetisation into the *x*-*y* plane (Figure 2-12i), where the spins are in phase and precess at a frequency ω_0. Over time, the spins dephase and coherence is lost (Figure 2-12ii). At a time TE/2, a 180º RF pulse is applied which causes the spins to flip by 180º in the *x*-*y* plane. The spins continue to precess at the same frequency (Figure 2-12iii). After a further time TE/2, the spins will rephase and maximum coherence will occur (Figure 2-12iv); this is the spin echo. The magnitude of the magnetisation at the echo will be smaller than the initial FID since the random dipole-dipole interactions cannot be refocused.

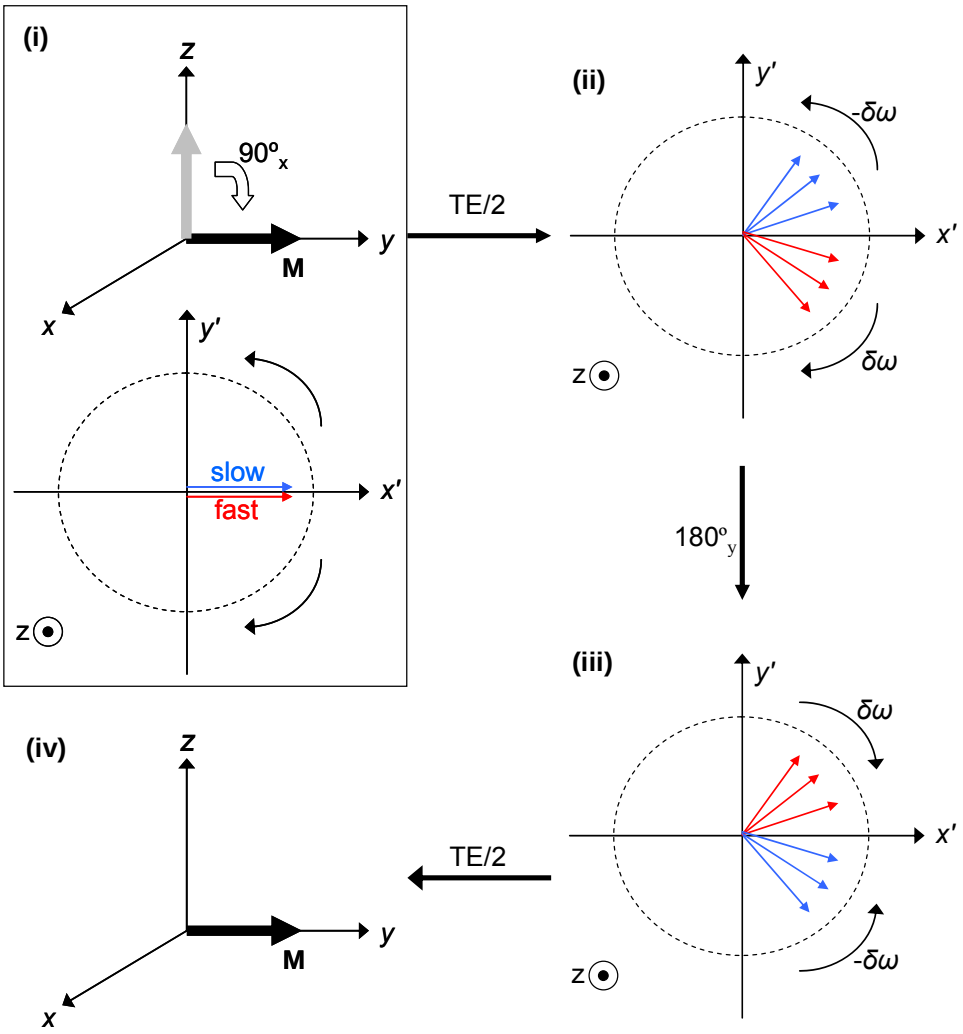

Figure 2-12: Illustration of spin precession during a spin echo sequence.

By repeating the above sequence at different echo times (TEs), a series of measurements of the echo peak amplitudes can be made as a function of echo time *TE* and T_2 can be determined using:

$$M_{echo} = M_0 \exp\left(\frac{-TE}{T_2}\right) \qquad \textbf{[2-49]}$$

where M_{echo} is the peak amplitude of the echo.

Development of sequences for measuring T_2 form a large part of this thesis and an extensive discussion on methods for measuring T_2 can be found in chapter 3.

2.2.6.2 Measuring T_1

Measurements of T_1 are based on the Bloch equation:

$$\frac{dM_z}{dt} = -\frac{M_z - M_0}{T_1} \qquad \textbf{[2-50]}$$

There are several techniques that can be used to exploit this relationship to measure T_1; the inversion recovery sequence is the most common (Figure 2-13).

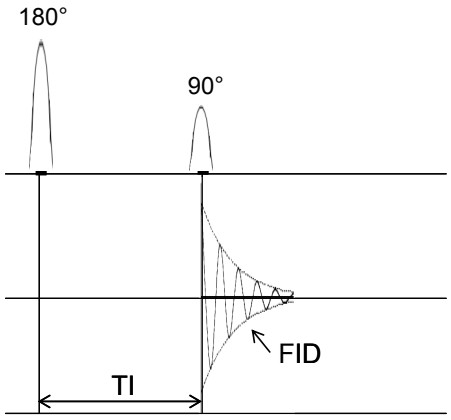

Figure 2-13: Inversion recovery sequence.

A 180º RF pulse is applied to the system to invert the magnetisation $\mathbf{M} = -M_0$, and a time later a 90º RF pulse is applied. The time between pulses is often called the inversion time (*TI*). The 90º pulse rotates any longitudinal magnetisation into the transverse plane. By repeating the experiment at varying inversion times, the recovery of the longitudinal magnetisation can be plotted as a function of time:

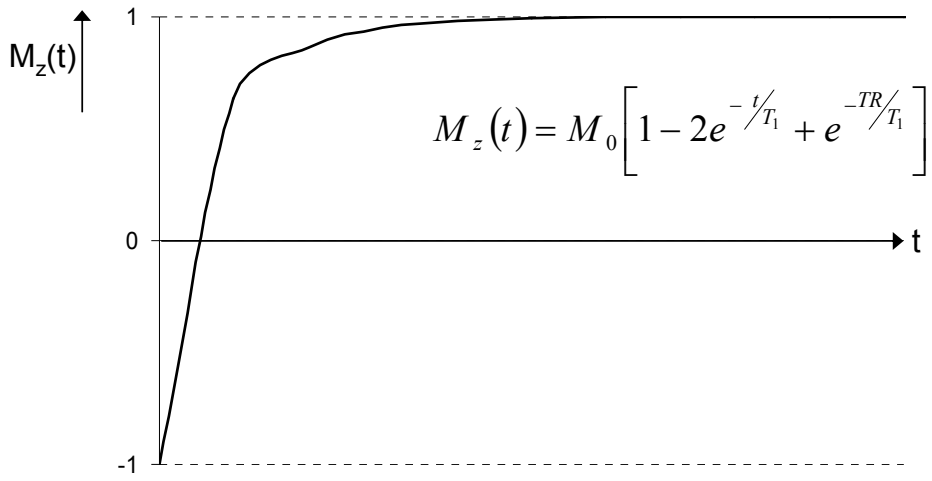

Figure 2-14: Inversion recovery of magnetisation.

It is crucial that the system is fully relaxed (i.e. in thermal equilibrium) before every 180º RF pulse is applied and so the repetition time should always be > $5T_1$.

2.3 MAGNETIC RESONANCE IMAGING

2.3.1 Introduction

The principles behind obtaining and constructing images using magnetic resonance will now be explained. The most basic sequence (spin warp imaging) will then be introduced, followed by some fast scanning sequences (echo planar imaging, fast spin echo and steady state imaging) and advanced techniques (3-D, partial Fourier, parallel imaging) that will be used in this work. The inherent properties of MRI allow images to be obtained with different contrasts and this will be discussed. Finally, there is a discussion on artifacts caused by patients, motion, gradients, magnetic susceptibility and image processing.

2.3.2 Image construction

2.3.2.1 k-space

The understanding of *k*-space, or reciprocal space, is crucial to the understanding of how the signal from magnetic resonance imaging is spatially encoded. Mansfield and Grannell [3] described a generalised theory of how images could be formed using *k*-space. They found that the inverse Fourier transform of the FID yielded spatial information about the layers in the solid under investigation and the results were analogous to those found using x-ray diffraction.

If a sample is placed in a homogeneous magnetic field, the precessional frequency for the protons is $\omega_0 = \gamma B_0$. When an RF pulse is applied to the sample, the resultant signal $S(t)$ is given by

$$S(t) = \int \rho(r) \exp[i\omega_0 t]\, dr \qquad \textbf{[2-51]}$$

where $\rho(r)$ is the spin density at a position r. If time dependent magnetic field gradients are applied, equation 2-51 becomes

$$S(t) = \int \rho(r) \exp\left[i\gamma \int_0^t \mathbf{G}(\tau)\cdot \mathbf{r} d\tau \right] dr \qquad \textbf{[2-52]}$$

The accumulated phase evolution induced by the switching gradients $\mathbf{G}(\tau)$ can be written as

$$\mathbf{k}(t) = \gamma \int_0^\tau \mathbf{G}(\tau) d\tau \qquad \textbf{[2-53]}$$

By applying this *k*-space transformation, equation 2-53 can be written as

$$S(k) = \int \rho(r) \exp[i\mathbf{k}\cdot\mathbf{r}]\, dr \qquad \textbf{[2-54]}$$

and it can now be seen that the proton density $\rho(r)$, which describes the shape of the object, can be reconstructed from $S(k)$ by Fourier transformation:

$$\rho(r) = \int S(k) \exp[-i\mathbf{k} \cdot \mathbf{r}]\, dk \qquad \textbf{[2-55]}$$

It is clear from equation 2-55 that a spatial map can be formed based on proton density, and by varying the gradients, the whole of *k*-space can be sampled. There are many different methods for sampling *k*-space. The sampling of *k*-space is affected by time and relaxation effects, since the signal must be sampled in a finite amount of time before the signal has decayed.

2.3.2.2 Slice selection

The inclusion of slice selection reduces the requirement of encoding gradients in three dimensions to just two dimensions. If a magnetic field gradient is applied in the *z* direction and a selective frequency RF pulse is applied, then a transverse slice across the body will be excited [4]. This is because only the spins along the gradient that have a precessional frequency within the bandwidth of the RF pulse will be excited. The thickness of the slice is dependent on the bandwidth of the pulse, but it is also related to the gradient strength across the field of view. For a given gradient strength (G_z), increasing the RF bandwidth (i.e. the range of frequencies, $\Delta\omega$) will increase slice thickness (Δz) and similarly, for a given RF bandwidth increasing the gradient strength will reduce the slice thickness because there is a larger range of frequencies. This can be seen from the following equation:

$$\Delta z = \frac{\Delta\omega}{\gamma G_z} \qquad \textbf{[2-56]}$$

Compromises must therefore be made between slice thickness, gradient strength and echo time. A rectangular slice profile is most commonly required for slice selection and this can be achieved using a truncated *sinc* pulse. The pulse is truncated to allow short pulse duration, but this means the pulse is imperfect.

When slice selection is applied, this results in spins dephasing. Therefore to re-establish the original phase of the spins, a gradient of opposite polarity and half the size of the original gradient must be applied (Figure 2-15). However, after a refocusing 180° pulse, the spins do not lose their original phase relationship, so there is no need for the extra rephasing gradient.

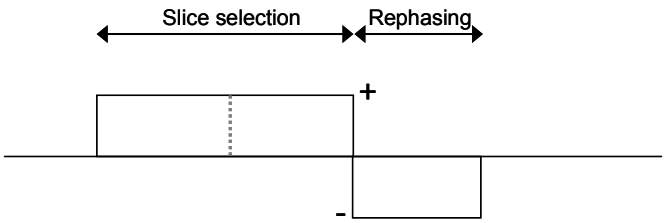

Figure 2-15: Slice selection gradient, which includes a rephasing component to maintain phase relationships between spins.

2.3.2.3 Spatial encoding

In the last section a slice was selected, but now it is necessary to determine where in the slice the received signal originated from. This is done using two gradients: phase encode and frequency encode (or readout). The phase encoding gradient is applied after slice selection but before the frequency encoding gradient.

After the slice selection gradient has been applied, all the spins are in phase. When a phase encoding gradient is applied, a linear variation in the precessional frequency of the spins occurs in the direction of the gradient. After the gradient is turned off, the spins precess at the Larmor frequency again, but with the addition of a phase shift. For each repetition of a sequence, a specific phase change is implemented by a specific gradient strength. The spins in the centre of the field of view will experience no phase change, whilst spins experiencing the largest effects of the gradient field (G_y) will experience the largest phase shifts. The modulation of phase with phase encoding gradient amplitude allows each position along the phase encode axis to be spatially encoded by the amount of phase shift. The phase encode gradient

strength is usually changed for every repetition of a particular sequence to allow another line of *k*-space to be filled with each increment in strength, although in early implementations, gradient duration was changed. Phase encoding is also used in the third dimension for three-dimensional imaging (see section 2.3.6).

After phase encoding has been applied during each repetition of the sequence, a frequency encoding gradient must be applied so that the decay of the signal arising from the excited spins can be readout. Whilst a frequency encoding gradient is turned on, spins will precess at a range of frequencies according to the strength of the gradient they are experiencing. The spins in the centre of the field of view will precess at the Larmor frequency, whilst the spins at the edge of the field of view will precess with a frequency higher or lower than the Larmor frequency according to the strength of the gradient experienced. A projection profile of the object is created by summing the signal amplitude at each position along the frequency encoding gradient and this contributes to a single line of *k*-space. After all of *k*-space has been filled, the frequency data is then Fourier transformed and an image is formed.

The sampling bandwidth affects the signal to noise ratio (SNR):

$$SNR \propto \frac{1}{\sqrt{BW}} \qquad \textbf{[2-57]}$$

However artifacts, including chemical shift artifacts, can occur if the bandwidth is too narrow so compromises must be made.

The simplest method for sampling *k*-space is still used regularly in clinical practice. It was introduced in 1980 by Edelstein et al. [5] and is called spin warp imaging (Figure 2-16).

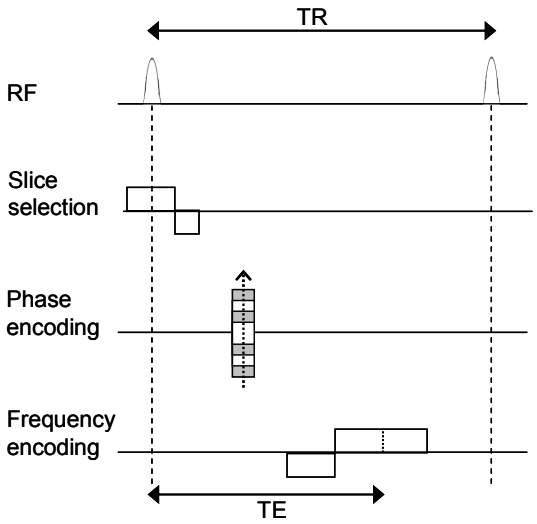

Figure 2-16: Pulse sequence diagram for spin warp imaging (not to scale).

In this sequence, a slice selective 90° pulse is applied to a sample, so equation 2-54 can be simplified to just two dimensions:

$$S(k_x, k_y) = \int\int \rho(x, y)\exp\left[i\left(k_x x + k_y y\right)\right] dxdy \qquad \textbf{[2-58]}$$

Phase and frequency encoding is performed using the gradient method described above. *K-space* is sampled by altering the amplitude or timing of the phase encoding pulse: fix the gradient strength then vary the duration, or, fix the duration then vary the gradient strength. Normally, the duration is kept constant and the gradient strength is altered; if there are static field inhomogeneities, the extra phase accumulated will be the same for each line of *k*-space. Figure 2-17 shows the *k*-space sampling strategy for this sequence.

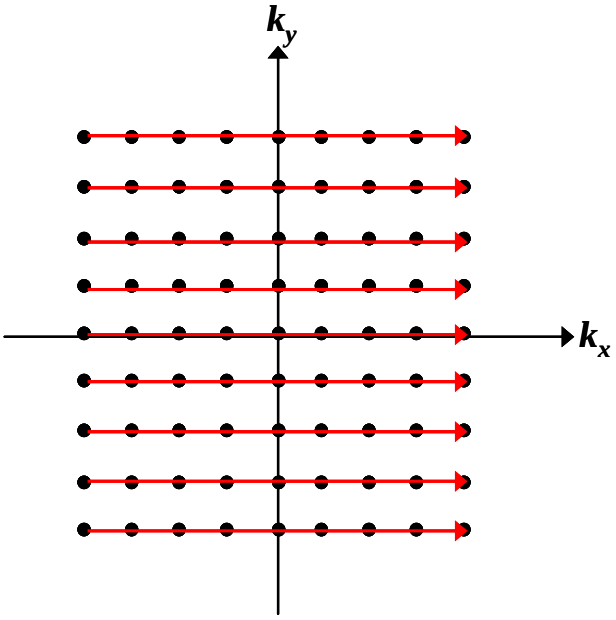

Figure 2-17: Strategy for sampling *k*-space in spin warp imaging.

Mathematically, the method in which *k*-space is sampled can be expressed using equation 2-59:

$$k_x = \gamma G_x t_x \quad \text{and} \quad k_y = n\gamma G_y t_y \qquad \textbf{[2-59]}$$

where t_x and t_y are the durations of the gradients applied in the *x* and *y* planes respectively and *n* is the number of phase encoding steps. By applying the Fourier transformation to equation 2-58, the proton density can now be written as

$$\rho(x,y) = \int\int S(k_x,k_y)\exp\left[-i(k_x x + k_y y)\right] dk_x dk_y \qquad \textbf{[2-60]}$$

and an image is produced by a two-dimensional Fourier transform of *k*-space. This sequence uses a gradient echo to obtain a signal so T_2' effects are not refocused and images produced will be T_2* weighted. To achieve pure T_2 weighting, a 180° pulse can be applied after the phase encoding pulse in order to use the spin warp sequence with a spin echo.

2.3.3 Echo planar imaging

Echo planar imaging (EPI) was developed by Sir Peter Mansfield in Nottingham in 1977 [6]. Spin warp sequences require multiple acquisitions, but the advantage of EPI is that two-dimensional *k*-space can be acquired in a single excitation, or shot, which dramatically improves temporal resolution. At the time of development, there were difficulties in implementing the sequence due to the rapid gradient switching required. However over recent years, technological advances have made this a frequently used technique, especially for studying brain function in terms of blood flow and changes in oxygenation level.

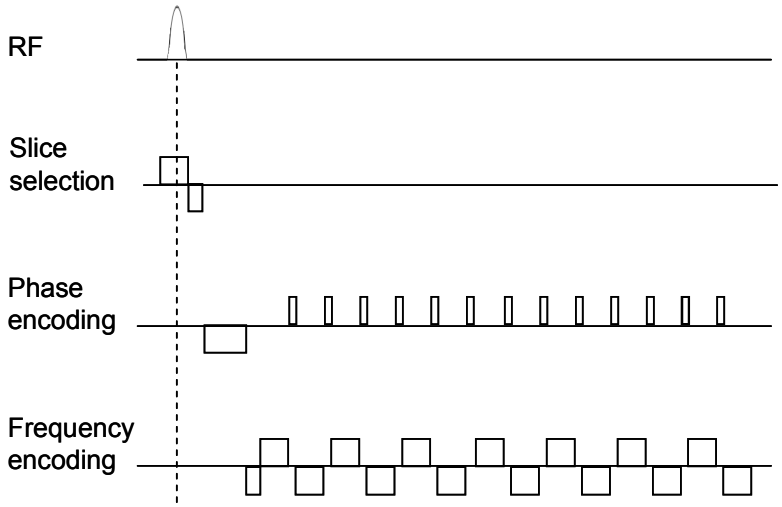

Figure 2-18: Pulse sequence diagram for echo planar imaging (not to scale).

Figure 2-18 shows a pulse diagram for the EPI sequence. Firstly a slice selective excitation pulse G_z (often a 90° pulse) is applied to the sample, followed by spatial encoding. The sampling strategy for this sequence does not begin in the centre of *k*-space, so pulses ($-G_x$ and $-G_y$) are applied in the k_x and k_y directions to move to the edge of *k*-space. From here, a train of gradient echoes are formed by alternating the frequency encode gradient from $+G_x$ to $-G_x$. Each time the frequency gradient is switched, the spins dephase and rephase resulting in a gradient echo. The first line of *k*-space is sampled by

traversing from $-k_x$ to $+k_x$. After the first line of *k*-space has been filled, a blipped phase encoding gradient $+G_y$ is applied, allowing the next line of *k*-space in the k_y direction to be acquired. The next frequency encode gradient is applied with the opposite polarity of the first and another line of *k*-space is acquired in the k_x direction by traversing from $+k_x$ to $-k_x$. This switching frequency encoding and blipped phase encoding continues until the entire of *k*-space has been sampled. This sampling strategy is shown in Figure 2-19.

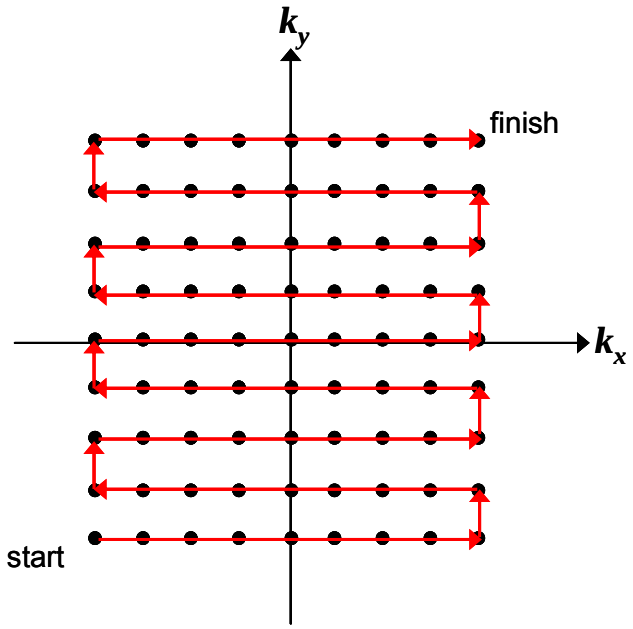

Figure 2-19: Strategy for sampling *k*-space in echo planar imaging.

Alternate lines of *k*-space are acquired with alternating polarity so this must be taken into account before the data is Fourier transformed. Resulting asymmetry in sampling leads to an artifact called the Nyquist ghost to be seen in the images along the phase encode direction. EPI also suffers from other artifacts which are explained, along with other MRI artifacts, in section 2.3.10.

2.3.4 Fast spin echo

The spin echo sequence was introduced in section 2.2.6, but technical developments have allowed this sequence to be performed faster by using a hybrid of EPI and spin warp techniques; this is known as the fast spin echo (FSE). The FSE sequence [7], or RARE (**r**apid **a**cquisition with **r**elaxation **e**nhancement) [8] is based on a multi echo sequence but different phase encoding gradients are used resulting in a reduced imaging time (Figure 2-20).

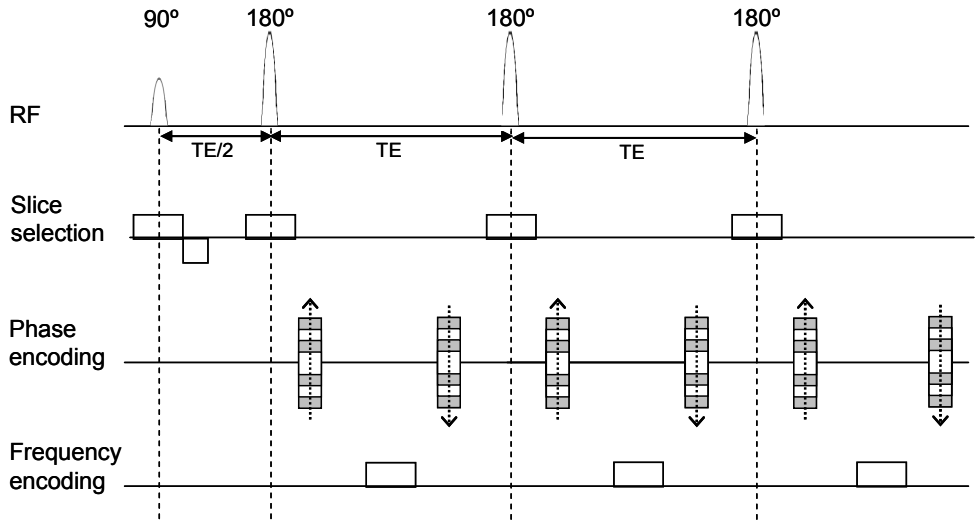

Figure 2-20: Fast spin echo sequence shown here with an echo train of three (not to scale).

The FSE sequence phase encodes immediately after the first 180° but then rewinds before the next 180° pulse is applied. For each 180° pulse applied within the TR, the phase encoding gradient is different. The phase rewinding gradient is the same size but in the opposite direction as the phase encoding gradient it is intended to rewind. The result of the altered phase encoding scheme is that within each TR, more than one line of *k*-space will be filled, reducing the scan time by what is known as a turbo factor. The turbo factor refers to the number of echoes used in each TR. Typically, the spacing between each 180° pulse is ~16-20 ms.

The effective TE of the sequence is given by the time between the 90° pulse and the echo obtained with no phase encoding. By reducing the effective TE, there will be more signal from the shorter T_2 components. By altering the order by which *k*-space is sampled, the T_2 contrast can be manipulated. Blurring artifacts are often seen using this technique due to T_2 decay through *k*-space (also a problem in EPI, but less obvious since lower resolution is used). By using different sampling strategies for the phase encoding these can be reduced [9].

2.3.5 Fast imaging in the steady state

2.3.5.1 Introduction

When RF pulses are repeatedly applied to a spin system and before the next RF pulse, the magnetisation approaches a steady state after each new RF pulse. The spin system takes a finite number of pulses before reaching a steady state which depends on the T_1 of the tissue and the flip angle of the RF pulse; it can also depend on T_2. There are two classes of steady state imaging: coherent and incoherent. During steady state incoherent sequences, any residual transverse magnetisation is spoiled before the next RF pulse is applied, whereas, during steady state coherent sequences, the transverse magnetisation is not spoiled and together with the longitudinal magnetisation contributes to the signal after another RF pulse is applied. Fast field echo (steady state incoherent) and balanced turbo field echo (steady state coherent) sequences will be discussed along with turbo gradient echo sequences.

2.3.5.2 Fast field echo

The fast field echo (FFE) sequence, also called SPGR (**sp**oiled **g**radient **r**ecalled echo), FLASH (**f**ast **l**ow **a**ngle **sh**ot) or spoiled GRASS (**g**radient **r**ecalled **a**cquisition in **s**teady **s**tate), eliminates the residual transverse

magnetisation and the longitudinal magnetisation reaches a steady state. If a short TR is used so that natural spoiling does not occur due to T_2 decay, then removal of the residual transverse magnetisation can be achieved by applying RF spoiling or variable gradient spoilers.

If a series of $\theta°$ RF pulses are applied to a spin system, the magnetisation after the first $\theta°$ pulse is:

$$M_z = M_0 \cos\theta \quad ; \quad M_{xy} = M_0 \sin\theta \qquad \textbf{[2-61]}$$

for the longitudinal and transverse components respectively. Between the first and second $\theta°$ pulses, the longitudinal magnetisation recovers towards the equilibrium magnetisation M_0, but is not necessarily completely recovered. At the same time, the transverse magnetisation is decaying. This process repeats with every $\theta°$ pulse until sufficient repetitions have occurred and the system reaches a steady state such that the same magnetisation values and behaviour occur after each $\theta°$ pulse. There is a balance between the longitudinal magnetisation created due to recovery of the spins and removed due to the RF pulses.

If TR >> T_2, then the sequence is naturally spoiled so the system has time for all the transverse magnetisation to decay. The longitudinal steady state magnetisation M_{ss} is given by:

$$M_{ss} = \frac{M_0\left(1 - e^{-TR/T_1}\right)}{1 - e^{-TR/T_1}\cos\theta} \qquad \textbf{[2-62]}$$

and the transverse magnetisation created by each pulse decays as:

$$M_{xy} = M_{ss} \sin\theta\, e^{-t_n/T_2} \qquad \textbf{[2-63]}$$

The maximum signal occurs at the Ernst angle θ_E [10]:

$$\theta_E = \cos^{-1}\left(e^{-TR/T_1}\right) \quad \textbf{[2-64]}$$

For TR << T_1, equation 2-64 can be simplified to:

$$\theta_E \approx \sqrt{\frac{2TR}{T_1}} \quad \textbf{[2-65]}$$

At short TR, the signal from this sequence is T_2 weighted.

2.3.5.3 Balanced turbo field echo

The balanced turbo field echo (bTFE) sequence, also known as FISP (**f**ast **i**maging with **s**teady state **p**recession), uses transverse, in addition to longitudinal magnetisation, for creating a steady state magnetisation. If the residual transverse magnetisation is not eliminated and TR ≤ T_2, there will be build up of signal towards the steady state dependent on both the longitudinal and transverse magnetisation. If field inhomogeneities are neglected then the magnetisation depends on the flip angle, TR, T_1, T_2 and the initial magnetisation components. However, the magnetisation is also dependent on the phase angle β (or resonant offset angle) through which the isochromats precess between each RF pulse. Variations in β are caused by field inhomogeneities and imperfect gradient refocusing. When spatially dependent, β can create banding patterns across the image particularly in regions where β = 0 or 2π. If all the imaging gradients are balanced (Figure 2-21) then the phase of the transverse spin magnetisation is preserved and all the spins evolve under equivalent free precession conditions over each TR without being affected by the phase and frequency encoding gradients.

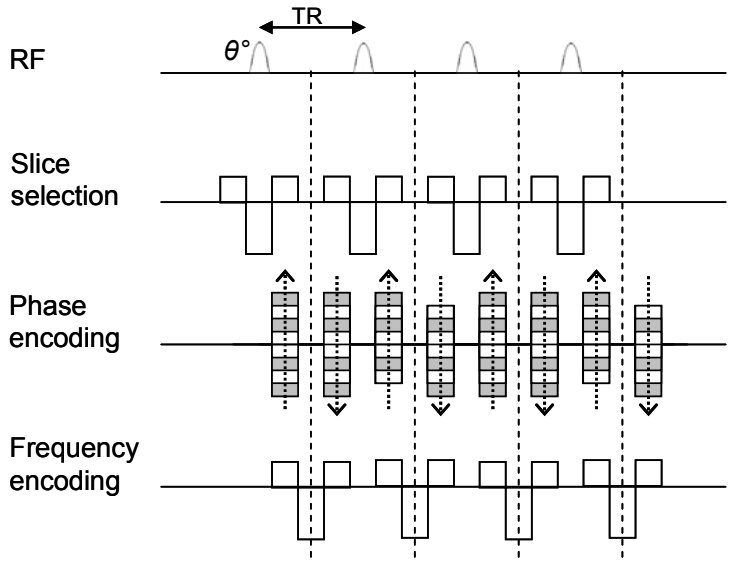

Figure 2-21: Pulse sequence diagram for a balanced turbo field echo sequence (not to scale).

The evolution of the magnetisation in multi-pulse sequences is very complicated. An RF pulse of flip angle θ tips the longitudinal magnetisation towards the transverse plane and effectively splits any existing transverse magnetisation into three components:

1. Transverse component that rephases

These spins produce the echo.

2. Transverse component that remains defocused

These spins are unaffected by the initial refocusing pulse, but may be affected by later refocusing pulses.

3. Longitudinal component

These spins can produce stimulated echoes following later refocusing pulses and can produce a T_1 contribution if the component has not decayed before the next refocusing pulse.

The evolution of the magnetisation soon gets extremely complicated and it is therefore common to describe the evolution using a vertex diagram (Figure 2-22).

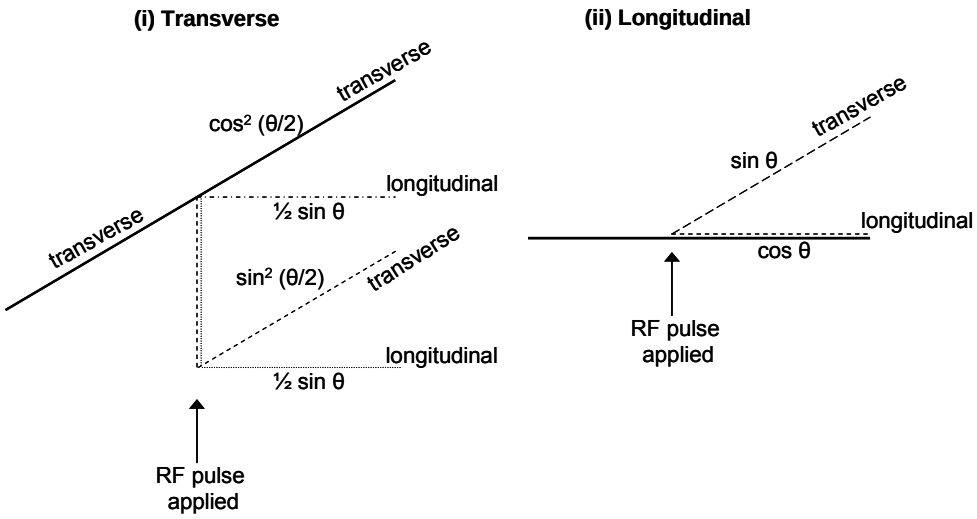

Figure 2-22: Vertex diagrams at an arbitrary pulse for (i) a transverse configuration and (ii) a longitudinal configuration.

In the limit TR << T_2, T_1 and $\beta = \pi$, the transverse magnetisation components can be expressed as [11]:

$$M_x = 0$$
$$M_y \approx \frac{M_0 \sin\theta}{\left(\frac{T_1}{T_2}+1\right) - \cos\theta\left(\frac{T_1}{T_2}-1\right)} \qquad \textbf{[2-66]}$$

and therefore the contrast is essentially T_2/T_1 weighted. The optimal signal for a fixed β, occurs at the flip angle θ_{opt} so that [11]:

$$\cos\theta_{opt} \approx \frac{T_1/T_2 - 1}{T_1/T_2 + 1} \qquad \textbf{[2-67]}$$

for the short TR limit and the peak signal can be simplified to:

$$M_y \approx \frac{1}{2} M_0 \sqrt{\frac{T_2}{T_1}} \qquad \textbf{[2-68]}$$

Therefore samples that have a high T_2/T_1 ratio, will have a high signal.

For a long TR, the FFE and bTFE sequences have similar properties for any given TE and flip angle. Essentially, bTFE is a fast version of the FFE sequence and this allows preparation phases to be added to the TFE sequence.

2.3.5.4 Turbo gradient echo

There are additional methods that increase the speed of gradient echo sequences. Ultra short TEs and TRs can be used to decrease scanning time by using a fraction of the echo and RF pulse (due to inherent symmetrical properties), less excitations (see section 2.3.7) and reducing the sampling time. By using a fraction of the echo and a fraction of the RF pulse, this allows the TE to be shortened and by increasing the bandwidth, the sampling time decreases (SNR decreases). By minimising the TE and sampling time, the TR can be minimised and by reducing the number of excitations, the scan time is shortened. This has advantages when scanning in the abdomen where motion, from breathing or peristalsis, requires a breathold whilst scanning, or for performing cine imaging of the heart or studying perfusion changes due to contrast administration.

Due to the ultra short TRs that are used in this sequence, the contrast may be sub-optimal. By using magnetisation preparation, it is possible to improve the tissue contrast. This can be done by applying additional pulses prior to the gradient echo phase which allow the tissues to develop a certain contrast, such as inversion recovery (IR) prepared or driven equilibrium (DE) prepared. IR preparation (180°) increases T_1 weighting and allows suppression of tissues depending on the time between the preparation phase and the main pulse train. DE preparation (90° – 180° - 90°), similar to a spin echo, is used to enhance T_2 weighting. This will be used in chapter 5 and will be called a T_2-preparation phase. The longer the T_2-preparation phase, the more T_2 decay will occur and the more T_2 weighted the contrast becomes. After the first 90° pulse, the transverse magnetisation will be similar for all tissues, but just before the 180°, the transverse magnetisation will have decayed by different

amounts in different tissues. The 180° inverts the magnetisation and the final 90° causes the magnetisation to be driven into the longitudinal plane.

2.3.6 Three-dimensional imaging

So far, only two-dimensional imaging has been discussed. However, it is possible to perform three-dimensional imaging by collecting several adjacent slices through a region of the imaged object. In order to obtain multiple slices, an additional phase encoding gradient is applied in the slice select direction (Figure 2-23).

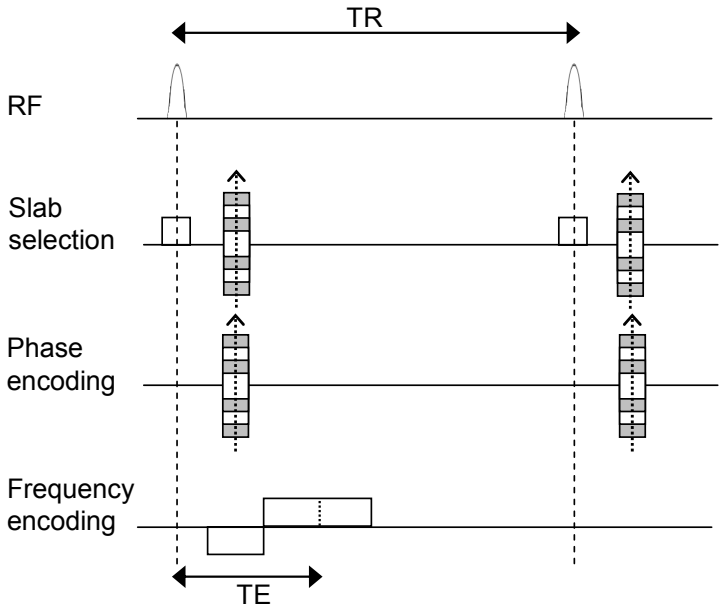

Figure 2-23: Pulse sequence diagram showing additional phase encoding gradient to perform three-dimensional imaging (not to scale).

Compared with multi-slice imaging, three-dimensional imaging provides an increase in SNR since signal is acquired from the same volume multiple times. It also allows thin, high resolution contiguous slices to be acquired. The extra phase encoding gradient can, however, cause wraparound artifacts at the ends of the volume, so the pulse is usually slab selective, and does result in a longer scan time.

2.3.7 Partial Fourier imaging

The Fourier transform of an object contains both real and imaginary components; the real component is symmetric and the imaginary component is asymmetric about the centre of *k*-space. This means that images can be reconstructed from under-sampled *k*-space and theoretically only half of *k*-space needs to be acquired. However, in practice the real data is not symmetrical, but by sampling a few extra lines in the un-sampled half of *k*-space this can be overcome.

By applying the partial Fourier technique in the frequency encoding direction (Figure 2-24i), shorter echo times can be achieved and by applying this in the phase encoding direction (Figure 2-24ii), the overall scan time is reduced. The field of view will not be affected, but the SNR will be reduced and image artifacts are introduced (see section 2.3.10).

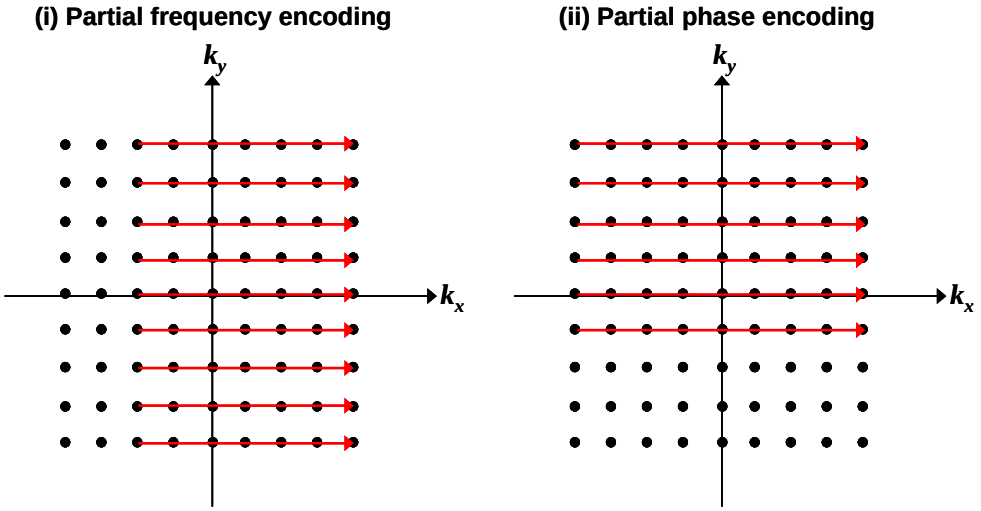

Figure 2-24: Strategies for partial *k*-space sampling in the (i) frequency and (ii) phase encoding directions.

2.3.8 SENSE

In 1997 Sodickson *et al.* [12] successfully performed the first experiments using parallel receivers to reduce scan time; this method was named SMASH

(**sim**ultaneous **a**cquisition of **s**patial **h**armonics). However this method had its restrictions (coil arrangement, slice geometry, reduction factors). In 1999 Pruessmann *et al*. [13] introduced a technique which would overcome these restrictions and named it SENSE (**sens**itivity **e**ncoding). The term sensitivity refers to the receiver coil property. The signal from an object that a receiver detects varies appreciably with its relative position; by knowing the sensitivity of the spatial receiver, information about the origin of the signal can be used to construct an image. Using SENSE allows a reduction in the number of Fourier encoding steps. Therefore spatial resolution can be maintained and scan time reduced, or, an increased field of view can be scanned whilst keeping the scan time constant. The term SENSE factor will be used in this work to describe the factor by which the amount of *k*-space sampled is reduced.

Using standard image construction techniques, reducing the sampling density reduces the field of view and results in aliasing (section 2.3.10). SENSE imaging involves creating an aliased image for each element in the receiver array using Fourier transform. From these intermediate images, a full image covering the entire field of view can be constructed. The signal superposition underlying the foldover effect must be undone and by knowing the sensitivity weighting of each receiver coil, a final image covering the whole of the desired field of view is obtained. A reference scan must be performed when using SENSE to obtain a sensitivity map to aid the unfolding of the signal superposition. The maximum SENSE factor that can be achieved is determined by the number of receiver coils in the array otherwise unfolding of the data would not be possible. However, increasing the SENSE factor will result in a reduced SNR and the SNR is fundamentally governed by the square root of the acquisition time and the coverage of each coil (coil profile). Therefore, SENSE should be used when speed is a higher priority than SNR.

2.3.9 Image contrast

In clinical practice, it is important to optimise tissue contrast in order to diagnose or determine progression of diseases. Image contrast is dependent on several parameters including TE, TR, T_2 and T_1. It is therefore very important to know relaxation parameters of the tissues under investigation since these are field dependent, and to know how altering the TE and TR can affect the weighting and contrast. With increased field strength, T_2 decreases and T_1 increases, so if a sequence was to be performed at two different field strengths, then in order to obtain similar contrast, the TR and TE values chosen would also be different. In order to get T_1 weighting in images, a short TR and long TE must be used, and to obtain T_2 weighting, a short TE and long TR must be used.

Tissue contrast can also be altered by introducing a molecule containing paramagnetic atoms (which contain unpaired electrons and have a small positive magnetic susceptibility), for example, gadolinium. This improves the contrast between adjacent tissues by shortening the T_1 and increasing the intensity of the target tissue (on T_1 weighted images).

2.3.10 Artifacts

2.3.10.1 Introduction

It has already been mentioned in this chapter that there are number of artifacts that can occur in MRI. Magnetic susceptibility, image processing, patient-related and gradient-related artifacts will be discussed here, but the effects of RF errors and magnetic field inhomogeneities will be discussed in chapter 3.

2.3.10.2 Magnetic susceptibility

Each tissue has an inherent magnetic susceptibility. Most of the tissues in the human body are diamagnetic (no unpaired electrons) and have a negative magnetic susceptibility. At tissue boundaries, there is a change in susceptibility producing spatial variations in the magnetic field. This causes dephasing of spins and ultimately results in signal loss and mis-registration. This effect can be used advantageously since phase changes at tissue interfaces can yield information about magnetic properties of tissues relative to each other.

2.3.10.3 Image processing

Nyquist ghost

The Nyquist ghost (or N/2 ghost) occurs due to the *k*-space sampling strategy that is used in EPI (section 2.3.3). The direction of traversal across *k*-space alternates for each phase encoding step and the signals deviate in every other line from their correct values due to errors in sampling and the presence of field inhomogeneities. The result of this is that, following the Fourier transform, an extra periodicity is introduced into the image. A ghost is then observed in the image which is shifted in the phase encoding direction by half the field of view.

Chemical shift

Protons from different molecules precess at different frequencies, for example the difference in precessional frequency of the hydrogen molecules in water and fat is 220 Hz at 1.5 T [14]. This difference in the precessional frequency is known as the chemical shift. The chemical shift increases with increased field strength or lower gradient strength.

Fat protons precess at a slightly lower frequency than protons in water. Therefore for an image containing both water and fat, there will be a shift in

the encoding of the anatomy along the frequency encoding direction. Increasing the strength of the frequency encoding gradient, increases the bandwidth per pixel and the fat and water can be contained within the same pixel. However, if the bandwidth is decreased by reducing the gradient strength, then the fat and water are separated by one or more pixels and mis-registration occurs but by having a large bandwidth, the SNR that can be achieved will be lower. The most common technique for removing chemical shift artifacts is to null the signal from either the water or fat using frequency selective pulses or an inversion recovery sequence.

Aliasing

Aliasing (or wraparound) is a result of undersampling *k*-space and results in some of the anatomy being displaced to the opposite side of the image. The Nyquist sampling limit must be satisfied to avoid this artifact. The data must be sampled such that the inverse of the size of the sampling step in *k*-space is larger than the size of the object to be imaged. If this is not satisfied, then the Fourier transform cannot distinguish frequencies in the data that are above the Nyquist frequency limit and lower frequencies are assigned instead. These signals, which are outside the field of view, are wrapped around to the opposite side of the image because they are forced to have lower frequencies. This can be overcome by using a low-pass filter in the frequency encode direction so that frequencies can be eliminated that are beyond the Nyquist limit. In the phase encoding direction, the number of phase encoding steps must be increased to reduce the effects of aliasing.

2.3.10.4 Patient-related

There are two sources of patient related artifacts: motion and the magic angle effect. Motion artifacts are caused either by the patient moving or by internal movement of organs (e.g. stomach, heart) or blood flow. The artifacts appear in the phase encoding direction. Random motion will result in blurring of the

image and periodic motion (e.g. heart) will result in ghosting of the moving object.

In short TE sequences, the orientation of some tissues, e.g. tendons/ligaments and tracts/vessels, to the magnetic field can affect the signal intensity [15-17]. Such tissues contain water that is bound to collagen and the protons within this water are subject to dipolar interactions whose strength depends on the orientation of the fibres to the magnetic field. These interactions result in dephasing of the spins after excitation and therefore no detectable MR signal. The dipolar interactions are modulated by the term

$$3\cos^2\theta - 1 \qquad \textbf{[2-69]}$$

where θ is the angle of the tissue with the magnetic field. When equation 2-69 is equal to zero, the dipolar interactions are minimised; this occurs when θ = 55°, 125°, etc. This is known as the magic angle and results in an increase in MR signal and measured T_2. The magic angle effect can be advantageous in terms of increased MR signal there contrast manipulation by altering the angle of the head with respect to the magnetic field. However, when comparing T_2 measurements of different regions, consideration of the magic angle may be required.

2.3.10.5 Gradient-related

Eddy currents and non-linearities in gradients can cause artifacts. Eddy currents are small electric currents that are induced in conducting (and superconducting) parts of magnet bore when the gradients are switched rapidly resulting in a distortion in the gradient profile (Figure 2-25).

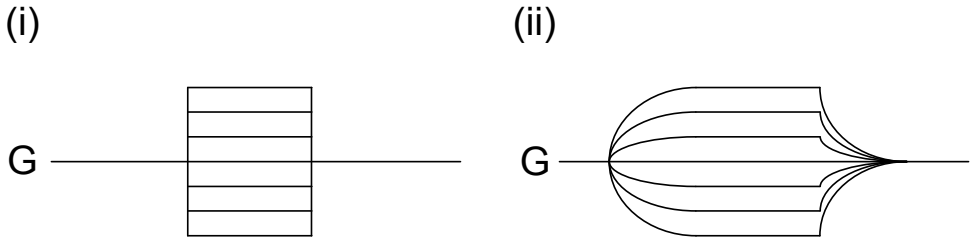

Figure 2-25: (i) Perfect gradient profile and (ii) gradient profile affected by eddy currents.

Also, gradient coils are never perfect which causes non-linearities in the gradient. Images are distorted, e.g. a circle may appear as an ellipse, due to gradient drop off at the extremes of the gradients (Figure 2-26). Spatial distortion can be minimised by either, reducing the field of view by reducing the gradient field strength, or, decreasing the frequency bandwidth whilst keeping the gradient field strength and number of sample constant.

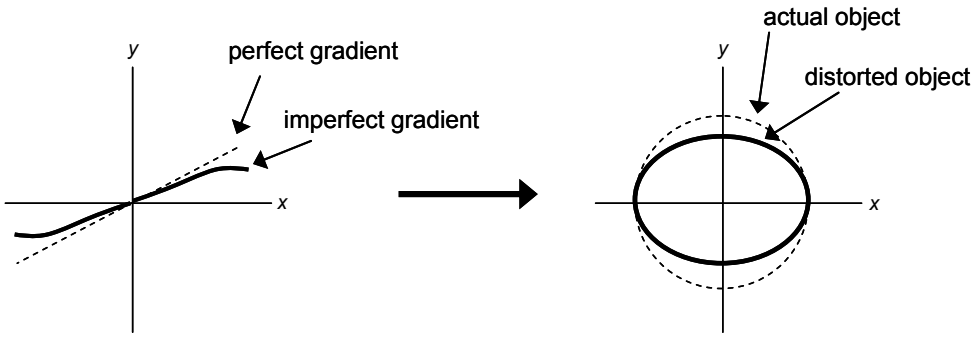

Figure 2-26: Imperfect gradients cause distortion of images. Adapted from [14].

2.4 INSTRUMENTATION

2.4.1 Overview

In this work, three MRI scanners have been used (1.5 T, 3.0 T and 7.0 T) from the Philips Achieva range. Figure 2-27 illustrates the basic setup of an MRI scanner. The four main components of an MRI scanner are: magnet, gradients, RF coils and a control computer.

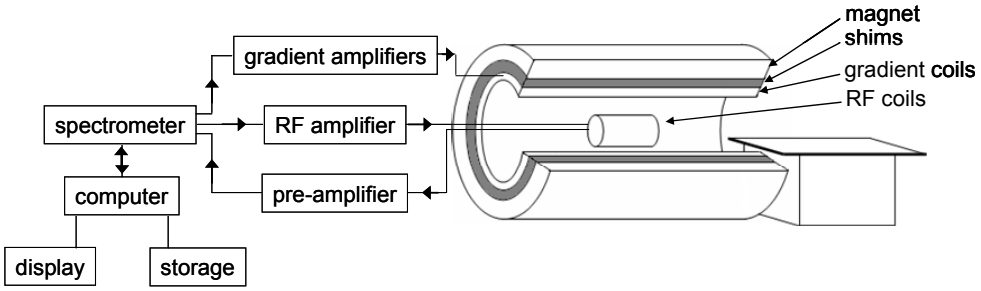

Figure 2-27: Overview of an MRI system.

2.4.2 Magnet

For MRI experiments, the magnetic field produced by the magnet should be homogeneous across the whole region being imaged and must not vary with time. Inhomogeneous fields lead to line broadening and image distortion due to spatially varying frequency offsets. Similarly, temporal variations also produce temporally varying frequency offsets resulting in image blurring.

The magnetic field decreases as the inverse of the square of the distance and the field outside the bore is termed the *fringe field*. However, if shielded magnets are used, the magnetic field will decrease much faster than this. Most computer equipment will not operate in fields above 0.5 mT and access must also be restricted to these areas for people with particular conditions, such as having pacemakers fitted or metal implants (section 2.5). Access is usually restricted above fringe fields of 0.5 mT and therefore the space required for a scanner is dictated by extent of the fringe field. Magnets can be passively and actively shielded; active shielding cancels fields from primary coils in regions where they are not required [18] and passive shielding uses a high permeability material such as iron to decrease the flux away from the magnet. The onsite Philips 7.0 T scanner resides in a large iron box weighing 213 tons which reduces the fringe field.

MRI scanners usually contain superconducting magnets since these are capable of supporting large electric currents without requiring an external

power supply. Once brought to field, these magnets provide a highly stable magnetic field. The higher the strength of the magnet, the longer and more costly the process of powering up is. Originally, the coils of superconducting magnets (< 9.4 T) were made of Niobium Titanium and cooled using two baths: one of liquid helium and one of liquid nitrogen. However, liquid nitrogen is no longer used and water or air cooled chillers are used instead to maintain the liquid helium cooling system.

Although superconducting magnets are intrinsically stable (in time), this is further improved by using a shim system. There are two shims systems used in our magnets: passive shims and subject specific room temperature shims. Passive shims, used in most clinical magnets, consist of pockets around the inside surface of the magnet bore into which pieces of ferrous material can be placed [19]. An initialisation sequence is used to determine the homogeneity of the magnetic field. The distribution of the ferrous material is then adjusted until the shimming magnetic field is equal and opposite to the residual magnetic field. The residual magnetic field is the difference between the inhomogeneous magnetic field in the bore and the target magnetic field. Room temperature shims are copper coils wound on a cylinder around, or integrated with, the gradient coils and are adjusted for each subject. The number of coils used is system dependent. Superconducting shims can also be used [20].

2.4.3 Gradients

Gradient coils are used to vary the magnetic field homogeneity, usually linearly, by a small fraction of the z component of the external magnetic field B_0. This allows spatial information from the received signal to be obtained and to achieve this, three orthogonal gradients are used in the x, y and z direction.

To achieve variation in the *z* direction simply a Maxwell pair coil could be used; a pair of coils with radius r, separated by a distance $\sqrt{3}r$ yields a uniform magnetic field gradient with zero magnitude half way between the coils. To achieve magnetic field variation in the *x*-*y* direction, a Golay coil arrangement is often used; this requires two pairs of saddle coils along the bore of the magnet and a very linear field is produced. However, continuing advances in this research area have yielded more complex coil systems. Gradient coils are usually shielded to reduce eddy currents [18].

Several factors determine gradient performance: power supply current, gradient coil efficiency and resistance, acoustic noise and peripheral nerve stimulation. Acoustic noise is due to vibrations of the coil. The magnetic field created by pulses of current through the gradient coil interacts with the main magnetic field due to the time varying Lorentz force. Noise levels increase with increasing field strength; active acoustic control systems have been developed to reduce the noise levels. On the Philips scanners this is called *softtone*. Peripheral nerve stimulation is caused by rapid time varying gradients. The rapid switching of the gradients causes rapid switching of magnetic fields which induce an electric field in the conducting human body sufficient to stimulate peripheral nerves.

2.4.4 Radiofrequency coils

Radiofrequency (RF) pulses are transmitted and signals received using transmit and receive RF coils. A body coil is a fixed part of the magnet that surrounds the subject and can be used both to transmit and to receive. However, local receive only coils can be used to increase the SNR; since SNR decreases as $1/r^2$, it is advantageous to have the receive coil close to the anatomy under investigation. Surface coils allow this since they are usually small and often flexible, although unlike the body coil, they do not allow for a very large field of view. In this work two types of coil have been used: a head

coil and a torso coil, both of which are capable of performing SENSE imaging. The coils used for scanning on the Philips Achieva 3.0 T scanner are shown in Figure 2-28.

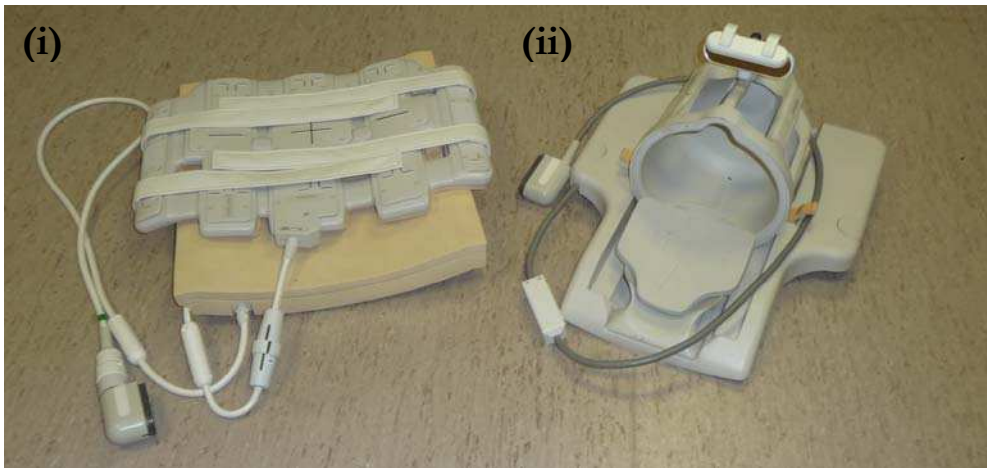

Figure 2-28: The (i) torso and (ii) head coil used on the Philips Acheiva 3.0 T scanner in this work.

A basic coil consists of a loop of wire with two capacitors (Figure 2-29). The impedance of the RF coil must be matched to the impedance of the amplifier to maximise signal transmission and reception by minimising reflections (C_M). The system must also be tuned to the Larmor frequency (C_T). This type of coil would be suitable for a surface coil, but for volume coils more complicated designs are used.

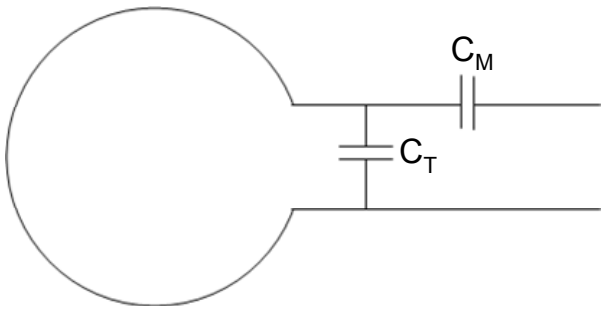

Figure 2-29: Configuration of a basic coil.

2.4.5 Controlling the scanner

The MRI scanner is controlled by a system of inter-connected computers. The user selects a sequence and enters appropriate parameters. The computer calculates the gradients and RF waveforms and appropriate timings and sends the information to the spectrometer, which converts the signal from digital to analogue. The RF pulses are amplified and transmitted by the appropriate coils; the resultant signal is converted back from analogue to digital and amplified before the computer reconstructs the data to produce images for the user to display and save for further analysis.

2.5 SAFETY

MRI scanners are potentially very dangerous and a high emphasis is placed on safe working conduct in and around magnet halls.

People with pacemakers, ferromagnetic foreign bodies or metallic implants should not be allowed to go near to, or in, an MRI scanner. It is also important that no loose metal objects are taken into the scanner room because they will be attracted to the centre of the magnet. This projectile effect of the metal object can cause serious injury especially if the object is sharp (e.g. scissors).

The energy that is transmitted by the RF pulses can be very high in some sequences which can lead to heating. People with tattoos can feel the effects of heating due to some tattoo ink containing metal. There is a restriction on all commercial scanners for the amount of power that can be deposited: specific absorption rate (SAR). The SAR is a measure of the rate at which RF energy is absorbed by the body when exposed to RF electromagnetic field. It is defined as the power absorbed per mass of tissue and has units of watts per kilogram.

Peripheral nerve stimulation (PNS) can be caused by the rapid switching of gradients particularly in the extremities. This is because the changing field increases with distance from the centre of the gradient coils. To reduce this problem, there is a dB/dt (change in field per unit time) limitation set by American and European regulatory agencies. Switching of the field gradients also causes a change in the Lorentz force experienced by the gradient coils, producing minute expansions and contractions of the coil. The frequency of the switching is in the audible range resulting in vibrations which produce loud noises. Appropriate ear protection must be worn (ear plugs and/or head phones), especially at high field.

The scanners used in this work contain superconducting magnets and therefore rely on cryogenic liquids. If the magnet is shut down in an emergency, it is quenched. This involves rapid boiling of liquid helium from the scanner and if there is insufficient ventilation to allow the helium to escape from a confined space, then the helium will displace the oxygen in the room and there is then a risk of asphyxiation. There is also the risk of cold burns due to cryogenic liquids, so care must be taken (gloves, face mask) when using cryogens.

Contrast agents are often used to enhance tissue identification. The most common intravenous contrast agents contain gadolinium. They are generally considered safe if they are administered intravenously and not consumed orally, but there have been some indication that there is a risk to patients with severe renal failure because of the specific formulation of chelate used.

The concerns in pregnancy are the same for MRI in general, except that the fetus may be more sensitive to the effects. The guidelines recommend that pregnant woman should only have an MRI scan when essential, particularly in the first three months since the effects of heating and noise could be a problem. Contrast agents should be avoided because they can enter the fetal bloodstream.

2.6 ETHICAL APPROVAL

It is important when studying volunteers, healthy or patients, to obtain ethical approval. All the studies carried out in this work were approved by the University of Nottingham Medical School Ethics Committee and all volunteers gave written informed consent.

2.7 References

1. Levitt, M.H., *Spin Dynamics.* 2008.
2. Bloembergen, N., E.M. Purcell, and R.V. Pound, *Relaxation Effects in Nuclear Magnetic Resonance Absorption.* Phys. Rev., 1948. **73**(7): p. 679-712.
3. Mansfield, P. and P.K. Grannell, *NMR 'diffraction' in solids?* J. Phys. C: Solid State Phys., 1973. **6**: p. L422-L426.
4. Garroway, A.N., P.K. Grannell, and P. Mansfield, *Image formation in NMR by a selective irradiative process.* J. Phys. C - Solid state phys, 1974. **7**: p. L457-L562.
5. Edelstein, W.A., et al., *Spin warp NMR imaging and applications to human whole-body imaging.* Phys. med. Biol., 1980. **25**(4): p. 751-756.
6. Mansfield, P., *Multi-planar image formation using NMR spin echoes.* J. Phys. C: Solid State Phys., 1977. **10**: p. L55-L58.
7. Listerud, J., et al., *First Principles of Fast Spin Echo.* Magnetic Resonance Quarterly, 1992. **8**(4): p. 199-244.
8. Hennig, J., A. Nauerth, and H. Friedburg, *RARE Imaging: A Fast Imaging Method for Clinical MR.* Mag. Res. Med, 1986. **3**: p. 823-833.
9. Mulkern, R.V., et al., *Contrast Manipulation and Artifact Assessment of 2d and 3d Rare Sequences.* Mag. Res. Im., 1990. **8**(5): p. 557-566.

10. Ernst, R.R. and W.A. Anderson, *Application of Fourier Transform Spectroscopy to Magnetic Resonance.* Rev. Sci. Instrum., 1966. **37**(1): p. 93-102.
11. Oppelt, A., et al., *FISP - a new fast MRI sequence.* Electromedica, 1986. **54**(1): p. 15-18.
12. Sodickson, D.K. and W.J. Manning, *Simultaneous acquisition of spatial harmonics (SMASH): fast imaging with radiofrequency coil arrays.* Mag. Res. Med., 1997. **38**(4): p. 591-603.
13. Pruessmann, K.P., et al., *SENSE: Sensitivity Encoding for fast MRI.* Mag. Res. Med., 1999. **42**: p. 952-962.
14. Hashemi, R.H., W.G. Bradley, and C.J. Lisanti, *MRI The Basics.* 2004.
15. Chappell, K.E., et al., *Magic Angle Effects in MR Neurography.* AJNR, 2004. **25**: p. 431-440.
16. Bydder, M., et al., *The Magic Angle Effect: A Source of Artifact, Determinant of Image Contrast, and Technique for Imaging.* J. Mag. Res. Im., 2007. **25**: p. 290-300.
17. Fullerton, G.D., I.L. Cameron, and V.A. Ord, *Orientation of Tendons in the Magnetic Field and Its Effect on T2 Relaxation Times.* Radiology, 1985. **155**: p. 433-435.
18. Mansfield, P. and B. Chapman, *Active magnetic screening of coils for static and time-dependent magnetic field generation in NMR imaging.* J. Phys. E: Sci. Instrum., 1986. **19**: p. 540-545.
19. McGinley, J.V.M., V.C. Srivastava, and G.D. DeMeester, *Passive shimming technique for MRI magnets.* Mag. Res. Im., 1997. **15**(3): p. XIX.
20. Konzbul, P., K. Sveda, and A. Srnka, *Superconducting Shim System with High Purity Magnetic Field for NMR and MRI Solenoid Magnet MIDI - 200.* IEEE Transactions on Magnetics, 1996. **32**(4): p. 2643-2646.

CHAPTER 3

MEASURING TRANSVERSE RELAXATION

3.1 INTRODUCTION

Over the years there have been many techniques developed to measure T_2 in NMR and MRI. This chapter introduces the key methods along with their advantages and disadvantages.

3.2 SPIN ECHO SEQUENCES

3.2.1 Introduction

There are two main techniques that employ the spin echo in order to measure T_2 and these will be discussed here. The Hahn spin echo and CPMG are most commonly used in MRI and NMR respectively.

3.2.2 Hahn spin echo

In 1950, Hahn introduced the concept of a spin echo [1]. By applying the appropriate RF pulses, the spin echo can be used to measure T_2; this was introduced in chapter 2. If the time between the RF pulses is known, the amplitude of the echo measured is related to T_2:

$$M(TE) = M_0 e^{-TE/T_2} \qquad \textbf{[3-1]}$$

where TE, the echo time, is twice the time between the 90° and 180° pulses. By repeating this experiment with different echo times, data can be fitted to

equation 3-1 to obtain an estimate for T_2. A simple pulse sequence diagram of the spin echo sequence is given in Figure 3-1.

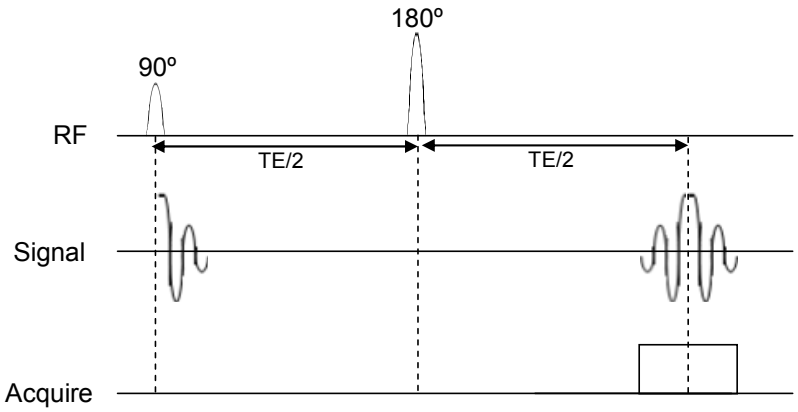

Figure 3-1: Single spin echo sequence (not to scale).

Molecular diffusion occurs between pulses and therefore the precessional frequency of each spin before and after each refocusing pulse may not be constant since the spin will be experiencing a slightly different applied field (due to inherent field inhomogeneities and susceptibility effects). This results in attenuation of the spin echo and an underestimation of the T_2 since the signal will appear to decay artificially fast. The time between repetitions, TR, should be more than five times the value of T_1 of the sample, otherwise the signal will be dependent on T_1 in addition to T_2 and equation 3-1 will no longer remain valid. By performing spin echo experiments using a long TR and just two RF pulses, the values calculated for T_2 are insensitive to sequence errors and the technique is deemed to be gold standard if the effect of spin diffusion in field inhomogeneities is not significant.

3.2.3 Diffusion

Self diffusion of molecules through inhomogeneous external fields can dominate the intrinsic irreversible T_2 spin-spin relaxation time, especially in liquids and gases. The spin echo method corrects the dephasing due to variations in the external magnetic field experienced by different molecules at

different positions, but the dephasing due to the change in position of a given molecule cannot be corrected for. Brownian motion of the magnetic moment arises from the random transport of the proton from one region to another where the applied field has slightly changed. The spin will also undergo a change in phase in addition to a change in position due to the rapid changes in the field experienced. The original equation for the transverse magnetisation (equation 3-1) can be rewritten to include the effects of diffusion:

$$M_{xy} = M_0 e^{-t/T_2} e^{-bD} \qquad \textbf{[3-2]}$$

where

$$b = \gamma^2 G^2 t^3 / 3 \qquad \textbf{[3-3]}$$

Here D is the diffusion constant, t is the time of the echo and G is the constant linear gradient, representing field inhomogeneity over diffusion distance of spins.

Diffusion causes additional signal loss (equation 3-2) to that caused by spin dephasing across a voxel due to an applied gradient. Gradient dephasing of the stationary spins can be refocused with a negative gradient lobe to form a gradient echo, but the signal loss due to diffusion of the spins during the application of the gradient cannot be recovered. If diffusion is not taken into account when calculating the relaxation time, an underestimation of T_2 will occur.

3.2.4 CP and CPMG

Diffusion is a particular problem with the standard spin echo sequence, but the Carr-Purcell multi echo mechanism suppresses diffusion effects by preventing the build up of phase accumulation for a given random walk [2].

The CP sequence [2] consists of a train of 180° pulses following the initial 90° pulse:

$$90°_x - TE/2 - 180°_x - [\ TE - 180°_x\ ]_n$$

Echoes are formed between successive 180° pulses as the spins refocus and the T_2 can be calculated by fitting the signal amplitude at each echo to

$$M_n(t) = M_0 e^{-2nt/T_2} \qquad \textbf{[3-4]}$$

This method acquires enough information to obtain a value for T_2 in a single relaxation curve compared with multiple exposures required using the Hahn method. It also reduces sensitivity to diffusion if the inter-pulse interval is appropriately chosen. Taking diffusion into account, the transverse magnetisation can be written as

$$M_{xy} = M_0 e^{-t/T_2} e^{-\gamma^2 G^2 D t^3 / 12n^2} \qquad \textbf{[3-5]}$$

where n is the number of 180° pulses applied in the train [2]. From this it can be seen that by increasing n for a fixed t, the diffusion component becomes negligible and the decay of the magnetisation is dominated by the intrinsic spin-spin dephasing (equation 3-5).

If the refocusing pulses used in this method are not exact, then cumulative errors will result in an inaccurate measurement of T_2. After each 180° pulse, spins will be flipped to above or below the $x'y'$ plane if the pulse is smaller or larger than 180°, leading to increasing loss in signal over the experiment and an underestimation of T_2. If the phase is alternated for each 180° pulse then the effect of pulse errors cancels out for the alternate echoes (phase alternated CP sequence):

$$90°_x - TE/2 - [180°_x - TE - 180°_{-x} - TE]_n$$

Meiboom and Gill (MG) [3] modified the CP sequence by introducing a phase shift between the 90° and 180° pulses so that the sequence becomes

$$90°_x - TE/2 - 180°_y - [\ TE - 180°_y\ ]_n$$

Any pulse errors will be corrected for by only sampling even echoes, since spins will be returned to the $x'y'$ plane after alternate 180° pulses and there will be no cumulative errors.

3.2.5 Errors in T_2 measurements

3.2.5.1 Introduction

In the previous section, errors in measurements of T_2 due to RF imperfections and diffusion have been mentioned. The following section contains a review of the sources and effects of RF errors and correction schemes that have been reported in the literature.

3.2.5.2 Sources of RF errors

Errors in measurements of T_2 occur due to radiofrequency (RF) pulse imperfections, static field (B_0) inhomogeneities and slice profile imperfections; the effects of these problems are increased at ultra-high field. In the presence of a static field inhomogeneity, the refocusing 180° pulse would be off resonance and hence imperfect so that the spin phases would not be fully reversed. In multi-slice imaging, data are acquired for each slice by interleaving so that T_1 relaxation can occur in one slice whilst the next is being excited; this helps to maximise time efficiency. For multi-slice imaging, slice selective pulses must be implemented to avoid cross talk between slices. At the edge of a slice, the spins will not experience a perfect 180° refocusing pulse and additional unwanted echoes are formed and complicate the evolution of magnetisation.

Majumdar *et al*. quantitatively describe the errors in measuring T_2 using multiple-echo MRI techniques due to RF pulse imperfections [4] and static field inhomogeneities [5]. Similar errors occur due to slice profile imperfections [6]. These will now be discussed.

If the 180° refocusing pulse is imperfect, the magnitude of the transverse magnetisation measured will be reduced and a longitudinal component will be introduced, resulting in a more rapid signal decay and underestimation of T_2. With successive application of imperfect refocusing pulses, the magnetisation that develops becomes increasingly more complicated (as described in section 2.3.5). To recap, after an imperfect refocusing pulse, there are three components of magnetisation:

1. Transverse component that rephases (subscript -1)
2. Transverse component that remains defocused (subscript +1)
3. Longitudinal component (subscript 0)

The evolution of the magnetisation, M, of a group of spins can be written using the subscripts given above so that after the first refocusing pulse the three initial magnetisation components are M_{-1}, M_{+1} and M_0 and after a second refocusing pulse the nine magnetisation components are M_{-1-1}, M_{-1+1}, M_{-10}, M_{+1-1}, M_{+1+1}, M_{+10}, M_{0-1}, M_{0+1}, and M_{00} (Figure 3-2). Contributions to the spin echo only occur if the last index is -1 and not preceded by a +1, the sum of the indices is less than zero and the sum of the indices should be odd for odd echoes and even for even echoes. Therefore, the spin echo after the first refocusing pulse is from M_{-1} and after the second from M_{-1-1}.

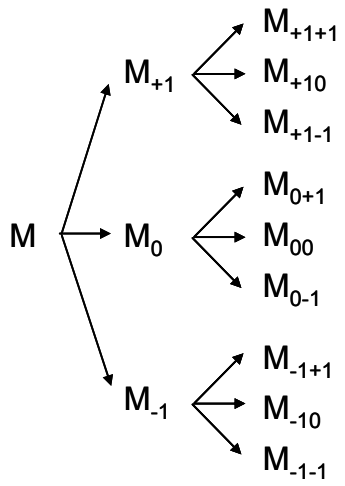

Figure 3-2: Magnetisation evolution due to imperfections of two refocusing pulses.

3.2.5.3 Effects of RF errors

There are some undesired effects of the multi-echo CP and CPMG imaging sequences: central line artifact [7], phase artifact [6, 7] and a T_1 mixing artifact [6]. These are a result of pulse imperfections, RF inhomogeneities in the coil and imperfect slice selection profiles and will be discussed below.

Central Line Artifact

If the 180° pulse is imperfect, there will be an FID following the pulse. If this does not decay before the spin echo, the FID signal sees the effect of the readout gradient and is frequency encoded in the readout direction. This results in a constant contribution to each line of k-space and appears as a bright line along the *x*-axis.

Phase Artifact

After an initial imperfect refocusing pulse, some magnetisation will form a longitudinal component which is defocused and since a phase encoding gradient is applied prior to the refocusing pulse, the defocused transverse magnetisation component has an additional phase of $+\varphi(y)$ at t = TE. For the echo $M_{0\text{-}1}$, the phase has been reversed to $-\varphi(y)$ at a time t = 2TE. However,

for the echo M_{-1-1} at $t = 2TE$, the effect of two perfect refocusing pulses is that the phase reversals cancel to give a phase of $+\varphi(y)$. For the M_{-1-1} echo, the phase encoding of $+\varphi(y)$ is reconstructed into the pixel (x, y). For the M_{0-1} echo, however, the phase encoding of $-\varphi(y)$ is misinterpreted and the signal is reconstructed into pixel $(x, -y)$. The result of this is an inverted ghost image superimposed on the expected image, but only echoes which have at least one subscript equal to +1 can produce the phase artifact.

T_1 Mixing Artifact

For pure T_2 decay, echoes should be formed from perfect 180° pulses (i.e. all subscripts equal to -1). However, when longitudinal components of magnetisation are formed (i.e. subscripts equal to 0), there will be some T_1 relaxation before the next refocusing pulse is applied and the signal intensity will be dependant on both T_2 and T_1. This will lead to an incorrect calculation of T_2, since the signal measured will not be purely dependant on T_2.

3.2.5.4 Correction of RF errors

Several approaches for reducing errors in T_2 and eliminating artifacts caused by imperfect RF pulses have been proposed and will now be discussed.

Maudsley's Sequence

Following initial excitation and phase encoding, there is no compensation of pulse errors for the off-resonance component of the refocused spin magnetisation in the phase alternated CP or CPMG sequences. Maudsley [8] assumed the off-resonance component of the magnetisation is induced following phase encoding and showed significant accumulation of pulse errors and a loss in signal. Maudsley suggested a modification to the phase alternated CP sequence that will compensate for off-resonance magnetisation components:

$$90°_y - TE/2 - [180°_x - TE - 180°_y - TE]_n$$

Simulations, by Maudsley, showed that this reduced the signal loss caused by the loss of the phase relationship that there is assumed to be between the transverse magnetisation and the phase of subsequent 180° pulses.

Phase Cycling

Graumann *et al*. [7] introduced a sequence that removes the centre line artifact by summing the signals of the following two sequences for CP:

$90°_{x}$ - TE/2 – $180°_{x}$ - $[TE – 180°_{x}]_{n}$ *and* $90°_{x}$ - TE/2 – $180°_{-x}$ - $[TE – 180°_{-x}]_{n}$

and for a CPMG sequence:

$90°_{x}$ - TE/2 – $180°_{y}$ - $[TE – 180°_{y}]_{n}$ *and* $90°_{x}$ - TE/2 – $180°_{-y}$ - $[TE – 180°_{-y}]_{n}$.

They apply rotation matrices to follow the evolution of the magnetisation; *virtual* and *real* images are created by adding or subtracting the magnetisation of all the echoes of the CP and CPMG sequence to obtain:

$$\textit{VIRTUAL}: \quad R_{x'}(\theta)\begin{pmatrix} M_{x'} \\ M_{y'} \\ M_{z'} \end{pmatrix} + R_{-x'}(\theta)\begin{pmatrix} M_{x'} \\ M_{y'} \\ M_{z'} \end{pmatrix} + R_{y'}(\theta)\begin{pmatrix} M_{x'} \\ M_{y'} \\ M_{z'} \end{pmatrix} + R_{-y'}(\theta)\begin{pmatrix} M_{x'} \\ M_{y'} \\ M_{z'} \end{pmatrix} \qquad \textbf{[3-6]}$$

$$\textit{REAL}: \quad R_{x'}(\theta)\begin{pmatrix} M_{x'} \\ M_{y'} \\ M_{z'} \end{pmatrix} + R_{-x'}(\theta)\begin{pmatrix} M_{x'} \\ M_{y'} \\ M_{z'} \end{pmatrix} - R_{y'}(\theta)\begin{pmatrix} M_{x'} \\ M_{y'} \\ M_{z'} \end{pmatrix} - R_{-y'}(\theta)\begin{pmatrix} M_{x'} \\ M_{y'} \\ M_{z'} \end{pmatrix} \qquad \textbf{[3-7]}$$

Where the rotation matrices are:

$$R_{\pm x'}(\theta) = \pm\begin{bmatrix} 1 & 0 & 0 \\ 0 & \cos\theta & \sin\theta \\ 0 & -\sin\theta & \cos\theta \end{bmatrix} \quad ; \quad R_{\pm y'}(\theta) = \pm\begin{bmatrix} \cos\theta & 0 & \sin\theta \\ 0 & 1 & 0 \\ -\sin\theta & 0 & \cos\theta \end{bmatrix} \qquad \textbf{[3-8]}$$

and the magnetisation is:

$$\begin{pmatrix} M_{x'} \\ M_{y'} \\ M_{z'} \end{pmatrix} = M_0 \begin{pmatrix} -\sin\phi \cdot \sin\beta \\ \sin\phi \cdot \cos\beta \\ \cos\phi \end{pmatrix} \qquad \textbf{[3-9]}$$

where φ is the flip angle and $\beta = \gamma \cdot t\left(G_x \cdot x + G_y \cdot y\right)$.

By summing equations 3-6 and 3-7, a vector is formed where the transverse components of the magnetisation are independent of the imperfect flip angle $\theta°$. For the first echo, the virtual image has zero intensity and the real image has an intensity $-2\sin^2(\theta/2)$, so no correction is required. However, after the second echo virtual and real images with different intensities occur which depend differently on T_1 and T_2. Thus there will be errors in the estimation of T_2 using this technique. Since this technique involves repeating the sequence four times, the time period required to acquire the data is obviously increased by four. However, the time required can be reduced by a factor of two, whilst still being possible to remove the artifacts, by using the PHAPS (**ph**ase **a**lternating **p**hase **s**hifted) sequence [7] so that:

for odd encoding intervals (i = 1, 3, 5, ...): $\left\{\begin{matrix} 90_{x'}180_{x'}....180_{x'} \\ 90_{x'}180_{y'}....180_{y'} \end{matrix}\right\}$

and for even encoding intervals (i = 2, 4, 6, ...): $\left\{\begin{matrix} 90_{x'}180_{-x'}....180_{-x'} \\ 90_{x'}180_{-y'}....180_{-y'} \end{matrix}\right\}$

Using this technique the signal will be the sum of two echoes at each echo time, resulting in an increase in signal to noise of $\sqrt{2}$.

Dephasing Gradient Scheme

Crawley and Henkelman [6] optimised a dephasing gradient scheme first introduced in 1984 [9] which attempts to eliminate unwanted echoes. By

modifying the time before and after the slice select gradients, the echoes are made to refocus at different times. If the times of the gradients are kept constant either side of each refocusing pulse, only magnetisation that is always perfectly refocused will form the spin echoes. However, by having to continually increase the time of the extra lobes on the slice select gradient, this reduces the ability of the sequence to measure short T_2s since the signal will decay too fast and it would not be possible to obtain enough data in a short period of time. However, they also showed that there is progressive signal loss with each spin echo formed and this will compromise the accuracy of the T_2 measured.

Phase Rewinding Gradients

Mulkern *et al*. and Zur *et al*. applied equal phase encoding gradient lobes just before and just after the even-numbered refocusing pulses [10, 11]. The phase of the 90° pulse and the phase of the even-numbered refocusing pulses are inverted whenever the phase encode level is changed. The unwanted central line artifact is therefore shifted to the edge of the field of view. However, the problem with this method is that the decay between echoes is not a simple T_2 exponential function because it also depends on T_1. This is because the signal is the sum of the primary echo and stimulated echoes. This effect becomes important when the RF pulse is imperfect.

Spoiling Gradients

The phase cycling scheme for the refocusing pulses [7, 12] is prone to errors arising from imperfect reproducibility and requires at least two excitations per projection step. For the exact determination of T_2, spurious echoes must be eliminated. Hennig [13] introduced a linear spoiling gradient in the slice selective direction which is applied before and after each of the *n* refocusing pulses. The size of the spoiling gradient G_{sn} must be varied to avoid cancellation of the cumulative effect. Since gradients in an imaging system are linear, Hennig set the spoiling gradient for the first refocusing pulse, G_{s1}, to zero and the size of the second spoiling gradient, G_{s2}, was the smallest

gradient possible to suppress the occurrence of the stimulated echo after the second refocusing pulse. The spoiling gradients for the later echoes were then defined as:

$$G_{sn} = nG_{s2} \qquad \textbf{[3-10]}$$

However, since then, Freeman *et al*. showed that a geometrically spaced spoiling scheme provides a better repeatability than the linear scheme [14]. The only relaxation term contributing to the echo decay measured whilst using the spoiler gradient scheme should be T_2, but since the off-resonance components are removed from the signal train this actually leads to a reduction in apparent T_2.

Optimal Inter-echo Spacing

In 1998, Shrager *et al*. [15] found that the optimal inter-echo time spacing in a multi-echo sequence should be non-linear in order to improve precision (SNR) of T_2 values measured. However in 2000, Does *et al*. [16] showed that if the echoes are collected non-linearly in time, then the progressive loss in magnetisation also introduces apparent non-mono-exponential components in the decay. This effect may distort relative amplitudes of a multi-component T_2 distribution or generate multiple T_2 components where they do not exist. The use of linearly spaced echo times will result in errors in the measurement of T_2 due to the effects of imperfect RF pulses and diffusion. The use of non-linear echo spacing within a multi-echo experiment must therefore be considered carefully to determine its suitability.

Composite Refocusing Pulses

Composite pulses are intended to reduce the effects of small imperfections of a refocusing pulse. Levitt and Freeman [17] proposed a

$$90°_0 - 180°_{90} - 90°_0$$

composite pulse where the subscript indicates the phase shift of the 180° pulse compared with the 90° pulses. Poon and Henkelman [18] introduce the somewhat more complicated Version S pulse

$55°_{230}$ - $49°_{285}$ - $93°_{33}$ - $49°_{61}$ - $14°_{138}$ - $103°_{237}$ - $35°_{213}$ - $32°_{187}$ - $122°_{162}$ - $46°_{198}$ - $122°_{233}$ - $24°_{88}$ - $66°_{49}$ - $66°_{23}$ - $57°_{269}$ - $42°_{224}$

which is implemented as a train of rectangular pulses with fixed duration but altering amplitude and phase. Poon and Henkelman compared their pulse with three others: Levitt and Freeman's composite pulse, a simple rectangular refocusing pulse and a sinc modulated slice selective refocusing pulse. Both the rectangular and sinc pulses are sensitive to B_1 inhomogeneities and the rectangular pulse is also sensitive to B_0 inhomogeneities. The $90°_0$ - $180°_{90}$ - $90°_0$ pulse is preferable to the simple pulses, but Poon and Henkelman show that the Version S pulse is more effective, but the pulse length is much longer than Levitt and Freeman's $90°_0$ - $180°_{90}$ - $90°_0$ composite pulse.

Adiabatic Inversion Pulses

Adiabatic inversion pulses are insensitive to variations in B_1 amplitude; provided the amplitude of the pulse is above a certain threshold, the flip angle of the pulse is controlled by RF phase modulation rather than the RF field (B_1) amplitude. There are two methods using adiabatic pulses that will be explained here: LASER/CP-LASER and HSC pulses.

LASER (**l**ocalisation by **a**diabatic **se**lective **r**efocusing) is an *in vivo* spectroscopic localisation sequence introduced by Garwood *et al*. in 2001 [19]. It is an adiabatic pulse train consisting of three sets of double spin echoes. Each pair of echoes is appropriately encoded by the gradients so that a volume is selected. Frequency selective adiabatic full passage (AFP) pulses are used; they have excellent slice profiles and therefore reduce slice profile inaccuracies that are encountered using conventional pulses in multi echo sequences.

Bartha *et al*. [20] introduced the CP-LASER sequence in 2002 which is a modified version of the LASER sequence (see Figure 3-3). It incorporates 4, 8 or 16 AFP pulses before the LASER localisation scheme which are phase cycled according to the MLEV scheme [21] to reduce signal loss due to imperfect refocusing pulses.

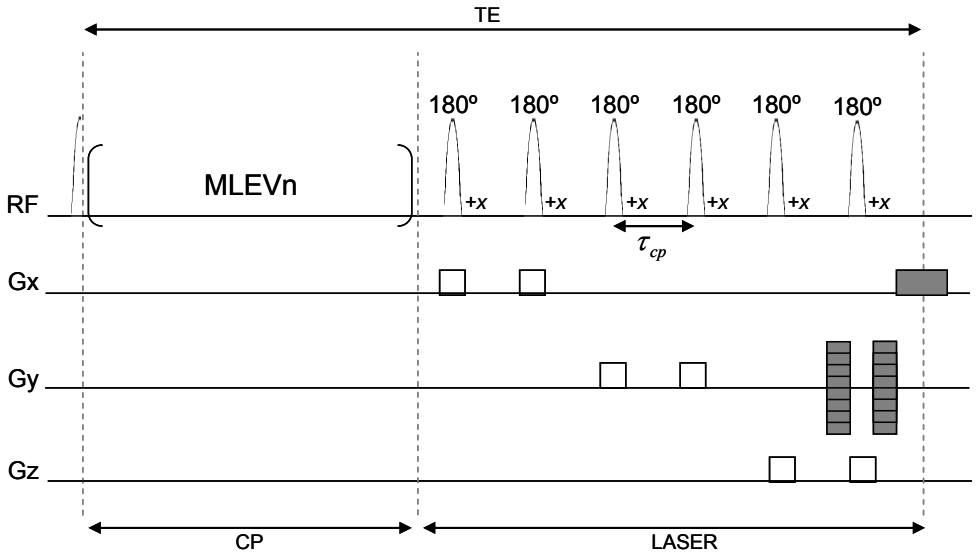

Figure 3-3: Pulse diagram for LASER and CP-LASER sequences. The shaded gradients are for phase encoding and frequency encoding and the open gradients are for slice selection. Crusher gradients are not shown here for simplicity. The CP component of the sequence consists of n = 0, 4, 8 or 16 refocusing pulses phase cycled according to the MLEVn scheme separated by τ_{cp}. (not to scale)

By increasing the length of the CP section of the sequence (0, 4, 8, 16 pulses), the echo time is increased for a given inter-pulse time (τ_{cp}) and the signal acquired during the readout will decrease. They measured R_2 by performing a three parameter (S_0, R_2 and B) least squares fit of the signal decay to the function

$$S = S_0 e^{-R_2 TE} + B \qquad \textbf{[3-11]}$$

LASER only images can also be acquired at the same echo time by increasing the inter-pulse time (τ_{cp}). Recently, they compared R_2 results obtained using

the CPMG sequence with those measured using the LASER sequence [22]. They found that the two sequences agreed well for longer τ_{cp} (> 3.5 ms), but deviated when τ_{cp} was shorter than 3.5 ms. The relaxation constants measured using this sequence are therefore dependent on the inter-pulse time.

Tyler *et al*. showed that by improving the RF pulses, the errors that occur in multi echo imaging can be overcome [23]. The application of a single hyperbolic secant (HSC) pulse will produce spin inversion, but it also introduces a phase shift which depends on the position in the slice and is therefore not a refocusing pulse. However, by applying two HSC pulses, the phase shift introduced by the first pulse is cancelled by the second and the spins refocus after the second pulse. Therefore if images are acquired after every second inversion pulse, adiabatic refocusing pulses can be used in a multi-echo sequence instead of standard sinc pulses. Since images are acquired after alternate HSC pulses, the effective inter-echo time is longer than for the standard sinc multi-echo sequence. This means there is a reduced accuracy in the measurement of short T_2s. There are a few solutions to this problem: half Fourier EPI acquisition will shorten the first echo time, the sequence could be applied twice with different echo times or a higher EPI gradient switching frequency could be used.

By combining the two HSC pulses into a composite pulse, the inter-echo time can be shortened by inverting the effective field halfway through the pulse. The phase shift that develops through the first half of the pulse is reversed through the second half of the pulse, removing the frequency dependent phase shift obtained when only a single HSC pulse is implemented. However, this type of composite adiabatic pulse has its disadvantages: it requires very high RF power and must be considered non-selective due to its poor slice profile. Therefore by using this pulse, it would not be possible to implement this sequence in a multi-slice mode.

Optimal Slice Selection Width

Most recently and most simply, Pell *et al*. [24] found that the errors in measurements of T_2 can be reduced by optimising the slice selection width used in the CPMG sequence. This is because the refocusing angle is more constant across the slice if the refocusing (180°) slice selection pulse is wider than the slice selective excitation (90°) pulse. This would suggest that performing the sequence using 3D imaging would be advantageous. Pell found that on their system, the refocusing pulse should be three times wider than the excitation pulse.

3.2.6 Conclusions

All the multiple spin echo methods described in this section give poor estimates of T_2 mainly due to RF inhomogeneities and pulse imperfections. The CPMG sequence is much quicker than the single spin echo experiment and the effect of diffusion in a single spin echo experiment is overcome when using the multi-echo technique. There are several approaches in the literature to reduce errors in measured T_2s and to reduce artifacts caused by imperfect RF pulses in multi-echo sequences.

For MRI, the single spin echo sequence is more suitable than the CPMG because whole body scanners have a very uniform B_0 field and poor pulse profiles, whereas NMR spectrometers have poorer B_0 uniformity but excellent pulse profiles. The effect of diffusion is assumed to be insignificant in homogeneous samples and whole body scanners. When the spin echo is combined with a spin warp sampling it is very slow ($TR > 5T_1$), but when combined with EPI, it is much faster. A single spin echo EPI sequence will therefore be used as a gold standard for measuring T_2 in this work since the measured T_2 values are not affected by RF pulse errors, field inhomogeneities or T_1 contributions (if $TR > 5T_1$).

Phantoms were used in this thesis to validate sequences against spin echo EPI for measuring T_2 (or inversion recovery EPI for measuring T_1). Two spherical test phantoms were used, containing NaCl and eight different physiological concentrations of agar and gadolinium ions between them. Gadolinium was used because it is a strong paramagnetic contrast agent and is the element with the greatest number of unpaired electrons; it causes the greatest increase in effective magnetic field and dipole-dipole interactions, resulting in T_1 shortening.

3.3 HYBRID GRADIENT AND SPIN ECHO SEQUENCES

3.3.1 Introduction

There are some sequences that combine spin echoes and gradient echoes to measure T_2 and T_2*. This section will introduce some methods for measuring T_2* and then discuss some hybrid spin echo – gradient echo sequences that are capable of measuring T_2 and T_2* simultaneously.

*3.3.2 Measuring T_2**

Dahnke and Schaeffter proposed a technique to overcome the signal loss due to intra-voxel dephasing caused by through-slice field gradients that leads to underestimation of T_2* [25, 26]. The sequence used was a modified multi-shot echo planar imaging sequence where the phase encoding gradient blips were replaced by a conventional phase encoding pulse applied after the slice selection. The sequence is repeated with different strengths of phase encoding gradient in order to cover all of *k*-space. A set of gradient echo images is obtained over a range of echo times according to the number of frequency encoding lobes implemented. T_2* maps are generally calculated by fitting the signal from either the odd or even gradient echoes to an exponential function (equation 3-10), but in the presence of a background gradient, the decay of the signal is no longer exponential. The dephasing of spins over time can be

described using a sinc function and this must be included in the fit to obtain an accurate T_2* (equation 3-11) [26].

$$M(TE) = M_0 \exp\left(-\frac{TE}{T_2^*}\right) \qquad \textbf{[3-12]}$$

$$M(TE) = M_0 \exp\left(-\frac{TE}{T_2^*}\right)\frac{\sin(\gamma\Delta B_0 TE/2)}{(\gamma\Delta B_0 TE/2)} \qquad \textbf{[3-13]}$$

Dahnke and Schaeftter fitted data using the sinc function and took it off to obtain the correct T_2*. They used this sequence to determine limits of detection of an iron oxide contrast agent by measurements of T_2* in the brain and in the liver [25].

3.3.3 GESFIDE

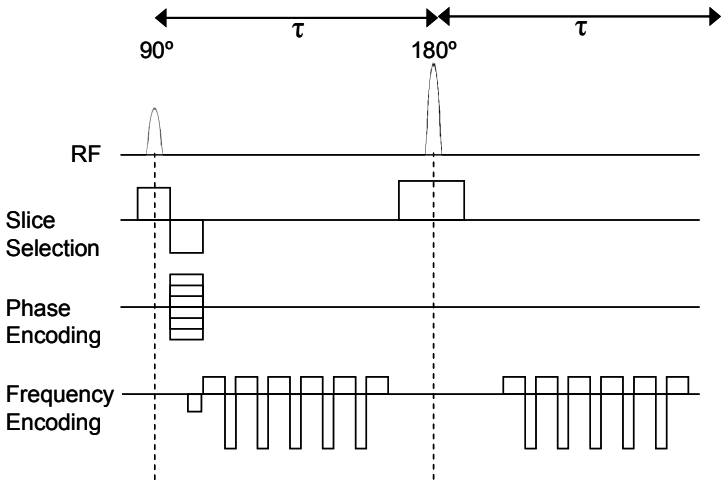

Figure 3-4: Pulse sequence diagram for GESFIDE (not to scale).

The GESFIDE (**g**radient **e**cho **s**ampling of **FID** and **e**cho) sequence was proposed by Ma and Wehrli in 1996 [27] following on from initial work by Ordidge *et al*. in 1994 [28]. In this method a 90º - τ - 180º - τ spin echo sequence is used and the dephasing and rephasing components of the signal

prior to and after the 180º RF pulse yield R_2* (= $1/T_2$*) and R_2 (= $1/T_2$) respectively (Figure 3-4). The natural logarithm of the signal was calculated and fitted on a pixel-by-pixel basis to linear equations:

Dephasing: $$\ln\left(M_{xy}(t)/A\right) = -R_2 * t \qquad \textbf{[3-14]}$$

Rephasing: $$\ln\left(M_{xy}(t)/B\right) = -R_2^- t \qquad \textbf{[3-15]}$$

to yield R_2* and R_2^- from which R_2 and R_2' could be obtained:

$$R_2 * = R_2 + R_2' \text{ and } R_2^- = R_2 - R_2' \qquad \textbf{[3-16]}$$

3.3.4 PRIME

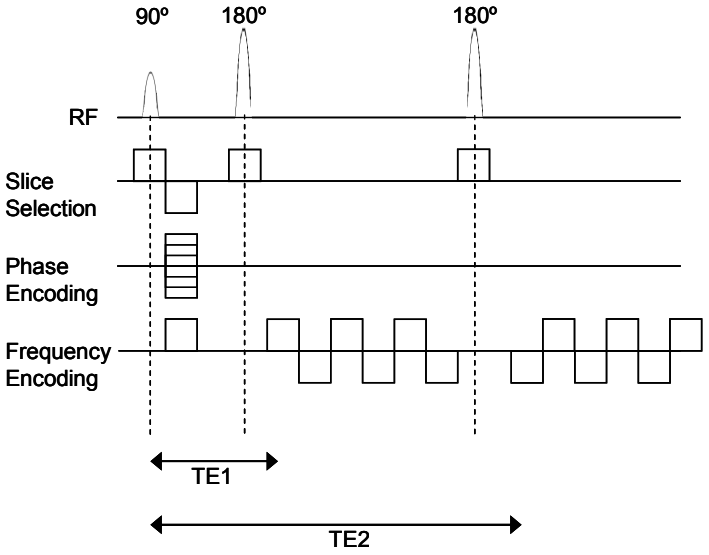

Figure 3-5: Pulse sequence diagram for PRIME (not to scale).

In 1997 Miszkiel *et al*. introduced the PRIME (**p**artially **r**efocused **i**nterleaved **m**ultiple **e**cho) sequence to quantify T_2' to assess brain iron deposition in HIV-infected patients and control subjects at 1.5 T [29]. The PRIME

sequence (Figure 3-5) comprises one spin echo and five gradient recalled echoes acquired for each of two 180º pulses. T_2 was calculated from a natural logarithmic fit to the intensities of the two spin echoes and T_2* was calculated from a natural logarithmic fit to the first six echoes of the first 180º pulse. It was then possible to calculate T_2', although T_2 will be sensitive to RF errors.

3.3.5 MASAGE-IEPI

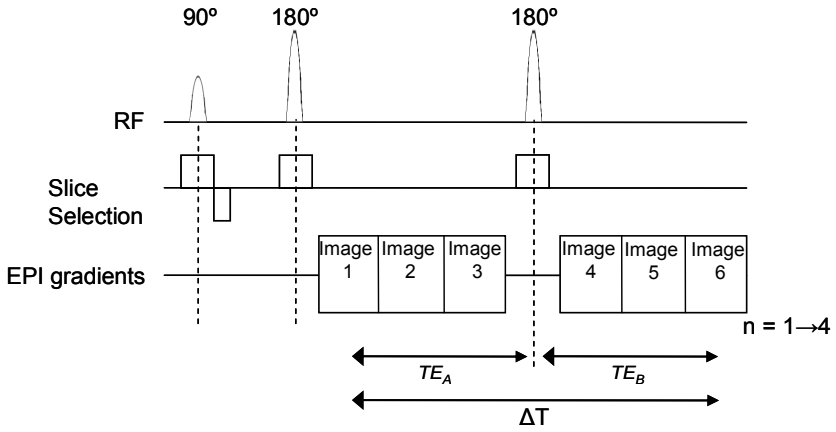

Figure 3-6: Pulse sequence diagram for MASAGE-IEPI (not to scale).

Thomas *et al.* [30] uses **m**ultiple **a**cquisition of **s**pin **a**nd **g**radient **e**choes using **i**nterleaved **e**cho **p**lanar **i**maging (MASAGE-IEPI). This incorporates an EPI sampling strategy to increase the acquisition speed. It is based on a four-shot EPI approach, where a quarter of three images are acquired after successive 90º and 180º pulses and after another 180º pulse was applied a quarter of three more images are acquired. By repeating this procedure three more times, six total images are obtained each with a different TEs (Figure 3-6). Two methods for quantifying T_2 are explained in this paper. The first, which they used, involved taking the ratio of any two echo times symmetrically placed around the second refocusing pulse and fitting the signal intensity of these ratio images to a mono-exponential decay as a function of time:

$$\frac{S_{pre}}{S_{post}} = e^{-R_2(TE_A - TE_B)} e^{-R_2'(\Delta T - TE_A - TE_B)} \quad \textbf{[3-17]}$$

where S_{pre} and S_{post} are the signal intensities before and after the second refocusing pulse (see Figure 3-6 for timings for first echo pair). The second approach involved fitting the base images directly:

$$S_{pre} = S_0 e^{-\left(R_2 + R_2'\right)TE_A} \quad \textbf{[3-18]}$$

$$S_{post} = S_0 e^{-\left(R_2 - R_2'\right)TE_B} e^{-R_2'\Delta T} \quad \textbf{[3-19]}$$

to obtain the time constants R_2^* ($\equiv R_2 + R_2'$) and R_2^- ($\equiv R_2 - R_2'$) and then calculating R_2 and R_2'. They chose to use the ratios method to obtain an R_2 map since they suggest that inaccuracies occur in the second method when the relaxation rates R_2 and R_2' are similar in magnitude.

3.3.6 GESSE

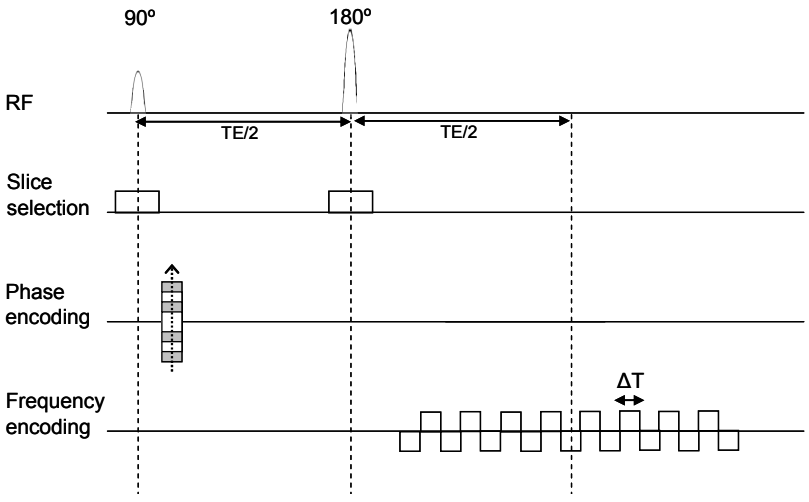

Figure 3-7: Pulse sequence diagram for GESSE (not to scale).

The GESSE (**g**radient **e**cho **s**ampling of the **s**pin **e**cho) sequence proposed by Yablonskiy *et al*. is a modified version of GESFIDE approach [31]. In the GESSE sequence only gradient echoes collected leading up to and after the spin echo are used; the FID of the 90º pulse is ignored to eliminate sensitivity to slice profile imperfections that may occur due to the 180º pulse and this results in a loss in SNR for GESSE compared with GESFIDE. T_2 was calculated pixel-by-pixel for the *n*th measurement according to:

$$R_2(n) = \frac{\ln\left(S\left(TE/2 - n\Delta T\right) \Big/ S\left(TE/2 + n\Delta T\right) \right)}{2n\Delta T} \qquad \textbf{[3-20]}$$

and converted to T_2 (= $1/R_2$).

An and Lin aimed to quantify T_2 and T_2^* at 1.5 T using a two-dimensional multi-echo gradient and spin echo sequence (Figure 3-8) [32] that was very similar to GESSE.

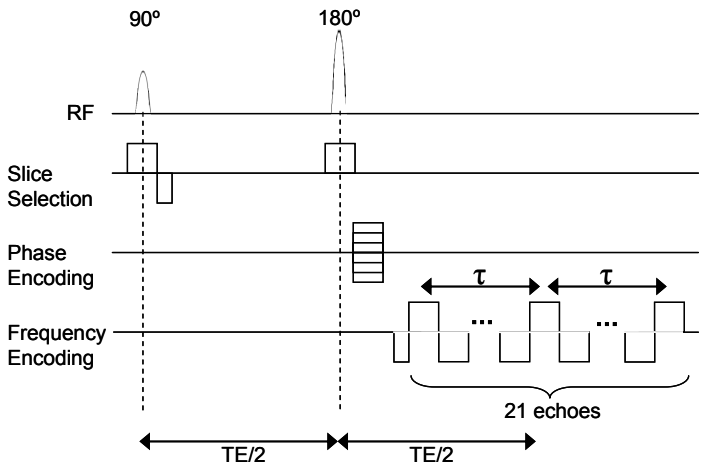

Figure 3-8: Pulse sequence diagram used by An and Lin to measure R_2 (not to scale).

In total 21 echoes were acquired with the spin echo occurring at the 11th echo and 10 echoes symmetrically either side of this. Only a single slice was

acquired to minimise potential crosstalk and signal interferences between adjacent slices. The relaxation rate R_2 was calculated using:

$$R_2 = \frac{\ln\left(\frac{S(TE-\tau)}{S(TE+\tau)}\right)}{2\tau} \qquad \textbf{[3-21]}$$

They only calculated R_2 values for five pairs of echoes (1-5 and 17-21 gradient echoes) since they showed that including echo pairs with too short of a τ compromised accuracy in the resulting R_2 value.

3.3.7 Conclusions

Some of the hybrid sequences discussed here, use data sampled around RF pulses. However, imperfect RF pulses will cause errors in calculations of T_2 and T_2*. In this work, the GESSE sequence will be used since any RF imperfections will not cause errors in the relaxation times, but alternative methods for calculating T_2 and T_2* will be investigated; the GESSE sequence will be discussed fully in chapter 7. Figure 3-9 summarises sampling strategies for variants of the hybrid gradient echo – spin echo sequences that have been discussed here.

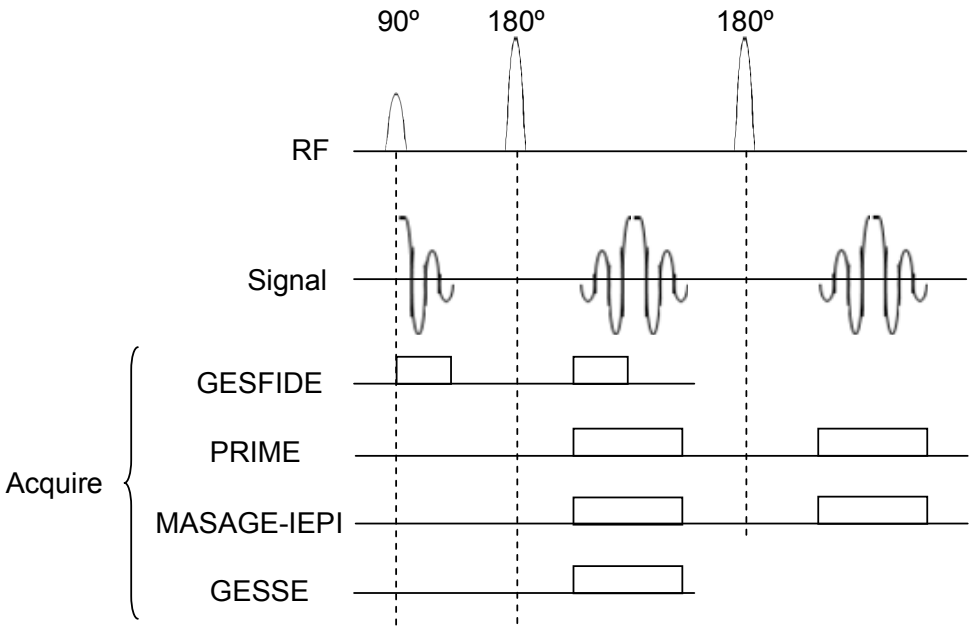

Figure 3-9: Sampling strategies for hybrid gradient echo-spin echo sequences that have been described in this section.

3.4 STEADY STATE FREE PRECESSION SEQUENCES

3.4.1 Introduction

Imaging in the steady state was introduced in chapter 2, but the potential of using SSFP (**s**teady **s**tate **f**ree **p**recession) sequences for measuring T_2 and T_1 has only been realised relatively recently [33-39]. It is particularly suitable for imaging in the abdomen because a high SNR and high in-plane resolution can be achieved, even without using SENSE. An explanation of the DESPOT and magnetisation prepared (IR and T_2-prep) bTFE sequences follow.

3.4.2 DESPOT1 and DESPOT2

In 2003 Deoni *et al*. introduced a method for simultaneous T_1 and T_2 mapping [34] based on a variable nutation angle method originally introduced in 1974 by Christiensen *et al* [40]. It is possible to map T_2 and T_1 based on the acquisition of two or more SPGR (**s**poiled **gr**adient **r**ecalled echo) images and

fully balanced SSFP (**s**teady **s**tate **f**ree **p**recession) images. These are referred to as DESPOT1 and DESPOT2 (**d**riven **e**quilibrium **s**ingle **p**ulse **o**bservation of $\mathbf{T_1}$ and $\mathbf{T_2}$ respectively). T_1 is obtained using the DESPOT1 method and this value is then used with the DESPOT2 method to obtain a value of T_2.

The signal intensity of the SPGR sequence is a function of T_1, TR, M_0 and flip angle, α:

$$M_{SPGR} = \frac{M_0\left[1-\exp\left(-TR/T_1\right)\right]\sin(\alpha)}{1-\exp\left(-TR/T_1\right)\cos(\alpha)} \qquad \textbf{[3-22]}$$

Therefore by keeping the TR constant and changing α, a curve dependent on T_1 can be generated and by representing the curve in a linear form, both T_1 and M_0 can be extracted.

In the SSFP sequence used to obtain T_2, the following equation is used to express the signal:

$$M_{SSFP} = \frac{M_0\left[1-\exp\left(-TR/T_1\right)\right]\sin(\alpha)}{1-\exp\left(-TR/T_1\right)\exp\left(-TR/T_2\right)-\left[\exp\left(-TR/T_1\right)-\exp\left(-TR/T_2\right)\cos(\alpha)\right]} \qquad \textbf{[3-23]}$$

There are several forms of this equation in the literature but this form, derived by Perkins and Wehrli in 1986 [41], was chosen to be the most appropriate since they used a short TR (< 10 ms) and the RF pulses are alternated by 180°. So once again, by keeping the TR constant and altering α, a signal curve dependent on T_1 and also T_2 can be obtained. Since T_1 is already known from the SPGR sequence, equation 3-21 can be rearranged into a linear form and solved for T_2 and M_0.

This approach allows the acquisition of T_1 and T_2 maps of a 256x256 matrix and 100 slices with < 1 mm^3 voxel size in less than 15 minutes. The primary

source of error in this technique is the accuracy of the flip angles achieved due to the B_1 field inhomogeneities and non-ideal slice profiles. By implementing the method in 3D, the slice profiles errors will be reduced in the centre portion of the volume.

The DESPOT2 technique is limited due to off-resonance banding artifacts in the SSFP images [42] resulting in voids in the T_2 maps. Deoni's 2004 paper introduces an additional component to the SSFP sequence by including phase-cycling which removes the banding and does not increase scan time. The full flip angle range is divided into at least two sub-sets (e.g. set A: 10°, 30°, 50°, ... and set B: 20°, 40°, 60°, ...) and acquired with a different phase increment (e.g. 0° and 180°). T_2 and M_0 maps are then calculated for each sub-set using a weighted least squares approach and combined using a weighted average to form T_2 maps with little artifact. This technique has been named DESPOT2-c to include the phase-cycling component. At high field strength (>1.5 T) the susceptibility effects increase and the SSFP signal has to be modeled in full with a three parameter non-linear fit for T_2, ω (resonant frequency) and ρ (proportional to the proton density) [43].

3.4.3 Magnetisation prepared

Magnetisation prepared SSFP sequences were first proposed in 1994 by Deimling and Heid [44], where a preparation step is applied before a *turbo* SSFP acquisition. For inversion recovery steady state imaging, steady state signal amplitude is [36]:

$$S_{ss} = M_0 \frac{e^{-TE/T_2^*}\left(1 - e^{-TR/T_1}\right)\sin(\alpha)}{1 - \left(e^{-TR/T_1} - e^{-TR/T_2}\right)\cos(\alpha) - e^{-TR/T_1}e^{-TR/T_2}} \qquad \textbf{[3-24]}$$

where α is the flip angle. This can be simplified if TR is much less than T_1 and T_2 to [37]:

$$S_{ss} = \frac{M_0 \sin(\alpha)}{\left(\frac{T_1}{T_2}+1\right)-\left(\frac{T_1}{T_2}-1\right)\cos(\alpha)} \qquad \textbf{[3-25]}$$

Scheffler *et al*. [36] obtained T_1 using a pixel-by-pixel fit using the Powell algorithm [45] and Schmitt *et al*. calculated T_1 and T_2 from the fit function:

$$S(nTR) = S_{ss}\left[1 - INV \cdot e^{-nTR/T_1^*}\right] \qquad \textbf{[3-26]}$$

where

$$INV = 1 + \frac{S_0}{S_{ss}} \qquad \textbf{[3-27]}$$

and T_1* is the apparent relaxation time. By performing a three parameter least squares fitting routine for T_1*, S_{ss} and INV, T_1 and T_2 can be calculated. M_0 can also be calculated directly from:

$$M_0 = \frac{S_{ss}(INV-1)}{\sin\left(\frac{\alpha}{2}\right)} \qquad \textbf{[3-28]}$$

Huang *et al*. introduced a T_2-prepared steady state sequence [33] which was used to measure T_2 in the myocardium by varying the echo time of the T_2-preparation phase. For the first TE, the T_2-preparation phase consisted of $90°_x$ – $90°_{-x}$ and for the second TE, the preparation phase was an $MLEV_4$ train (see section 3.2.5.4) of refocusing pulses $90°_x - \tau - [180°_y - 2\tau]_4 - \tau - 90°_x$. In phantom experiments they used 6 different TEs (2.59, 22, 44, 55, 66, 88 ms) and for *in vivo* experiments, they collected 5 images with alternating TEs of 2.59 and 55 ms during a 25 second breathold. They fitted the data to a mono-exponential model of T_2, independently of the numbers of TEs collected and calculated T_2 maps pixel-by-pixel.

3.4.4 Conclusions

The DESPOT2 technique relies on measuring T_1 first using DESPOT1 and therefore acquisition time is increased and the IR-bTFE technique is susceptible to errors in the measurement of T_2 arising from flip angle errors [38] and off-resonance effects [37]. Also, DESPOT is not useful in the gastrointestinal tract where visceral motion degrades the images and any segmented k-space approach e.g. rapid IR-bTFE for T_1 in the abdomen [46] is not appropriate for stomach and intestine relaxometry which show irregular motion during a breath-hold or respiratory triggering. In order to focus on T_2 measurements, it seems ideal to use a spin echo version of the IR-bTFE sequence to change the emphasis from T_1 to T_2 and therefore reduce errors in the measured T_2s. This will form the basis for the technique developed further in chapter 5.

3.5 SUMMARY

Three techniques have been reviewed in this section for measuring T_2: spin echo, hybrid gradient echo-spin echo and steady state imaging sequences. The advantages and disadvantages have been discussed. In this work, spin echo EPI will be used as a gold standard to measuring T_2. Also the GESSE sequence in section 3.3.6 will be used in the brain and liver. Optimisation of fitting algorithms to obtain T_2 will be investigated and then applied in the brain to measure relaxation in health and disease. Finally, a spin echo version of the IR-bTFE sequence in section 3.4.3 will be developed, optimised and applied in the abdomen and gastrointestinal tract.

3.6 References

1. Hahn, E.L., *Spin Echoes.* Physical Rev, 1950. **80**(4): p. 580-594.

2. Carr, H.Y. and E.M. Purcell, *Effects of Diffusion on Free Precession in Nuclear Magnetic Resonance Experiments.* Phys. Rev., 1954. **94**(3): p. 630-638.
3. Meiboom, S. and D. Gill, *Modified Spin-Echo Method for Measuring Nuclear Relaxation Times.* Rev. Sci. Instrum., 1958. **29**(8): p. 688-691.
4. Majumdar, S., et al., *Errors in the Measurements of T_2 Using multiple-Echo MRI Techniques I. Effects of Radiofrequency Pulse Imperfections.* Mag. Res. Med, 1986a. **3**: p. 397-417.
5. Majumdar, S., et al., *Errors in the Measurements of T_2 Using Multiple-Echo MRI Techniques II. Effects of Static Field Inhomogeneity.* Mag. Res. Med, 1986b. **3**: p. 562-574.
6. Crawley, A.P. and R.M. Henkelman, *Errors in T_2 estimation Using Multislice Multiple-Echo Imaging.* Mag. Res. Med, 1987. **4**: p. 34-47.
7. Graumann, R., A. Oppelt, and E. Stetter, *Multiple-Spin-Echo Imaging with a 2D Fourier Method.* Mag. Res. Med, 1986. **3**: p. 707-721.
8. Maudsley, A.A., *Modified Carr-Purcell-Meiboom-Gill sequence for NMR Fourier imaging applications.* J Mag Res, 1986. **69**: p. 488-491.
9. Duijn, J.H., J.H.N. Creyghton, and J. Schmidt, *Suppression of artefacts due to imperfect π pulses in multiple echo Fourier imaging.* Proc. 3rd Annual Meeting of SMRM, 1984: p. P197.
10. Mulkern, R.V., et al., *Contrast Manipulation and Artifact Assessment of 2d and 3d Rare Sequences.* Mag. Res. Im., 1990. **8**(5): p. 557-566.
11. Zur, Y., M.L. Wood, and L.J. Neuringer, *Spoiling of transverse magnetization in steady state sequences.* Mag. Res. Med., 1991. **21**(2): p. 251-263.
12. Zur, Y. and P. Bendel, *The effects of simultaneous pulsing in different gradient coils on the nuclear-magnetic-resonance imaging of oblique slices.* Med. Phys., 1987. **14**(2): p. 172-177.
13. Hennig, J., *Multiecho Imaging Sequences with Low Refocusing Flip Angles.* J. Mag. Res., 1988. **78**: p. 397-407.

14. Freeman, A.J., P.A. Gowland, and P. Mansfield, *Optimization of the ultrafast look-locker echo-planar imaging T_1 mapping sequence.* Mag. Res. Im., 1998. **16**(7): p. 765-772.
15. Schrager, R.I., G.H. Weiss, and R.G.S. Spencer, *Optimal time spacings for T_2 measurements: monoexponential and biexponential systems.* NMR Biomed., 1998. **11**: p. 297-305.
16. Does, M.D. and J.C. Gore, *Complications of nonlinear echo time spacing for measurements of T_2.* NMR Biomed., 2000. **13**: p. 1-7.
17. Levitt, M.H. and R. Freeman, *Composite Pulse Decoupling.* J. Mag. Res, 1981. **43**: p. 502.
18. Poon, C.S. and R.M. Henkelman, *Practical T2 Quantitation for Clinical Applications.* J. Mag. Res. Im., 1992. **2**: p. 541-553.
19. Garwood, M. and L. DelaBarre, *The Return of the Frequency Sweep: Designing Adiabatic Pulses for Contemporary NMR.* J. Mag. Res, 2001. **153**: p. 155-177.
20. Bartha, R., et al., *In Vivo ^1H_2O T_2^+ Measurement in the Human Occipital Lobe at 4T and 7T by Carr-Purcell MRI: Detection of Microscopic Susceptibility Contrast.* Mag. Res. Med., 2002. **47**: p. 742-750.
21. Shaka, A.J., S.P. Rucker, and A. Pines, *Iterative Carr-Purcell Trains.* J. Mag. Res., 1988. **77**: p. 606-611.
22. Nikolova, S., C.V. Bowen, and R. Bartha, *Experimental validation of a T-2 rho transverse relaxation model using LASER and CPMG acquisitions.* J. Mag. Res, 2006. **181**(1): p. 35-44.
23. Tyler, D.J., et al., *Rapid and accurate measurement of transverse relaxation times using a single shot multi-echo echo-planar imaging sequence.* Mag. Res. Im., 2004. **22**: p. 1031-1037.
24. Pell, G.S., et al., *Optimized clinical T2 relaxometry with a standard CPMG sequence.* J. Mag. Res. Im., 2006. **23**(2): p. 248-252.
25. Dahnke, H. and T. Schaeffter, *Limits of Detection of SPIO at 3.0 T Using T_2* Relaxometry.* Mag. Res. Med, 2005. **53**: p. 1202-1206.

26. Fernandez-Seara, M.A. and F.W. Wehrli, *Postprocessing Technique to Correct for Background Gradients in Image-Based R_2* Measurements.* Mag. Res. Med, 2000. **44**: p. 358-266.

27. Ma, J. and F.W. Wehrli, *Method for Image-Based Measurement of the Reversible and Irreversible Contribution to the Transverse-Relaxation Rate.* J. Mag. Res. Series B, 1996. **111**: p. 61-69.

28. Ordidge, R.J., et al., *Assessment of Relative Brain Iron Concentrations Using T2-weighted and T2*-weighted MRI at 3 Tesla.* Mag. Res. Med, 1994. **32**: p. 335-341.

29. Miszkiel, K.A., et al., *The measurement of R2, R2* and R2' in HIV-infected patients using the prime sequence as a measure of brain iron deposition.* Mag. Res. Im., 1997. **15**(10): p. 1113-1119.

30. Thomas, D.L., et al., *Rapid Simultaneous Mapping of T2 and T2* by Multiple Acquisition of Spin and Gradient Echoes Using Interleaved Echo Planar Imaging (MASAGE-IEPI).* Neuroimage, 2002. **15**: p. 992-1002.

31. Yablonskiy, D.A. and E.M. Haacke, *An MRI Method for Measuring T2 in the Presence of Static and RF Magnetic Field Inhomogeneities.* Mag. Res. Med, 1997. **37**: p. 872-876.

32. An, H. and W. Lin, *Quantitative Measurements of Cerebral Blood Oxygen Saturation Using Magnetic Resonance Imaging.* J. Ce. Blood Flow Met., 2000. **20**: p. 1225-1236.

33. Huang, T.Y., et al., *T2 measurement of the human myocardium using a T2-prepared transient-state TrueFISP sequence.* Mag Res Med, 2007. **57**(5): p. 960-6.

34. Deoni, S.C.L., B.K. Rutt, and T.M. Peters, *Rapid Combined T_1 and T_2 Mapping Using Gradient Recalled Acquisition in the Steady State.* Mag. Res. Med, 2003. **49**: p. 515-526.

35. Gulani, V., et al., *Towards a single-sequence neurologic magnetic resonance imaging examination: multiple-contrast images from an IR TrueFISP experiment.* Invest Radiol, 2004. **39**(12): p. 767-74.

36. Scheffler, K. and J. Hennig, *T_1 Quantification With Inversion Recovery TrueFISP*. Mag. Res. Med, 2001. **45**: p. 720-723.
37. Schmitt, P., et al., *Inversion Recovery TrueFISP: Quantification of T1, T2, and Spin Density*. Mag. Res. Med., 2004. **51**: p. 661-667.
38. Newbould, R. and R. Bammer, *Flip Angle Sensitivity in IR-trueFISP T_1 and T_2 Mapping*. Proc. 13th Annual Meeting of ISMRM, 2005b: p. 2191.
39. Stehning, C., S. Winkelmann, and H. Dahnke, *Simultaneous T1, T2 and spin density quantification in 5 seconds using inversion recovery SSFP*. Proc. 15th Annual Meeting of ISMRM, 2007.
40. Christiensen, K.A., et al., *Optimal Determination of Relaxation Times of Fourier Transform Nuclear Magnetic Resonance. Determination of Spin-Lattice Relaxation Times in Chemically Polarized Species*. J. Phys. Chem., 1974. **78**: p. 1971-1977.
41. Perkins, T.G. and F.W. Wehrli, *CSF signal enhancement in short TR gradient echo images*. Mag. Res. Im., 1986. **4**: p. 465-467.
42. Deoni, S.C.L., et al., *Rapid T_2 Estimation With Phase-Cycled Variable Nutation Steady-State Free Precession*. Mag. Res. Med, 2004. **52**: p. 435-439.
43. Deoni, S.C., *Transverse Relaxation Time (T2) and Susceptibility Measurement wih Phase-Cycled Steady-State Free Precession*. Proc. 15th Annual Meeting of ISMRM, 2007: p. P 1783.
44. Deimling, M. and O. Heid, *Magnetisation Prepared True FISP Imaging*. Proc. 2nd Annual Meeting Soc. Mag. Res., 1994: p. 495.
45. Press, W.H., et al., *Numerical Recipes in C (Second Edition)*. 1996: p. 412-420.
46. Bokacheva, L., et al., *Single breath-hold T1 measurement using low flip angle TrueFISP*. Magn Reson Med, 2006. **55**(5): p. 1186-90.

CHAPTER 4

METHODS FOR MEASURING NORMAL PHYSIOLOGY IN THE GASTROINTESTINAL TRACT

4.1 INTRODUCTION

The study of anatomical changes due to gastrointestinal (GI) diseases using MRI is well established [1], but the study of the normal physiological response of the GI tract to food using MRI is concentrated in just a few specialist research centres. MRI is potentially a very powerful technique for studying gastrointestinal physiology, as it is non-ionising, non-invasive and can measure many different, related functions within a single experiment e.g. gastric emptying, mixing of meals and small bowel water volumes.

Over the last decade, MRI has been used to study the fate of food in the stomach and intestine, in particular the effects of meal viscosity [2, 3] and fat content [4-6]. MRI is also a useful tool for measuring flow and shear rates [7] in the gut and investigating the brain's response to the taste of food [8].

Obesity, diabetes and cardiovascular disease are all high risk conditions which can be caused by a high fat diet. Fat enhances the appeal of foods due to its attractive sensory attributes (flavour and texture) [9] and elicits many different effects in the mouth and in the gastrointestinal tract. It is present in many foods where it contributes to viscosity, and it is known that there are interactions between viscosity, aroma and taste which modify the perceived flavour. There is a complex interaction between the mouth, brain and GI tract which is known as the brain-gut axis. The brain's response to different factors such as taste, texture, viscosity of different food types can be studied using functional magnetic resonance imaging.

This chapter introduces key features of the gastrointestinal tract and different methods that can be used to study the fate of food. A technique for measuring small bowel water content is validated for use at 3.0 T.

4.2 THE GASTROINTESTINAL TRACT

4.2.1 Anatomy and functions of the gastrointestinal tract

The GI tract (Figure 4-1) is a system of organs; the major functions are ingestion of food, digestion of food, absorption of nutrients, and defecation. Digestion begins in the oral cavity where amylase, a digestive enzyme found in saliva, begins to break down carbohydrates. Once the food is mixed and softened, it is swallowed and enters the stomach via the oesophagus. The stomach is a major site for processing food and is responsible for mechanical grinding, dilution, chemical breakdown and mixing. In the stomach, the food is broken down further, and the gastric conditions provide a suitable environment for digestive enzymes (e.g. pepsin) to break down proteins. When food arrives in the stomach, the hormone gastrin is secreted which stimulates the gastric glands to produce the enzyme pepsin. From the stomach, the partially digested food, known as chyme, is transported to the small bowel via the pyloric sphincter, where further chemical and mechanical processing occurs. Chyme is a combination of partially digested food, hydrochloric acid, water and digestive enzymes.

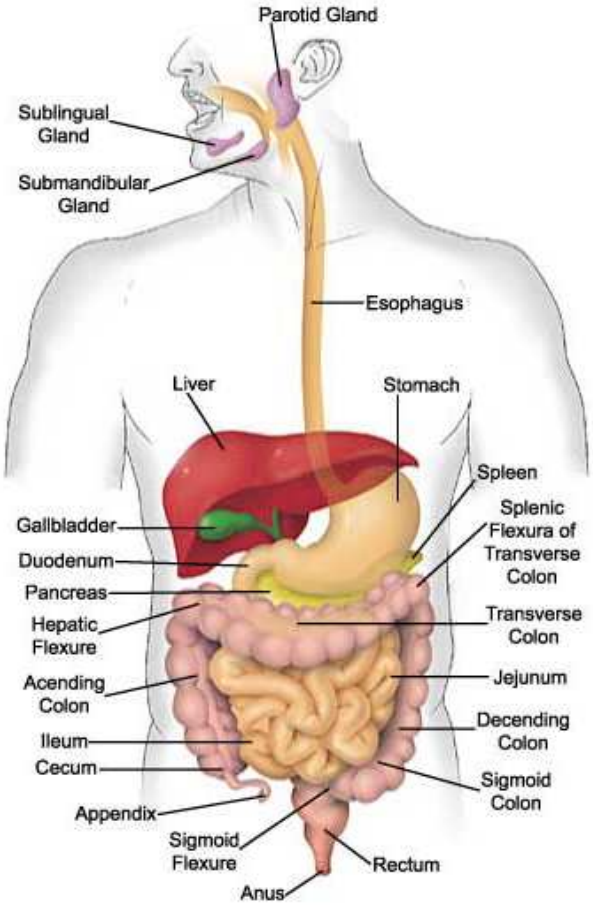

Figure 4-1: The gastrointestinal tract.
(http://www.sciencehelpdesk.com/unit/bg3/2)

Food is transported from the stomach to the rectum through peristalsis in the small bowel and remainder of the digestive tract, allowing food to be mixed with the digestive juices and absorbed. The small bowel consists of three compartments: the duodenum, the jejunum and the ileum. When food containing fat enters the duodenum, the gallbladder contracts and releases bile. This causes the hormone cholecystokinin (CCK) to be secreted. Bile, produced in the liver and stored in the gallbladder, emulsifies fat to increase the surface area in order to aid enzyme action and neutralise acid in partly digested food. The duodenum also produces the hormone secretin, which stimulates secretion of sodium bicarbonate by the pancreas to enhance the neutralising effects of CCK. CCK is also responsible for the release of

digestive enzymes from the pancreas, which act as catalysts for the digestion of fat, protein and carbohydrate. The main function of the jejunum is to absorb nutrients. The ileum is the final section of the small intestine and its main function is to absorb vitamin B12, bile salts and any other unabsorbed nutrients.

The chyme from the ileum then enters the large intestine, which also has three components: the cecum, the colon and the rectum. The colon consists of four parts: the ascending colon, the transverse colon, the descending colon, and the sigmoid colon. No further chemical digestion occurs in the large intestine so any food products that are not absorbed in the small bowel are mixed in the large intestine with other waste products from the body and become feces. The large intestine absorbs water and feces are stored in the sigmoid colon before moving to the rectum to begin the process of defecation.

4.2.2 Methods for studying gastrointestinal function

Until recently, the methods that were available to study GI function in humans had limitations. Naso-gastric or naso-duodenal/jejunal intubation [10-12] is a simple approach, but it is highly invasive and the presence of the tube might pertubate normal GI behaviour [13]. This technique is limited to studying liquid meals that can easily be extracted from the stomach, duodenum or jejenum through the tube at regular time intervals to perform further tests to observe, for example, dilution changes.

Gamma scintigraphy has been used to monitor gastric emptying of multi-phase meals, by labeling the different food components with different radioactive isotopes [14-16]. However, this technique does not provide any insight into the secretions that occur in the GI tract.

Carbon-13 labeled meals can be used to measure gastric emptying [17]. Once they are consumed, serial breath tests are performed to measure the amount of

labeled CO_2 in the breath over time. However, meals that can be investigated in this way will be restricted due to the extra complications of adding a label into the meal. Intraluminal manometry [18, 19], used to measure motility, also involves intubation and is therefore highly invasive and likely to perturb normal function. Ultrasound can be used to measure intra-gastric flow velocities [20], but air-liquid interfaces prevent imaging of the entire gastric contents thus limiting its application in the intestine.

Gastric emptying has been monitored using electrical impedance tomography [21, 22], which is cheap and non-invasive, but it does not have good spatial resolution or contrast to meal distribution. Conducting electrodes are attached to the skin and small alternating currents are applied to some or all of the surface electrodes and the resulting electrical potential is measured. An image of conductivity or permittivity of the part of the body under observation can be inferred from these electrical measurements.

4.2.3 MRI of the gastrointestinal tract

In the early days of MRI, assessment of GI physiology using MRI was limited due to image artifacts caused primarily by breathing and internal organ motion. With the development of fast MRI sequences, this problem has now been overcome. Using echo planar imaging (EPI), it has been possible to assess gastric motility at low field (0.5 T) since images can be acquired in under 130 ms. Since spin-echo EPI produces intrinsically T_2 weighted images, there is excellent contrast between water-based liquid meals and surrounding tissues, and between solid and liquid components of a meal [7, 23]. Therefore, additional MRI contrast agents are not required to improve contrast.

Although the stomach can easily be scanned with EPI at 0.5 T or higher field strengths, EPI is not suitable for imaging the intestine at 0.5 T because of susceptibility artifacts, which only increase with increased field strength.

Ultra-fast imaging techniques, such as fast spin echo (FSE, RARE or HASTE), balanced turbo field echo (bTFE) and fast field echo (FFE or FLASH) have been applied to the GI tract and are suitable for use at high field strengths. However, the increase in RF power deposition will cause an increase in the imaging time when the field strength is increased to keep within specific absorption rate (SAR) safety limits. If SENSE is used, then shorter scan times and lower RF power deposition can be achieved. Due to the variety of ultra-fast sequences now available on commercial scanners, it is generally possible to outline the stomach, bowel or colon contents in turn by changing the contrast accordingly.

4.2.4 Measuring gastric changes using MRI

Gastric emptying is very important in terms of studying digestion of food and satiety. The rate of gastric emptying depends on the volume, chemical composition, nutritional value and physical state of the food. External factors such as emotion and intense pain also have the potential to affect gastric emptying [24]. In addition to gastric emptying, it is also useful to measure changes in viscosity of contents in the stomach due to dilution and digestion [2, 3]. Preprocessed fatty foods often contain calories added as a fat emulsion stabilised by emulsifiers so monitoring fat emulsification in the stomach is useful in understanding rates of gastric emptying [5].

It is important to be able to measure rates of gastric emptying when studying the gastrointestinal tract in normal gastric function or to study effects of disease. Gastric volumes can be measured from T_2 weighted images using Analyze® software (Mayo Clinic, Rochester, MN, USA) by defining the contents of the stomach as regions of interest (ROIs) and summing these ROI volumes from contiguous slices. Boulby *et al*. [25] validated the technique in 1997 by inserting a bag, with a tube attached, into the stomach and infused known volumes of fluid into the bag. The experiment was also carried out ex vivo. There was found to be a slight underestimation of the volumes in vivo

compared to ex vivo which they attributed to inhomogeneities caused by the large air/water interface in the region of interest. However, the largest errors were obtained by volunteers breathing and moving on the bed; these were of the order of 50 ml in 200-700 ml. An edge-finding tool now available within the Analyze software can be used, since there is clear definition between the stomach contents and the surrounding tissue and this limits errors introduced by user variations.

4.2.5 Measuring small bowel water content using MRI

Small bowel water content (SBWC) is potentially an important parameter in studying normal gastrointestinal physiology, and also clinical conditions such as irritable bowel syndrome and Celiac disease. There are four main factors contributing to the SBWC: gastric emptying, water absorption, small bowel secretions and progression to the colon. After eating, the interaction between the stimulation of gastric, intestinal and pancreatico-biliary secretions (increasing intestinal contents) and absorption of water, nutrients and sodium (decreasing intestinal contents) are very complex.

SBWC depends on intestinal motility as well as the balance between absorption and secretion. Fasting intestinal motility is highly episodic with intermittent propulsive motor patterns migrating down the gut every 1-2 hours to clear any debris. The migrating motor complex (MMC) is the pattern of activity in the intestine during periods between meals; the activity can be noisy and heard externally. The periodic nature of the MMC is controlled by the central nervous system. The fed pattern facilitates absorption by constant small mixing movements propelling it towards the large intestine.

Anatomical diseases of the small bowel (e.g. Crohn's disease) are visualised by distending the small bowel lumen with water by using preparations that prevent absorption and contrast agents are often used to improve image quality [26, 27]. This approach is not acceptable when studying normal

physiology as water is naturally secreted and absorbed in the small bowel. This uncomfortable technique would not be tolerated well, especially by patients with functional disorders, and the technique involved would disrupt normal behaviour.

4.3 VALIDATION OF METHODS: Quantifying Small Bowel Water Content

4.3.1 Introduction

Assessment of water absorption and secretion in the small bowel was initially explored at low field using echo-planar magnetic resonance imaging [28, 29], but over the last decade there have been significant improvements in image quality due to increased field strengths, improved sequence and coil design. Other work was carried out by Schiller *et al* in 2005 to measure the fluid content of the stomach and small and large bowels using MRI [30], but no validation or error analysis was reported.

Our group has recently developed a non-invasive method of assessing SBWC at 1.5 T which has been validated by naso-duodenal intubation of volunteers and comparing infused volumes with measured MRI intestinal water volumes [31]. An MRCP sequence (magnetic resonance cholangiopancreatography) was used to monitor changes in SBWC. MRCP is a turbo spin-echo sequence (TSE) originally developed to study the biliary tract [32, 33]. Water in the small bowel can be very widely distributed and therefore accurately quantifying the free water volume in the small bowel is particularly challenging even with the gold standard intubation technique. Small volumes of water may be lost due to partial volume effects associated with techniques such as MRI; therefore only significant pockets of fluid can be observed and hence measured in the small bowel.

The method used to estimate SBWC assumes that in the MRCP images, any pixel in the abdomen with signal intensity above a given threshold (S_{th}) is filled with 'free' water. This threshold is chosen to allow for intra- and inter-subject variations in the scanner due to scanner instabilities, subject repositioning and coil loading. An internal marker was used to set the threshold S_{th}; anything placed externally from the subject would have been at the edge of the field of view, which experiences very variable receive characteristics due to the use of wrap-around receive coils. Cerebral spinal fluid (CSF) was used as the internal marker because it is the centre of the field of view, is accurately regulated and is covered by multiple imaging slices. A conversion factor was found which calculates S_{th} from the CSF signal measured. Schiller *et al* [30] used the gallbladder as an internal marker, but this would not be suitable for studies requiring subjects to consume a meal containing fat, as the gallbladder would empty and subsequently refill over the course of the experiment. Bile also contains cholesterol which does not make it a good intrinsic standard signal for water.

The SBWC method has only been validated at 1.5 T to date. The obvious development from this initial work was to determine whether it would be possible to use the technique at 3.0 T. Increasing the field strength would provide an increase in SNR but susceptibility artifacts due to the air/water interface in the small bowel would be worse with the increase in field strength. Therefore, the method needs to be validated at this field strength, since the calculation of the threshold S_{th} may be dependent on field strength, the sequence and the RF coil used.

4.3.2 Aims

The aim of this study was to obtain the conversion factor from MRI CSF signal to calculate the threshold level S_{th} using an intubation technique to allow quantification of the SBWC and to validate measured SBWC from MRI images against known infused volumes at 3.0 T.

4.3.3 Method

4.3.3.1 Volunteer selection

19 healthy volunteers (8 male, 11 female) who had no history of gastrointestinal disease, were recruited with a mean age of 25 years (range 19 - 43). The mean body mass index (BMI) of the volunteers was 22.3 kg m^{-2} (range 18.5 - 25.2). All volunteers attended the centre in the morning having fasted overnight.

4.3.3.2 Study protocol

All imaging was carried out on a 3.0 T Philips Achieva whole body MRI scanner using a coronal turbo spin echo sequence (TSE or RARE) (Multi-slice 2D single shot imaging, TE_{eff} = 400 ms, TR_{eff} = ∞, 20 slices, SL = 7 mm, FOV = 400 mm, scan percentage 80 %, acquired voxel size = 1.25 x 1.57 x 7 mm^3, interpolated to 0.78 x 0.78 x 7 mm^3, number of refocusing pulses = 130, SENSE factor = 2.0, total scan time = 44 s acquired over two breatholds).

Volunteers were seated and a local anaesthetic (Xylocaine spray – Astrazeneca) was administered to the back of the throat. A gel-lubricated, 14fg (4.7 mm diameter) Salem sump tube (Sherwood Medical Co.) was passed via the nose into the stomach and taped in position at approximately 70 cm from the nares. The passage of the tube was aided by sipping a small volume of still bottled water. A small volume of gastric aspirate was removed and its pH checked with litmus paper; an acid value demonstrated that the tube was correctly sited in the stomach. The volunteer was instructed to lie in the right lateral position to aid the passage of the tube into the duodenum.

After approximately 30 minutes the position of the tube was checked using MRI. The lumen of the tube was filled with 7 ml (equivalent to the tube's

dead space) of the test solution described below and the positioning of the tube was verified using the TSE sequence (Figure 4-2 and Figure 4-3). If the tube did not pass the pylorus or was coiled back in the stomach (Figure 4-4), it was slowly retracted by about 15 cm until it could be seen lying over the greater curvature of the stomach in the MRI images. The tube was then slowly pushed again towards the duodenum. Final positioning of the tube in the duodenum was verified using the TSE sequence (Figure 4-2).

Having achieved the desired positioning of the tube, a baseline data set was acquired and then eight 40 ml boluses of the test solution were infused into the small bowel (320 ml total infusion) in less than 15 minutes. The test solution comprised 145 mM l^{-1} NaCl and 15 mM l^{-1} mannitol in water. This solution was also used for the optimisation and validation carried out previously at 1.5 T because it was previously shown, using the intestinal perfusion technique, to induce no net flux (absorption) when infused into a jejunal segment [34]. Immediately after each bolus was infused a TSE data set was acquired. After completing the entire infusion protocol, the volunteer was taken out of the scanner room and the naso-duodenal tube was removed.

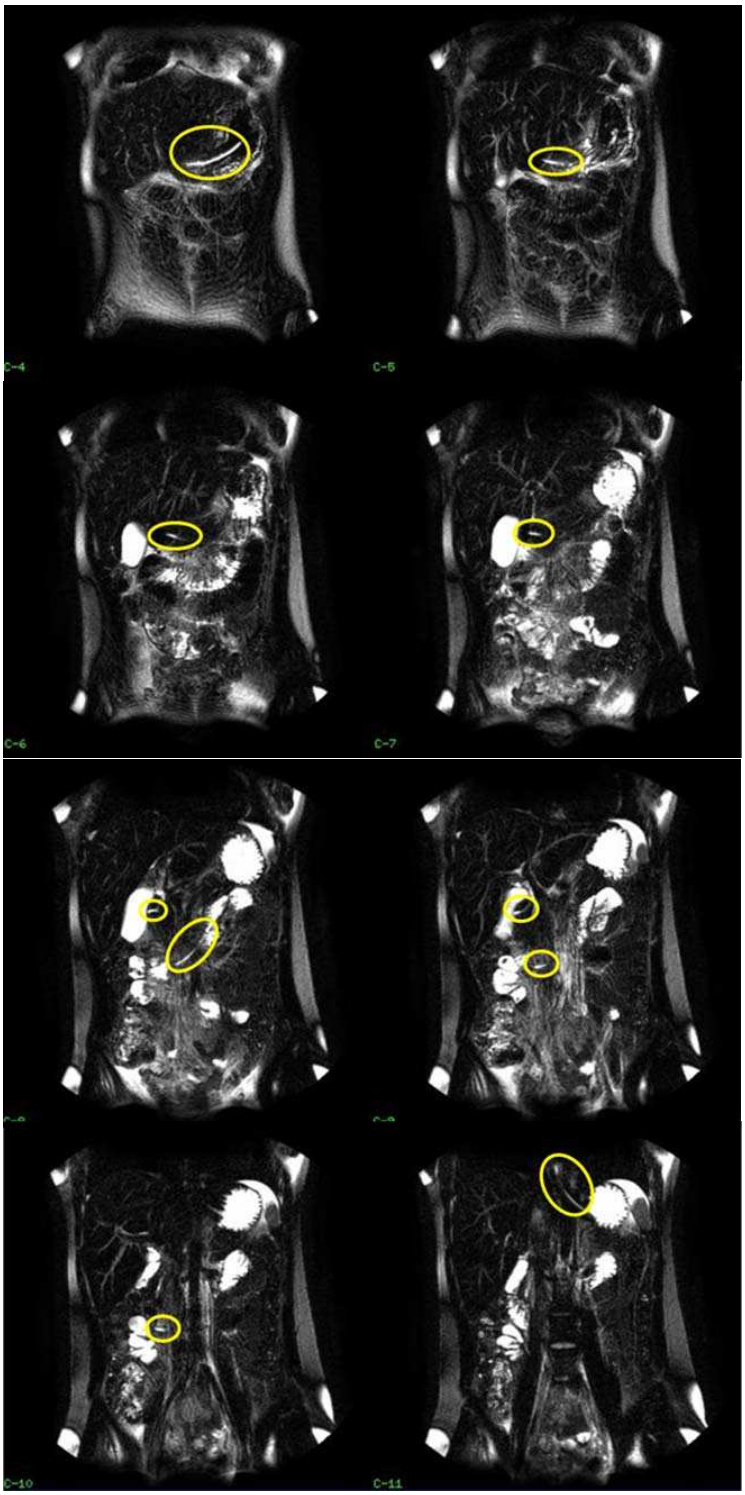

Figure 4-2: TSE images acquired before infusion to verify positioning of tube (tube highlighted on images)

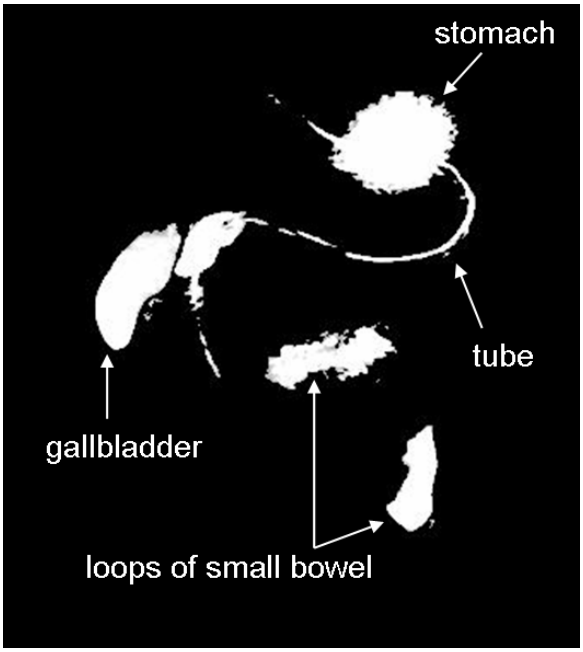

Figure 4-3: Segmented maximum intensity projection (MIP) image of the tube created from TSE images.

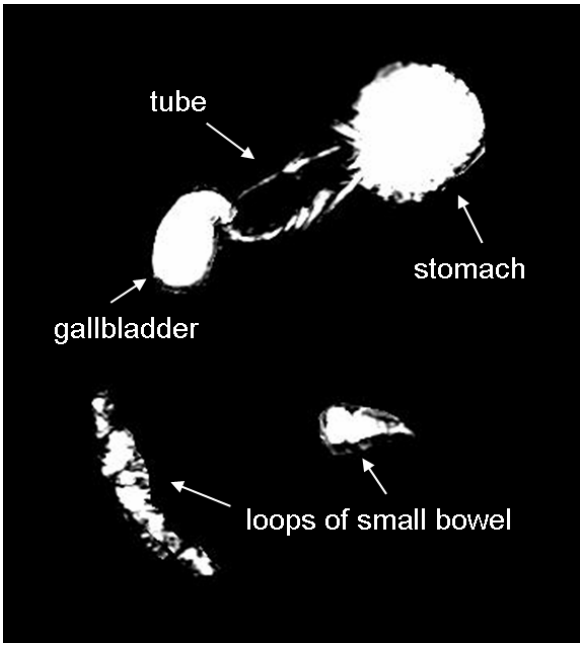

Figure 4-4: Segmented maximum intensity projection (MIP) image of a tube that has curled round the stomach instead of progressing into the duodenum.

4.3.3.3 Optimisation

The optimisation process involved finding the conversion factor from the CSF signal in each of the subject's MRI images, to the threshold level S_{th} that, when applied to the MR images to remove unwanted signal, gave the most accurate estimate of the small bowel water. The first six subjects data ('training subjects') was used to find this conversion factor. This conversion factor was then used to measure the SBWC of the remaining 12 subjects data ('validation subjects') to determine the accuracy of the technique by comparing the measured MRI volumes with the known infused volumes.

The following method, developed by Hoad *et al*. [31] was used to determine S_{th} based on the CSF signal in each TSE data set. In-house software written in IDL® (Research Systems Inc. Boulder, Colorado, USA) by Dr Caroline Hoad for measuring SBWC on the 1.5 T scanner was adapted to measure SBWC on the 3.0 T scanner in this work. The operator selected the centre of the CSF region on each slice in which it was visible, and the software then drew a box on the screen which was 61 pixels wide and 512 long on the 512 x 512 matrix image (enough to cover the whole spinal region). A histogram ($H(S)$, Figure 4-5i) of the signal intensity was generated (bin size = 200) from all slices and normalised to be equivalent of six slices (6 x 61 x 512 pixels) to keep the total number of pixels in the histogram calculations constant. The histograms contained a broad peak (corresponding to background noise and tissue) and a long tail (corresponding to CSF). The second differential provides a robust method for selecting the start of this tail. The method for obtaining the second differential is given below.

The histogram was smoothed twice using a running average with five points ($sH(S)$). The first differential of the smoothed histogram was calculated:

$$H'(S_j) = \frac{(sH(S_j) - sH(S_{j+1}))}{2} \qquad \textbf{[4-1]}$$

where $H'(S_j)$ is the first differential of the smoothed histogram and $sH(S_j)$ is the amplitude of the smoothed histogram at bin number j. The first differential was smoothed using a running average of five points ($sH'(S_j)$), and the second differential was generated:

$$H''(S_j) = \frac{(sH'(S_j) - sH'(S_{j+1}))}{2} \qquad \textbf{[4-2]}$$

where $H''(S)$ is the second differential of the histogram (Figure 4-5ii). The image intensity (S_p) corresponding to the highest positive peak in $H''(S)$ was identified and then the value of the signal intensity distinguishing background tissue from CSF on the histogram (S_{CSF}) was defined as the point from which the second differential falls towards zero and does not increase again at higher signals according to

$$(S_{CSF} > S_p) \text{ and } (H''(S_{CSF}) \leq 10) \text{ and } (H''(S > S_{CSF}) \leq 20) \qquad \textbf{[4-3]}$$

Figure 4-5 shows typical graphs for $H(S)$ and $H''(S)$ and the corresponding CSF histogram level that is then converted to the threshold level (S_{th}).

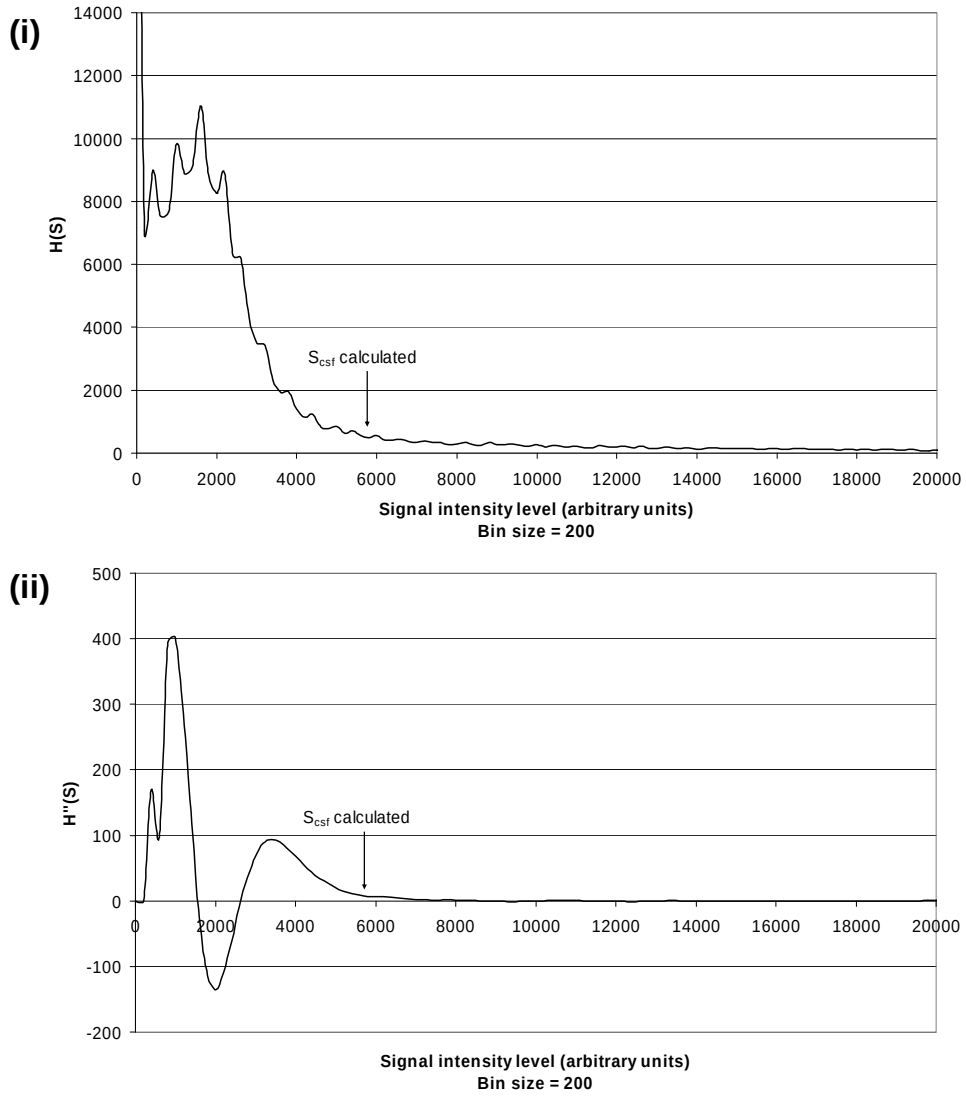

Figure 4-5: Illustration of the CSF histogram level (S_{CSF}) calculation. (i) Raw histogram data from the whole of the CSF region (multiple slices). (ii) Second differential data used to set the threshold level with the corresponding calculated level shown on the data.

The appropriate conversion factor from S_{CSF} (measured from the images) to S_{th}, the threshold required to measure the most accurate water volumes in the small bowel, was then found from the 'training subjects' data. Different multiples of S_{CSF} were used to provide different values of S_{th} for each data set. For each value of S_{th}, volumes of fluid in the bowel were calculated for the baseline scan and after each 40 ml bolus infusion, by integrating the volume of all image pixels with signal greater than each value of S_{th}, after manually

excluding regions containing the kidneys, gallbladder, bladder and visible blood vessels. The segmentation, threshold and integration were done using the in-house IDL software. As for the validation stage at 1.5 T, the stomach was not excluded due to possible duodeno-gastric reflux resulting in fluid entering the stomach. The baseline SBWC (measured prior to infusion) was subtracted from subsequent values, to give an MR estimate of infused volume. For each multiple of S_{CSF}, the mean SBWC measured were plotted against infused volume. The multiple which gave the closest result to identity was used as the conversion factor between S_{CSF} and S_{th} for the validation experiments.

4.3.3.4 Validation

The data from the 'validation subjects' were analysed in the same way, except that the threshold S_{th} was calculated using the conversion factor calculated in the optimisation stage. A Bland-Altman plot [35] was used to show the differences between the SBWC measured using MRI and the known infused volumes.

4.3.3.5 Reproducibility

To calculate the inter-observer variability in the SBWC measurements, two additional observers with substantial experience in studying MRI small bowel images, measured volumes from 20 different data sets randomly chosen from the validation subjects' data (covering a wide range of volumes measured). To calculate intra-observer variability of the SBWC volume measurement, I measured the same 20 data sets as used to assess inter-observer variability on two separate occasions, separated by a gap of a year to remove any bias from the first set of measurements. The 95 % confidence intervals for the differences between observers were calculated using the Bland-Altman method [35-37].

4.3.3.6 Comparison between 1.5 T and 3 T

Seven volunteers were asked to fast overnight and were scanned at 1.5 T, 3.0 T and at 1.5 T again, using validated MRCP (1.5 T) and TSE (3.0 T) sequences accordingly. Fasted small bowel water volumes were then measured in each subject and compared between field strengths for reproducibility. One of the volunteers was scanned again in the same manner since they had a particularly high fasted SBWC on the first occasion.

4.3.4 Results

All volunteers tolerated the experiment well except for one who withdrew after administration of the anesthetic to the throat. One data set was excluded because it was observed that fluid had moved from the small bowel into the colon and therefore 11 subjects' data was used in the validation process. In all included subjects the small bowel could be seen filling in the MR images as the test solution was infused (Figure 4-6).

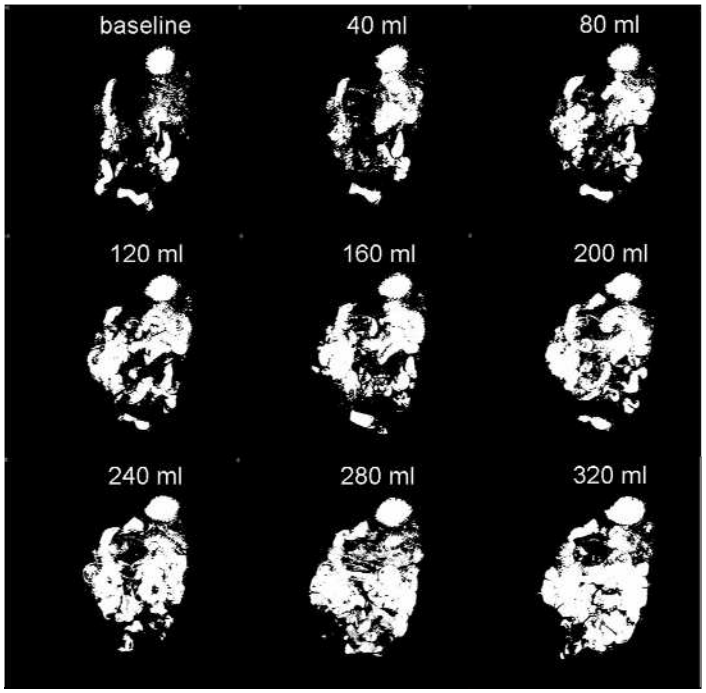

Figure 4-6: A roadmap showing the small bowel filling with test solution after each 40 ml bolus was infused.

4.3.4.1 Optimisation

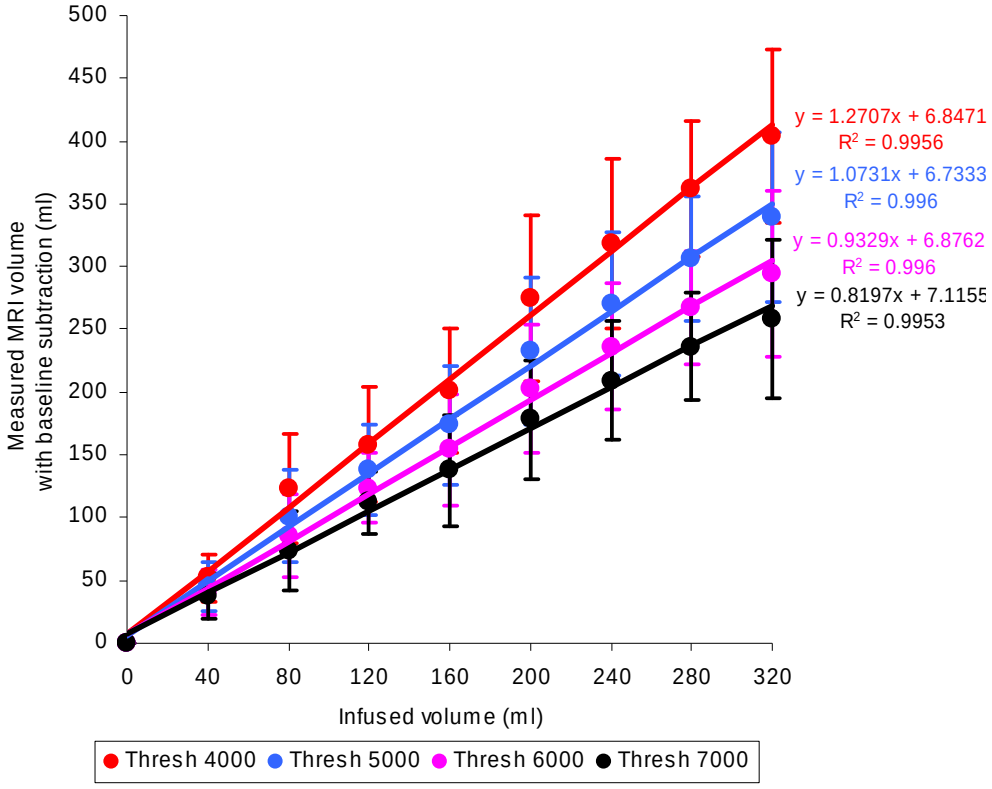

Figure 4-7: Measured small bowel water content against infused volumes for different image thresholds. Linear lines of best fit are shown with equations and R^2 values.

A graph of measured SBWC versus infused volume for the optimisation data using different multiples of S_{CSF} to give S_{th} is shown in Figure 4-7. From this, the closest line to identity was found to lie between S_{th} of 5000 and 6000. The conversion factor to obtain the threshold was calculated to be:

$$S_{th} = 1.02 S_{CSF} \qquad \textbf{[4-4]}$$

This is much lower than the conversion factor calculated for 1.5 T (S_{th} = $2.56 S_{CSF}$).

4.3.4.2 Validation

Figure 4-8 shows all measured volumes against infused volumes and infused volumes with added baseline volumes. The corresponding Bland-Altman plot is given in Figure 4-9.

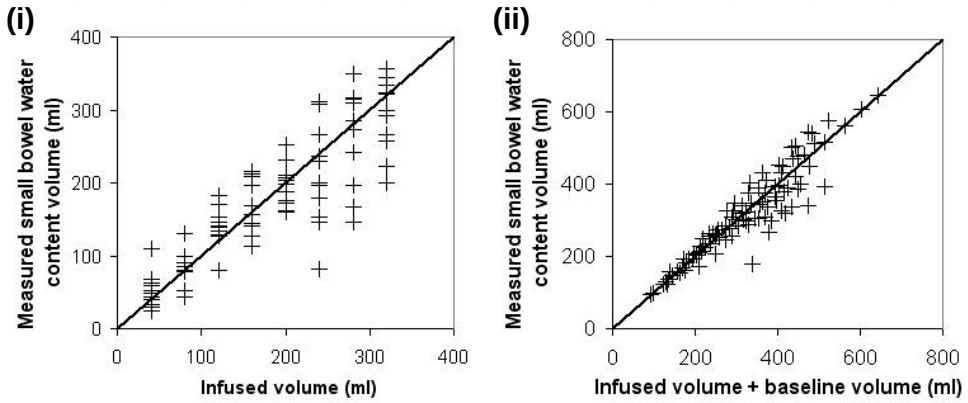

Figure 4-8: Measured small bowel water volumes using MRI against known infused volumes (i) with baseline volume subtracted and (ii) with baseline volume included. The line of identity is shown in both graphs.

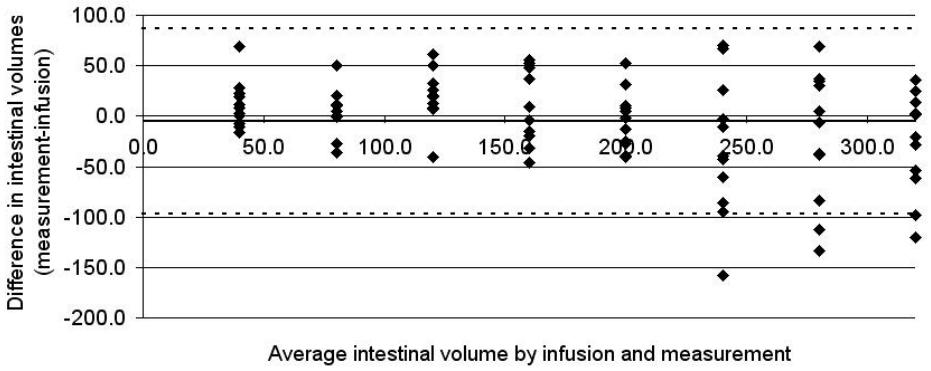

Figure 4-9: Bland-Altman plot for measured small bowel water volumes and known infused volumes.

The mean difference between measured and infused volumes is -5 ml and the mean measured limits of agreement are 97 ml below to 87 ml above the actual value. These figures show there are increasing differences between measurements with increased infused volumes and so according to Bland and

Altman [35], the data was converted to logarithms to allow calculation of the 95 % limits of agreement (Figure 4-10). The mean difference between measured and infused volumes (without the baseline subtracted) was -2 % with a standard deviation (SD) of 14 % (1.5T: 2 % with SD of 10 %). The 95 % limits of agreement were from 25 % below to 29 % above the infused value with baseline volumes included (N = 88) (1.5 T: 16 % below to 22 % above, N = 72).

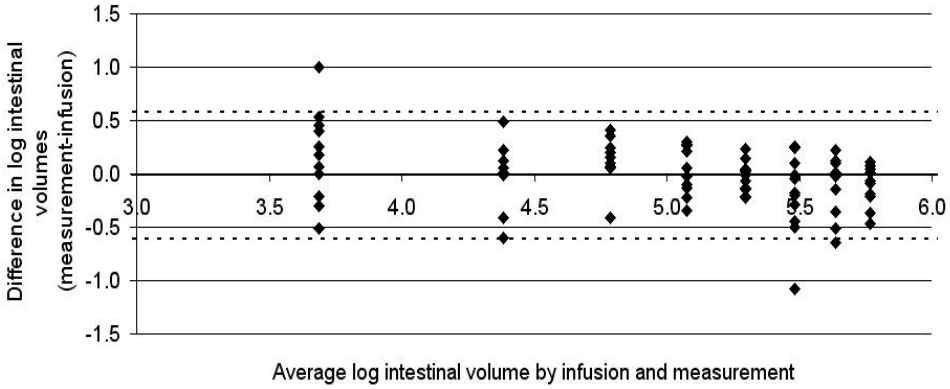

Figure 4-10: Bland-Altman plot for measured small bowel water volumes and known infused volumes taking the log of the volumes.

4.3.4.3 Reproducibility

For inter-observer variability, the 95 % limits of agreement of SBWC volume measurements between different observers were calculated from the Bland-Altman plots for paired observers (Table 4-1). For the intra-observer repeatability, 80 % of the calculated values of S_{th} were exactly the same and 20 % were 1 bin different on the histogram scale (bin size = 200 for 3.0 T and 100 for 1.5 T) (1.5 T, 70 % identical and 30 % 1 bin different). For the inter-observer, 50 % of the S_{th} values were identical, 45 % were 1 bin different and 5 % were 2 bins different (at 1.5 T, 55 % identical, 40 %1 bin different and 5 % 2 bins different).

Observer pair	Lower bound	Upper bound
1 & 2	-22 %	11 %
1 & 3	-8 %	23 %
2 & 3	-5 %	30 %
Intra-observer	-14 %	13 %

Table 4-1: Bland-Altman 95 % limits of agreement of SBWC volume measurements between different observers and intra-observer. N = 20 data sets were measured and all data is given as percentages of volumes measured.

4.3.4.4 Comparison between 1.5 T and 3 T

Figure 4-11 shows similar slices obtained at both field strengths for a single volunteer. It can be seen that the susceptibility effects and fat suppression are worse at 3.0 T compared with 1.5 T. There is therefore more background signal on the images acquired at 3.0 T.

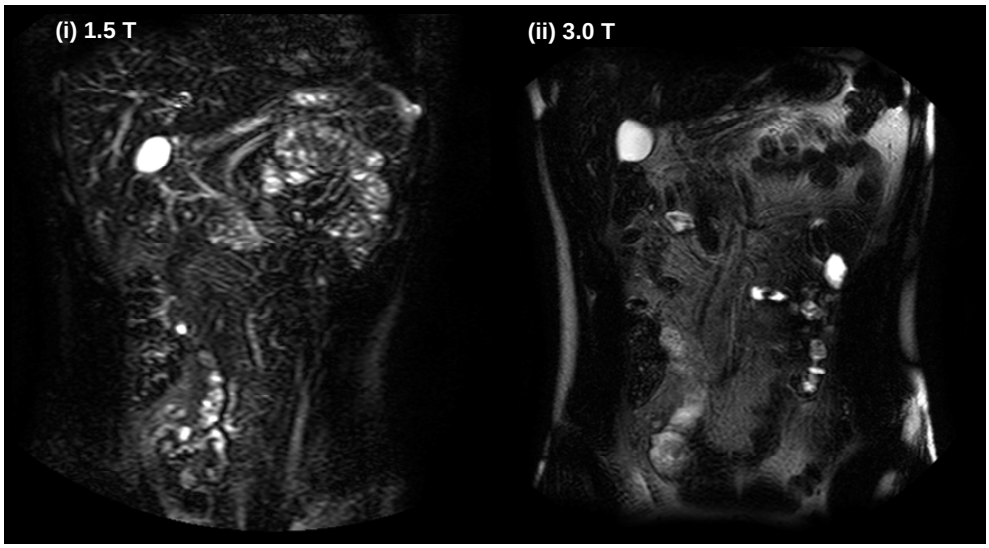

Figure 4-11: Images of a single slice from one volunteer at (i) 1.5 T and (ii) 3.0 T.

Figure 4-12 shows the fasted SBWC measured for each volunteer at different field strengths. One of the volunteers was scanned twice and the red lines indicate the volumes measured for this volunteer. The measured SBWC across field strengths was generally consistent for each volunteer showing that the technique has been correctly validated at 3.0 T. Two of the volunteers

had high fasted small bowel water volumes; one of these volunteers was scanned again on a separate occasion and found to have a higher fasted small bowel water volume again.

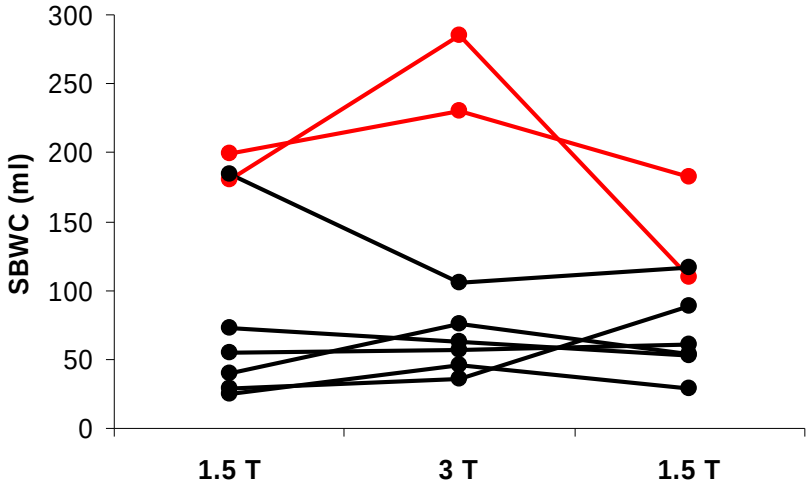

Figure 4-12: Seven volunteers were scanned at 1.5 T, 3.0 T and 1.5 T in order to measure repeatability across field strengths of fasted small bowel water content. The red lines indicate the volumes measured for a single volunteer when the protocol was repeated on two separate occasions.

4.3.5 Discussion

The TSE MRI images obtained using the 3.0 T provided improved SNR images of the bowel compared with those obtained at 1.5 T. The technique has previously been shown to be suitable for measuring small bowel water at 1.5 T and this study has shown the technique is suitable for use at 3.0 T with appropriate optimisation of the conversion factor. The small bowel water volume was shown to be overestimated (2 %) at 1.5 T, but here there was a slight underestimation (-2 %) at 3.0 T. Overall, there was a higher level of agreement between the infused and measured volumes at 1.5 T compared with 3.0 T which could be attributed to the increased susceptibility between air/water interfaces at 3.0 T. Since the fat suppression and susceptibility effects are worse at 3.0 T, more segmentation errors will occur due to distinguishing water from fat.

Both intra- and inter-variability were within limits of agreement found for the validation data. The variations that occurred between observer measurements were due to differences in the manual segmentations and the calculation of S_{th}. For the intra-observer, 4 out of 20 thresholds were measured differently and for the inter-observer, 10 out of 20 thresholds were not the same for all three observers.

The technique assumes that pixels with a signal above the threshold contains only water and that pixels with signal below the threshold contain none, but due to the voxel size used, this is probably unlikely to be true due to partial volume effects; a small proportion of water is probably excluded from the measured value. Improved resolution would reduce this problem, but then the overall scanning time would be increased; this could introduce more errors such as movement of the water through the bowel. Naturally, the water distribution in the small bowel, especially in fasted subjects, may be very sparse and therefore this would increase errors obtained in further studies compared with the experiment performed here due to increased partial volume effects.

The fasted SBWC measured for the volunteers did not significantly change between field strengths ($p > 0.78$ across all comparisons, Wilcoxon test). This indicates that small bowel water volumes measured using the 1.5 T and 3.0 T scanners could be compared directly if necessary since the sequences have been successfully validated for these two scanners. This was an extremely important result as the conversion factors for the two field strengths were considerably different: $1.02S_{CSF}$ for 3.0 T and $2.56S_{CSF}$ for 1.5 T. This reflects the differences in acquired sequence resolution (3.0 T: 1.25 x 1.57 x 7 mm^3 and 1.5 T: 1.56 x 2.83 x 7 mm^3) and effective echo times (3.0 T: TE_{eff} = 400 ms and 1.5 T: TE_{eff} = 320 ms) which would affect the CSF histogram data used. Since the sequence involves spin echoes, any T_2* effects will only be

due to imperfections in the RF pulse profiles. However, the T_2 effects will vary between the scanners, since different effective echo times are used.

4.3.6 Conclusion

A technique for measuring SBWC has been validated for use at 3.0 T using naso-duodenal intubation and infusing known quantities of mannitol saline solution. The images were thresholded, according to the optimisation, and segmented to estimate small bowel water content. The mean difference between the measured MRI volumes and the infused volumes (with baseline added) was -2 % with a standard deviation of 14 % and a maximum error of 29 %. Measured small bowel water volumes between two observers differed by a maximum of 30 % whilst measurements made by the author on two separate occasions differed by only 14 %.

This technique is extremely useful because it is non-invasive and non-ionising and therefore provides a method for studying small bowel water in healthy people and in patients without disturbing natural gastric processes. This technique will be applied in subsequent chapters of this thesis.

4.4 FUTURE DEVELOPMENTS

The method used in this chapter to non-invasively measure SBWC does have limitations. The conversion factor to calculate the threshold must be optimised since it is scanner, sequence and coil dependent. With continuing technical developments of coils, sequences etc, it would be advantageous to have a method that would avoid re-optimisation of the conversion factor which is time consuming and invasive to use intubation techniques e.g. predicting S_{th} from phantom measurements.

4.5 References

1. Debatin, J.F. and M.A. Patak, *MRI of the small and large bowel.* Eur. Radiol., 1999. **9**: p. 1523-1534.
2. Marciani, L., et al., *Gastric response to increased meal viscosity assessed by echo-planar magnetic resonance imaging in humans.* Journal of Nutrition, 2000. **130**: p. 122-127.
3. Marciani, L., et al., *Echo-Planar Imaging Relaxometry to Measure the Viscosity of a Model Meal.* J. Mag. Res, 1998. **135**: p. 82-86.
4. Marciani, L., et al., *Effect of intragastric acid stability of fat emulsions on gastric emptying, plasma lipid profile and postprandial satiety.* Br J Nutr, 2008. **5**: p. 1-10.
5. Marciani, L., et al., *Enhancement of gastric acid stability of a fat emulsions meal delays gastric emptying and increases cholecystokinin release and gallbladder contraction.* Am J Physiol Gastrointest Liver Physiol, 2007. **292**(6): p. G1607-1613.
6. Goetze, O., et al., *The effect of macronutrients on gastric volume responses and gastric emptying in humans: a magnetic resonance imaging study.* Am J Physiol Gastrointest Liver Physiol, 2006. **292**: p. G11-G17.
7. Evans, D.F., et al., *Prolonged monitoring of the upper gastrointestinal tract using echo planar magnetic resonance imaging.* Gut, 1993. **34**: p. 848-852.
8. Aziz, Q. and D.G. Thompson, *Brain-gut axis in health and disease.* Gastroenterology, 1998. **114**(3): p. 559-578.
9. Guinard, J.-X. and P. Brun, *Sensory-specific Satiety: Comparison of Taste and Texture Effects.* Appetite, 1998. **31**: p. 141-157.
10. Flourie, B., et al., *Effect of pectin on jejunal glucose absorption and unstirred layer thickness in normal man.* Gut, 1984. **25**: p. 936-941.
11. Krag, E. and S.F. Phillips, *Active and Passive Bile Acid Absorption in Man. Perfusion studies of the ileum and jejunum.* J Clin. Invest, 1974. **53**: p. 1686-1694.

12. Spiller, R.C., B.J. Jones, and D.B. Silk, *Jejunal water and electrolyte absorption from two proprietary enteral feeds in man: importance of sodium content.* Gut, 1987. **28**: p. 681-687.
13. Read, N.W., et al., *Effect of gastrointestinal intubation on the passage of a solid meal through the stomach and small intestine in humans.* Gastroenterology, 1983. **84**(6): p. 1568-1572.
14. Ostick, D.G., et al., *Simple clinical method of measuring gastric emptying of solid meals.* Gut, 1976. **17**: p. 189-191.
15. Harris, D., et al., *Assessment of gastric emptying using gamma scintigraphy.* J Clin Pharm Ther, 1987. **12**(5): p. 343-346.
16. Lawaetz, O. and H. Dige-Petersen, *Gastric emptying of liquid meals: validation of the gamma camera technique.* Nucl. Med. Commun, 1989. **10**(5): p. 353-364.
17. Maes, B.D., et al., *Gastric emptying flow curves separated from carbon-labeled octanoic acid breath test results.* Am. J. Physiol. Gastrointest. Liver Physiol., 1998. **275**: p. 169-175.
18. Bortolotti, M., V. Annese, and G. Coccia, *Twenty-four hour ambulatory antroduodenal manometry in normal subjects (co-operative study).* Neurogastroenterol. Mot., 2000. **12**: p. 231-238.
19. Scott, S.M., et al., *The nocturnal jejunal migrating motor complex: defining normal ranges by study of 51 healthy adult volunteers and meta-analysis.* Neurogastroenterol. Mot., 2006. **18**: p. 927-935.
20. Hausken, T., et al., *Antroduodenal motility and movements of luminal contents studied by duplex sonography.* Gastroenterology, 1992. **102**(5): p. 1583-1590.
21. Barber, D.C. and B.H. Brown, *Applied Potential Tomography (Review Article).* J Phys E: Sci Instrum, 1984. **17**: p. 723-733.
22. Henderson, R.P. and J.G. Webster, *An Impedance Camera for spatially Specific Measurements of the Thorax.* IEEE Trans Biomed, 1978. **25**: p. 250-254.
23. Stehling, M.K., et al., *Gastrointestinal Tract: Dynamic MR Studies with Echo-Planar Imaging.* Radiology, 1989. **171**: p. 41-46.

24. Nakae, Y., et al., *Cold pain prolongs gastric emptying of liquid but not solid meal: an electrical impedance tomography (EIT) study.* J. Gastroenterol., 2000. **35**: p. 593-597.
25. Boulby, P., et al., *Use of echo planar imaging to demonstrate the effect of posture on the intragastric distribution and emptying of an oil/water meal.* Neurogastroenterol. Mot, 1997. **9**: p. 41-47.
26. Lomas, D.J. and M.J. Graves, *Small bowel MRI using water as a contrast medium.* BJR, 1999. **72**: p. 994-997.
27. Lauenstein, T.C., et al., *Optimization of Oral Contrast Agents for MR Imaging of the Small Bowel.* Radiology, 2003. **228**: p. 279-283.
28. Hykin, J., et al., *Measurement of GI water content using EPI at 0.5 tesla.* MAGMA, 1994. **2**: p. 471-473.
29. Adkin, D.A., et al., *Echo-Planar Magnetic Resonance Imaging to Assess Water Volume in the Distal Small Bowel.* Pharmaceutical Research, 1995. **12**(8): p. 1134-1139.
30. Schiller, C., et al., *Intestinal fluid volumes and transit of dosage forms as assessed by magnetic resonance imaging.* Aliment Pharmacol Ther, 2005. **22**: p. 971-979.
31. Hoad, C.L., et al., *Non-invasive quantification of small bowel water content by MRI: a validation study.* Phys. Med. Biol., 2007. **52**: p. 6909-6922.
32. Barish, M.A., J.A. Soto, and E.K. Yucel, *Magnetic Resonance Cholangiopancreatography of the Biliary Ducts: Techniques, Clinical Applications, and Limitations.* Top. Mag. Res. Imaging, 1996. **8**(5): p. 302-311.
33. Takehara, Y., *MR Pancreatography: Technique and Applications.* Top. Mag. Res. Im., 1996. **8**(5): p. 290-301.
34. Spiller, R.C., et al., *Inhibition of jejunal water and electrolyte absorption by therapeutic doses of clindamycin in man.* Clin. Sci. (Lond), 1984. **67**(1): p. 117-120.

35. Bland, J.M. and D.G. Altman, *Statistical methods for assessing agreement between two methods of clinical measurement.* Lancet, 1986. **i**: p. 307-310.
36. Bland, J.M. and D.G. Altman, *Measuring agreement in method comparison studies.* Stat. methods in Med. Res., 1999. **8**: p. 135-160.
37. Bland, J.M. and D.G. Altman, *Comparing methods of measurement: why plotting difference against standard method is misleading.* Lancet, 1995. **346**: p. 1085-1087.

CHAPTER 5

MEASURING T_2 IN THE ABDOMEN AT 3.0 T

5.1 INTRODUCTION

In the previous chapter some methods for investigating the fate of food in the gastrointestinal tract were explored, but by measuring intrinsic properties of magnetic resonance imaging the field of gastrointestinal imaging can be explored much further. With the increase in the number of 3.0 T whole body clinical MRI scanners, the possibility of high field abdominal MRI has opened up, but further development and optimisation of sequences for this application is needed if this area is to fulfill its potential [1-6].

The transverse relaxation time, T_2, has proved to be an important parameter in studying the fates of model meals within the gastrointestinal tract [7-12]. Marciani *et al*. showed that it was feasible to carry out viscosity measurements *in vivo* using spin echo EPI to measure T_2 by calibrating *in vitro* transverse relaxation times of a simple polysaccharide meal against viscosity [12]. As the viscosity of a sample increases, the transverse relaxation rate ($=1/T_2$) also increases. Following this initial work, the technique has been used to investigate correlations between viscosity, dilution and gelation (all inferred by measuring T_2) with gastric emptying and satiety after consumption of different gel test meals [9-11]. In addition to gel test meals, the study of gastric motor function on fat emulsions [8] and the effects of gastric drugs [7] have also been investigated using transverse relaxation rates; it is possible to quantify droplet size due to the effects of diffusion in field inhomogeneities around the droplets [8].

However to date there have only been a few reports of abdominal tissue relaxation times at 3.0 T [13, 14]. By knowing the T_2 values of healthy tissues, it would be possible to measure changes due to disease. For example chronic liver disease resulting from the development of liver fibrosis could be investigated by measuring T_2. There are several indirect diagnostic tests for fibrosis including ultrasound and MRI, but the only method for assessing disease progression is to examine biopsy samples. However, biopsies are unreliable and highly invasive and it would therefore be useful to be able to measure disease progression non-invasively using MRI. Superparamagnetic iron oxide (SPIO) is a contrast agent that is often used to improve the detectability of liver abnormalities in T_2 or T_2* images [15, 16].

As discussed in chapter 3, it is often difficult to measure T_2 accurately and in a reasonable time *in vivo* because of diffusion [17], sensitivity to RF pulse errors [18-20] and static field inhomogeneities [21]. In fact T_2 is a difficult parameter to even define *in vivo*, since transverse relaxation is generally multiexponential; measurement of the full relaxation time spectrum is not generally feasible *in vivo*, and therefore the apparent monoexponential relaxation time measured will depend on the echo times used.

The balanced turbo field echo (bTFE, also called TrueFISP, bSSFP or FIESTA) produces images of high signal to noise ratio (SNR) [22] in a single shot. Most spin warp sequences are affected by motion in the abdomen due to breathing and peristalsis so the use of single shot imaging sequences helps to reduce motion artifacts whilst maintaining a reasonable scanning time. The bTFE sequence is particularly useful in the abdomen where EPI image quality suffers due to susceptibility artifacts, TSE (half or full Fourier) techniques are limited by a high specific absorption rate (SAR) and FFE techniques have a low SNR and are affected by motion since they are slow.

It has previously been shown that it is possible to measure T_1 and T_2 using segmented or single shot bTFE with an inversion preparation pulse applied immediately before the bTFE pulse train (IR-bTFE) [23-26]. This technique is susceptible to errors in the measurement of T_2 arising from flip angle errors [27] and off resonance effects [26].

An alternative and potentially more sensitive method for quantifying T_2 using bTFE is to use the spin echo preparation step introduced in chapter 3:

$$90° - TE/2 - 180° - TE/2 - 90°$$

This technique is called SE-bTFE and is alternatively known as the T_2-prep bTFE [28]. However quantifying T_2 from the bTFE data is not trivial as the final magnetisation at the centre of *k*-space will depend not only on the preparation phase but also on the number and timing of the RF pulses used in image formation [29, 30]. The final magnetisation is also sensitive to T_1 and the bTFE flip angle [27] and so the sequence also has potential to simultaneously measure both T_2 and T_1.

This chapter will determine the limits of accuracy and sensitivity in T_2 measurements made with T_2-prep bTFE using numerical and analytical simulations based on pulse by pulse application of the Bloch equations, and hence optimise the sequence for the measurement of monoexponential T_2 relaxation times. The initial optimisation was carried out using analytical techniques since they are fast, but then the investigation of systematic errors was necessarily carried out using Monte Carlo simulations. It also aims to establish a normal range of T_2 relaxation times for a variety of abdominal tissues at 3.0 T in healthy subjects.

5.2 METHODS

5.2.1 The sequence

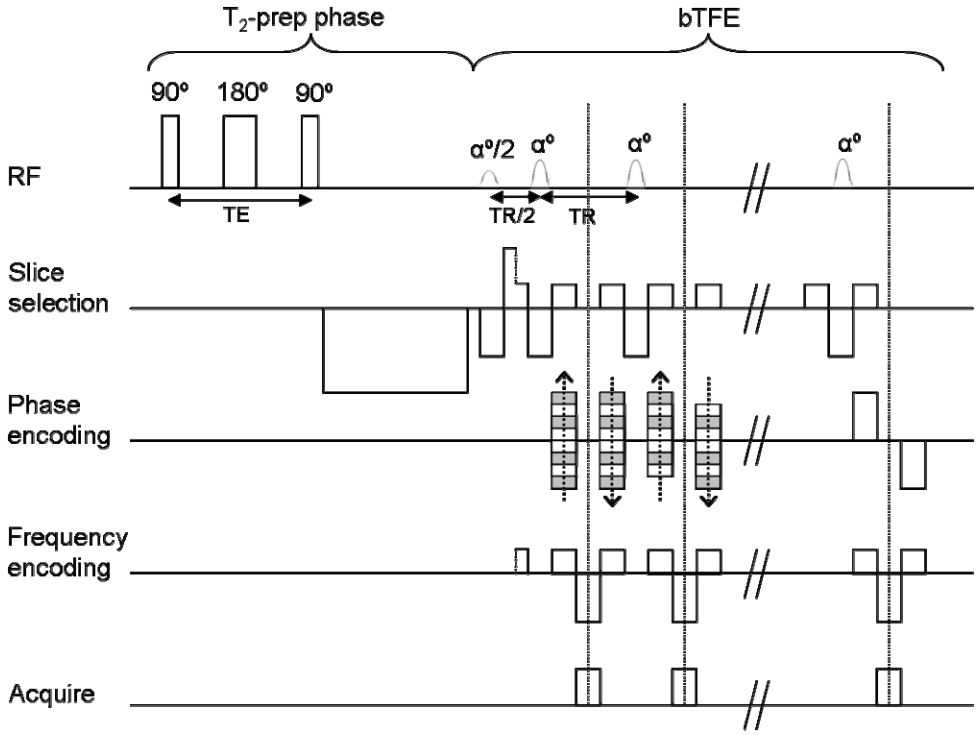

Figure 5-1: Pulse sequence diagram showing the T_2-prep and bTFE components of the sequence (not to scale).

The sequence was basically a standard Philips protocol and consisted of a T_2-preparation step, followed by a slice selective, half-Fourier bTFE acquisition block (Figure 5-1). The T_2-preparation step used a composite refocusing pulse and consisted of a

$$90_x^\circ - TE/2 - [\, 90_{-x}^\circ \, 180_y^\circ \, 90_{-x}^\circ] - TE/2 - 90_{-x}^\circ$$

non-selective pulse train, to encode the echo amplitude at TE into the longitudinal magnetisation, which then dominated the signal at the centre of *k*-space in the bTFE readout. The bTFE readout consisted of an α/2 preparation pulse to minimise oscillations in the signal in the early lines of

k-space, and then successive alternating ± α pulses. By varying the TE time, a decay curve was generated, dominated by the T_2 of the tissue, but also dependent on T_1 and M_0. By varying the bTFE flip angle (α) more information about the T_1 can be inferred and so a variable flip angle technique involving sampling at two extra bTFE flip angles is also investigated with the aim of improving the accuracy of the fitted parameters. These will be referred to as the standard and variable flip angle methods throughout this chapter. The only change to the standard software was that the sequence was coded by Dr. Caroline Hoad to loop through a range of echo times in subsequent dynamics, to reduce time spent on scanner adjustment.

5.2.2 Signal model

Signal intensities in the experimental pulse sequence were simulated both to fit the data and optimise the sequence. The bTFE matrix size was typically 160 x 256 with a reduced FOV of 70 % in the phase encoding direction, giving 23 bTFE α^o pulses to the centre of *k*-space and 112 α^o pulses in total. There was a time delay of 15 seconds at the end of the bTFE acquisition to allow the system to fully relax to maximise the SNR and avoid having to take account of longitudinal suppression between shots. Both the simulation and fitting programs modeled the signal at the centre of *k*-space by repeated, stepwise, application of operators representing the rotations due to the RF pulses around the *x*- and *y*-axis (equations 5-1 and 5-2) and relaxation (equation 5-3):

$$\begin{pmatrix} M_x(t^+) \\ M_y(t^+) \\ M_z(t^+) \end{pmatrix} = \begin{pmatrix} 1 & 0 & 0 \\ 0 & \cos\alpha & \sin\alpha \\ 0 & -\sin\alpha & \cos\alpha \end{pmatrix} \begin{pmatrix} M_x(t^-) \\ M_y(t^-) \\ M_z(t^-) \end{pmatrix} \quad \textbf{[5-1]}$$

$$\begin{pmatrix} M_x(t^+) \\ M_y(t^+) \\ M_z(t^+) \end{pmatrix} = \begin{pmatrix} \cos\alpha & 0 & -\sin\alpha \\ 0 & 1 & 0 \\ \sin\alpha & 0 & \cos\alpha \end{pmatrix} \begin{pmatrix} M_x(t^-) \\ M_y(t^-) \\ M_z(t^-) \end{pmatrix} \quad \textbf{[5-2]}$$

$$\begin{pmatrix} M_x(t) \\ M_y(t) \\ M_z(t) \end{pmatrix} = \begin{bmatrix} e^{-\frac{t}{T_2}} & 0 & 0 & 0 \\ 0 & e^{-\frac{t}{T_2}} & 0 & 0 \\ 0 & 0 & e^{-\frac{t}{T_1}} & M_o(1-e^{-\frac{t}{T_1}}) \end{bmatrix} \begin{pmatrix} M_x(0) \\ M_y(0) \\ M_z(0) \\ 1 \end{pmatrix} \quad \textbf{[5-3]}$$

where M_x, M_y and M_z are the magnitudes of the magnetisation in the *x*, *y* and *z* directions immediately before ($M(t^-)$) and immediately after ($M(t^+)$) the RF pulse, which was assumed to occur instantaneously, and at the start ($M(0)$) and end ($M(t)$) of a period of relaxation. The initial magnetisation before the application of the first RF pulse was assumed to be (M_x M_y M_z) = (0 0 M_0). Although these equations could be adapted to take account of off-resonance effects, for simplicity, only the on-resonance signal was investigated in the simulations. When fitting experimental data, the slice profile of the bTFE pulses was taken account in the signal model by summing the signal across the slice profile of the imaging pulse (α) which was defined at 30 points using a Bloch simulation. As the T_2-prep pulses were non-selective these were assumed to have a perfect slice profile in the simulation. The data were found to be sensitive to T_2, T_1 and M_0 and so were always fitted for these parameters, as they are generally unknown in experimental data.

The effect of imperfect RF pulses on the shape of the signal decay curves, against echo time were simulated with a pulse amplitude scaling factor β in both the T_2-preparation and the bTFE pulses:

T_2-prep: $\beta.90_x^\circ$ - TE/2 -[$\beta.90_{-x}^\circ$ $\beta.180_y^\circ$ $\beta.90_{-x}^\circ$] - TE/2 - $\beta.90_{-x}^\circ$

bTFE: $\beta.\alpha$

5.2.3 Sequence optimisation

In order to determined the echo times (TE) giving the optimum signal to noise ratio in the measurement of T_2 in abdominal tissues, the covariance matrix [31, 32] was required. The covariance matrix [C] can be written:

$$[C]=\begin{bmatrix} \sum\frac{1}{\sigma^2}\left(\frac{\partial S_{\text{mod}}}{\partial T_2}\right)^2 & \sum\frac{1}{\sigma^2}\left(\frac{\partial S_{\text{mod}}}{\partial T_2}\right)\left(\frac{\partial S_{\text{mod}}}{\partial T_1}\right) & \sum\frac{1}{\sigma^2}\left(\frac{\partial S_{\text{mod}}}{\partial T_2}\right)\left(\frac{\partial S_{\text{mod}}}{\partial M_0}\right) \\ \sum\frac{1}{\sigma^2}\left(\frac{\partial S_{\text{mod}}}{\partial T_1}\right)\left(\frac{\partial S_{\text{mod}}}{\partial T_2}\right) & \sum\frac{1}{\sigma^2}\left(\frac{\partial S_{\text{mod}}}{\partial T_1}\right)^2 & \sum\frac{1}{\sigma^2}\left(\frac{\partial S_{\text{mod}}}{\partial T_1}\right)\left(\frac{\partial S_{\text{mod}}}{\partial M_0}\right) \\ \sum\frac{1}{\sigma^2}\left(\frac{\partial S_{\text{mod}}}{\partial M_0}\right)\left(\frac{\partial S_{\text{mod}}}{\partial T_2}\right) & \sum\frac{1}{\sigma^2}\left(\frac{\partial S_{\text{mod}}}{\partial M_0}\right)\left(\frac{\partial S_{\text{mod}}}{\partial T_1}\right) & \sum\frac{1}{\sigma^2}\left(\frac{\partial S_{\text{mod}}}{\partial M_0}\right)^2 \end{bmatrix}^{-1}$$

$$=\begin{bmatrix} S_{22} & S_{21} & S_{2M} \\ S_{12} & S_{11} & S_{1M} \\ S_{M2} & S_{M1} & S_{MM} \end{bmatrix}^{-1}$$

[5-4]

where S_{mod} is the modeled signal and σ is the noise. From the diagonal components of the covariance matrix, the errors in T_2, T_1 and M_0 can be calculated:

$$\sigma_{T2}^2=-\frac{S_{11}S_{MM}-S_{1M}S_{M1}}{-S_{M2}S_{21}S_{1M}+S_{M2}S_{1M}S_{11}+S_{12}S_{21}S_{MM}-S_{12}S_{2M}S_{M1}-S_{22}S_{11}S_{MM}+S_{22}S_{1M}S_{M1}}$$

$$\sigma_{T1}^2=-\frac{S_{22}S_{MM}-S_{M2}S_{2M}}{-S_{M2}S_{21}S_{1M}+S_{M2}S_{1M}S_{11}+S_{12}S_{21}S_{MM}-S_{12}S_{2M}S_{M1}-S_{22}S_{11}S_{MM}+S_{22}S_{1M}S_{M1}}$$

$$\sigma_{M0}^2=\frac{S_{12}S_{21}-S_{22}S_{11}}{-S_{M2}S_{21}S_{1M}+S_{M2}S_{1M}S_{11}+S_{12}S_{21}S_{MM}-S_{12}S_{2M}S_{M1}-S_{22}S_{11}S_{MM}+S_{22}S_{1M}S_{M1}}$$

[5-5]

The Bloch relaxation and rotation functions (equations 5-1 to 5-3) were differentiated and applied in a stepwise manner to find the differential of the signal functions with respect to the sequence fitting parameters. These were then used to calculate the covariance matrix and hence the signal to noise ratio for the standard method ($\alpha = 30°$) in the fitted values of T_2, T_1 and M_0, for 10 different echo times ranging from 20 to 4000 ms using either a power

or exponential time series (always starting with the shortest available echo time of 20 ms). For the variable flip angle method, 10 different echo times at α = 30° (ranging from 20 to 4000 ms) and 2 different echo times at α = 10° and α = 20° were optimised. The TE values used for the extra bTFE flip angles were the 8^{th} and 10^{th} echo times used when α = 30°. Simulations showed that the signal plateau is different for varying T_1 values so using extra echo times at different flip angles should provide additional information for improved T_1 accuracy. The echo times (TE) were optimised for both long (T_2 = 500 ms, T_1 = 2000 ms, e.g. CSF, bile, stomach/bowel contents) and short (T_2 = 50 ms, T_1 = 500 ms, e.g. liver, kidney, spleen) T_2/T_1 combinations for both the standard and variable flip angle methods. Table 5-1 summarises the TE sets that have been optimised for different methods and T_2/T_1 combinations and provides a code which will be referred to throughout this chapter.

	α	short T_2/T_1 = 50/500 ms	long T_2/T_1 = 500/2000 ms
Standard	30°	TE set: S1	TE set: L1
Variable FA	30° (10°, 20°)	TE set: S2	TE set: L2

Table 5-1: Code for the echo times for the standard and variable flip angle methods for short and long T_2/T_1 combinations.

The parameters TR and α were not optimised. The value of α (30°) was chosen to be the highest possible within the SAR limits to achieve the maximum signal and the TR was the shortest possible to obtain a reasonable in-plane resolution within the abdomen; this also reduces banding artifacts (explained later).

5.2.4 Monte Carlo simulations

Monte Carlo simulations were used to investigate any systematic errors caused by noise or RF pulse errors.

To investigate the effect of imperfect RF pulses on the shape of the signal T_2 decay curves, curves of the signal at the centre of *k*-space against echo time (TE) were simulated with a pulse amplitude scaling factor β in both the T_2-preparation pulses and the bTFE RF pulses. The range of β ($0.8 \leq \beta \leq 1.1$) was determined from experimental B_1 maps in the abdomen measured using a multiple flip angle technique and EPI acquisition. This technique uses a wide range of flip angles with some over 90º to produce a set of images from which the signal is then fitted to a sine curve using a program written by Mr. Olivier Mougin.

To investigate the effects of random noise on the fitted T_2 results, the signal intensity at the centre of *k*-space was simulated for $\alpha = 30º$ and both long (T_2 = 500 ms, T_1 = 2000 ms) and short (T_2 = 50 ms, T_1 = 500 ms) T_2/T_1 combinations. The optimum echo times for these T_2/T_1 combinations, found from the previous section (TE sets L1 and S1, Table 5-1), were used in the simulations to generate the initial data. To simulate the Riccian noise distribution in magnitude MR images, Gaussian noise (characterised as standard deviation as a percentage of M_0) was added to simulated complex data, and then the magnitude was calculated. This was repeated to give 500 data sets with different samples of the noise distribution. Each data set was fitted for T_2, T_1 and M_0 using the Powell algorithm [33, 34], with the data being corrected for Riccian noise using a look-up table (based on the results of [35]), but also excluding data points below a minimum threshold ($< 1.5\sigma\sqrt{\pi/2}$, where σ = variance of the noise) (a similar approach was used for experimental data). The mean and standard deviation of the fitted parameters were found. The number of repeats was chosen to be 500 since preliminary results with 1% noise showed that this gave a reasonably stable measure of the mean and standard deviations. Different levels of Gaussian distributed noise (0.05, 0.1, 0.3, 0.6, 1.0 % of the equilibrium magnetisation, M_0) were investigated. Experimental data was found to have a noise level

of approximately 0.3 % of M_0 (this is around 3% in the T_2-prep images which have a signal of less than 10% of M_0).

To investigate the interaction between flip angle errors and noise in the fit, data sets were simulated for β ranging from 0.8 to 1.1 and Gaussian noise levels of 0.3% and 0.6%. The data were fitted for T_2, T_1 and M_0 either assuming β = 1 or allowing for β to be an additional parameter in the fit. Again 500 data sets with different noise distributions for each value of β were simulated to find the effect of RF pulse errors on the mean and standard deviation in the fitted parameters.

5.2.5 Phantom validation

Two gel quadrant phantoms, containing NaCl and 8 different physiological concentrations of agar and gadolinium ions between were used to validate the sequence. The phantoms were scanned using the T_2-prep bTFE sequence in a 3.0 T Philips Achieva scanner using the SENSE head coil for reception. Data sets were acquired using both the standard and variable flip angle technique and using different combinations of TE values. Firstly, all the optimised TE sets given in Table 5-1 were used and secondly, 18 TE values (20 – 10000 ms) were used. Different combinations of sequence parameters were used for the standard and variable flip angle methods as shown in Table 5-2.

Imaging Parameters		Expt 1	Expt 2	Expt 3	Expt 4	Expt 5	Expt 6
TR (ms)		3	5	5	5	3	3
matrix size		160x256	160x256	160x256	160x256	80x128	80x128
pulses to centre of *k*-space		23	23	23	23	45	12
flip Angle (°)	Standard	30	30	50	10	30	30
	Variable	30,10,20	30,10,20	50,10,20	-	30,10,20	30,10,20
half or full Fourier		Half	Half	Half	Half	Full	Half

Table 5-2: Sequence parameters for the T_2-prep bTFE experiments.

For all experiments the slice thickness was 10 mm and the shot to shot interval was 15 seconds to allow full relaxation of the spins. The data were fitted to the model described above for T_2, T_1, M_0 and β as all these parameters are known to influence the shape of the decay curve and are generally unknown in the experiment. β was not fitted using the Powell algorithm; it was fitted by finding the minimum sum of squares between the measured and modeled signal using a stepwise approach either increasing or decreasing from β = 1. The slice profile of the bTFE pulses was also modeled by summing the signal across the slice profile of the imaging pulse (α) which was defined at 30 points using a Bloch simulation. As the T_2-prep pulses were non-selective these were assumed to have a perfect slice profile in the simulation.

T_1 and T_2 were also measured using inversion recovery EPI (with a hyperbolic secant inversion pulse) and single spin echo EPI respectively, both run with a long repetition time. The IR data was fitted to:

$$S(TI) = S_0\left(1 - Ae^{-TI/T_1}\right) \qquad \textbf{[5-6]}$$

where A takes account of any residual imperfections in the inversion pulse across the sample, despite the use of an adiabatic inversion. The spin echo data was fitted to a monoexponential decay. These are very simple sequences in terms of the spin history, making them insensitive to RF pulse errors [36] and are considered to be a gold standard for measuring T_1 and T_2 (chapter 3).

5.2.6 In vivo measurements

Ten healthy volunteers (5 male, 5 female, mean age 26 years (range 23-32)) were scanned and T_2 was measured in various abdominal tissues using the standard T_2-prep bTFE sequence. A further five healthy volunteers (2 male,

3 female, mean age 29 years (range 24 - 44)) were scanned using the variable flip angle T_2-prep bTFE technique and abdominal tissue measurements of T_2 and T_1 were made.

Measurements were made at 3.0 T using the SENSE Torso coil. The sequence parameters used are given in Table 5-2 Experiment 1, with a FOV of 400 mm and slice thickness of 10 mm. Two slices were acquired, one in the transverse plane positioned through the liver and spleen, where there was a reduced FOV of 70 % and the other in the coronal plane positioned through the kidneys with a full FOV. For the standard method, the TE set optimised for the short T_2/T_1 combination was used (*TE set: S1*) since most abdominal tissues have $T_2 < 100$ms. For the variable flip angle technique, a large number of TEs were used to improve the accuracy of T_1; the TE values used were *TE set S1* plus for $\alpha = 30°$, TE = 1000, 1500, 2000, 2500, 4000, 5000, 6000, 8000, 10000 ms and for $\alpha = 10, 20°$, TE = 2000, 8000 ms. Volunteers held their breath for no more than 10 seconds during each bTFE measurement, but were allowed to freely breathe during the wait time of 15 s between consecutive measurements. The total acquisition time was 2.5 minutes for the standard technique and 6 minutes for the variable flip angle technique. Regions of interest (ROIs) were drawn in the various abdominal tissues and the mean data from these regions were fitted for T_2, T_1, M_0 and β as described previously.

5.3 RESULTS

5.3.1 Signal model

Simulations showed that RF pulse errors will cause the decay curve to deviate from a simple decay; the shape of the curve depends on T_2, β and T_1, and the final plateau level depends on T_2, T_1, M_0 and β. Figure 5-2 illustrates the effect of a 10 % change in the pulse amplitude scaling factor on the shape of the decay curve ($0.9 \leq \beta \leq 1.1$). The interaction of β and T_1

on the shape of the decay curve (Figure 5-3) shows that small change in the accuracy of the RF pulses causes small deviations from the original decay curve plateau.

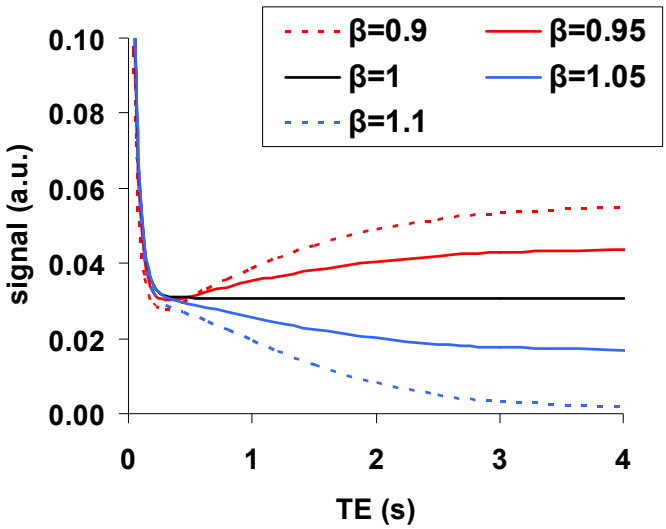

Figure 5-2: Simulations showing how non-ideal pulses affect the acquired signal. Differing β values for T_2 = 50 ms, T_1 = 500 ms and M_0 = 1.

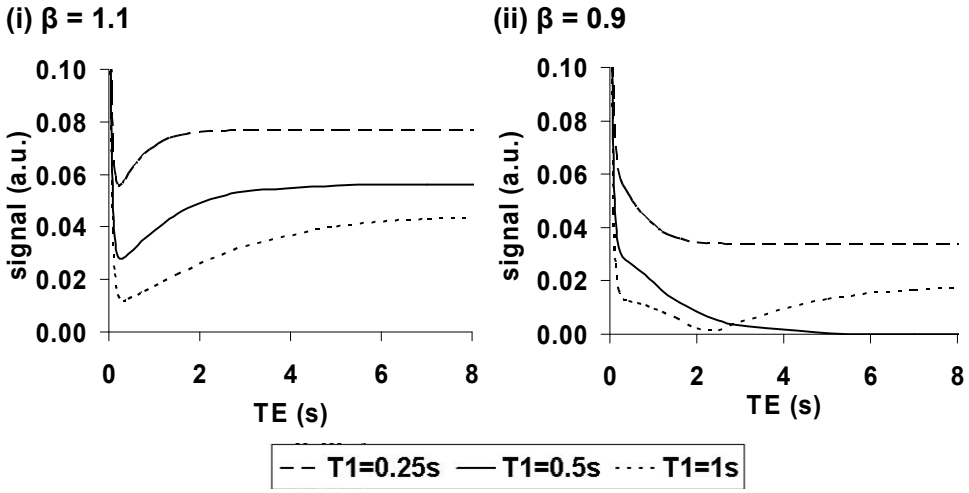

Figure 5-3: Simulations showing how non-ideal pulses affect the acquired signal. Differing T_1 values for T_2 = 50 ms, M_0 = 1 and (i) β = 1.1 or (ii) β = 0.9.

5.3.2 Sequence optimisation

The optimum TE values for the standard and variable flip angle techniques are given in Table 5-3 for both short and long T_2/T_1 combinations.

	α	TEs (in ms) (short T_2/T_1 = 50/500 ms)	TEs (in ms) (long T_2/T_1 = 500/2000 ms)
Standard	30°	20, 28, 42, 62, 92, 136, 200, 294, 434, 636 **(TE set: S1)**	20, 35, 61, 106, 185, 322, 561, 977, 1703, 2968 **(TE set: L1)**
Variable FA	30° (10°, 20°)	20, 27, 35, 47, 63, 83, 111, 148, 197, 262 (148, 262) **(TE set: S2)**	20, 35, 61, 106, 185, 322, 561, 977, 1703, 2968 (977, 2968) **(TE set: L2)**

Table 5-3: Optimum TE data sets for the standard and variable flip angle techniques for the short and long T_2/T_1 combinations.

5.3.3 Monte Carlo simulations

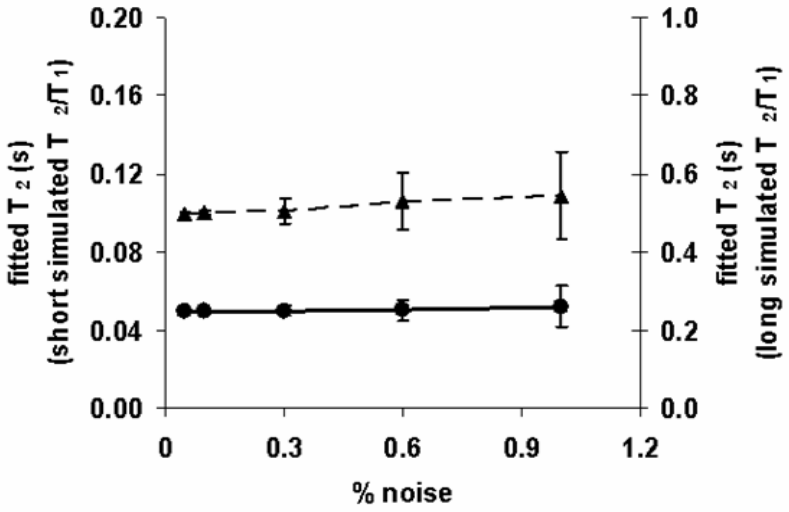

Figure 5-4: (mean ± std. dev) Results from Monte Carlo noise simulations showing the systematic and random errors of fitting T_2 using the T_2-prep bTFE sequence for the short T_2/T_1 simulated sample (circles) and long T_2/T_1 simulated sample (triangles).

Figure 5-4 shows that if data is simulated with no RF pulse error but different levels of noise, then there is a trend for the fitted value of T_2 to increase with increasing noise level, although this was not significant compared to the variance in the fitted value of T_2.

Figure 5-5 shows the results of simulating the combined effects of errors in the pulse angles and noise on the fitted values of T_2 and T_1, and the effect of including the pulse flip angles in the fit. It can be seen that including the flip angle scaling factor in the fit generally reduces the systematic error in the fitted values of T_2 without significantly increasing the variance in the fitted values. However at the 0.6 % noise level, including the flip angle scaling factor in the fit sometimes increases the systematic errors in the fitted values of T_2; it was observed that this was because this level of noise often (randomly) produced a dip in the decay curve similar to those seen when signal data is simulated with $\beta < 1$ (Figure 5-2), which fitted well to the model with a higher T_2 and lower α than originally simulated. For the short T_1/T_2 combination, including the flip angle in the fit also reduces the systematic error in the fitted value of T_1 without increasing the variance in the fitted results. However for the long T_1/T_2 combination the systematic and random errors in the fitted value of T_1 are very large.

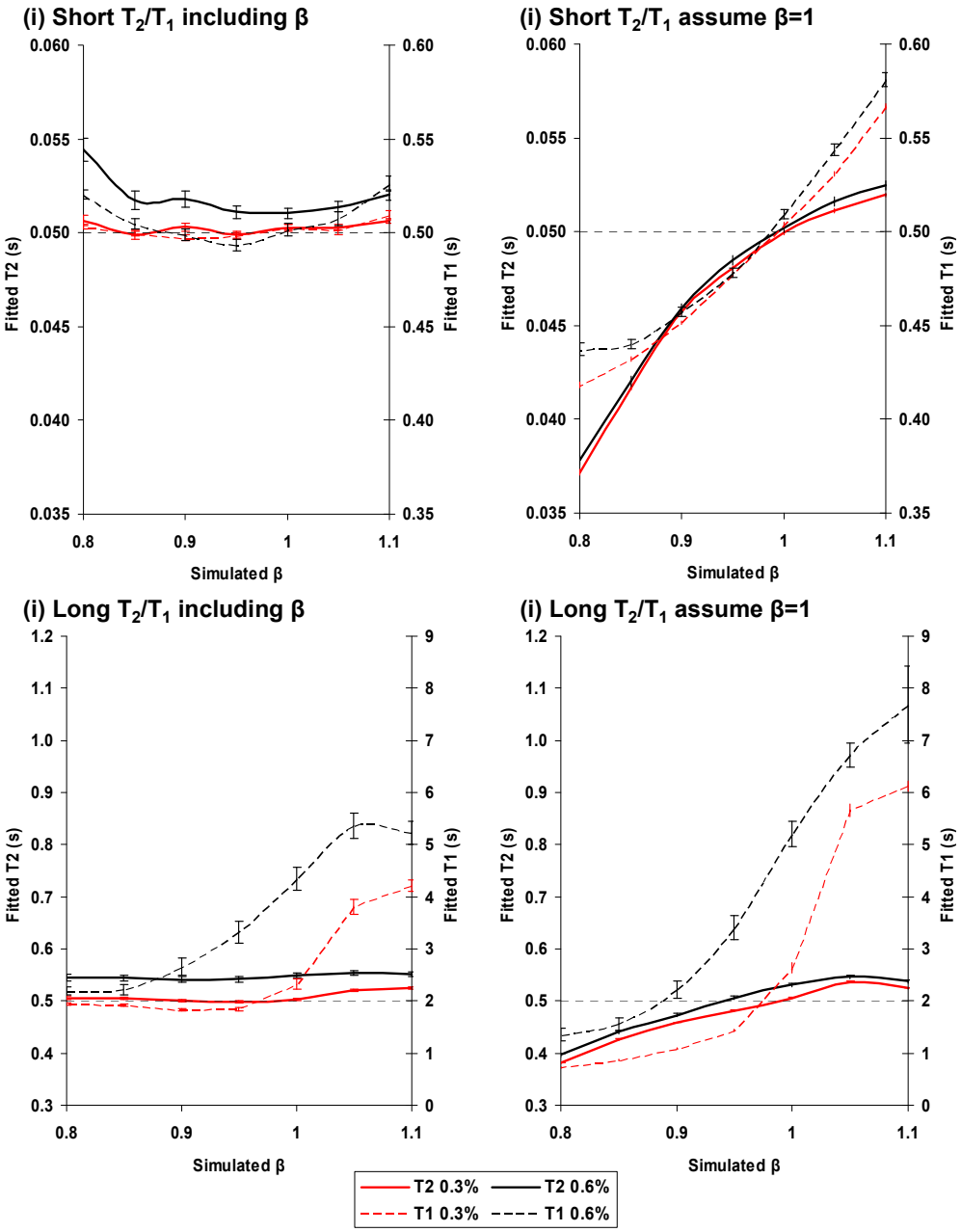

Figure 5-5: (mean ± SEM) Results from Monte Carlo simulations showing the systematic and random errors of fitting T_2 (solid line) and T_1 (dashed line) using the T_2-prep bTFE sequence due to the interaction between flip angle errors and noise for the short T_2/T_1 simulated sample (TE set S1) and for the long T_2/T_1 simulated sample (TE set L1). The effects of including β as an additional parameter in the fit or assuming β=1 in the fit are also shown. Two different levels of noise were considered: 0.3 % (red) and 0.6 % (black) of M_0.

5.3.4 Phantom validation

The mean T_2 and T_1 values measured using the standard T_2-prep bTFE sequence (from six experimental conditions (Table 5-2), not experiment 4 for TE set L1) against those measured using EPI are shown in Figure 5-6 for TE sets S1 and L1.

Using TE set S1, the fitted T_2 values are very accurate (Figure 5-6i), but the long fitted T_1 values are underestimated (Figure 5-6ii). By using TE values optimised for the long T_2/T_1 combination, the accuracy of the T_1 is much improved (Figure 5-6iv). However, since the simulated T_2 in the long T_2/T_1 combination is longer than the T_2s of the samples used here, the fitted T_2s are now slightly underestimated (Figure 5-6iii).

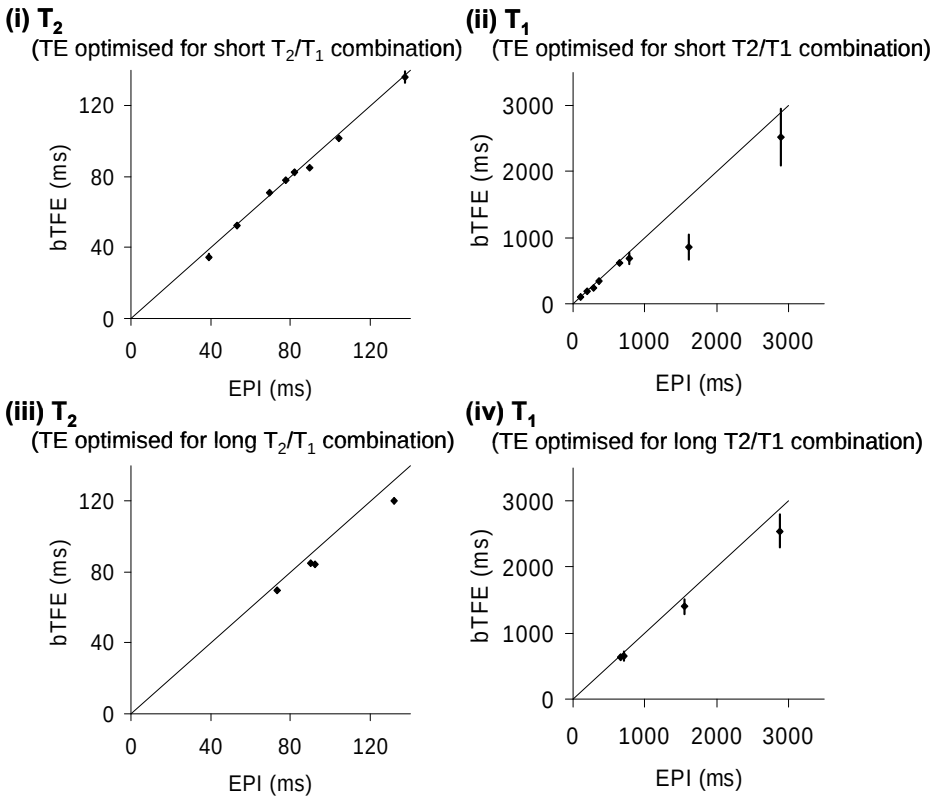

Figure 5-6: (mean ± std. dev.) Validation curves for (i, iii) T_2 and (ii, iv) T_1 measured using standard T_2-prep bTFE against EPI (SE and IR respectively). Optimum TE sets were used for the T_2-prep bTFE (i, ii) TE set S1 and (iii, iv) TE set L1. The identity line is shown.

Similarly, the variable flip angle T_2-prep bTFE sequence was used to measure T_2 and T_1 (from five experimental conditions (Table 5-2)) and compared with those measured using EPI; TE sets S2 and L2 were used. The results are shown in Figure 5-7.

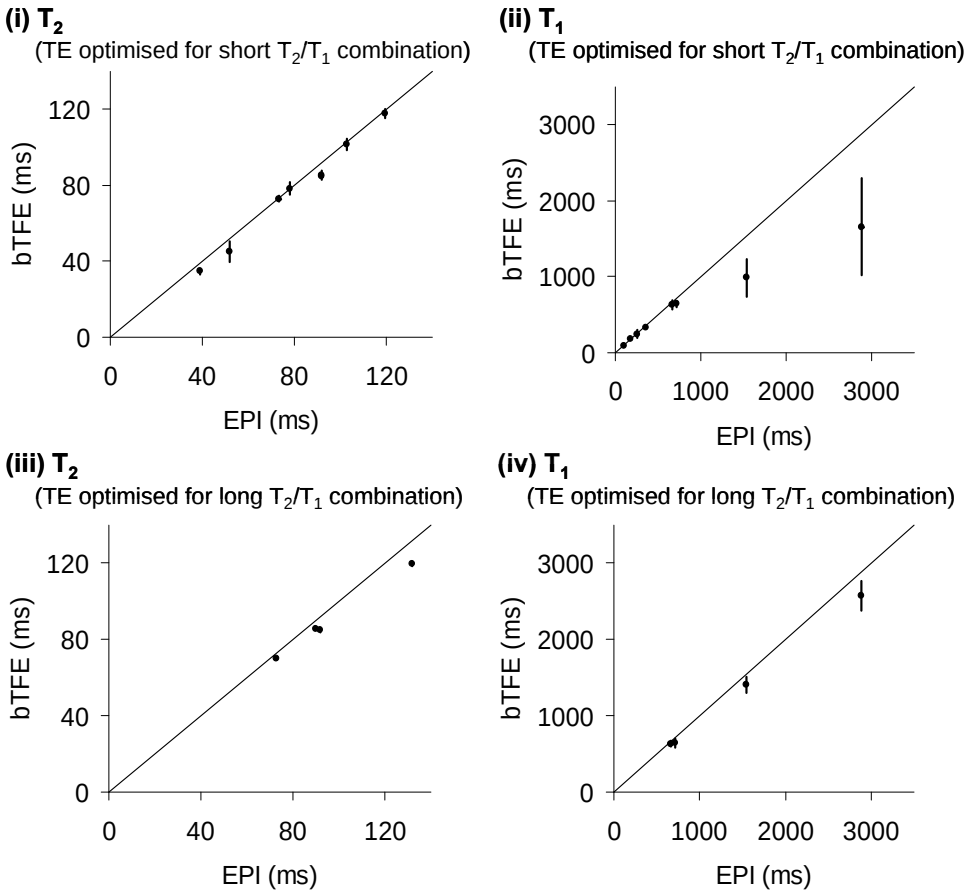

Figure 5-7: (mean ± std. dev.) Validation curves for (i, iii) T_2 and (ii, iv) T_1 measured using variable flip angle T_2-prep bTFE against EPI (SE and IR respectively). Optimum TE sets were used for the T_2-prep bTFE (i, ii) TE set S2 and (iii, iv) TE set L2. The identity line is shown.

The fitted T_2 and T_1 values obtained using the variable flip angle technique (Figure 5-7) are very similar to those measured using the standard method (Figure 5-6). However, since the longest echo time in TE set S2 (262 ms) is shorter than for TE set S1 (637 ms), the fitted T_1 values are now less accurate (compare Figure 5-6 ii and Figure 5-7ii).

Data was also acquired using the variable flip angle T_2-prep bTFE sequence (Experiment 1 from Table 5-2) using a large TE set (18 values). The results of this show that using more TEs gives a more accurate fit (Figure 5-8).

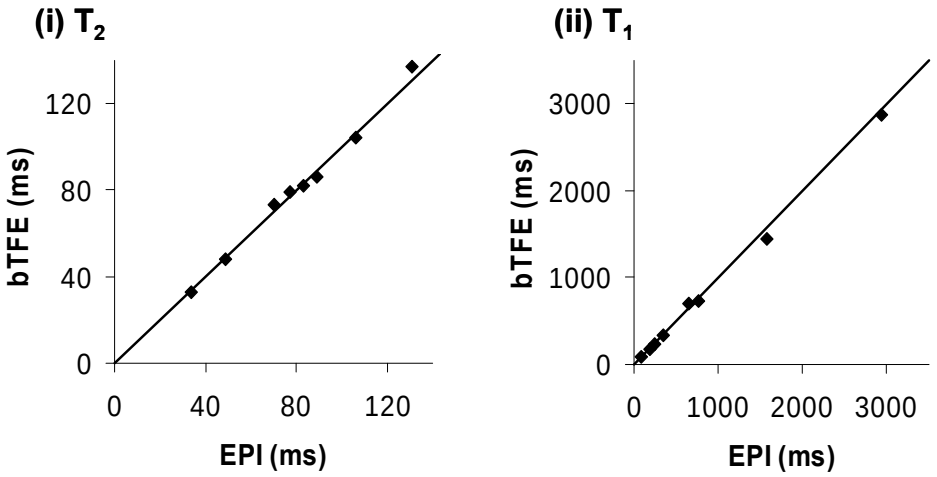

Figure 5-8: (mean ± std. dev.) Validation curves for (i) T_2 and (ii) T_1 measured using the variable flip angle T_2-prep bTFE (single experiment) against EPI (SE and IR respectively). 18 TE values were used: TE set S1 plus for α = 30°, TE = 1000, 1500, 2000, 2500, 4000, 5000, 6000, 8000, 10000 ms and for α = 10, 20°, TE = 2000, 8000 ms. The identity line is shown.

5.3.5 In-vivo measurements

Typical transverse and coronal images for the T_2-prep bTFE sequence with TE = 20 ms are shown in Figure 5-9, along with corresponding T_2 maps. Some regions fit poorly in areas of low signal from off resonance effects close to 2π and susceptibility effects. Figure 5-10 shows (i) T_2 and (ii) T_1 measurements in the abdomen using the standard (2.5 min acquisition) and variable flip angle (6 min acquisition) T_2-prep bTFE sequences along with some literature values given by de Bazelaire *et al*. [13] who measured T_2 in a 15 s breathold (T_2-prepared single shot half Fourier FSE) and T_1 in a 30 s breathold (IR-prepared single shot half Fourier FSE). In some volunteers, it was not possible to measure the relaxation times of all the tissues because either the tissue was not visible or the signal had already decayed before acquisition (i.e. short T_2).

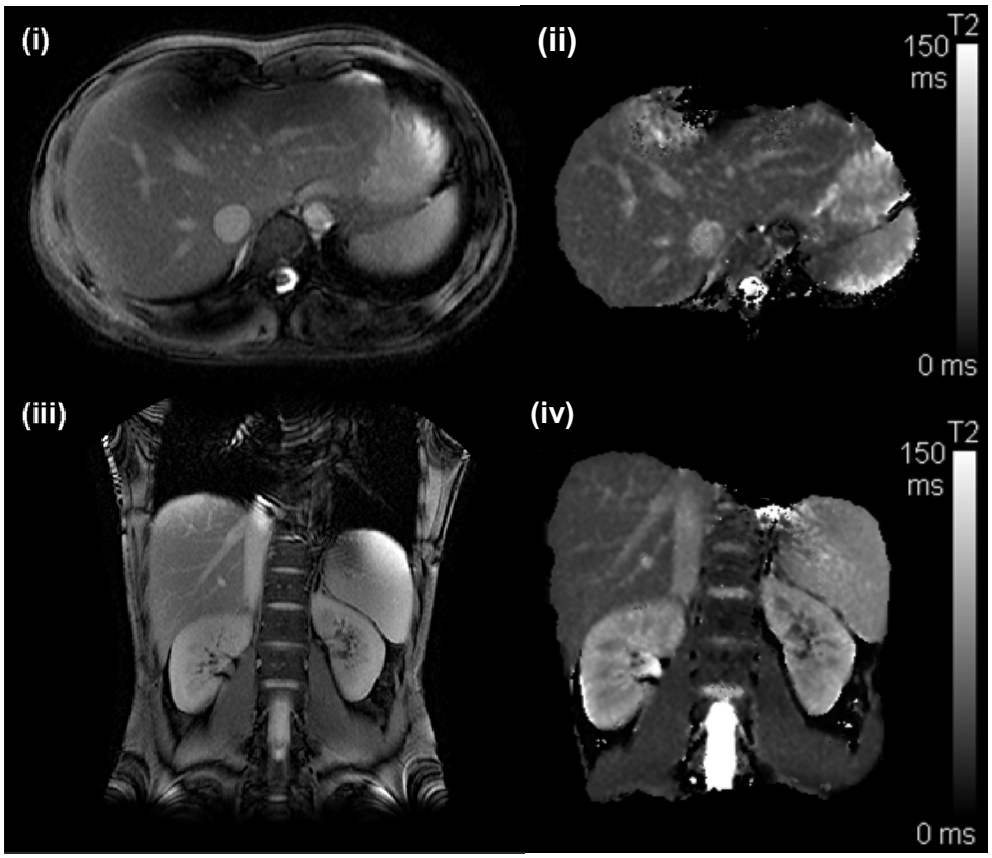

Figure 5-9: Typical (i) transverse and (iii) coronal images obtained using the standard T_2-prep bTFE sequence at TE = 20 ms for $\alpha = 30°$ shown with (ii, iv) corresponding T_2 maps.

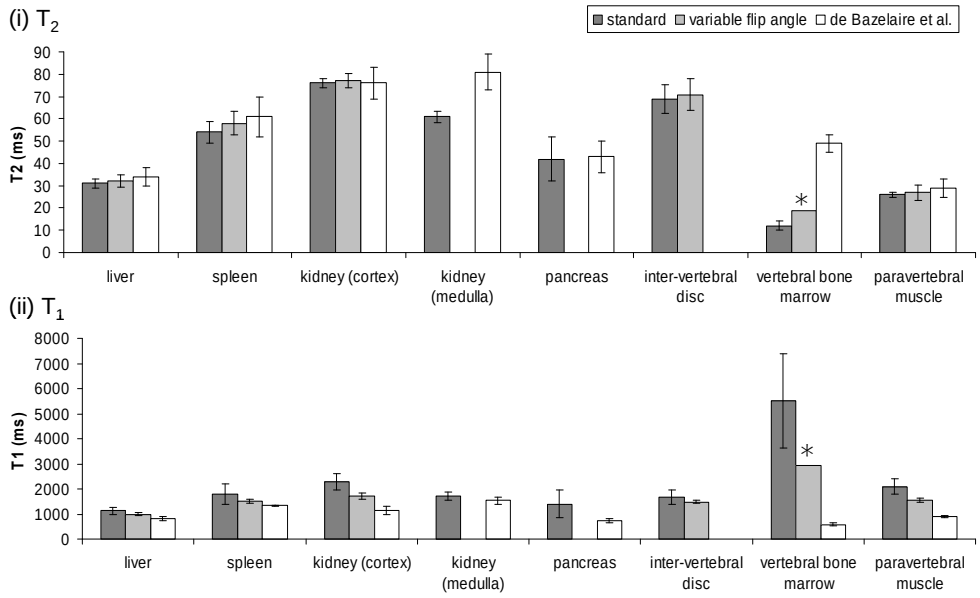

Figure 5-10: (mean ± SEM) (i) T_2 and (ii) T_1 values measured for different abdominal tissues using the standard and variable flip angle T_2-prep bTFE sequences. Literature values from de Bazelaire *et al.* [13] are also given for comparison. (*N=1)

5.4 DISCUSSION

It is possible to use the T_2-prep bTFE sequence to measure T_2 (and in some cases T_1) in the abdomen in a clinically feasible time with high image quality. The simulations showed that random noise will give rise to random errors in the fitted values of T_2 but also some systematic errors for high noise values (Figure 5-4 and Figure 5-5). However, experimentally at 3.0 T, the noise levels are low compared to the values simulated (< 0.3% for Experiment 1 of Table 5-2). These simulations also showed that the fit for T_2 was minimally sensitive to errors in RF pulse amplitude particularly if the pulse amplitude factor (β) was included in the fit (Figure 5-5i), although the fitted values of T_1 and M_0 were sensitive to the flip angle (Figure 5-5iii-iv) as these parameters compensate for the effects of an imperfect flip angle on the signal decay curve and therefore cannot be measured using the standard method. Since the sequence is sensitive to the flip angle it is particularly important to include the slice profile in the fitting program.

These errors in the fit mirror those found by Newbould *et al*. [27] using IR-bTFE, but with the T_1 and T_2 reversed. IR-bTFE curves are dominated by the T_1 signal changes and so the pulse errors are compensated for in the T_2 and M_0 fitted parameters. The T_2-prep bTFE is dominated by T_2 signal changes, and hence the T_1 and M_0 parameters show the largest errors. However, as the aim is to measure T_2 and the process of fitting the data for T_2 uses a model of the evolving magnetisation, these parameters cannot be removed from the fit without increasing the error in T_2.

Good agreement was found between T_2 measured using T_2-prep bTFE and spin echo EPI for a wide variety of pulse sequence parameters and relaxation times. Some experimental decay curves exhibited dips similar to those seen in Figure 5-2 in the case of pulse errors in the preparation step, illustrating the importance of proper modeling of this data. It is important to optimise the echo times used for the relaxation times (T_2 and T_1) of the tissues measured otherwise the T_2-prep bTFE sequence underestimates the values of the fitted T_2 or T_1.

T_2 and T_1 values at 3.0 T have been reported for eight different abdominal tissues using the standard and variable flip angle approach. The T_2 values measured using the standard and variable flip angle approach are comparable to those acquired by de Bazelaire *et al.* [37] at 3.0 T using a half Fourier TSE sequence. However differences were observed in both the kidney and bone marrow results. For the kidney data the cortex values given here are higher than the medulla, whereas de Bazelaire *et al.* found almost no difference between the tissue types. This may have been due to better tissue discrimination and a larger region of interest using coronal images in this experiment. The bone marrow T_2 data measured from this work were significantly lower than those of de Bazelaire *et al*. Again these differences may be due to the orientation of the slice and the choice and number of TE values used in this experiment. By using the variable flip angle method, the

T_1 values were closer to those measured by de Bazelaire *et al*. compared with the standard method.

The T_2-prep bTFE pulse sequence is readily available on most clinical scanners which run cardiac exams. The fitting algorithm is also relatively straightforward to implement if knowledge of the exact pulse sequence is available. The bTFE sequence does suffer from banding artifacts at 2π phase changes caused by B_0 field inhomogeneities, however these can be limited by using very short TE/TR combinations and shimming over the tissues of interest and did not present significant problems in our *in vivo* studies. If this is a problem, in and out of phase images can be combined to overcome this artifact.

An alternative method for measuring T_2 in abdominal tissues would be to use a half Fourier TSE readout for the single shot acquisition [13]. In terms of implementation, it was found to be easier to add a spin echo before the bTFE pulse train rather than to alter the spin echo train in the TSE sequence. Furthermore bTFE generally gives higher signal to noise ratio than half Fourier TSE for most abdominal tissues, and practically the bTFE sequence can be run at a high in-plane resolution without using SENSE which can be an advantage for larger BMI (body mass index) subjects where there is not enough room for an additional receiver coil to be wrapped around the abdomen. Alternatively, spoiled gradient echo (SGE) and bTFE sequences have been combined for the measurement of relaxation times in neurological tissues in 3D at high resolution but in a rather longer imaging time [38, 39], but the SGE is not useful in gastrointestinal tract where visceral motion degrade the images. Any segmented k-space approach e.g. rapid IR-bTFE [40] for T_1 in the abdomen or radial FSE [41] for T_2 in the liver are not appropriate for stomach and intestine relaxometry which show irregular motion during a breath-hold or respiratory triggering.

This technique will be used to measure fate of model meals in the gastrointestinal tract [10, 11] as it is both quick to run and does not suffer from motion artifacts, offering the potential to monitor changes in T_2 sequentially during meal digestion. With optimised sequences it would be possible to measure T_2 and T_1 *in vivo* to study the fate of food within the gastrointestinal tract since dilution and viscosity changes can be inferred be measuring relaxation times. This can be used to investigate the reaction of the gastrointestinal tract after ingestion of certain food types. For example, studying the effects of high fibre in order to determine why some people are less tolerant than others by investigating changes in water content and distribution in the colon. Alternatively, the T_2 of different fat emulsions have been previously measured using EPI at 0.5 T and shown to vary according to droplet size [8]. However for quantification of fat emulsions *in vivo* and at high field, the T_2-prep bTFE sequence would be a preferable method for measuring T_2 compared with EPI since it does not suffer with susceptibility artifacts.

5.5 CONCLUSIONS

The T_2-prep bTFE can be used to measure T_2 accurately in phantoms and *in vivo* in the abdomen with low sensitivity to RF pulse errors and no degradation of images from motion artifacts allowing application of the technique to measuring T_2 in the stomach. Random errors in measurements increase with increasing noise in the system. RF pulse errors increase systematic errors in the fitted data of T_1 and M_0 when using the standard method making this method inappropriate for measuring these parameters in addition to T_2. However, by optimising the echo times used for tissues of particular interest, the accuracy of T_1 can be improved.

5.6 FUTURE WORK

The accuracy of the fitted T_1 needs to be addressed further. In the work carried out here, a variable flip angle technique was implemented, but provided little improvement in the fitted T_1 value. The number of echo times acquired for each flip angle and the number of flip angles used should be investigated to determine if any more information could be gained by varying the flip angles. Alternatively, it is possible to measure T_1 using inversion recovery bTFE, so a combination of spin echo and inversion recovery bTFE could provide enough information to obtain both T_2 and T_1 without significantly increasing the scanning time. The T_2 (and T_1) measurements should be tested for repeatability on the same occasion and on separate occasions.

This work has assumed that there are no off-resonance contributions to the signal. Therefore, the consequence of off-resonance contributions should be investigated to ascertain what effect off-resonance components would have on the fitted parameters T_2, T_1 and M_0.

5.7 References

1. Choi, J.Y., et al., *Abdominal applications of 3.0-T MR imaging: Comparitive review versus a 1.5-T system.* Radiographics, 2008. **28**(4): p. e30.
2. Barth, M.M., et al., *Body MR Imaging at 3.0 T: understanding the opportunities and challenges.* Radiographics, 2007. **27**(5): p. 1446-1462.
3. Akisik, F.M., et al., *Abdominal MR Imaging at 3.0 T.* Radiographics, 2007. **27**(5): p. 1433-1444.
4. Hussain, S.M., P.A. Wielopolski, and D.R. Martin, *Abdominal magnetic resonance imaging at 3.0 T: problem or a promise for the future?* Top. Mag. Res. Im., 2005. **16**(4): p. 325-35.

5. Merkle, E.M. and B.M. Dale, *Abdominal MRI at 3.0 T: The Basics Revisitied.* AJR, Am J Roentgenol, 2006. **186**: p. 1524-1532.
6. Schindera, S.T., et al., *Abdominal magnetic resonance imaging at 3.0 T what is the ultimate gain in signal-to-noise ratio?* Acad Radiol, 2006. **13**(10): p. 1236-43.
7. Marciani, L., et al., *Echo-planar magnetic resonance imaging of Gaviscon alginate rafts in-vivo.* J. P. P., 2002. **54**: p. 1351-1356.
8. Marciani, L., et al., *Fat Emulsification Measured Using NMR Transverse Relaxation.* J. Mag. Res, 2001. **153**: p. 1-6.
9. Marciani, L., et al., *Effect of meal viscosity and nutrients on satiety, intragastric dilution, and emptying assessed by MRI.* Am. J. Physiol. Gastrointest. Liver Physiol., 2001. **280**: p. G1227-G1233.
10. Hoad, C.L., et al., *In Vivo Imaging of Intragastric Gelation and Its Effects on Satiety in Humans.* J. Nutr., 2004. **134**: p. 2293-2300.
11. Marciani, L., et al., *Gastric response to increased meal viscosity assessed by echo-planar magnetic resonance imaging in humans.* Journal of Nutrition, 2000. **130**: p. 122-127.
12. Marciani, L., et al., *Echo-Planar Imaging Relaxometry to Measure the Viscosity of a Model Meal.* J. Mag. Res, 1998. **135**: p. 82-86.
13. de Bazelaire, C., et al., *MR Imaging Relaxation Times of Abdominal and Pelvic Tissues Measured in Vivo at 3.0 T: Preliminary Results.* Radiology, 2004. **230**(3): p. 652-659.
14. Stanisz, G.J., et al., *T1, T2 Relaxation and Magnetisation Transfer in Tissue at 3T.* Mag. Res. Med, 2005. **54**: p. 507-512.
15. Yoshikawa, T., et al., *Gradient- and Spin-Echo T2-Weighted Imaging for SPIO-Enhanced Detection and Characterization of Focal Liver Lesions.* J. Mag. Res. Im., 2006. **23**: p. 712-719.
16. Dahnke, H. and T. Schaeffter, *Limits of Detection of SPIO at 3.0 T Using T_2* Relaxometry.* Mag. Res. Med, 2005. **53**: p. 1202-1206.
17. Carr, H.Y. and E.M. Purcell, *Effects of Diffusion on Free Precession in Nuclear Magnetic Resonance Experiments.* Phys. Rev., 1954. **94**(3): p. 630-638.

18. Majumdar, S., et al., *Errors in the Measurements of T_2 Using multiple-Echo MRI Techniques I. Effects of Radiofrequency Pulse Imperfections.* Mag. Res. Med, 1986a. **3**: p. 397-417.
19. Poon, C.S. and R.M. Henkelman, *Practical T2 Quantitation for Clinical Applications.* J. Mag. Res. Im., 1992. **2**: p. 541-553.
20. McKenzie, C.A., et al., *Fast Acquisition of Quantitative T_2 Maps.* Mag. Res. Med, 1999. **41**: p. 208-212.
21. Majumdar, S., et al., *Errors in the Measurements of T_2 Using Multiple-Echo MRI Techniques II. Effects of Static Field Inhomogeneity.* Mag. Res. Med, 1986b. **3**: p. 562-574.
22. Oppelt, A., et al., *FISP - a new fast MRI sequence.* Electromedica, 1986. **54**(1): p. 15-18.
23. Stehning, C., S. Winkelmann, and H. Dahnke, *Simultaneous T1, T2 and spin density quantification in 5 seconds using inversion recovery SSFP.* Proc. 15th Annual Meeting of ISMRM, 2007.
24. Gulani, V., et al., *Towards a single-sequence neurologic magnetic resonance imaging examination: multiple-contrast images from an IR TrueFISP experiment.* Invest Radiol, 2004. **39**(12): p. 767-74.
25. Scheffler, K. and J. Hennig, *T_1 Quantification With Inversion Recovery TrueFISP.* Mag. Res. Med, 2001. **45**: p. 720-723.
26. Schmitt, P., et al., *Inversion Recovery TrueFISP: Quantification of T1, T2, and Spin Density.* Mag. Res. Med., 2004. **51**: p. 661-667.
27. Newbould, R. and R. Bammer, *Flip Angle Sensitivity in IR-trueFISP T_1 and T_2 Mapping.* Proc. 13th Annual Meeting of ISMRM, 2005b: p. 2191.
28. Hoad, C.L., E.F. Cox, and P.A. Gowland, *Measuring T_2 using a T_2 prepared Balanced Turbo Field Echo Sequence.* Proc. 14th Annual Meeting of ISMRM, 2006.
29. Huang, T.-Y., et al., *Are TrueFISP Images T_2/T_1 - Weighted?* Mag. Res. Med, 2002. **48**: p. 684-688.
30. Scheffler, K., *On the Transient Phase of Balanced SSFP Sequences.* Mag. Res. Med., 2003. **49**: p. 781-783.

31. Press, W.H., et al., *Numerical Recipes in C (Second Edition).* 1996: p. 695-698.
32. Taylor, J.R., *An Introduction to Error Analysis (Second Edition).* 1982: p. 181-226.
33. Press, W.H., et al., *Numerical Recipes in C (Second Edition).* 1996: p. 412-420.
34. Powell, M.J.D., *Efficient method for finding minimum of function of several variables without calculating derivatives.* Computer Journal, 1964. **7**(2): p. 155-162.
35. Henkelman, R.M., *Measurement of signal intensities in the presence of noise in MR images.* Mag Res Med, 1995. **34**: p. 910.
36. Tyler, D.J., et al., *Rapid and accurate measurement of transverse relaxation times using a single shot multi-echo echo-planar imaging sequence.* Mag. Res. Im., 2004. **22**: p. 1031-1037.
37. de Bazelaire, C.M., et al., *MR imaging relaxation times of abdominal and pelvic tissues measured in vivo at 3.0 T: preliminary results.* Radiology, 2004. **230**(3): p. 652-9.
38. Deoni, S.C.L., T.M. Peters, and B.K. Rutt, *High-Resolution T_1 and T_2 Mapping of the Brain in a Clinically Acceptable Time with DESPOT1 and DESPOT2.* Mag. Res. Med, 2005. **53**: p. 237-241.
39. Deoni, S.C.L., B.K. Rutt, and T.M. Peters, *Rapid Combined T_1 and T_2 Mapping Using Gradient Recalled Acquisition in the Steady State.* Mag. Res. Med, 2003. **49**: p. 515-526.
40. Bokacheva, L., et al., *Single breath-hold T1 measurement using low flip angle TrueFISP.* Magn Reson Med, 2006. **55**(5): p. 1186-90.
41. Altbach, M.I., et al., *Radial fast spin-echo method for T2-weighted imaging and T2 mapping of the liver.* J Magn Reson Imaging, 2002. **16**(2): p. 179-89.

CHAPTER 6

MEASURING THE FATE OF FOOD IN THE GASTROINTESTINAL TRACT AT 3.0 T

6.1 INTRODUCTION

Chapters 4 and 5 described methods for quantifying the fate of food in the gastrointestinal tract. A technique for measuring small bowel water content (SBWC) was validated for use at 3.0 T and a sequence was developed to measure the transverse relaxation time, T_2.

The advantage of MRI is that many gastrointestinal (GI) measurements can be made in a short time period which allows for serial imaging to be performed. This chapter combines techniques for measuring SBWC and T_2, along with gastric emptying (section 4.2.4), to investigate the behaviour of alginate beads in the stomach and to determine the effects of fasting and feeding on water absorption and secretion in the gastrointestinal tract.

6.2 INVESTIGATIONS OF ALGINATE BEADS IN THE GI TRACT

6.2.1 Introduction

With the escalating problem of obesity, the food industry is trying to alter delivery of nutrients with the intention of increasing and prolonging satiety after eating. Alginates, extracted from native brown seaweed, are widely used in the food industry due to their ability to retain water and their gelling, thickening and stabilising properties. More recently, alginates have proved valuable in other applications such as an immobilisation matrix for the encapsulation of biomaterials for controlled delivery applications [1, 2].

Monitoring the behaviour and properties of alginate beads *in vivo* as well as in vitro [3] is important in optimising systems for both encapsulation and controlled delivery. *In vivo* studies are important to determine the influence of the alginate particles on the gastric emptying, satiety and meal transit through the body [4]. Rayment *et al*. [3] showed that there was a good correlation between T_2 and alginate concentration which suggests that the relaxation time T_2 of the water present is a powerful indicator of the micro-structural changes which occur in the alginate gel network during the simulated gastric conditions. Therefore, by measuring the transverse relaxation time, T_2, the mobility of the water protons in the bead samples and surrounding tissues can be probed and hence the gelation state can be inferred. Furthermore, by comparing the *in vivo* results with the previous in vitro studies [3], it would enable the refinement of the in vitro simulated conditions so that they better reflect actual digestion conditions.

6.2.2 Aims

To investigate the behaviour of alginate beads, of a few millimetres in diameter, in the gastrointestinal tract, by measuring gastric emptying and changes in T_2.

6.2.3 Methods

6.2.3.1 Volunteer selection

Ten healthy volunteers (7 male, 3 female, mean age 24 years, range 18-45 years), with no history of gastrointestinal disease, were recruited for the study. The volunteers fasted overnight, abstained from alcohol for the previous 24 hours and caffeine and strenuous exercise for the previous 18 hours prior to the start of the study since these factors are known to affect gastrointestinal function. Volunteers were allowed to consume a small glass of water an hour before attending the test centre. Volunteers attended the

centre on two separate occasions and consumed both test meals in a random order.

6.2.3.2 Meal descriptions

Two bead types were used to model a solid meal in the study [3]:

- 126 ml of solid centre (strongly gelled)
- 222 ml of liquid centre (weakly gelled)

The beads were made from 200 ml of 1.5% alginate solution dropped into a CaCl solution. The solid beads were approximately 4 mm in diameter and the liquid beads were approximately 4.3 mm in diameter [3].

The beads were consumed over a 15 minute period (T = 0-15 mins) with 500ml of distilled water to assist drinking without chewing. A high fat preload meal of 50 ml Calogen® (SHS International, Liverpool, UK), containing 233 kCal was given to the volunteer 15 minutes (T = -15mins) before the bead meal to help retain the low calorie bead meal in the stomach and switch the stomach from a fasted to a fed state as shown for a similar meal [5].

6.2.3.3 Study protocol

All scanning was carried out using a 3.0 T Philips Achieva whole body MRI scanner using a SENSE torso transmit/receive coil. Measurements were made repeatedly at T = 15, 35, 60, 90 mins for gastric volume and T_2 measurements, and again at T = 120, 150 mins for further gastric volume measurements.

Half Fourier TSE images were acquired in the transverse plane. The sequence was multi-slice with TE = 59 ms and TR = 1511 ms; each slice

was acquired in less than 1 s and 20 slices (no gap) were acquired over two breatholds. The reconstructed resolution was 0.78 x 0.78 x 10 mm^3.

T_2-prep bTFE images were acquired using timing parameters given in chapter 5, Table 5-2 Experiment 1 with TE = 20, 40, 60, 80, 100, 150, 200, 400 ms. A single transverse slice was acquired to include a region in the stomach where there were a lot of beads. The data was acquired during separate breatholds with a 10 s gap between different TEs. The reconstructed resolution was 1.56 x 1.56 x 10 mm^3.

6.2.3.4 Data analysis

Gastric volume measurements were made using Analyze® (Mayo Foundation, USA). Regions of interest (ROIs) were manually drawn in the stomach around the total meal. The total volume at the different time points was then calculated by summing across the slices. Gastric half emptying times ($T_{1/2}$) were calculated by fitting an exponential decay and straight line curve to the data [6]. R^2 values were calculated and the best overall fit to the data was used to determine the final fitting function. No constraint was placed on the initial volume at T = 0 in the fit. This was because people would have different amounts of Calogen® remaining in the stomach and different initial rates of emptying. The percentage of the meal remaining at the 60 minute time point was calculated from the measured volume at 60 minutes and the total consumed volume (50 ml Calogen® + weak/strong bead volume consumed + 500 ml water) which was assumed to be 100 % volume. The bead meal was also split into separate 'liquid' (water and remaining Calogen®) and 'bead layer' (beads and interstitial solution) components. The gastric emptying and percentage volume remaining measurements were repeated for each component.

The T_2-prep bTFE data was fitted for T_2, T_1 and M_0 using the Powell algorithm as described earlier in chapter 5 to obtain values for T_2 of the bead

layer. The beads packed together with solution surrounding them and hence the T_2 measured will include a component from the surounding fluid which will vary depending on the packing of the beads. Hence changes in the observed T_2 may reflect changes in the bead characteristics and/or their packing density which would change as they swell/shrink.

6.2.4 Results

Six volunteers managed to consume all the strong beads in the time allowed compared to three volunteers for the weak beads. Only one volunteer failed to drink all the 500 ml water given with the beads. The median total volumes consumed (Calogen® + water + beads) were 729 ml and 676 ml for the weak and strong bead meals respectively.

Figure 6-1 shows an image of the bead meal in the stomach. There is clear layering of the beads allowing for separation of a bead layer (beads with surrounding solution) and the remaining liquid meal. The median gastric half emptying times and percentage volume changes are summarised in Table 6-1. Data was not normal (Shapiro-Wilk test) and so Wilcoxon paired tests were carried out and a significance level of $p < 0.05$ was assumed. Only eight paired measurements were made for the half emptying time of the liquid only meal because the fitted curves for this data were extremely poor for two liquid volume data sets (1 weak, 1 strong) and therefore the data were excluded.

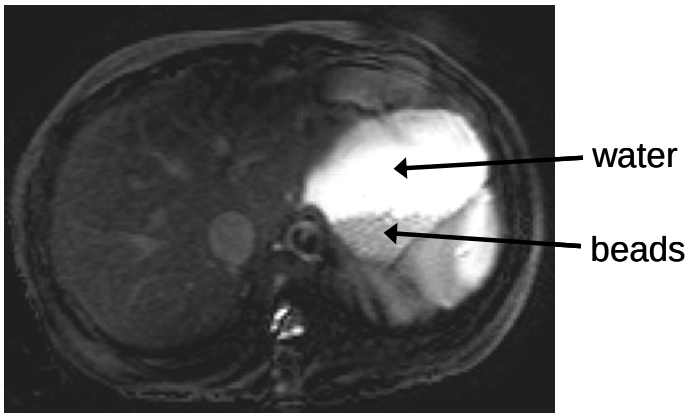

Figure 6-1: Images of weak beads in the stomach obtained using the standard T_2-prep bTFE sequence at TE = 20 ms and α = 30°.

Gastric emptying measure	Weak bead meal Median (IQR)	Strong bead meal Median (IQR)	p value
$T_{1/2}$ – total meal	48.30 mins (39.90 - 63.68)	47.75 mins (41.33 - 64.05)	p = 0.8 (N = 10)
$T_{1/2}$ – bead only	38.95 mins (32.78 - 41.83)	54.25 mins (39.60 - 74.83)	p = 0.059 (N = 10)
$T_{1/2}$ – liquid only	55.10 mins (50.40 - 75.08)	53.70 mins (45.60 - 68.40)	p = 0.78 (N = 8)
% vol. at T = 60 – total meal	29.7 % (22.9 - 34.7)	35.0 % (24.9 - 46.0)	p = 0.037 (N = 10)
% vol. at T = 60 – bead only	39.0 % (32.8 - 41.8)	54.3 % (39.6 - 74.8)	p = 0.059 (N = 10)
% vol. at T = 60 – liquid only	25.2 % (16.6 - 33.8)	24.1 % (19.5 - 38.5)	p = 0.65 (N = 10)

Table 6-1: Summary of gastric emptying measurements: gastric half emptying times ($T_{1/2}$) and the percentage of the meal remaining at the 60 minute time point.

Artifacts across the stomach in the images meant that data could not be used at some time points for some volunteers. Median T_2 data from the bead layer in the stomach is given in Figure 6-2. The T_2 values of the beads in the stomach initially increased and subsequently decreased. Before ingestion, the T_2 of the strong beads was shorter than the T_2 of the weak beads [3].

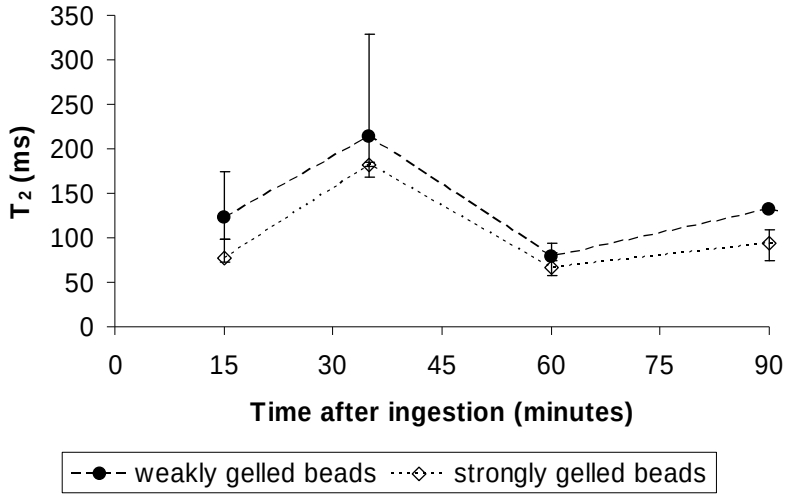

Figure 6-2: (median and interquartile range) Change in T_2 of the beads in the stomach after ingestion measured using the T_2-prep bTFE sequence.

6.2.5 Discussion

Using MRI it was possible to visualise the alginate milli-beads in the stomach; the beads were clearly visible (provided they were surrounded by a small amount of fluid) since the bead size was much larger than the in-plane resolution. The data provided valuable insight into how the bead meal was distributed in the stomach and the time course of the gastric phase of the meal.

Although gastric half emptying times were not significantly different for the two beads, gastric sieving of the beads did occur, with the percentage volumes of bead layer remaining in the stomach larger than the percentage volumes of the liquid layer at 60 minutes after ingestion. The packing of the beads was assumed to be constant and spherical. This sieving was enhanced for the stronger beads which showed significantly increased percentage meal and bead layer volume remaining at 60 minutes compared to the weak beads, with no difference seen between the liquid components of the meal at this time. The reasons for not detecting this process using the gastric half emptying times alone may have been due to the exponential or linear functions poorly modeling the emptying for this mixed meal. The difference

in emptying between the weak and strong bead layers shows that the stomach was detecting differences between the bead types; it is possible this effect cold be enhanced with harder beads. Similarly, a previous study by Marciani *et al*. [7] also showed that gastric emptying times were increased when particle strength was increased.

In the acidic conditions in vitro, the beads showed no change in T_2 when initially put in the gastric salt solution at T = 15 minutes, but a decrease occurred when the gastric solution pH was reduced to 2.0 using HCl. *In vivo* the beads showed an initial increase followed by a decrease in T_2 as the beads shrunk in the stomach. The beads shrink in acidic conditions due to a decrease in the repulsive charge due to protonation of free carboxylate groups on the alginate [3]. Furthermore, due to dissociation of calcium ions at low pH, an acid gel can be formed where COO^- groups become protonated, allowing the alginate chains to come closer together and form hydrogen bonds [8]. For the *in vivo* work, there is no 'control' solution measurement and there was an increase in T_2 occurring at T = 35 minutes after ingestion suggesting the beads may have swelled slightly or were not packing as tightly allowing for more water to be included in the estimate of the bead layer T_2. The decrease seen later from T = 60 minutes onwards may indicate the beads were shrinking and hence would indicate that the stomach pH had dropped to a low value at this point. This would be expected due to the stimulation of gastric acid secretion by gastric distention [9].

6.2.6 Conclusion

Both the weak and strongly gelled beads were visible in the stomach on the images acquired. Gastric emptying was delayed slightly by the presence of the stronger beads, due to gastric sieving. It was possible to accurately measure T_2 in the stomach since there is little movement over the region of interest over a couple of minutes. The bead T_2s were found to increase 35

minutes after ingestion and then decrease again; this is consistent with the acidic condition of the stomach affecting the strength of the bonding between alginate chains.

6.3 RESPONSES OF THE GI TRACT TO FASTING AND FEEDING

6.3.1 Introduction

Irritable bowel syndrome (IBS) is a condition which is particularly interesting to the gastrointestinal MRI group here in Nottingham. The condition is poorly understood, but many patients believe that their symptoms are exacerbated by eating certain foods, particularly bran [10]. The role of the small bowel in IBS has been neglected until recently [11], with the stomach and colon being the main focus. It is therefore important to be able to assess gastrointestinal function to understand the changes which occur postprandial in healthy volunteers before attempting to study changes in disease. Using MRI, it is possible to study the GI tract from the stomach all the way through to the colon.

We usually require volunteers to fast overnight before MRI studies of gastrointestinal function the following morning to guarantee an empty stomach. Using MRI, it is possible to check that the volunteer has fasted by performing an initial scan before any feeding occurs. However, it has been observed that the fasted small bowel often contains an appreciable resting water content. Bran is thought to induce water secretion in the small bowel and affect transit time. Therefore, it would be useful to ascertain the effect of high and low fibre diets on the fasting small bowel water content (SBWC) and to determine if the diet affects changes in SBWC from fasting to feeding.

Previous studies have shown that the SBWC drops following a rice pudding breakfast [12]. It is suspected this is because the meal switches the small bowel from a fasting to a fed state, and that the sugar in the fruit drink stimulated rapid water absorption. Using test meals that vary in calorie content, it would be possible to determine if it is the calorie content that switches the small bowel from a fasting to a fed state. It has also been suggested that a fatty, liquid preload causes an increase in small bowel water content due to contraction of the gallbladder, releasing bile [13].

6.3.2 Hypotheses

1. Having a low fibre diet on the day prior to scanning would result in a lower fasting SBWC compared with a high fibre diet.
2. Dietary fibre content will have an effect on the change in SBWC after feeding of a rice pudding breakfast. The higher the fibre content, the faster the small bowel transit.
3. Fibre will induce intestinal secretions and alter T_2 and T_1 in the colon.
4. Ingesting glucose after a period of fasting stimulates water absorption from the small bowel compared with a non-nutrient iso-osmolar mannitol solution.
5. Adding a fatty preload would enhance small bowel water content by stimulating pancreatico-biliary secretions.

6.3.3 Aims

- To compare the fasting SBWC and colon T_2 and T_1 after consumption of low and high fibre diets and to see the subsequent change in SBWC and colon T_2 and T_1 due to ingestion of a rice pudding and fruit juice breakfast.

- To compare the gastric emptying and changes in intestinal volumes after consumption of meals with varying calorie content and to determine the effect of increasing the fat content of the meal.

6.3.4 Methods

Two separate studies were carried out using healthy volunteers. Study 1 investigated the effects of fibre, fasting and feeding on the small bowel water content (SBWC) and colonic relaxation times. Fasting SBWC and colonic T_2 and T_1 were measured following a low or high fibre evening meal, before eating a rice pudding meal and observing changes in these parameters due to feeding. Study 2 examined the effect of the rate of absorption of the test meal nutrients on small bowel water content by comparing a glucose test meal known to be rapidly absorbed with a mannitol meal known to be non-absorbable. In addition to this, the effect of consuming a fat preload with the glucose meal was investigated.

The volunteers had no history of gastrointestinal disease and were asked to abstain from alcohol for 24 hours and from caffeine and exercise for 18 hours prior to morning scanning sessions.

6.3.4.1 STUDY 1: Effects of fibre, fasting and feeding on the small bowel and colon

Fourteen healthy volunteers formed the study group. The mean age of the group was 25 years (range = 22-28 years) and consisted of 8 male and 6 female volunteers. Volunteers were asked to attend the centre on four occasions in total to undergo a two-way cross-over study. At 6.00 pm, volunteers were given one of two evening test meals. The following morning the volunteers were asked to arrive at the centre at 8.00 am having fasted and were scanned (T = -30 mins). The volunteers were given a breakfast test meal to consume at T = 0 mins and were scanned immediately

after (T = 15 mins) and 45 minutes later (T = 60 mins). This process was repeated for both evening test meals.

Two model evening meals with differing fibre contents were used in the study. Both meals consisted of:

- 220 g Dolmio Fusilli Pasta Pouch with 170 g Dolmio Tomato & Basil Pasta Sauce pouch and 30 g Sainsbury's mild English cheddar
- 150 g Sainsbury's Low fat Raspberry yoghurt
- 300 ml still bottled mineral water

With either:

- 30 g Kellog's Rice Krispies with 125 ml semi-skimmed milk

(LOW FIBRE)

- 40 g Kellog's All Bran with 125 ml semi-skimmed milk

(HIGH FIBRE)

Both evening meals contained approximately 800 kCal, but the low fibre meal only contained 4.1g of fibre compared with 14.7 g fibre in high fibre meal. Volunteers consumed both meals, on separate study days, in a randomised order.

The breakfast meal was a standard rice pudding meal used in previous studies [12]. It consisted of:

- 213 g Sainsbury's creamed rice pudding
- 15 g coarse wheat bran (Holland and Barratt)
- 34 g Sainsbury's seedless raspberry jam
- 100 ml Sainsbury's pure orange juice from concentrate

The total calorie content for this meal was approximately 330 kCal.

6.3.4.2 STUDY 2: Effects of meal calorie content on small bowel water content

Eleven healthy volunteers formed the study group. The mean age of the group was 24 years (range = 20-30 years) and consisted of 9 male and 2

female volunteers. Volunteers were asked to attend at 7:30 am having fasted overnight on three separate occasions and consumed one of the three test drinks in a random order. They were scanned before consuming the drink (T = -30 mins) immediately afterwards (T = 10 mins) and then every 30 minutes for 3.5 hours. The meals were given in a random order.

Three model meals with differing calorie contents were used in the study:

A: 350 ml still bottled water with 17.5 g of mannitol powder (28 kCal)
B: 350 ml still bottled water with 17.5 g of glucose powder (70 kCal)
C: 50 ml of a fat preload (Calogen®, SHS International, Liverpool, UK) followed 15 minutes later by 350 ml still bottled water with 17.5 g glucose powder (303 kCal)

The preload converted fasting motility patterns to the fed state. The mannitol and glucose solutions had the same osmolarity and were isotonic.

6.3.4.3 MRI scanning protocol

Images were acquired on a 3.0 T Philips Achieva MRI Scanner using a SENSE torso coil.

Gastric emptying and SBWC

The single shot TSE sequence in section 4.3 was used to measure gastric volumes and small bowel water content. (TE_{eff} = 400 ms, TR_{eff} = ∞, 20 slices, slice thickness = 7 mm, field of view (FOV) = 400 mm, scan percentage 80 %, acquired voxel size = 1.25 x 1.57 x 7 mm^3 interpolated to 0.78 x 0.78 x 7 mm^3, number of refocusing pulses = 130, SENSE factor = 2.0, total scan time = 44 s acquired over two breatholds). Figure 6-3 shows an example of the images acquired using this sequence.

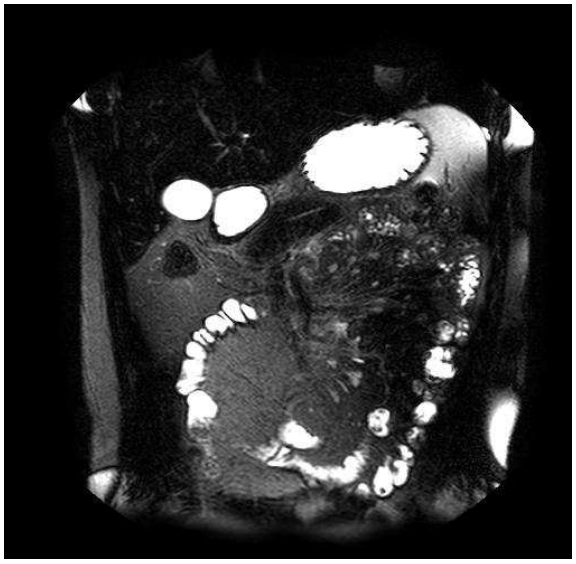

Figure 6-3: Typical slice used for gastric volumes and SBWC analysis acquired from TSE sequence.

T_2-prep bTFE

The variable flip angle T_2-prep bTFE sequence was used to obtain T_2 and T_1 measurements. For the T_2-prep bTFE, timing parameters used are those given in chapter 5, Table 5-2 Experiment 1. For $\alpha = 30°$, TE = 20, 43, 93, 201, 434, 637, 1000, 2000, 4000, 8000 ms and for $\alpha = 10^o, 20^o$, TE = 2000, 8000 ms (Total imaging time for T_2-prep bTFE sequence < 4 mins). Figure 6-4 shows a typical single coronal slice acquired using this sequence at TE = 20 ms.

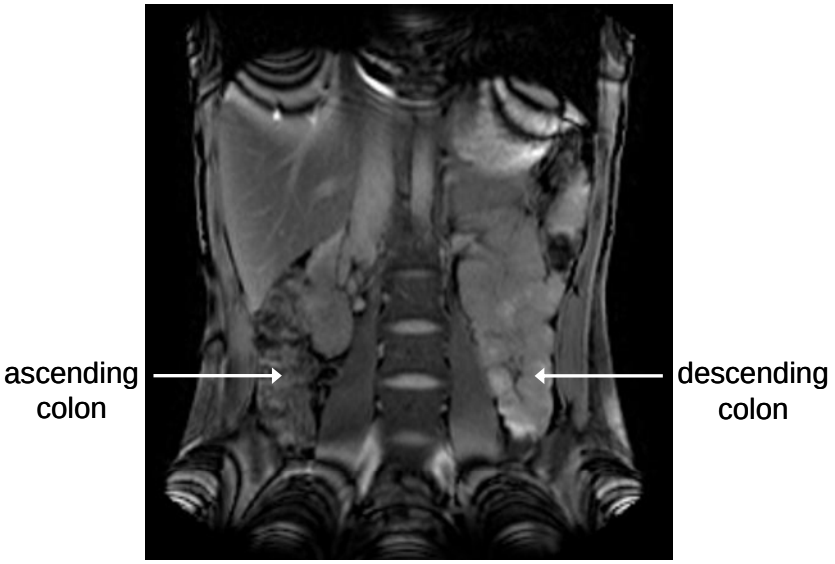

Figure 6-4: Coronal image acquired using the variable flip angle T_2-prep bTFE at TE = 20 ms and α = 30°.

6.3.4.4 Data analysis

Gastric emptying

Gastric volume measurements were made using Analyze® (Mayo Foundation, USA). Regions of interest (ROIs) were manually drawn around the meal in the stomach on each slice and summing across the slices to determine the total volume at the different time points. The percentage of ingested volume remaining in the stomach at 70 minutes was calculated. This was calculated from the total volumes ingested (mannitol meal *A* or glucose meal *B* = 350 ml, glucose with preload meal *C* = 400 ml).

SBWC

The SBWC was calculated for each volunteer using in-house software written by Dr Caroline Hoad in IDL® (Research Systems Inc, Boulder, Colorado, USA) and adapted for use at 3.0 T in chapter 4. At each time point, the volume of all image pixels above a threshold was integrated, after exclusion of signal from regions other than bowel.

T_2-prep bTFE

T_2 and T_1 were calculated by drawing ROIs on the images using Analyze® in both the ascending and descending colon and fitted using the Powell algorithm as described in chapter 5.

6.3.4.5 Statistical analysis

All data was tested for normality using the Shapiro-Wilk Test. For paired comparisons, the paired student t-test was used if the data was normal and Wilcoxon signed ranks if the data was not normal. For three-way comparisons, Friedman mean ranks, which avoid any assumptions about normality, were used. Two-way analysis of variance (ANOVA) was used to assess the significance of differences over time. Post hoc assessments were then performed using Bonferroni. A p-value < 0.05 was considered to be statistically significant.

6.3.5 Results

6.3.5.1 STUDY 1: Effects of fibre, fasting and feeding on the small bowel and colon

Figure 6-5 and Figure 6-6 show individual subject comparison between fasting SBWC and colonic T_2 and T_1 after the low and high fibre meals. It can be seen that there are only small differences between the SBWC after the different evening meals for each volunteer. It was found that 6 volunteers showed the lowest SBWC after the high fibre diet and 8 volunteers were found to have the lowest small bowel water content after consumption of the low fibre diet. The median (and interquartile range) was found to be 50 ml (40 - 67 ml) and 49 ml (40 – 70 ml) for the low and high fibre evening meals respectively (red lines on graph in Figure 6-5); this difference was not significant ($p = 0.72$, student t-test). The fasting colonic T_2 and T_1 values were only measured in four volunteers and in some cases,

the images were too poor to draw regions of interest because artifacts made it difficult to determine the colon. There were no significant differences in the fasting colonic T_2 and T_1 values (p=1, Wilcoxon paired test); this was not surprising since N = 4.

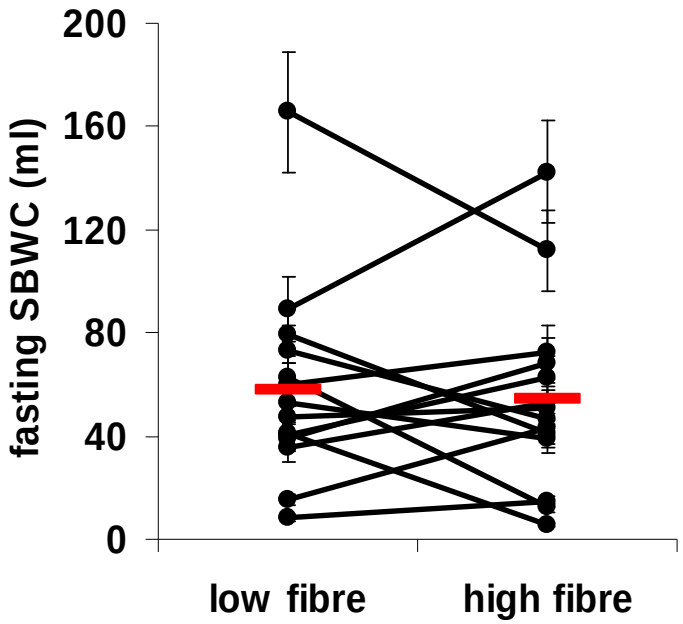

Figure 6-5: Individual subject comparison of fasting small bowel water content after prior feeding of low and high fibre evening meals and median fasting small bowel water content for each meal type (red line).

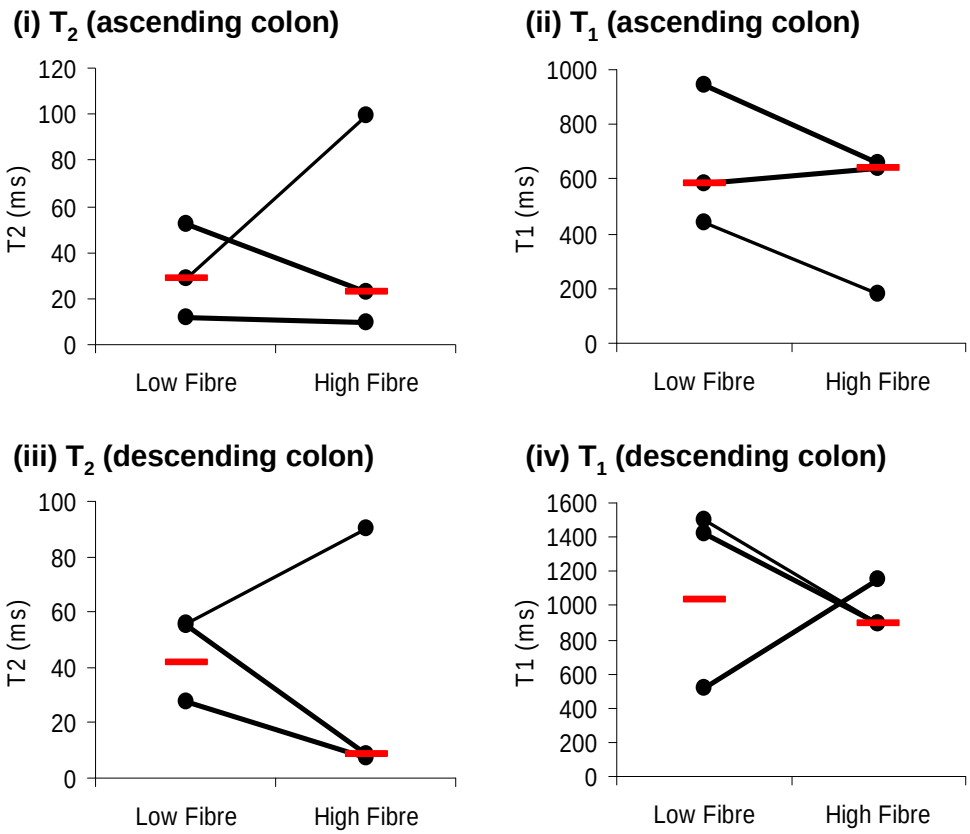

Figure 6-6: Individual subject comparison of fasting colonic (i, iii) T_2 and (ii, iv) T_1 after prior feeding of low and high fibre evening meals showing the median T_2 and T_1 for each meal type (red line).

Figure 6-7 shows the changes in SBWC between fasting and consuming the rice pudding breakfast. The breakfast was given to each volunteer at T = 0 mins and they were given 15 minutes to consume the meal. On 22 out of 28 occasions a drop was seen in the SBWC immediately after the rice pudding meal was ingested ($p < 0.0001$, ANOVA). The evening meal had no effect on the following mornings changes in SBWC ($p = 0.34$, ANOVA).

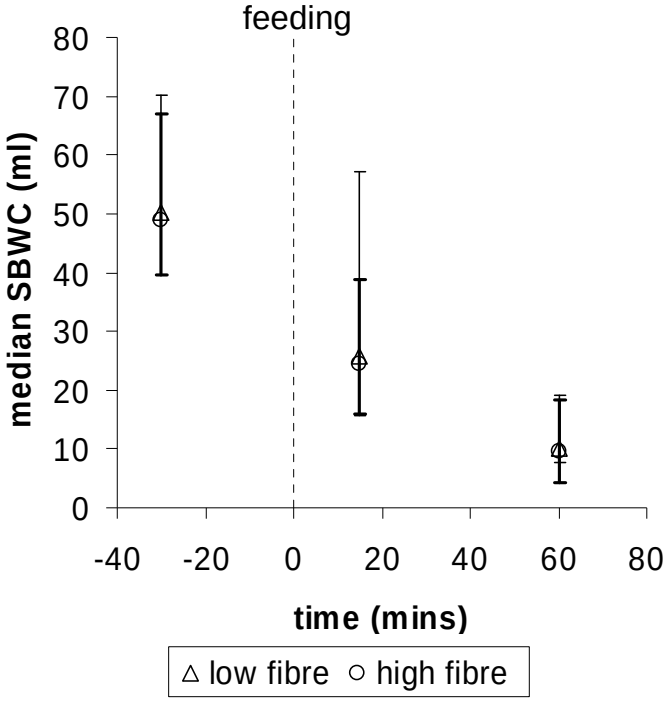

Figure 6-7: (median ± interquartile range) Change in small bowel water content after prior feeding of low and high fibre evening meals and then morning feeding of standard rice pudding and fruit juice breakfast.

Figure 6-8 shows the changes in colonic T_2 and T_1 between fasting and consuming the rice pudding breakfast. There were no significant changes in the T_2 or T_1 immediately after the rice pudding breakfast in any region of the colon ($p > 0.88$, Wilcoxon paired test).

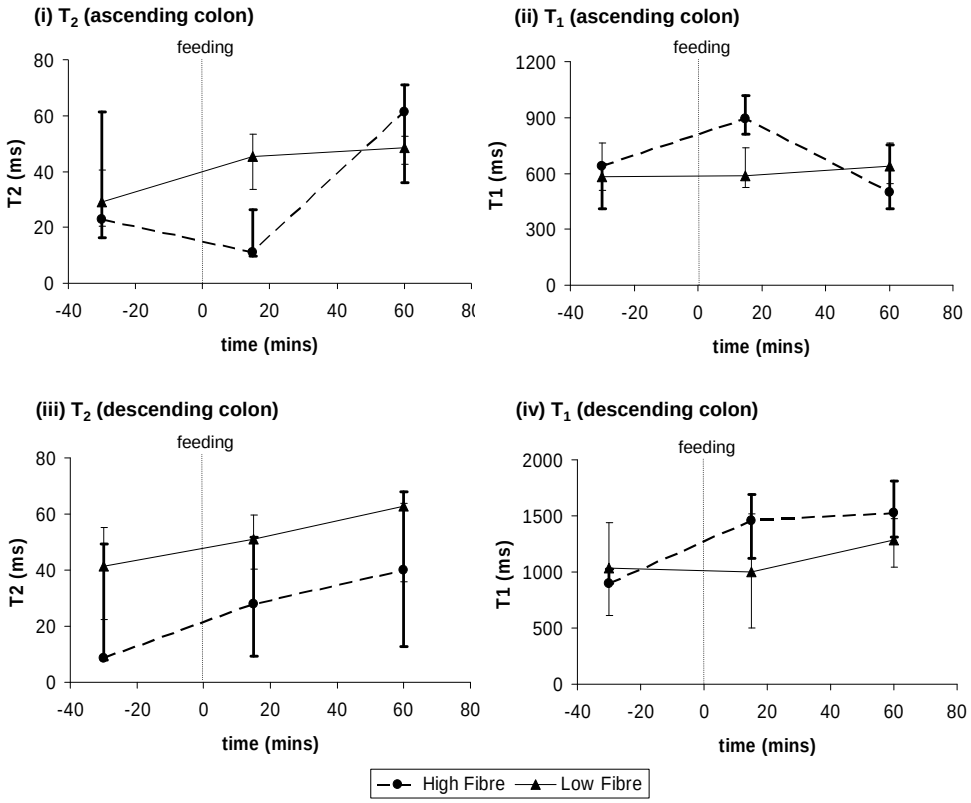

Figure 6-8: (median ± interquartile range) Change in colonic (i, iii) T_2 and (ii, iv) T_1 after prior feeding of low and high fibre evening meals and then morning feeding of standard rice pudding and fruit juice breakfast.

Since neither time nor dietary fibre had any significant effect on the colonic T_2 and T_1, the data were combined and paired comparisons made between T_2 and T_1 in the ascending and descending colon. Figure 6-9 and Figure 6-10 show differences between the ascending and descending colon for T_2 and T_1 respectively. There were no significant differences between the two regions for the T_2 measurements ($p = 0.88$, Wilcoxon paired test). However, there was a significant difference between the two regions for the T_1 measurements ($p = 0.0035$, student t-test); the T_1 is higher in the descending colon.

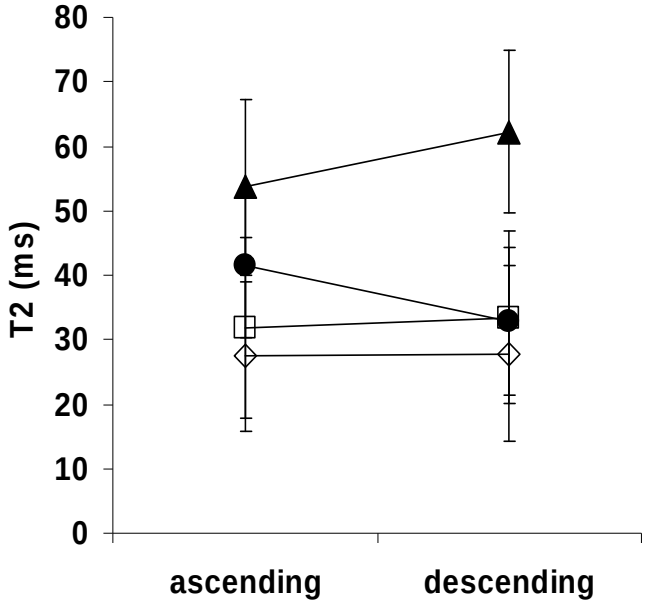

Figure 6-9: (mean ± SEM) Paired comparisons between T_2 in the ascending and descending colon. Each volunteer is indicated by a different symbol.

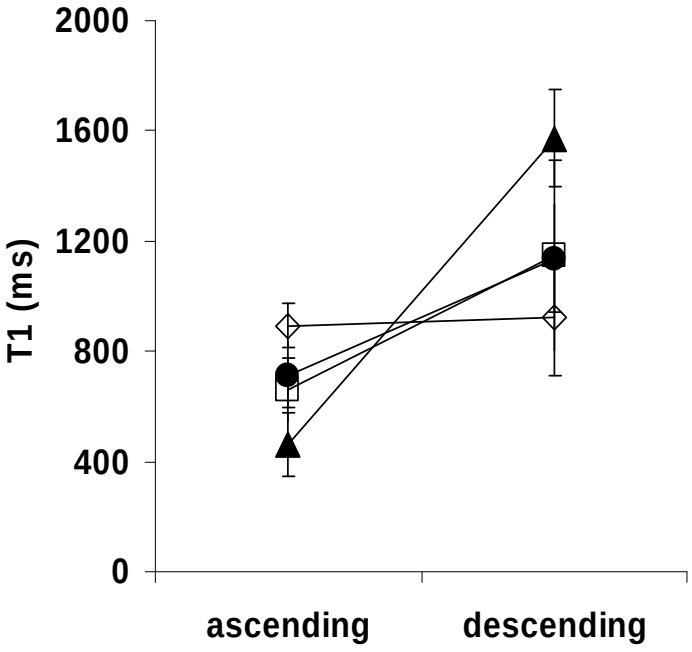

Figure 6-10: (mean ± SEM) Paired comparisons between T_1 in the ascending and descending colon (p = 0.0035, student t-test). Each volunteer is indicated by a different symbol.

6.3.5.2 STUDY 2: Effects of meal calorie content on small bowel water content

Gastric emptying

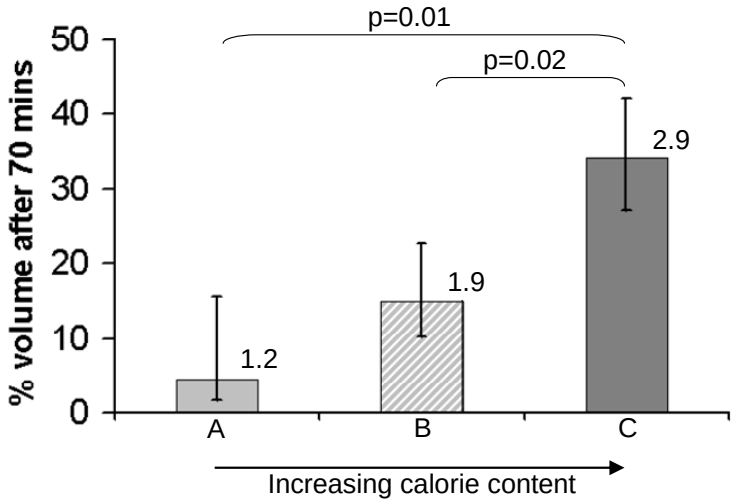

Figure 6-11: (median and interquartile range) Graph showing the percentage of ingested volume remaining in the stomach after 70 minutes for mannitol meal A, glucose meal B and glucose with preload meal C. Friedman mean ranks are given above each bar and the significant p-values of the Wilcoxon paired tests are shown.

Figure 6-11 shows the median percentage of ingested volume remaining in the stomach after 70 minutes with the interquartile ranges (N = 10). For each meal, there was one volunteer whose stomach was out of the field of view of the image for that time point. Friedman ranks were calculated and showed a significant difference between the three meals, with ranks close to 1, 2, 3 in order of increasing calorie content (p = 0.001). There were significant differences between the glucose with preload meal *C* and the other two meals. There was no difference between mannitol meal *A* and glucose meal *B* which were closer in calorie content (Wilcoxon paired test).

Intestinal volumes

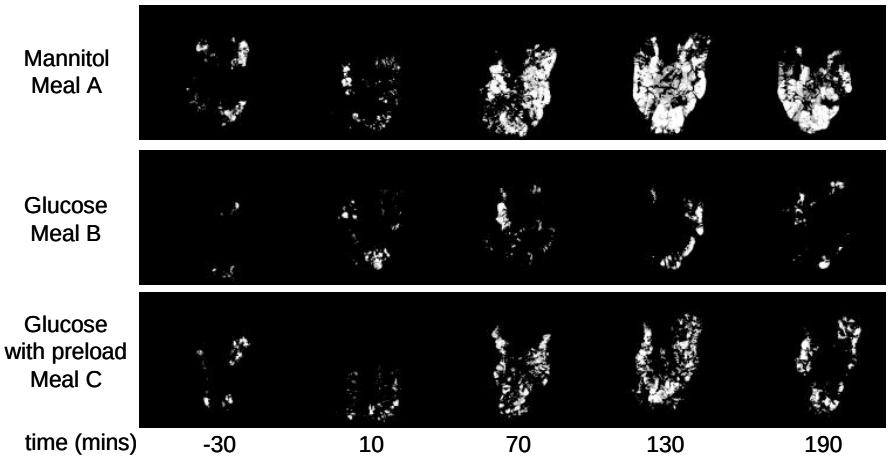

Figure 6-12: MIP images showing the change in intestinal water distribution over time for a single volunteer for each model meal.

Figure 6-12 shows the maximum intensity projection (MIP) images of the intestine for each meal over the morning session for a single volunteer, for increasing calorie content. The highest intestinal water volume was seen after mannitol meal *A* was consumed. The intestinal water content was very low after glucose meals *B* and *C*, but glucose with preload meal *C* resulted in a slightly higher intestinal water volume towards the end of the study session.

Figure 6-13i shows there is a very large difference between mannitol meal *A* and glucose meals *B* and *C* for the intestinal water content. Glucose with preload meal *C* produced a slightly higher volume in the bowel throughout the morning compared with glucose meal *B*. As seen in Figure 6-13i, the intestinal water volume resulting from mannitol meal *A* remains reasonably constant until the water is excreted from the body.

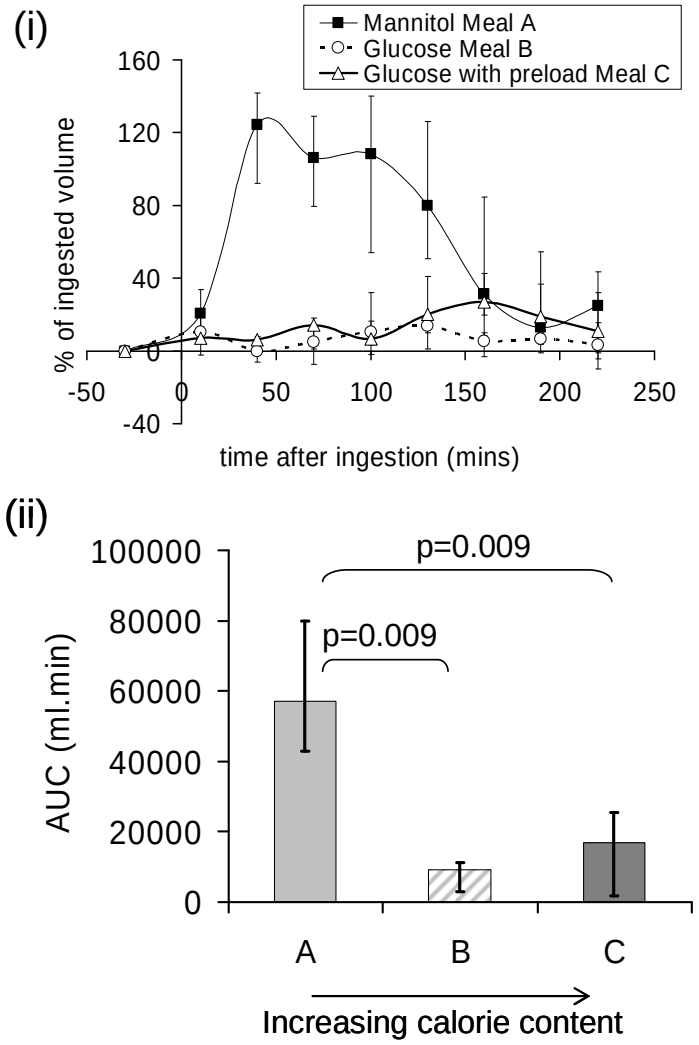

Figure 6-13: (median and interquartile range) (i) Change in intestinal volume, calculated as a percentage of the ingested volume, over the study session was measured for each volunteer and (ii) the area under the curve calculated.

The AUC of the intestinal water volumes against time (Figure 6-13ii) showed a highly significant difference between the meals using the Friedman ranks (for increasing calorie content, ranks = 3.0, 1.36, 1.64, $p < 0.001$). The AUC was higher for mannitol meal *A* than glucose meals *B* and *C* (Figure 6-13ii, $p = 0.009$, Wilcoxon paired test).

It was predicted from previous experimental findings [12, 13] that there would be a decrease in intestinal water volumes after glucose meal *B* and an increase in small bowel water volume after mannitol meal *A*. When

analysing individual volunteer small bowel volumes (N = 11), it was seen that 6 volunteers water content fell after consuming glucose meal *B* and 10 volunteers water content increased after consuming mannitol meal *A*.

Combined gastric and intestinal volumes

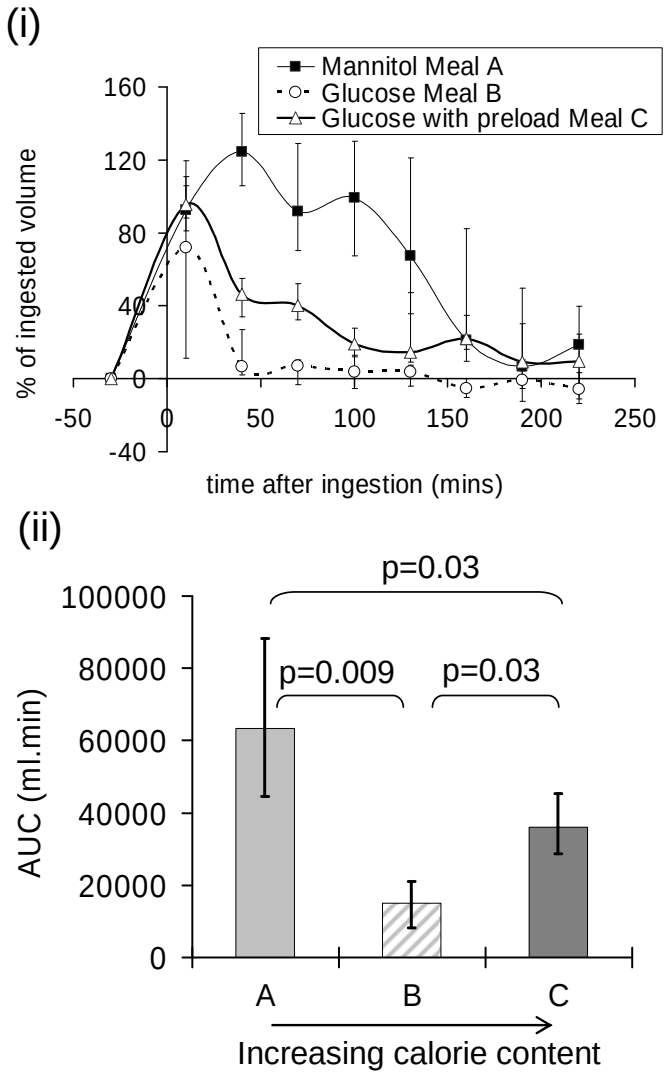

Figure 6-14: (median and interquartile range) (i) Change in the volume of the stomach and intestine, calculated as a percentage of the ingested volume, over the study session was measured for each volunteer and (ii) the area under the curve calculated.

Figure 6-14i shows the change in combined gastric and intestinal volumes over the study session. There was a large fall in water volume between the

10 and 40 minute time points for glucose meals *B* and *C*, suggesting rapid water absorption in the small bowel. The water volume after glucose with preload meal *C* did not fall as rapidly as the volume after glucose meal *B* because the preload delayed gastric emptying and therefore absorption in the small bowel was not so immediate.

Conversely, the combined gastric and intestinal volume increased between the 10 and 40 minute time points increased for mannitol meal *A* so that the combined volumes were above 100 % of the ingested volume. This suggests that water was being secreted in the small bowel. The final drop in this curve was due to large amounts of the water having been defecated by the volunteers before the study session had finished (N = 11).

The AUC of the combined gastric and small bowel time-volume curves (Figure 6-14ii) were found to be significantly different as a group using the Friedman ranking test (for increasing calorie content, ranks = 2.82, 1.18, 2.0, $p = 0.001$). There is a significant difference between glucose meal *B* and the other 2 meals (Figure 6-14ii, Wilcoxon paired test), suggesting again that water was rapidly absorbed in the intestine after consumption of glucose.

6.3.6 Discussion

This study is one of the first to measure colonic relaxation times and use a validated MRI method to study small bowel contents postprandial. As such it has revealed many unanticipated findings.

Study 1 showed that dietary fibre content had no effect on the fasting SBWC, which was found to be about 50 ml, or fasting T_2/T_1 values. The SBWC transit time after consuming a rice pudding breakfast was not affected by the fibre content of the previous days diet either. After ingesting the mixed liquid/solid test meal (rice pudding with bran), the SBWC fell

over the 45 minute period after eating by 40 ml suggesting the contents were absorbed in the small bowel, or possibly emptied into the colon. However, previous reports would suggest that absorption in the small bowel occurs at a rate of 1-2 ml per minute [14] which reflects the decline of around 40 ml in 45 minutes seen here. Marciani *et al*. [15] have shown that there was no significant difference in SBWC 90 minutes following a rice pudding breakfast with or without bran. Following this initial decrease, the SBWC increased between 90 and 180 minutes before reaching a plateau. They found that the SBWC was higher after the high bran breakfast. However, they also found in another study that there was a significant difference in SBWC when comparing healthy volunteers with IBS patients following the high bran rice pudding breakfast [11]. The patients had a much higher fasting and postprandial SBWC, which may reflect the bloated feeling reported by many suffering with diarrhoea predominant IBS. After the rice pudding meal, there were no significant changes in colonic T_2 or T_1; more subjects would be required to ascertain if there are any changes in colonic T_2 or T_1 due to fibre content. However, it was shown that overall, T_1 is significantly higher in the descending colon compared with the ascending colon. This suggests that there is a change in the chemical composition of colonic contents as they progress through the colon.

Study 2 showed that gastric emptying was slowed by increasing the calorie content of the meal which agrees with previous studies [16]. The comparison of glucose meal *B* with mannitol meal *A* showed the importance of absorption in causing the postprandial fall. Mannitol meal *A*, which cannot be absorbed, showed a very rapid rise in SBWC as gastric contents emptied into the small bowel and were further increased by the net secretion of intestinal fluid that mannitol is known to cause [17]. After the liquid glucose meal *B*, the SBWC fell and remained low at levels seen 45 minutes after the rice pudding meal.

The SBWC following glucose meals *B* and *C* behaved reasonably similar up to 100 minutes, remaining below 20 ml. However, between 100 and 160 minutes, for glucose with preload meal *C*, the SBWC increased due to emptying of stomach contents. Although the difference in the areas under the time-volume curves were not significantly different ($p = 0.33$), the fatty preload would have induced secretions of bile from the gallbladder into the small bowel (30 - 40 ml) increasing the SBWC. The slowing of gastric emptying after the fat preload could be attributed to emulsification of the fat within the stomach, which is known to affect gastric emptying [18, 19].

Comparisons of combined gastric and intestinal volumes show clearly the significant differences between the three liquid meals. Glucose meal *B* was absorbed most rapidly and the fat content of glucose with preload meal *C* delayed absorption. Mannitol meal *A* induced intestinal secretions.

Four meals were compared, 3 liquid and 1 mixed liquid/solid, and all 3 nutrient meals produced a similar fall in SBWC, only the un-absorbable, non-nutrient mannitol produced a rise. However, the glucose with fat preload meal *C*, showed a delayed time to maximum peak ($T = 160$ mins) before falling compared with glucose meal *B* ($T = 10$ mins) and mannitol meal *A* ($T = 40$ mins). The increased time to peak can be attributed to the high fat content of the preload which showed much slower emptying of gastric contents, delaying entry into small bowel.

Knowledge of water distribution in the fasting state for healthy volunteers is important in order to determine abnormalities that occur due to GI diseases, such as IBS. The idea that overall gut transit is accelerated in diarrhoea predominant-IBS, and therefore time for water absorption is reduced, suggests that non-absorbable mannitol could prove useful as a model for diarrhoea.

6.3.7 Conclusions

Fasted SBWC was not affected by dietary fibre content, although other studies suggest that bran does affect other phases of SBWC absorption/secretion [11, 15]. T_2 and T_1 were not significantly affected by dietary fibre content or the rice pudding breakfast, but T_1 is significantly higher in the descending colon compared with the ascending colon. Gastric emptying is slowed by increasing the calorie content of a meal which slows the rate of water absorption in the small bowel. Of the 4 meals compared (3 liquid and 1 mixed liquid/solid), all 3 nutrient meals resulted in a fall in SBWC whereas the non-absorbable, non-nutrient mannitol produced a rise. This agrees with previous experiments that showed enhanced absorption when the switching the small bowel from a fasting state to a fed state [12].

6.4 FUTURE WORK

The T_2-prep bTFE sequence, used to measure T_2 and T_1, has enormous potential for investigating dilution changes due to digestion, especially in patients who suffer from irritable bowel syndrome. Furthermore it would be interesting to see if this sequence would be suitable for measuring relaxation times of the colon wall in addition to the colon contents to understand water absorption and secretion within the colon.

Currently, the understanding of the physical factors which influence the access of drugs and bioactives, such as bile and proteases, to their site of action at the colonic mucosa is limited due to the lack of non-invasive measurement techniques. MRI allows non-invasive studies of colonic function in undisturbed physiological conditions, which could be used to improve understanding of the spatial and physical properties of colonic contents to help in designing better drug delivery vehicles. T_2-prep bTFE technique developed here for measuring T_2 and T_1 could prove extremely useful for investigating colonic structure and content.

By measuring changes in SBWC (absorption and secretion) it would be possible to study the effects of feeding, drug delivery or changes due to disease. For example, the development of rehydration liquids designed to optimise water absorption after illness or exercise, or to continue investigating the effects of different food groups (e.g. fat, carbohydrates) on SBWC. Mannitol was shown to be very promising for using as a model for diarrhoea and would be useful for simulating effects found in patients who have diarrhoea predominant IBS.

6.5 References

1. Draget, K.I., G. SkjakBraek, and O. Smidsrod, *Alginate based new materials.* Int. J. Biol. Macromol., 1997. **21**(1-2): p. 47-55.
2. Brekken, C., et al., *A novel probe for localized manganese delivery.* Proc. 3rd Annual Meeting of Soc. Mol. Im., 2004.
3. Rayment, P., et al., *Investigation of alginate beads for gastro-intestinal functionality, Part1: In vitro characterisation.* Food Hydrocolloids, 2009. **23**(3): p. 816-822.
4. Hoad, C., et al., *Investigation of alginate beads for gastro-intestinal functionality, 2: in vivo characterisation.* Food Hydrocolloids, 2009. **23**(3): p. 833-839.
5. Houghton, L.A., et al., *Motor-activity of the gastric antrum, pylorus, and duodenum under fasted conditions and after a liquid meal.* Gastroenterology, 1988. **94**(6): p. 1276-1384.
6. Elashoff, J.D., T.J. Reedy, and J.H. Meyer, *Analysis of gastric-emptying data.* Gastroenterology, 1982. **83**(6): p. 1306-1312.
7. Marciani, L., et al., *Assessment of antral grinding of a model solid meal with echo-planar imaging.* AJPJI, 2001. **280**: p. G844-G849.
8. Norton, I.T., W.J. Frith, and S. Ablett, *Fluid gels, mixed fluid gels and satiety.* Food Hydrocolloids, 2006. **20**: p. 229-239.

9. Grotzinger, U., S. Bergegardh, and L. Olbe, *Effect of fundic distension on gastric acid secretion in man.* Gut, 1977. **18**: p. 105-110.
10. Francis, C.Y. and P.J. Whorwell, *Bran and irritable bowel syndrome: Time for reappraisal.* Lancet, 1994. **344**: p. 39-40.
11. Marciani, L., et al., *Abnormalities of small bowel and colonic water content in diarrhoea-predominant irritable bowel syndrome: novel insights from magnetic resonance imaging.* Gut, 2007. **56**: p. A65.
12. Marciani, L., et al., *Gastrointestinal Effects of Bran: A MRI Study.* Proc. 14th Annual Meeting of ISMRM, 2006: p. 840.
13. Hoad, C.L., et al., *Gastric Emptying, Transit Times and Visualisation of Alginate Beads in the Gastro-Intestinal Tract.* Proc. 14th Annual Meeting of ISMRM, 2006: p. 839.
14. Spiller, R.C., B.J. Jones, and D.B. Silk, *Jejunal water and electrolyte absorption from two proprietary enteral feeds in man: importance of sodium content.* Gut, 1987. **28**: p. 681-687.
15. Marciani, L., et al., *Bran induced small bowel secretion. Assessment by novel non-invasive MRI technique.* Gastroenterology, 2006. **130**(S2): p. A743.
16. Calbet, J.A.L. and D.A. MacLean, *Role of caloric content on gastric emptying in humans.* J. Physiol., 1997. **498**(2): p. 553-559.
17. Billich, C.O. and R. Levitan, *Effects of Sodium Concentration and Osmolarity on Water and Electrolyte Absorption from the Intact Human Colon.* J. Clinical. Invest., 1969. **48**: p. 1336-1347.
18. Marciani, L., et al., *Enhancement of gastric acid stability of a fat emulsions meal delays gastric emptying and increases cholecystokinin release and gallbladder contraction.* Am J Physiol Gastrointest Liver Physiol, 2007. **292**(6): p. G1607-1613.
19. Marciani, L., et al., *Effect of intragastric acid stability of fat emulsions on gastric emptying, plasma lipid profile and postprandial satiety.* Br J Nutr, 2008. **5**: p. 1-10.

CHAPTER 7

MEASURING T_2 AT ULTRA-HIGH FIELD

7.1 INTRODUCTION

In chapters 5 and 6, the T_2-prep bTFE sequence was used to measure T_2 in abdominal tissues and also to measure the effects of digestion on food in the stomach and colon. However, the T_2-prep bTFE sequence does suffer from banding artifacts in regions of B_0 inhomogeneity, which, although had no profound effect on the studies carried out in this thesis, may mean the sequence is not suitable in all contexts. For instance, this sequence was unsuitable for use at ultra high field because it was not possible to get a flip angle much bigger than 10° in the bTFE pulses, due to SAR constraints, resulting in low SNR. It was only possible to achieve a larger flip angle by increasing the TR (repetition time), but then the banding artifacts became a problem.

It has previously been shown to be possible to measure T_2 using hybrid gradient echo-spin echo sequences (chapter 3) such as GESFIDE, GESSE and PRIME and since these sequences have a gradient echo component, they also yield T_2* and hence T_2'. Given that T_2' is assumed to be related to iron, and is only dependent on local field inhomogeneities, these sequences lend themselves to measuring T_2 and T_2* in regions of the body where there could be variations in iron due to disease, such as in the brain or liver. Some examples of these applications will now be discussed.

MRI can be used for vessel size imaging. Vessel size index, VSI,

$$VSI \propto \left(\frac{\Delta R_2^*}{\Delta R_2} \right)^{3/2} \qquad \textbf{[7-1]}$$

measured using MRI, involves simultaneous measurement of R_2 ($=1/T_2$) and R_2^* ($=1/T_2^*$) before and after the injection of an intravascular super-paramagnetic contrast agent [1]. The ratio is calculated because it is independent of the degree of deoxyhemoglobin concentration change due to injecting a contrast agent, but is related to properties of the vascular environment [2]. The contrast agent increases the difference in magnetic susceptibility between blood vessels and the surrounding tissue and therefore increases R_2 and R_2^*. There are two reasons for this increase. In gradient echo experiments reversible spin dephasing occurs, and when the heterogeneity of the phase distribution across the voxel increases due to magnetic field pertubations ΔR_2^* increases. R_2 is less affected by this phenomenon provided there is insignificant diffusional motion. There are theoretical models of the effects of paramagnetic contrast agents on tissue relaxation in the literature [3-5]. Amongst others applications, changes in relaxation rates have been applied to imaging tumour angiogenesis [6-8] since tumour vessels have diameters, on average, 2 to 3 times greater than normal proliferating blood vessels.

MRI is often used to study diseases where iron is thought to accumulate in the brain such as Parkinson's disease, Alzheimer's disease, multiple sclerosis and AIDS and by measuring the levels of iron in the body, it may be possible to enhance understanding of such diseases and therefore aid disease diagnosis, progression and treatment. There are two types of iron in the brain: heme and nonheme iron. The two most important types of nonheme iron are transferrin (iron transport) and ferritin (iron storage). The distribution of iron across the brain is heterogeneous and postmortem studies have shown that the highest concentrations of iron are in the globus pallidus, red nucleus, substantia nigra and putamen regions; the higher the concentration of iron, generally the shorter the relaxation time T_2 [9]. Ferritin is thought to be one of only two types of iron that is present in the human brain in sufficient quantities to affect MR contrast [10]. However, inferring iron concentration from MRI is not trivial; the relaxation of solvent protons is proportional to the concentration of

paramagnetic ions [11]. However, ferritin has unusual magnetic properties, since it is both antiferromagnetic and superparamagnetic, which means that the normal relaxation theory does not hold. The proton-exchange dephasing model (PEDM) was proposed by Gossuin *et al.* [12] and accounts for the irreversible components of T_2; it is very similar to the static dephasing scheme proposed by Yablonskiy *et al*. [5].

T_2 can also be an indication of myelin water fraction. Changes in myelin water is linked to schizophrenia [13, 14], Alzheimer's disease [15] and multiple sclerosis (MS), where it has been shown that there is a decrease in myelin water in MS lesions [16-18]. Measurements of T_2 at short echo times yield myelin water fraction and at high field, detailed assessment of myelin pathology would help determine changes in pathology due to MS [19].

In addition to the brain, another region of the body that contains a high concentration of iron is the liver. Measuring T_2 and T_2*, in combination with other measurements made using MRI (e.g. fat accumulation (^{1}H MR spectroscopy), elastography, portal blood flow and hepatic perfusion (arterial spin labeling)), it would be possible to assess the progression of liver fibrosis and cirrhosis, brought on by chronic liver disease [20]. This would normally be assessed by liver biopsy, but this has limitations (e.g. sampling errors, variation in observer interpretation) and is invasive for the patients.

This chapter discusses a hybrid gradient echo-spin echo (GESSE) sequence capable of measuring T_2 and T_2* simultaneously. Similar techniques have been used by other groups in the past at lower field as discussed in chapter 3. After optimisation and validation, the sequence was used to measure the first deep grey matter T_2 values at 7.0 T and to measure variations in T_2 and T_2' across different field strengths. The variation in T_2 and T_2* of white matter tracts in the brain is then investigated and finally deep grey T_2 and T_2* values are studied to determine changes due to Parkinson's disease.

7.2 THE GESSE SEQUENCE

7.2.1 The sequence

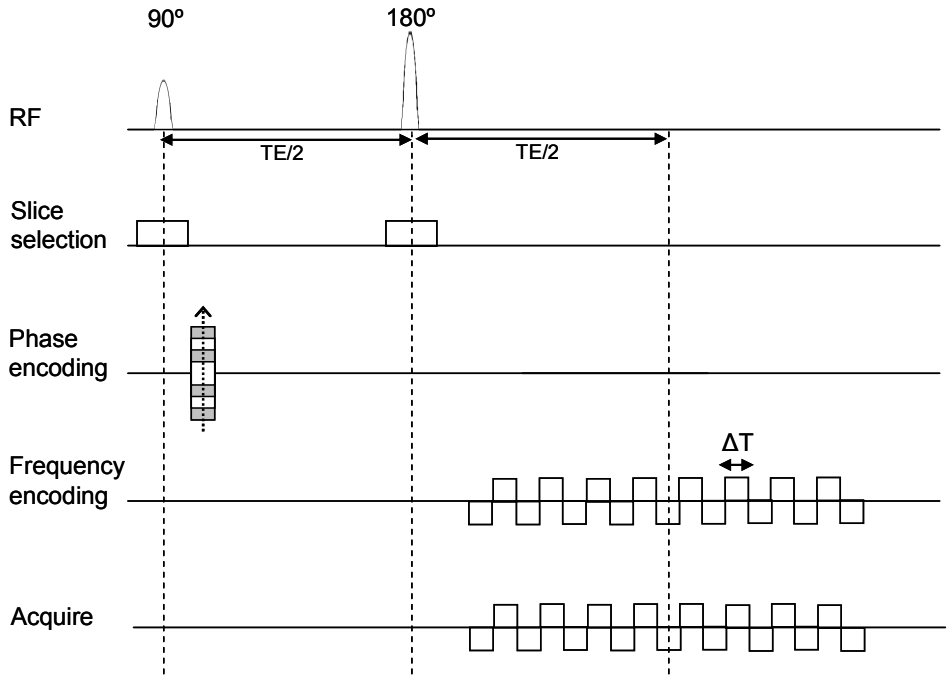

Figure 7-1: Pulse sequence diagram for gradient echo-spin echo GESSE (not to scale).

The GESSE sequence [5] consists of a series of gradient echoes (i.e. similar to an EPI readout gradient) superimposed on a spin echo (Figure 7-1). This is repeated N times (N = number of phase encoding steps) and a phase encoding gradient is applied before the start of the readout. In practice this was implemented using the *EPI test mode* on the Philips scanners.

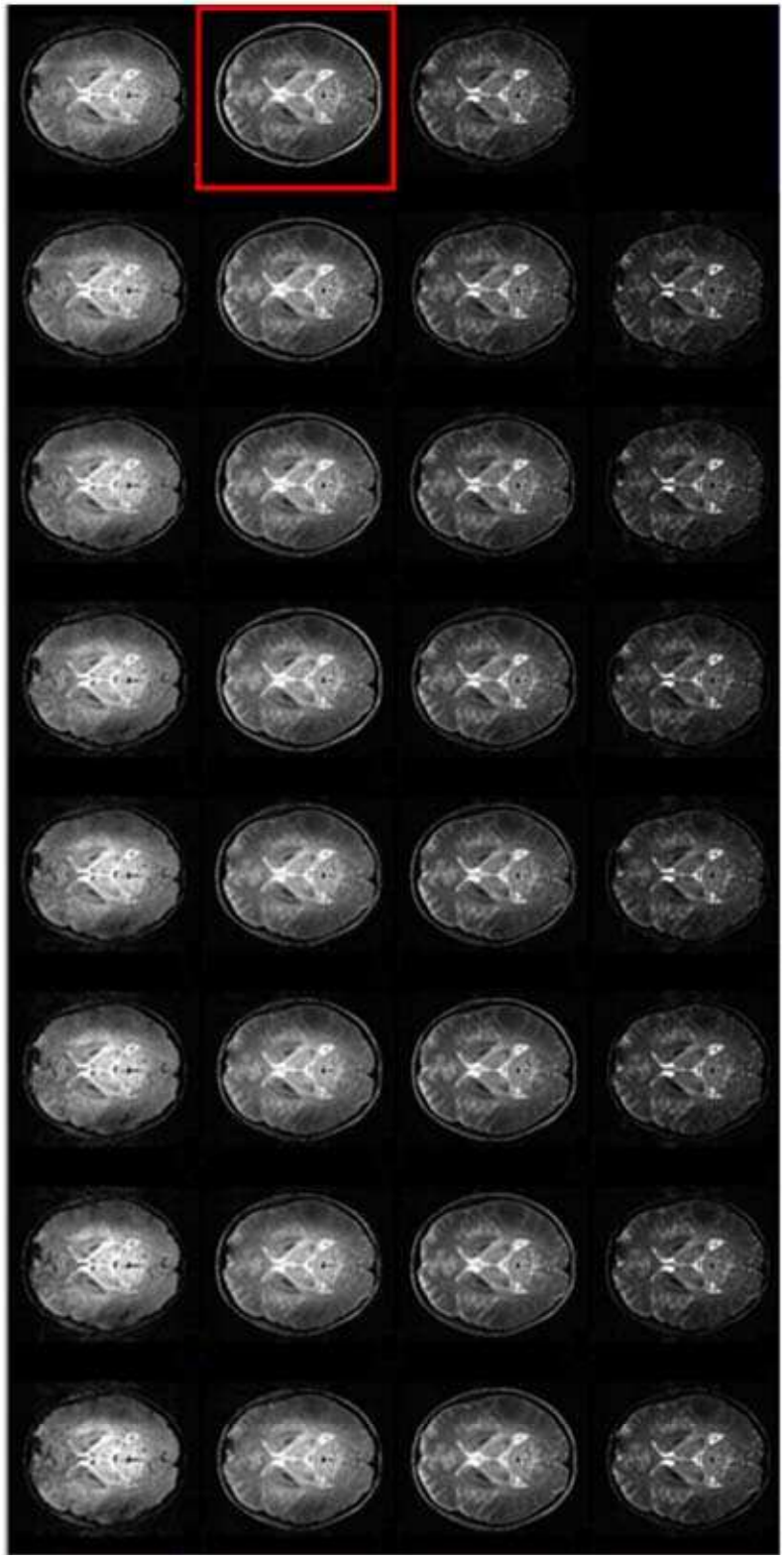

Figure 7-2: Typical images acquired from 31 gradient echoes in the GESSE sequence. The central image corresponds to the peak of the spin echo, indicated by a red box.

Figure 7-2 shows a typical image set acquired using the GESSE sequence. Figure 7-3i shows signal decay curves of grey matter (GM) and cerebral spinal fluid (CSF) obtained from the two regions of interest (Figure 7-3ii). The image in Figure 7-3ii is the image corresponding to the spin echo in Figure 7-2. It is interesting to note that in regions of short T_2*, such as the CSF, the spin echo has the traditional signal shape, unlike regions with a long T_2*, such as grey matter, where the signal simply decays.

To test the effect of different T_2' on the signal, data was simulated with T_2 = 70 ms but with different T_2' values (Figure 7-4). The decay curve obtained for simulated T_2' = 180 ms is close to a straight line and the signal in the decay curve for simulated T_2' = 53 ms increases before decaying away like the traditional spin echo. This indicates that CSF has a short T_2' and grey matter has a longer T_2'.

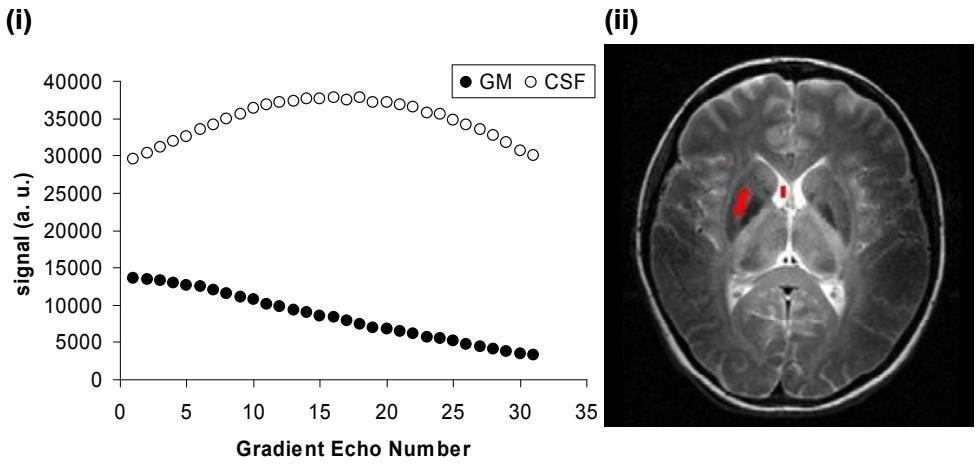

Figure 7-3: (i) Typical GESSE signal decays of grey matter (GM) and cerebral spinal fluid (CSF) and (ii) the ROIs used.

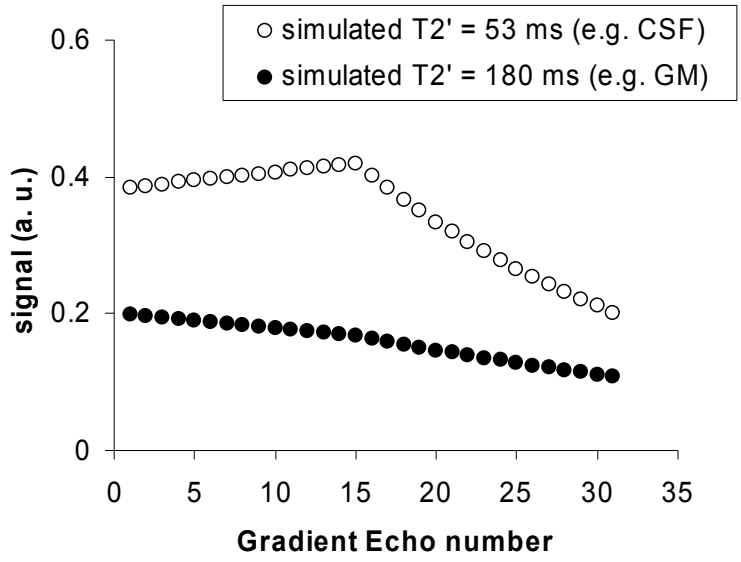

Figure 7-4: Simulations of signal with T_2 = 70 ms and different T_2' values (assumed CSF T_2' = 53 ms, GM T_2' = 180 ms).

7.2.2 Methods

7.2.2.1 Fitting algorithms

Previous work [5, 21, 22] has highlighted sensitivity to noise, so particular attention has been given to optimal fitting of this data. Two methods of fitting the GESSE data (different to that used by Yablonskiy *et al*. [21]) to obtain T_2 are investigated and compared in this work. One uses a ratios method similar to that proposed by An and Lin [22] and the other uses the Powell algorithm [23, 24] (used in chapter 5 for T_2-prep bTFE) to minimise differences between experimental/simulated data and modeled data. The two fitting algorithms are compared analytically to determine the method that provides the minimum error in the fitted T_2 values.

Method A

The relationship [22] between the symmetric gradient echo signals a time $i\Delta T$ before (S_-) and after (S_+) the spin echo at TE (i < M/2, M = total number of gradient echoes) is given by:

$$\frac{1}{T_2} = \frac{\ln\left(\frac{S_{-i}}{S_{+i}}\right)}{2i\Delta T} \qquad \textbf{[7-2]}$$

so that a linear fit of $\ln(S_{-i}/S_{+i})$ against $2i\Delta T$ will yield a value of T_2. An and Lin [22] highlighted a problem with noise in low signal pairs. A solution to this is to use a weighted average to take account of different noise contributions from different echoes. This fitting method involves calculating a T_2 for each gradient echo pair and calculating a mean value. There is an associated error with each of the T_2 values calculated and these must be combined to obtain an overall error in the final T_2. Equation 7-2 can be rewritten in terms of a relative ratio as

$$R_2 = \frac{1}{2i\Delta T}\ln\left(\frac{A}{B}\right) \qquad \textbf{[7-3]}$$

where

$$R_2 = 1/T_2$$
$$A = S_0 \exp\left[-\left(TE - i\Delta T\right)R_2\right]\exp\left[-i\Delta T R_2{}'\right]$$
$$B = S_0 \exp\left[-\left(TE + i\Delta T\right)R_2\right]\exp\left[-i\Delta T R_2{}'\right]$$

and

TE = echo time for spin echo
n = total number of echo pairs, i = 1...n
ΔT = gradient echo spacing

It was assumed that noise is independent of echo time such that $\sigma = \sigma_0 / \sqrt{\Delta T}$, to take bandwidth into account, and that the noise is Gaussian. Therefore, for a single pair of echoes, the error in R_2 is

$$\sigma_{R_2} = \sqrt{\left(\frac{\partial R_2}{\partial A}\sigma\right)^2 + \left(\frac{\partial R_2}{\partial B}\sigma\right)^2} \qquad \textbf{[7-4]}$$

Since $\frac{\partial R_2}{\partial A} = \frac{1}{2Ai\Delta T}$ and $\frac{\partial R_2}{\partial B} = -\frac{1}{2Bi\Delta T}$, equation 7-4 becomes

$$\sigma_{R_2}^2 = \frac{\sigma_0^2}{4i^2\Delta T^3}\left[\left(\frac{1}{A}\right)^2 + \left(\frac{1}{B}\right)^2\right] \qquad \textbf{[7-5]}$$

To convert the error in R_2 into the error in T_2

$$\sigma_{T_2} = \frac{\partial T_2}{\partial R_2}\sigma_{R_2} = \frac{\sigma_{R_2}}{R_2^2} \qquad \textbf{[7-6]}$$

For multiple echo pairs, the mean R_2 from all echo pairs is

$$\overline{R}_2 = \frac{\sum R_{2i}\omega_i}{\sum \omega_i} \qquad \textbf{[7-7]}$$

where R_{2i} and ω_i ($= 1/\sigma$) are the estimated R_2 and the weighting on the signal from the ith pair of echoes respectively. The error in the mean R_2 from all echo pairs is therefore

$$\sigma_{\overline{R}_2}^2 = \left(\frac{1}{\sum \omega_i}\right)^2 \sum (\sigma\omega_i)^2 \qquad \textbf{[7-8]}$$

The weighting is given by the noise level so

$$\sigma_{\overline{R_2}}^2 = \left(\frac{1}{\sum 1/\sigma}\right)^2 \sum \left(\sigma/\sigma\right)^2 = \left(\frac{1}{\sum 1/\sigma}\right)^2 n \qquad \textbf{[7-9]}$$

By combining equations 7-6 and 7-9, the standard error in the mean T_2 value can therefore be written as

$$\sigma_{\overline{T_2}} = \frac{T_2^2 \sqrt{n}}{\sum_{i=0}^{i=n} \sigma_{T\,2i}} \qquad \textbf{[7-10]}$$

where n is the number of gradient echo pairs and σ_{T2i} is the standard error in T_2 from the *i*th gradient echo pair.

<u>*Method B*</u>

A fitting program was written to model the signal, $S(t)$, obtained at each gradient echo:

$$S(t) = S_0 \exp - \left(\frac{TE + i\Delta T}{T_2} + \frac{|i\Delta T|}{T_2'}\right) \qquad \textbf{[7-11]}$$

where S_0 is the initial magnetisation and i = -½(M+1), -½M, ..., 0, ..., ½M, ½(M+1) (M = number of gradient echoes). The Powell algorithm [23, 24], also used in chapter 5, was used to fit data for T_2, T_2' and S_0.

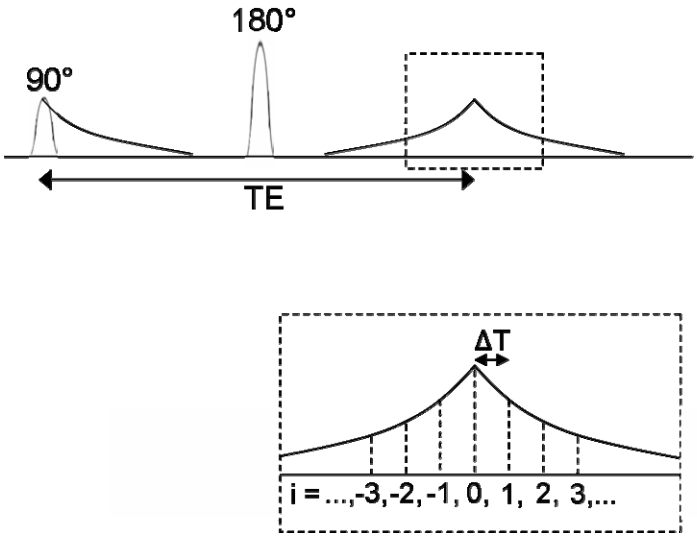

Figure 7-5: Spin echo and gradient echo components of GESSE showing timings.

It is relatively trivial to calculate T_2* and S_0 from the decay component ($i \geq 0$) of the spin echo from:

$$S(t) = S_0 \exp\left(-\frac{TE + i\Delta T}{T_2 *}\right) \qquad \textbf{[7-12]}$$

using the Powell algorithm [23, 24].

A covariance matrix (introduced in chapter 5) was used to obtain an error in the fitted values of T_2 [25, 26]. To measure how well the model agrees with the data, the chi-square merit function can be used:

$$\chi^2\left(T_2, T_2', S_0\right) = \sum\left(\frac{S_{\text{mod}} - S_{measured}}{\sigma}\right)^2 \qquad \textbf{[7-13]}$$

where S is the signal calculated from the fitting model (S_{mod}) and the measured (experimental or simulated) data ($S_{measured}$) and σ is the noise in the measured data. The covariance matrix [C] can be written:

$$[C]=\begin{bmatrix} \sum\frac{1}{\sigma^2}\left(\frac{\partial S_{\mathrm{mod}}}{\partial T_2}\right)^2 & \sum\frac{1}{\sigma^2}\left(\frac{\partial S_{\mathrm{mod}}}{\partial T_2}\right)\left(\frac{\partial S_{\mathrm{mod}}}{\partial T_2'}\right) & \sum\frac{1}{\sigma^2}\left(\frac{\partial S_{\mathrm{mod}}}{\partial T_2}\right)\left(\frac{\partial S_{\mathrm{mod}}}{\partial S_0}\right) \\ \sum\frac{1}{\sigma^2}\left(\frac{\partial S_{\mathrm{mod}}}{\partial T_2'}\right)\left(\frac{\partial S_{\mathrm{mod}}}{\partial T_2}\right) & \sum\frac{1}{\sigma^2}\left(\frac{\partial S_{\mathrm{mod}}}{\partial T_2'}\right)^2 & \sum\frac{1}{\sigma^2}\left(\frac{\partial S_{\mathrm{mod}}}{\partial T_2'}\right)\left(\frac{\partial S_{\mathrm{mod}}}{\partial S_0}\right) \\ \sum\frac{1}{\sigma^2}\left(\frac{\partial S_{\mathrm{mod}}}{\partial S_0}\right)\left(\frac{\partial S_{\mathrm{mod}}}{\partial T_2}\right) & \sum\frac{1}{\sigma^2}\left(\frac{\partial S_{\mathrm{mod}}}{\partial S_0}\right)\left(\frac{\partial S_{\mathrm{mod}}}{\partial T_2'}\right) & \sum\frac{1}{\sigma^2}\left(\frac{\partial S_{\mathrm{mod}}}{\partial S_0}\right)^2 \end{bmatrix}^{-1}$$

$$=\begin{bmatrix} S_{TT} & S_{TP} & S_{TS} \\ S_{PT} & S_{PP} & S_{PS} \\ S_{ST} & S_{SP} & S_{SS} \end{bmatrix}^{-1}$$

[7-14]

From the diagonal components of the covariance matrix, the errors in T_2, T_2' and S_0 can be calculated:

$$\sigma_{T2}^2 = -\frac{S_{PP}S_{SS} - S_{PS}S_{SP}}{-S_{ST}S_{TP}S_{PS} + S_{ST}S_{TS}S_{PP} + S_{PT}S_{TP}S_{SS} - S_{PT}S_{TS}S_{SP} - S_{TT}S_{PP}S_{SS} + S_{TT}S_{PS}S_{SP}}$$

$$\sigma_{T2'}^2 = -\frac{S_{TT}S_{SS} - S_{ST}S_{TS}}{-S_{ST}S_{TP}S_{PS} + S_{ST}S_{TS}S_{PP} + S_{PT}S_{TP}S_{SS} - S_{PT}S_{TS}S_{SP} - S_{TT}S_{PP}S_{SS} + S_{TT}S_{PS}S_{SP}}$$

$$\sigma_{S0}^2 = \frac{S_{PT}S_{TP} - S_{TT}S_{PP}}{-S_{ST}S_{TP}S_{PS} + S_{ST}S_{TS}S_{PP} + S_{PT}S_{TP}S_{SS} - S_{PT}S_{TS}S_{SP} - S_{TT}S_{PP}S_{SS} + S_{TT}S_{PS}S_{SP}}$$

[7-15]

Similarly, errors in T_2* and S_0 can be calculated by forming a 2 x 2 covariance matrix and obtaining the diagonal components to find the errors in fitted T_2* and S_0. The chi-square merit function becomes:

$$\chi^2(T_2^*, S_0) = \sum\left(\frac{S_{\mathrm{mod}} - S_{measured}}{\sigma}\right)^2 \qquad \textbf{[7-16]}$$

For two parameters, the covariance matrix [C] is:

$$[C]=\begin{bmatrix} \sum \frac{1}{\sigma^2}\left(\frac{\partial S_{\mathrm{mod}}}{\partial T_2}\right)^2 & \sum \frac{1}{\sigma^2}\left(\frac{\partial S_{\mathrm{mod}}}{\partial T_2 *}\right)\left(\frac{\partial S_{\mathrm{mod}}}{\partial S_0}\right) \\ \sum \frac{1}{\sigma^2}\left(\frac{\partial S_{\mathrm{mod}}}{\partial S_0}\right)\left(\frac{\partial S_{\mathrm{mod}}}{\partial T_2 *}\right) & \sum \frac{1}{\sigma^2}\left(\frac{\partial S_{\mathrm{mod}}}{\partial S_0}\right)^2 \end{bmatrix}^{-1} \qquad \textbf{[7-17]}$$
$$=\begin{bmatrix} S_{TT} & S_{TS} \\ S_{ST} & S_{SS} \end{bmatrix}^{-1}$$

and so the errors in T_2* and S_0 are:

$$\sigma^2_{T2*} = -\frac{S_{SS}}{S_{TT}S_{SS} - S_{TS}S_{ST}} \qquad \textbf{[7-18]}$$
$$\sigma^2_{S0} = \frac{S_{TT}}{S_{TT}S_{SS} - S_{TS}S_{ST}}$$

To compare the results from methods A and B, the error in T_2 (σ_{T2}) and the error in T_2* (σ_{T2*}) were calculated for each method for different numbers of gradient echoes (M) and gradient echo spacing (ΔT) for TE = 50ms.

7.2.2.2 Sequence optimisation

By varying the scanning parameters, the errors in the fitted T_2 and T_2* were investigated for various numbers of gradient echoes (M) and differing TE and T_2 values using the covariance matrix method above. The maximum allowed gradient echo spacing (ΔT) for a given TE and M was used since the preliminary calculations showed this to yield the lowest error in T_2. Using method B, since this also yields T_2*, the echo time was optimised for different values of M, and the value of M was optimised for different values of TE. For the calculations, a 1 % random Gaussian noise was assumed but this was scaled for the bandwidth of the readout as described above. Two combinations of parameters were assumed for the brain at 7.0 T: T_2 = 50 ms, S_0 = 1 and either $T_2' = 250$ ms (long) or $T_2' = 100$ ms (short).

7.2.2.3 Phantom validation

This sequence has been calibrated at 3.0 T and 7.0 T using two spherical test phantoms, containing NaCl and 8 different physiological concentrations of agar and gadolinium ions between them (chapter 3). Measurements were made using a SENSE head coil. GESSE was implemented as a single slice sequence and the imaging parameters were 256 x 256 matrix with a 0.82 x 0.82 x 8 mm^3 voxel size. Six GESSE experiments with different timing parameters were performed on each scanner; timings are given in Table 7-1 and Table 7-2 below for 3.0 T and 7.0 T experiments respectively. Method B was used to obtain fitted T_2 values for each experiment and a mean T_2 for each quadrant calculated.

	Exp 1	Exp 2	Exp 3	Exp 4	Exp 5	Exp 6
# gradient echoes	31	21	31	31	21	15
gradient echo spacing (ms)	1.46	1.47	1.46	1.46	1.5	1.51
TE (ms)	55	55	65	55	65	55
TR (ms)	3000	3000	3000	4000	4000	3000
Imaging time (mins)	3	4	3	4	6	4

Table 7-1: Imaging and timing parameters at 3.0 T for phantom GESSE experiments.

	Exp 1	Exp 2	Exp 3	Exp 4	Exp 5	Exp 6
# gradient echoes	31	21	31	31	21	15
gradient echo spacing (ms)	0.84	0.84	0.84	0.84	0.84	0.85
TE (ms)	40	40	50	40	50	40
TR (ms)	3000	3000	3000	4000	4000	3000
Imaging time (mins)	3	2	3	4	3	3

Table 7-2: Imaging and timing parameters at 7.0 T for phantom GESSE experiments.

Gold standard measurements (chapter 3) were made with a single slice, single shot spin echo EPI sequence to measure T_2, acquired with $TR > 5T_1$. Imaging parameters were 256 x 256 matrix with a 1.17 x 1.17 x 10 mm^3 voxel size and data was acquired for 20 different echo times (3.0 T: 60 – 500 ms, 7.0 T: 30 –

200 ms). Data was fitted using a weighted linear logarithmic fit to obtain a fitted T_2 value for each quadrant, taking into account the effect of noise. Two data sets were acquired using this technique and a mean of the fitted T_2 values taken.

7.2.2.4 In vivo measurements

Brain

The first measurements of T_2 in deep grey structures obtained at ultra-high field have been made here. Eight healthy subjects (6 male, 2 female, mean age = 38 years, range 23-64 years) were scanned with a Philips Achieva 7.0 T scanner using the GESSE sequence. Imaging parameters were number of slices = 9, slice gap = 1.5 mm, slice order descending, 256 x 256 matrix, 0.81 x 0.81 x 3 mm^3 voxel size. Timing parameters were TR = 1000 ms, TE = 55 ms, gradient echo spacing (ΔT) = 1.43 ms and number of gradient echoes (M) = 31.To improve SNR, NSA = 3 was used and the sequence performed twice then averaged and motion corrected together giving a total imaging time of 16 minutes. Three of the male subjects (mean age = 26 years, range 24-27 years) were also scanned on the 3.0 T Philips Achieva MRI scanner using a SENSE head coil (body transmit coil). The same imaging parameters were used as for the 7.0 T except NSA = 2 was used, and again two data sets were obtained then averaged and motion corrected together giving a total imaging time of 8 minutes. The two sets of images were co-registered and the data was fitted for T_2 using method A. Regions of interest were drawn using Analyze® software (Mayo Foundation, USA). Two different sets of slices were acquired to cover the majority of the head, but analysis was focused on deep grey tissues.

Liver

In order to determine if it was feasible to use the sequence in the liver, a female volunteer (aged 25 years) was scanned using SENSE body coils, at 1.5 T and 3.0 T. To minimise breathing artifacts, breath triggering was used so that data was acquired between exhalation and inhalation; this increased scan

time. Scanning parameters were 9 slices with a slice gap of 4 mm, a 288 x 288 matrix with 1.39 x 1.39 mm^2 resolution (slice thickness 8 mm (1.5 T) and 7 mm (3.0 T)). Regions of interest were drawn using Analyze® software (Mayo Foundation, USA) and then fitted using method B (Powell algorithm).

	1.5 T	3.0 T
# gradient echoes	25	19
gradient echo spacing (ms)	1.60	1.13
TE (ms)	55	35
TR (ms)	882	3000

Table 7-3: Timing parameters for GESSE at 1.5 T and 3.0 T for liver imaging experiments.

7.2.3 Results

7.2.3.1 Fitting algorithms

Figure 7-6 shows the comparison between the errors obtained in the fitted T_2 values from methods A and B for different combinations of T_2 and T_2'. They are in excellent agreement for high values of M, but deviate more at lower values of M, with method A giving the lower errors. They show that the maximum achievable value of ΔT for a given TE and M should be used. The effect of altering the value of T_2' is negligible for these simulations.

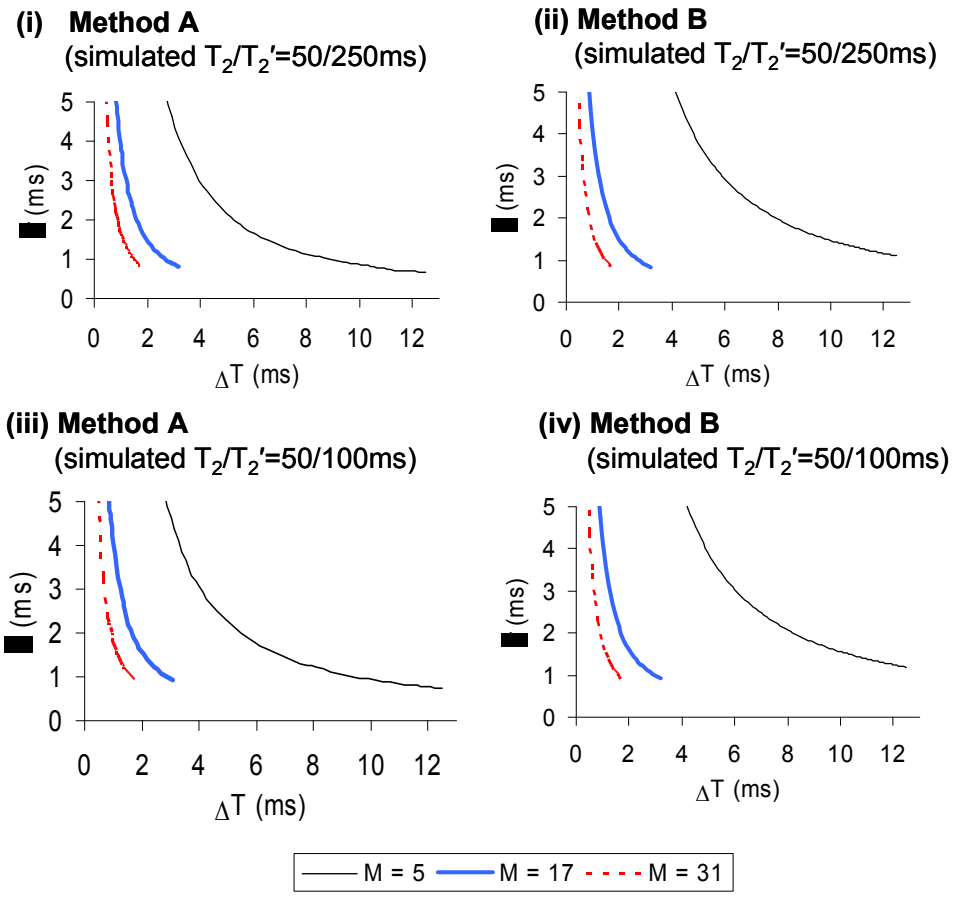

Figure 7-6: Error in T_2 (σ) obtained for T_2 = 50 ms and (i, ii) T_2' = 250 ms or (iii, iv) T_2' = 100 ms using (i, iii) method A and (ii, iv) method B for different gradient echo spacing, ΔT.

7.2.3.2 Sequence optimisation

Figure 7-7 shows the variation of the errors in T_2 and T_2* with TE (using method B) for short and long values of T_2'.

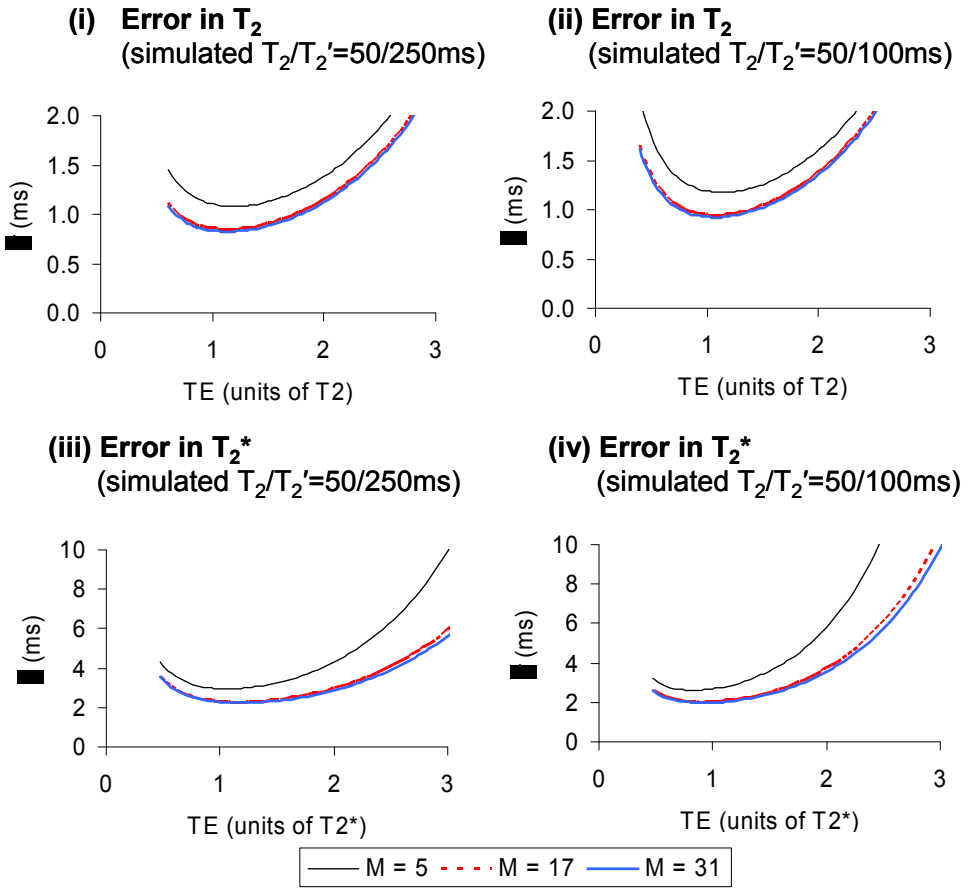

Figure 7-7: Effect of varying TE on the error (σ) in (i, ii) T_2 and (iii, iv) T_2* obtained at different values of M (5, 17, 31 echoes) using method B with data simulated for T_2 = 50 ms and (i, iii) T_2' = 250 ms or (ii, iv) T_2' = 100 ms.

The optimum TE was found to be relatively independent of the number of gradient echoes. In order to minimise the error in T_2, the TE should be approximately equal to the T_2 of the tissue; this agrees with results published by Yablonskiy *et al.* [21]. For the T_2/T_2' combinations chosen for this work, the optimum TEs were found to be:

TE = 56 ms (or $1.12T_2$) for T_2/T_2' = 50/250 ms (Figure 7-7i)
TE = 52 ms (or $1.04T_2$) for T_2/T_2' = 50/100 ms (Figure 7-7ii)

Overall the errors in T_2* are significantly larger than the errors on T_2, but similarly to T_2, in order to minimise the error in T_2*, the TE should be set to

approximately the value of T_2*. For the T_2/T_2' combinations chosen for this work, the optimum TEs were found to be:

TE = 46 ms (or 1.1T_2*) for $T_2/T_2'/T_2$* = 50/250/42 ms (Figure 7-7iii)
TE = 38 ms (or 1.15T_2*) where $T_2/T_2'/T_2$* = 50/100/33 ms (Figure 7-7iv)

Figure 7-8 shows the effect of increasing the number of gradient echoes (M) on the error obtained in T_2 and T_2* for different values of TE (using method B). The error in T_2 increased at small M, but for M > 10 there was little benefit of further increasing M. However, there is more benefit of increasing M when trying to minimise the error in T_2*.

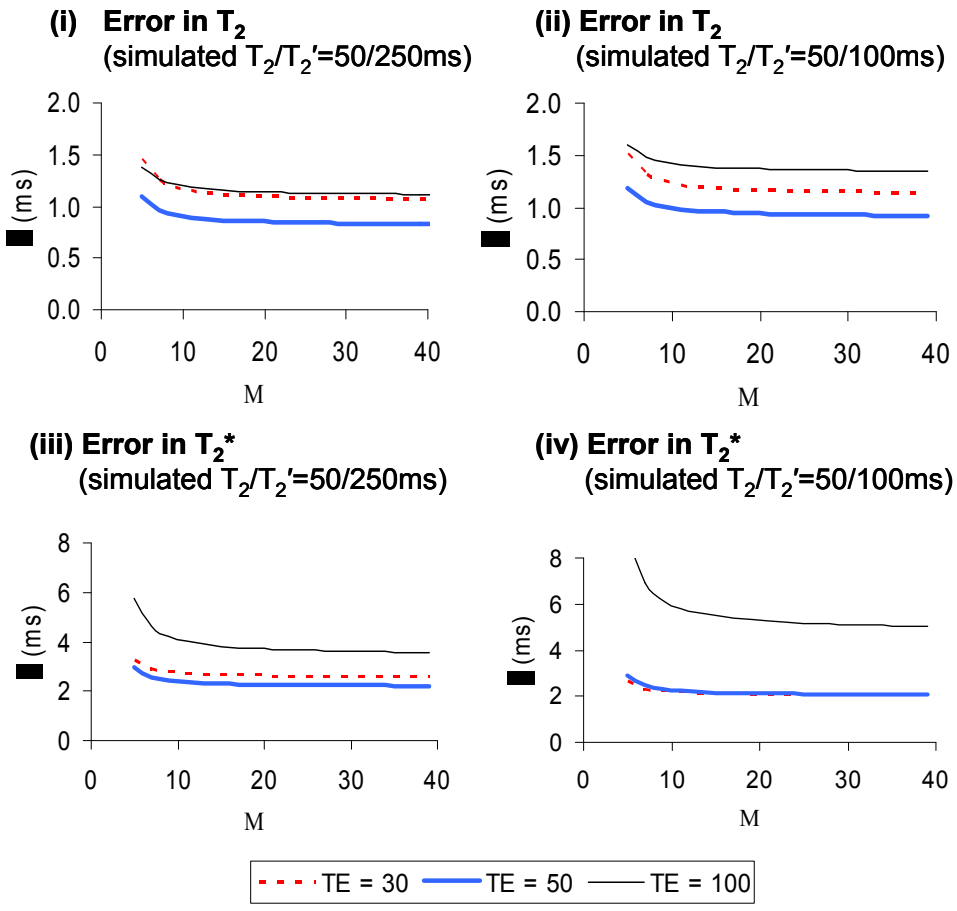

Figure 7-8: Effect of increasing M on the error (σ) in (i, ii) T_2 and (iii, iv) T_2* obtained at different TEs (30, 50, 100 ms) using method B with data simulated for T_2 = 50 ms and (i, iii) T_2' = 250 ms or (ii, iv) T_2' = 100 ms.

Therefore, to measure T_2/T_2' combinations at 7.0 T in the ratio 1:5 (T_2/T_2' = 50/250 ms), TE should be set to $1.12T_2$ and the number of gradient echoes (M) should be greater than 15. For a shorter T_2', so that T_2/T_2' is in the ratio 1:2 (T_2/T_2' = 50/100 ms) the TE should be set to $1.04T_2$ and the number of gradient echoes (M) should also be greater than 15. For minimising the errors in T_2*, the TE used should be shorter than the optimal TE for minimising T_2.

7.2.3.3 Phantom validation

The calibration curves for measuring T_2 using the GESSE sequence at 3.0 T and 7.0 T are shown in Figure 7-9 below, showing the method for fitting T_2 is correct. They show good reproducibility and the two sequences are in good agreement.

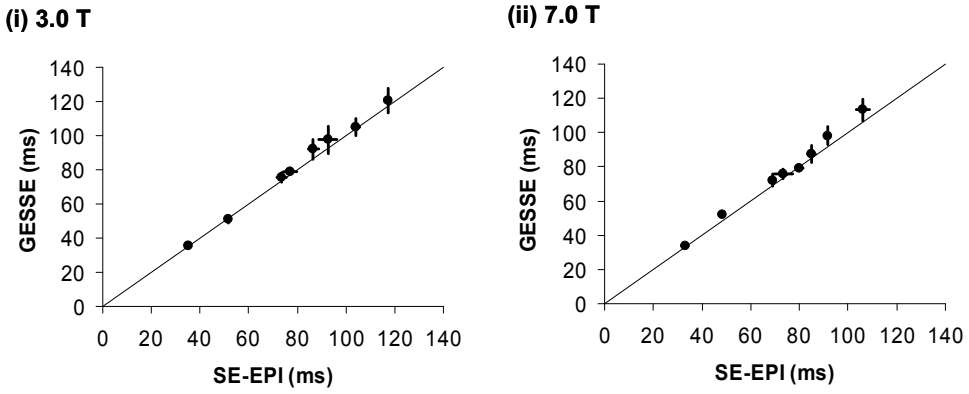

Figure 7-9: (mean ± std. dev.) Phantom validation for the GESSE sequence against SE-EPI at (i) 3.0 T and (ii) 7.0 T for measuring T_2. Six GESSE and two SE-EPI experiments were carried out. The identity line is shown.

7.2.3.4 In-vivo measurements

Brain

Figure 7-10 shows a T_2 map of the brain obtained at 7.0 T using the GESSE sequence and fitted using method A. Figure 7-11 shows T_2 values for white matter, grey matter and some deep brain structures fitted using method A. It

was observed that grey/white matter contrast was lost in the occipital regions in all subjects at both field strengths and therefore only regions showing good contrast were used here.

(i) 3.0 T

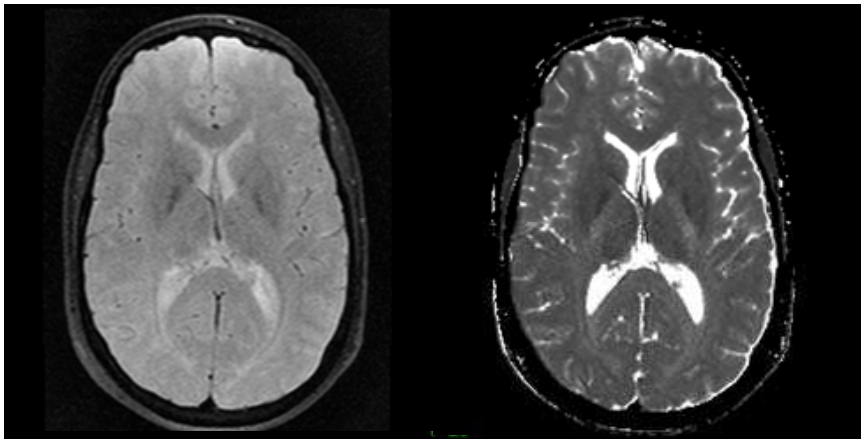

(ii) 7.0 T

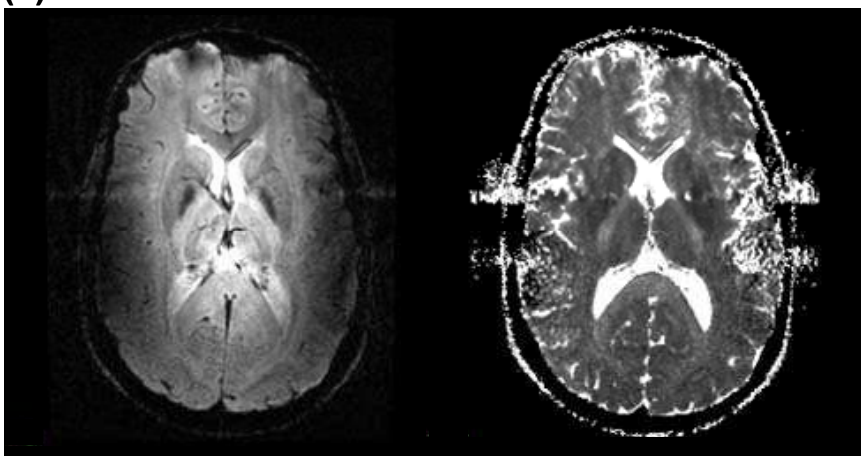

Figure 7-10: Central gradient echo corresponding to spin echo image of GESSE sequence and the T_2 map at (i) 3.0 T and (ii) 7.0 T.

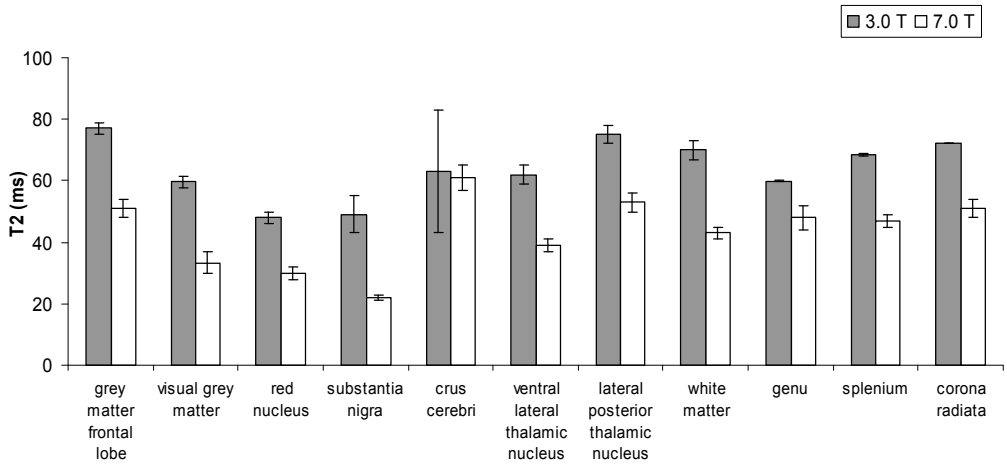

Figure 7-11: T_2 measurements of deep grey and cortical tissue at 3.0 T and 7.0 T fitted using method A.

Liver

Figure 7-12 shows T_2 maps of the liver obtained using the GESSE sequence at 1.5 T and 3.0 T. There are clearly motion artifacts due to the stomach and the vessels in the liver have caused some degradation to the maps due to blood flow, but it was possible to measure T_2 in the liver using this technique. At 1.5 T liver $T_2 = 64 \pm 3$ ms and at 3.0 T liver $T_2 = 37 \pm 3$ ms (mean ± std. dev.).

(i) 1.5 T

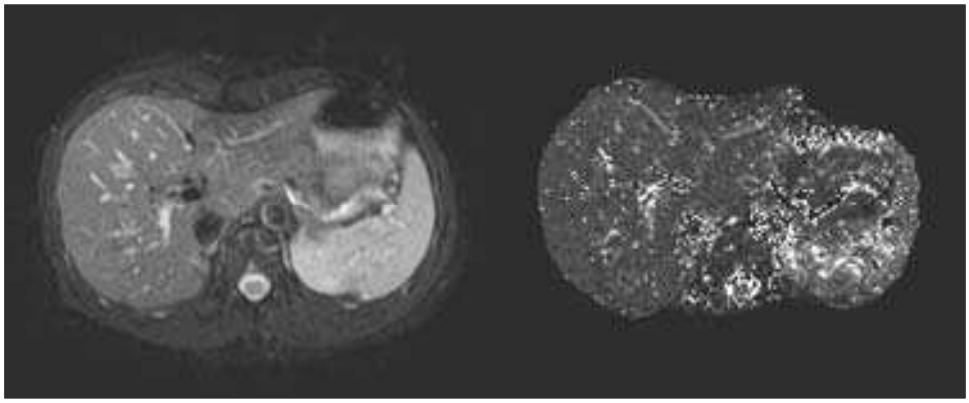

(ii) 3.0 T

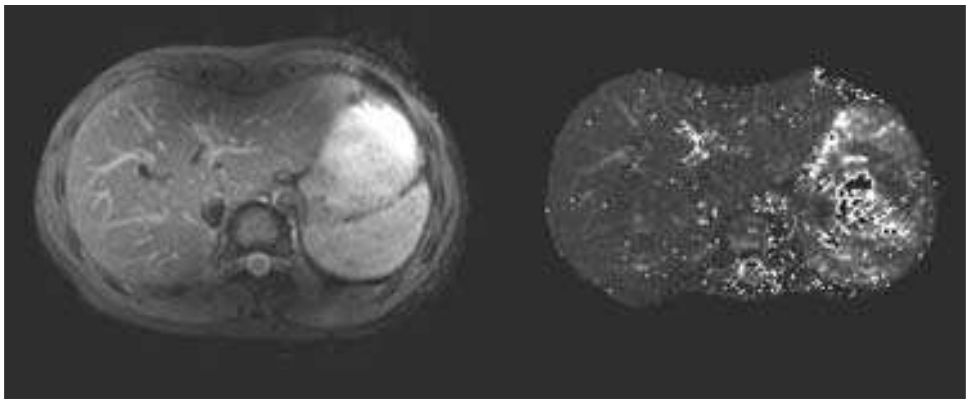

Figure 7-12: Central gradient echo corresponding to spin echo image of GESSE sequence and liver T_2 maps obtained using GESSE at (i) 1.5 T and (ii) 3.0 T.

7.2.4 Discussion

Previous fitting methods have just taken an average ratio, but method A employed in this work uses a weighted average so all the acquired data can be used. Methods A and B agree well for fitting T_2 when the data is over determined (large number of gradient echoes, M), but method A gives better results when the data is less well determined, which is expected since method A is analytical. However since the optimum fit occurred at large M (where the fits gave the same results), and since method B also gives the value of T_2' and hence T_2*, method B was used in the subsequent optimisations. The optimum TE was found to be relatively independent of the number of gradient echoes.

The error in T_2 increased at small M, but for M > 10 there was little benefit of further increasing M (Figure 7-8), although, the effect of ΔT on image quality would become important. To measure T_2/T_2' combinations at 7.0 T, for example in the ratio 1:5 (T_2/T_2' = 50/250 ms), TE should be set to $1.12T_2$ and the number of gradient echoes (M) should be greater than 15. For a shorter T_2', so that T_2/T_2' is in the ratio 1:2 (T_2/T_2' = 50/100 ms) the TE should be set to $1.04T_2$ and the number of gradient echoes (M) should also be greater than 15. For minimising the errors in T_2*, the TE used should be shorter than the optimal TE for minimising T_2. These results show the importance of optimising the scanning parameters according to the scanning region of interest (e.g. brain, liver) and generally it was found that the TE should be approximately equal to the T_2 of the tissue of interest.

This sequence is insensitive to RF pulse errors. Errors in either of the pulse flip angles will cause equal attenuation of all the images and will simply lead to a reduction in SNR. It is also insensitive to T_1 saturation since the echo time is kept constant, assuming that stimulated echoes are crushed by the imaging gradients. As implemented, GESSE had a lower SNR than EPI, but the EPI images were very distorted in parts of the brain at 7.0 T. However, a higher resolution was achieved using GESSE compared with EPI for similar imaging times.

The T_2 values measured in the quadrant phantoms using the GESSE sequence were in good agreement with those measured using the gold standard SE-EPI at both 3.0 T and 7.0 T indicating that this is a relatively simple method for measuring and calculating T_2. At long T_2s, the GESSE tended to measure a longer T_2 than the SE-EPI. It has been shown that the optimal TE should be approximately equal to the T_2 of interest, but the TEs chosen for the phantom experiments (7.0 T: TE = 40-50 ms, 3.0 T: TE = 55-65 ms) were quite short for measuring the long T_2 components of the phantom.

Under clinical imaging conditions standard gel phantoms exhibit mono-exponential T_2 with minimal diffusion effects. However, T_2 is a difficult parameter to measure, or even define, in-vivo because most tissues exhibit multi-exponential decay and voxels can contain components with very different T_2s so that if data is fitted to an apparent single exponential decay, the fitted T_2 depends on the echo times used and the T_1, T_2 or T_2* weighting of the imaging sequence. Transverse decay rate is enhanced by diffusion in any local field inhomogeneities (e.g. around venous vessels or iron deposits). This can be mitigated using multi-echo sequences with short interpulse spacing, but such sequences are often affected by errors due to RF pulse inhomogeneities. Consequently there is great variability in the T_2 values reported in the literature. The GESSE sequence is insensitive to RF pulse errors but is sensitive to diffusion; however, the gradients are refocused so this has little effect. All the T_2 values obtained *in vivo* agree well with published literature values [27, 28]. The loss of grey/white matter contrast in the occipital lobe of the T_2 maps has been previously reported [29, 30] and has been attributed to increased iron content in the occipital lobe. Inter-subject variability is less in white matter at 7.0 T which may be due to a more variable iron content in grey matter. The apparent sensitivity of this T_2 measurement to iron content suggests studying the variations in T_2 and T_2* in white matter tracts and comparing this with myelination levels and also the variations of T_2 and T_2* in deep grey structures in Parkinson's disease.

7.2.5 Conclusions

It is possible to accurately measure T_2 and T_2* simultaneously *in vivo* in the liver and brain at various field strengths using GESSE. Phantoms were used to calibrate T_2 values measured using GESSE against spin echo EPI. The maximum gradient echo spacing allowed should be used and the errors in the fitted T_2 values decrease when the number of gradient echoes increases, but there is a limit to which increasing the number of gradient echoes further

reduces the error in the fitted T_2. The signal is insensitive to RF pulse errors and any errors will simply lead to a reduction in SNR.

7.3 STUDY 1. Cross-field variations of T_2 in grey and white matter

7.3.1 Introduction

It is important to accurately know T_2 and T_2' at different field strengths when optimising sequences, particularly for choosing an optimal echo time that maximises blood oxygenation level dependent contrast in functional magnetic resonance imaging experiments [31]. In addition to this, there is considerable interest in evaluation of iron content in the human brain (chapter 7.1) and variations in T_2 with field strength may provide valuable information.

The aim of this study was to accurately measure T_2 and T_2' in the human brain at three different field strengths (1.5 T, 3.0 T and 7.0 T) in four subjects using the GESSE sequence and to compare the results with T_2 values measured using spin echo EPI.

7.3.2 Methods

Four healthy subjects (1 male, 3 female, mean age = 30 years, range 24 - 43 years) were scanned on Philips Achieva scanners at 1.5 T, 3.0 T and 7.0 T using the GESSE sequence to characterise the variation of T_2 and T_2' in the brain with field strength. A SENSE head coil was used with a 256 x 256 matrix and a 1 x 1 x 3 mm^3 voxel size. A single slice was imaged high in the brain to obtain regions of white and grey matter. Table 7-4 contains the parameters used for the GESSE sequence.

	1.5 T	3.0 T	7.0 T
# gradient echoes	31	31	25
gradient echo spacing (ms)	1.54	1.43	1.43
TE (ms)	55	55	50
TR (ms)	2000	2000	2000
Imaging time (mins)	8	3	3

Table 7-4: Imaging and timing parameters for GESSE used for cross-field experiments.

Single shot, single slice SE-EPI was again used as a gold standard to measure T_2 and compared with those measured using the GESSE sequence. Twelve echo times were measured in order to calculate T_2 at the different field strengths: 1.5 T 90 – 200 ms, 3.0 T 55 – 120 ms, 7.0 T 30 – 85 ms. The voxel size was 1.5 x 1.5 x 1.5 mm^3 and a TR > $5T_1$ was used. On a separate occasion, the same volunteers were scanned at 7.0 T using high resolution SE-EPI with a 1 x 1 x 1 mm^3 voxel and 64 x 64 FOV to determine if there were any partial volume effects in the low resolution SE-EPI. Eight different TE values were used between 42 and 150 ms. Two slices were acquired: one to include frontal grey matter regions and the second to include occipital grey matter regions. Method B (Powell algorithm) was used to fit data acquired using the GESSE sequence to obtain values for T_2 and T_2' and a linear log fit was used to calculate T_2 from the SE-EPI data using the same regions.

7.3.3 Results

Figure 7-13 shows images from a single volunteer obtained at each field strength using the GESSE and SE-EPI sequences. For the SE-EPI, images acquired at the shortest and longest echo times are shown and for the GESSE, the images obtained from the first and last gradient echoes are shown. Due to the nature of the sequences and the timings used, there is more T_2* weighting in the SE-EPI images and more T_2 weighting in the GESSE images.

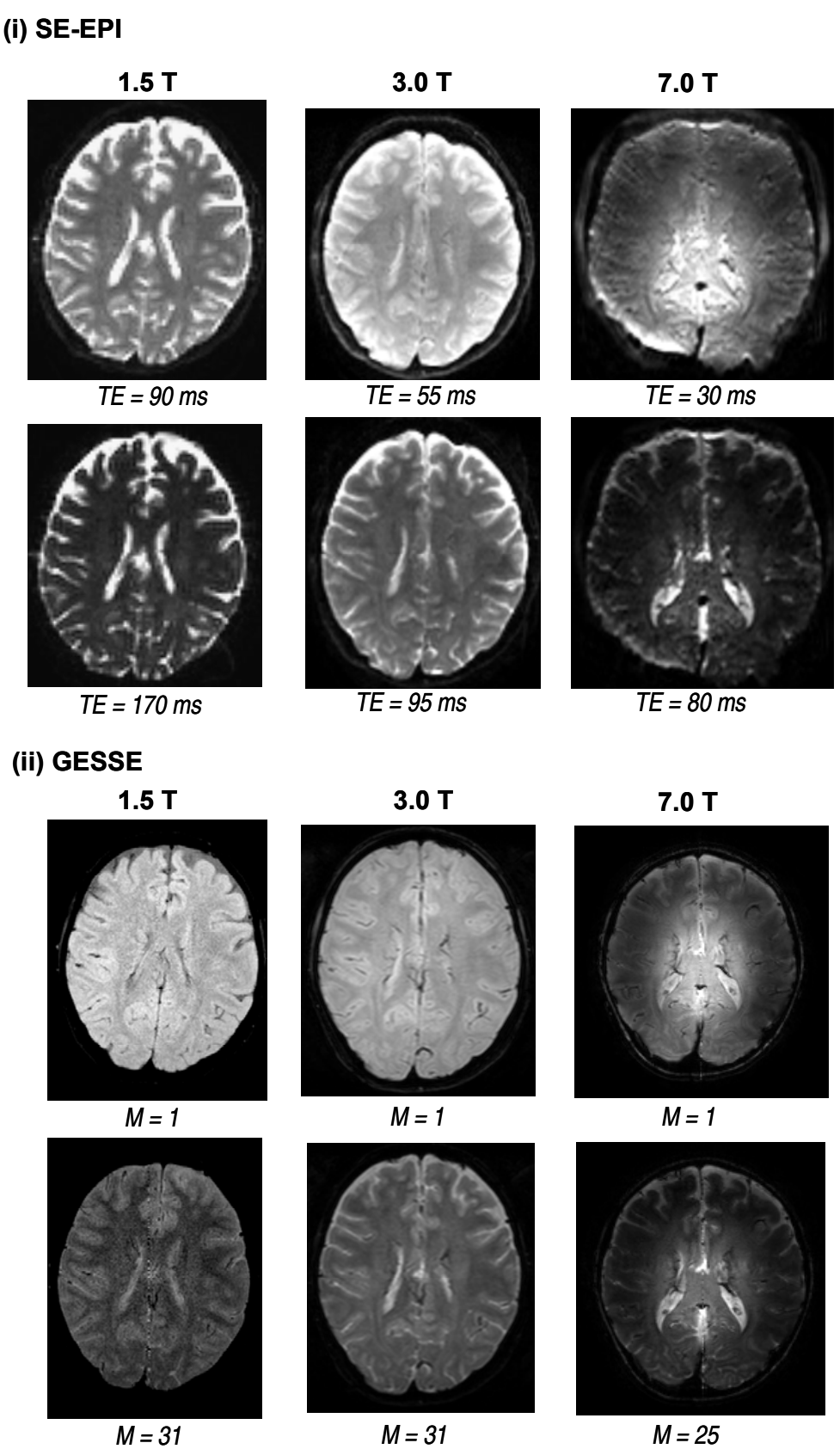

Figure 7-13: Images showing single slice data at short and long echo times for (i) spin echo EPI and (ii) GESSE data at 1.5 T, 3.0 T and 7.0 T.

Figure 7-14 shows T_2 values calculated using GESSE and SE-EPI at each field strength in the white matter and in frontal and occipital grey matter. Frontal grey matter has a longer T_2 than white matter and white matter has a longer T_2 than occipital grey matter. This grey matter variation is consistent with the literature [29, 30]. The relationship between the three field strengths is apparently linear for GESSE ($R^2 > 0.99$ for all regions), whereas the relationship between the field strengths is apparently exponential for the SE-EPI ($R^2 > 0.97$ for all regions). Figure 7-14iii shows an apparently exponential relationship between T_2' and field strength so maybe the T_2 obtained using SE-EPI contains T_2' contributions. To determine if there were any partial volume effects contributing to the differences between GESSE and SE-EPI, high resolution SE-EPI was compared with standard SE-EPI and GESSE at 7.0 T (Figure 7-14iv). The T_2 values obtained using the high resolution spin echo EPI sequence and different echo time GESSE sequences agreed with those obtained using the standard SE-EPI and GESSE sequences (to within the standard deviation quoted) for the white matter and the frontal grey matter. However, there is a difference in the occipital grey matter. The GESSE and high resolution SE-EPI are in agreement, but the standard SE-EPI measures a longer T_2.

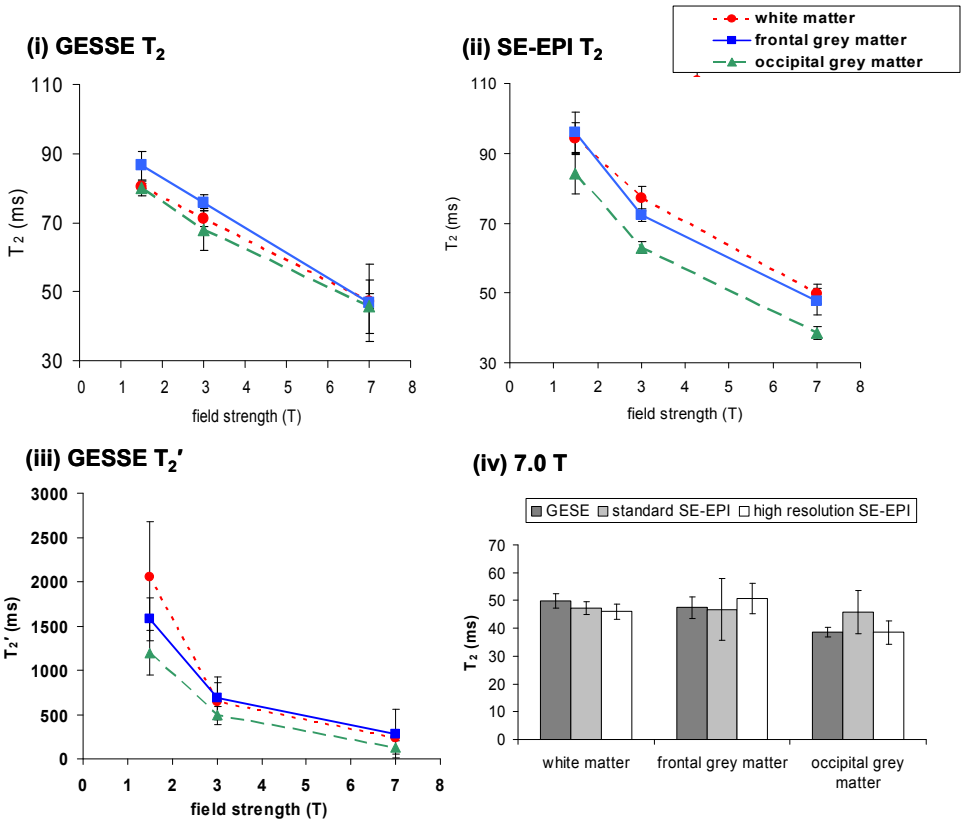

Figure 7-14: (mean ± std. dev.) Relaxation times of white matter and grey matter (frontal and occipital): (i) cross-field T_2 using GESSE, (ii) cross-field T_2 using SE-EPI, (iii) cross-field T_2' using GESSE and (iv) T_2 measured at 7.0 T using GESSE, standard and high resolution SE-EPI.

It was observed that grey/white matter contrast in the images was lost at the back of the head in all subjects at 7.0 T, due to an apparent drop in grey matter T_2. This explanation is consistent with the change in T_2' between different regions of grey matter given in Figure 7-14iii.

7.3.4 Discussion

GESSE and SE-EPI are insensitive to RF pulse errors and have long echo times making them more sensitive to longer T_2 components and any local field inhomogeneities. The GESSE and SE-EPI results given here generally agree well, except for a tendency for EPI to measure longer T_2s than GESSE in the white matter, which would be expected due to the increased weighting

to long T_2s in spin echo EPI compared to GESSE and the CSF (cerebrospinal fluid) contribution to white matter in Virchow-Robin spaces which cannot be distinguished at the resolution used here. The T_2s measured using GESSE varied linearly with field strength whereas the T_2s measured using SE-EPI varied exponentially. Since the relationship between T_2' measured using GESSE and field strength was also exponential, this implies that the SE-EPI is also measuring T_2' contributions. The T_2 values measured at 7.0 T using high resolution spin echo EPI agreed well with those measured using GESSE and the standard spin echo EPI for the white and frontal grey matter. However, there was a discrepancy between the standard and high resolution SE-EPI for the occipital grey matter; the GESSE and high resolution SE-EPI agreed well. This indicates that partial volume effects are affecting the measured T_2s.

Although it was possible to measure T_2 at ultra high field in the brain using spin echo EPI, there were considerable distortions in the images obtained, especially at the rear of the head, which made it very difficult to distinguish between different regions of the brain. However, the GESSE images were not distorted, allowing for much clearer identification of brain anatomy. The variation of grey matter T_2 between anterior and posterior regions has been reported by other groups [29, 30] and this has been attributed to increased iron content at the rear of the brain.

7.3.5 Conclusions

Measurements of T_2 and T_2* relaxation times in the human brain were made at 1.5 T, 3.0 T and 7.0 T using the GESSE sequence. T_2 decreases with increasing field strength; the GESSE sequence suggested a linear relationship whereas the SE-EPI sequence suggested an exponential relationship. Measurements of T_2' suggested that the SE-EPI sequence contains T_2' contributions in addition to T_2.

The GESSE sequence is more suitable for measuring T_2 at ultra-high field compared with SE-EPI because the GESSE sequence does not suffer with distortions at the rear of the head. GESSE also has the advantage of simultaneously measuring T_2' in addition to T_2 without any additional scanning.

7.4 STUDY 2. Characterising T_2 and T_2* in white matter tracts at 7.0 T

7.4.1 Introduction

Myelin has a low water content, but contains amide groups which bind to water and alters T_2. T_2 and T_2* have been shown to vary between white matter tracts [32, 33], suggesting there may be correlations between relaxation times and myelin density or axonal structure. To date, there have been a number of MRI studies measuring myelin water at field strengths greater than 1.5 T (Laule 2004, Mackay 2004, Vavasour 1998). Recently, Laule *et al*. [19] correlated histological findings (luxol fast blue staining for myelin) with myelin water measured in multiple sclerosis (MS) brain samples using MRI at 7.0 T. They found that tissue contrast at 7.0 T was enhanced, compared with lower fields, due to the increase in achievable resolution or improved contrast and SNR given by the increased field strength.

It is important to know the structure of white matter tracts in healthy brains in order to know and understand the changes that occur due to disease. MRI has the advantage of being non-invasive, allowing patients to be diagnosed and then monitored over several years to study disease progression and development.

7.4.2 Aims

The aim of this study is to investigate the relationship between the relaxation times and known features of myelin density and axonal structure, by studying adjacent white matter tracts and comparing known differences in myelin density to the T_2 and T_2* relaxation times of these tracts.

7.4.3 Method

Eight healthy subjects (4 male, 4 female, mean age = 45, range 40-49 years) were scanned using the GESSE sequence on a Philips Achieva 7.0 T MRI scanner. The sequence parameters were 0.93 x 0.93 x 3 mm^3 voxel size, TE = 40 ms, TR = 1500 ms, gradient echo spacing (ΔT) = 1.16 ms, number of gradient echoes (M) = 31, number of slices = 18, total imaging time = 9 mins.

To obtain values for T_2 and T_2*, regions of interest (ROIs) were manually drawn using Analyze® software (Mayo Foundation, USA) for the internal capsule (IC), corticospinal tract (CST), anterior, middle and posterior regions of the corpus callosum CC (genu, CC_mid and splenium) and the internal and external sagittal stratum (ISS and ESS) (Figure 7-15).

Statistics analysis was carried out to compare differences between regions. Data was tested for normality (Shapiro-Wilk test) and if data were normal then a paired student t-test was used, but for non-normal data, a Wilcoxon paired test was used. Differences between male and female T_2 and T_2* were also tested for each region of interest. The data was assumed not to be normal because N was too small and so a Mann-Whitney test was used. Data was Bonferroni corrected for multiple comparisons and a significance level of $p < 0.05$ was assumed.

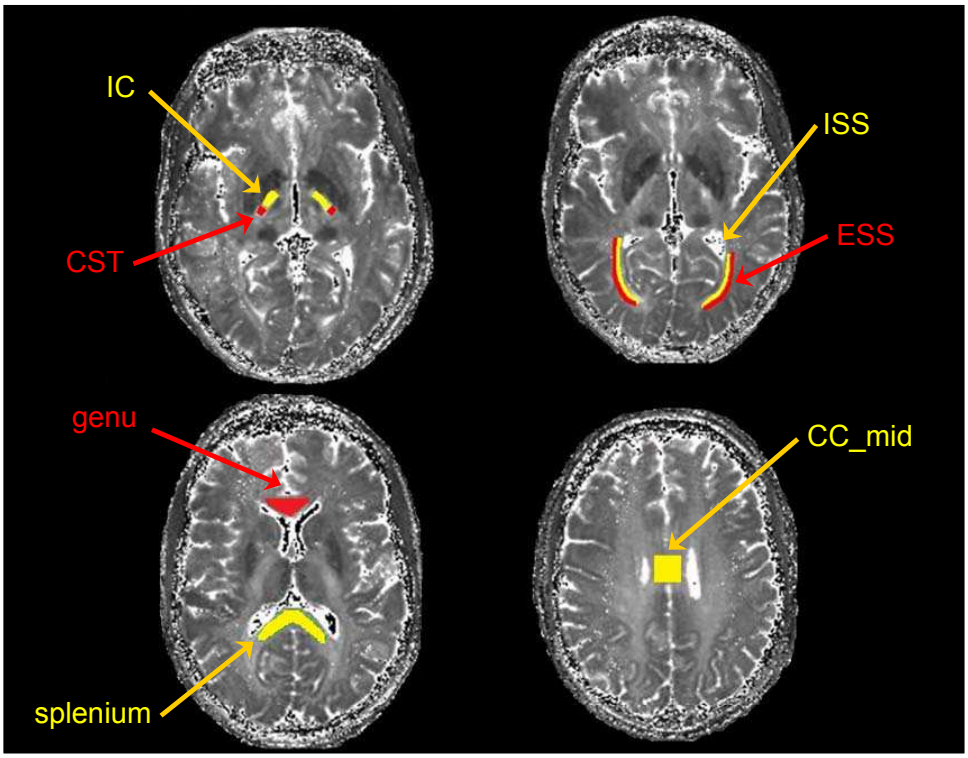

Figure 7-15: T_2 maps showing the regions of interest drawn to obtain relaxation times. (abbreviations: IC = internal capsule, CST = corticospinal tract, ISS = internal sagittal stratum, ESS = external sagittal stratum, CC_mid = central corpus callosum)

7.4.4 Results

Figure 7-16 shows T_2 and T_2* relaxation times of white matter tracts in the brain at 7.0 T for eight volunteers. The results are also plotted as individual subject (Figure 7-18) and differences (Figure 7-17) in T_2 and T_2* to allow comparisons of regions of known differences in histological studies. The T_2 was found to be longer in the corticospinal tract compared with the internal capsule ($p = 0.0449$, paired t-test), and the T_2 and T_2* are longer in the external sagittal stratum compared with the internal sagittal stratum (T_2 $p = 0.0073$ paired t-test, T_2* $p = 0.0078$ Wilcoxon paired test). In the corpus callosum, the T_2 of the genu was shorter than the middle of the corpus callosum ($p = 0.0114$, paired t-test) and shorter than the splenium ($p = 0.0243$, paired t-test). The T_2* was significantly shorter in the genu compared with the top of the corpus callosum ($p = 0.0405$, paired t-test) but not significantly

different between the genu and the splenium (p = 0.123, paired t-test). There was no significant difference in T_2 or T_2* between the splenium and the top of the corpus callosum (p >> 0.05, paired t-test). The T_2 and T_2* are significantly longer in the external sagittal stratum (T_2 p = 0.0073 paired t-test, T_2* p = 0.0078 Wilcoxon paired test). There was a significant difference found between male and female T_2 and T_2* in the top of the corpus callosum (T_2 and T_2* p = 0.0286, Mann-Whitney) with the females had significantly longer T_2 and T_2* values (Figure 7-19).

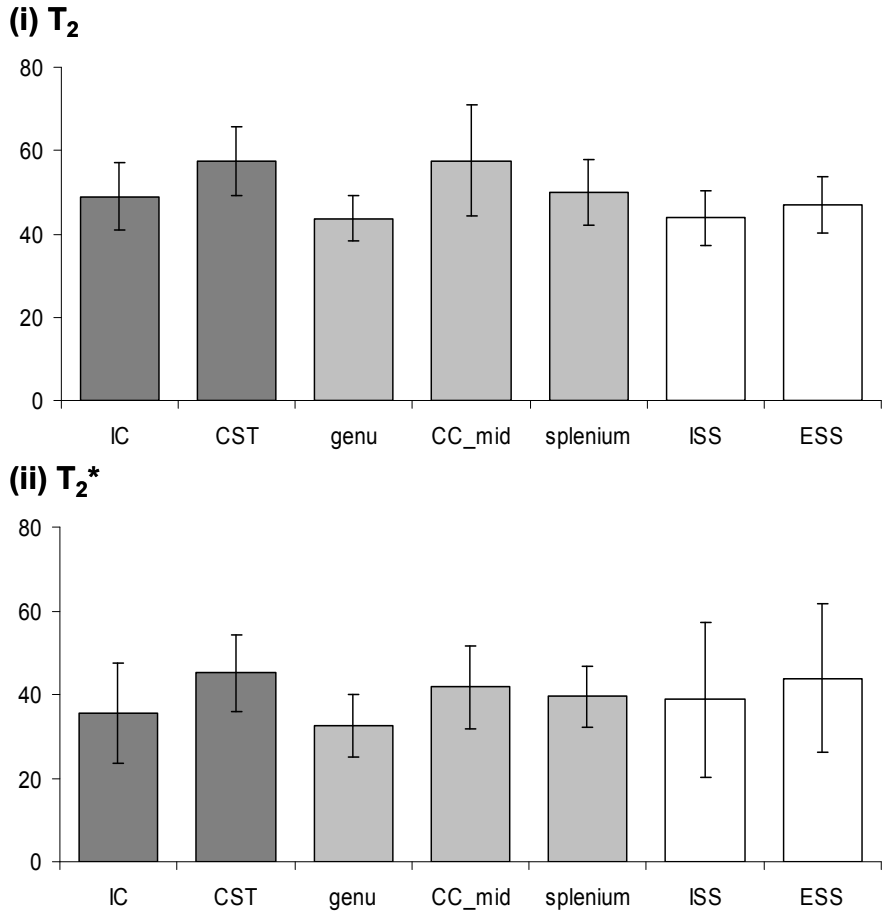

Figure 7-16: (mean ± std. dev., in ms) (i) T_2 and (ii) T_2* values of white matter tracts. (abbreviations: IC = internal capsule, CST = corticospinal tract, CC_mid = central corpus callosum, ISS = internal sagittal stratum, ESS = external sagittal stratum).

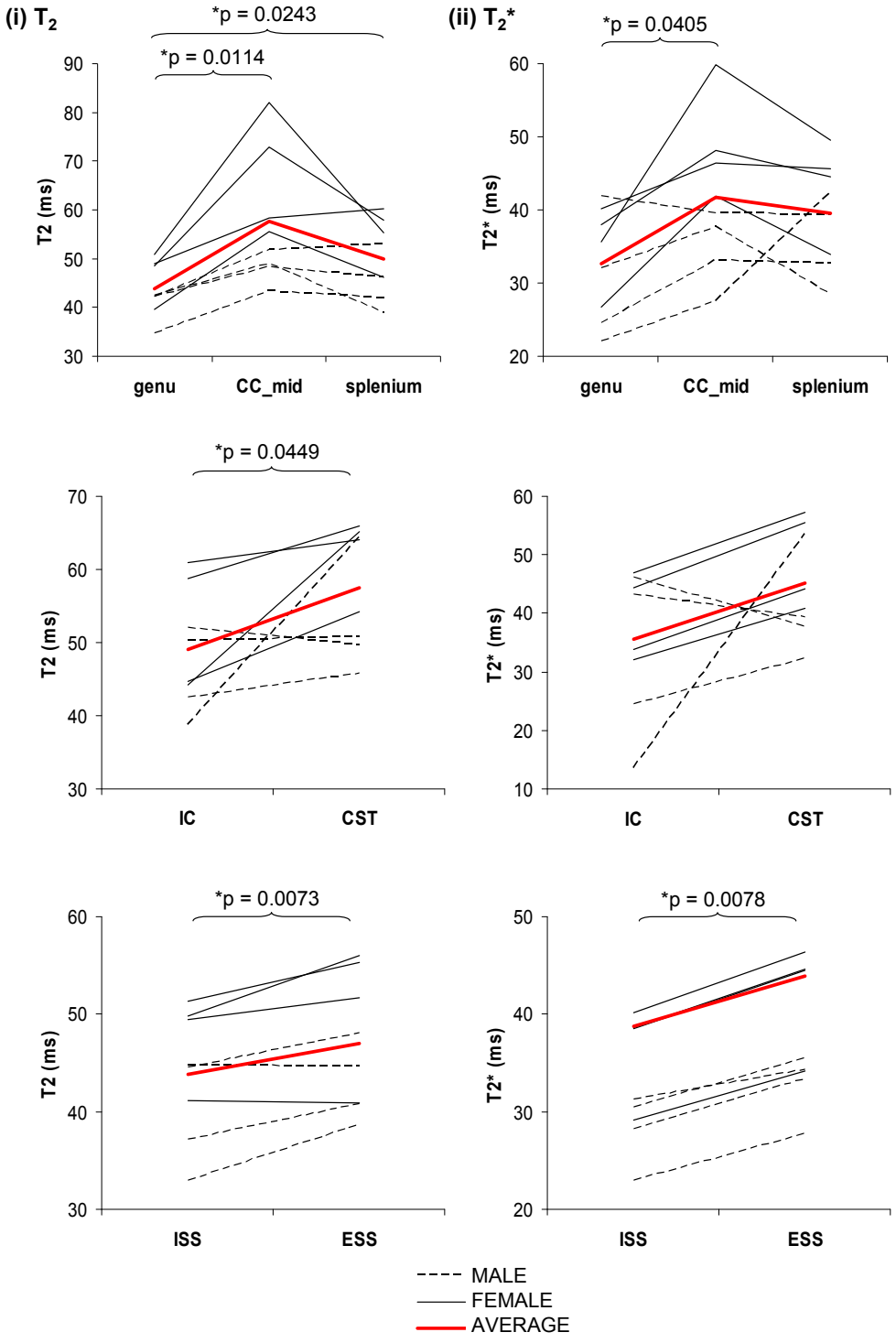

Figure 7-17: (mean ± std. dev.) Individual (i) T_2 and (ii) T_2* values of neighbouring white matter tracts. Significant differences between neighbouring tracts are highlighted. (abbreviations: IC = internal capsule, CST = corticospinal tract, CC_mid = central corpus callosum, ISS = internal sagittal stratum, ESS = external sagittal stratum)

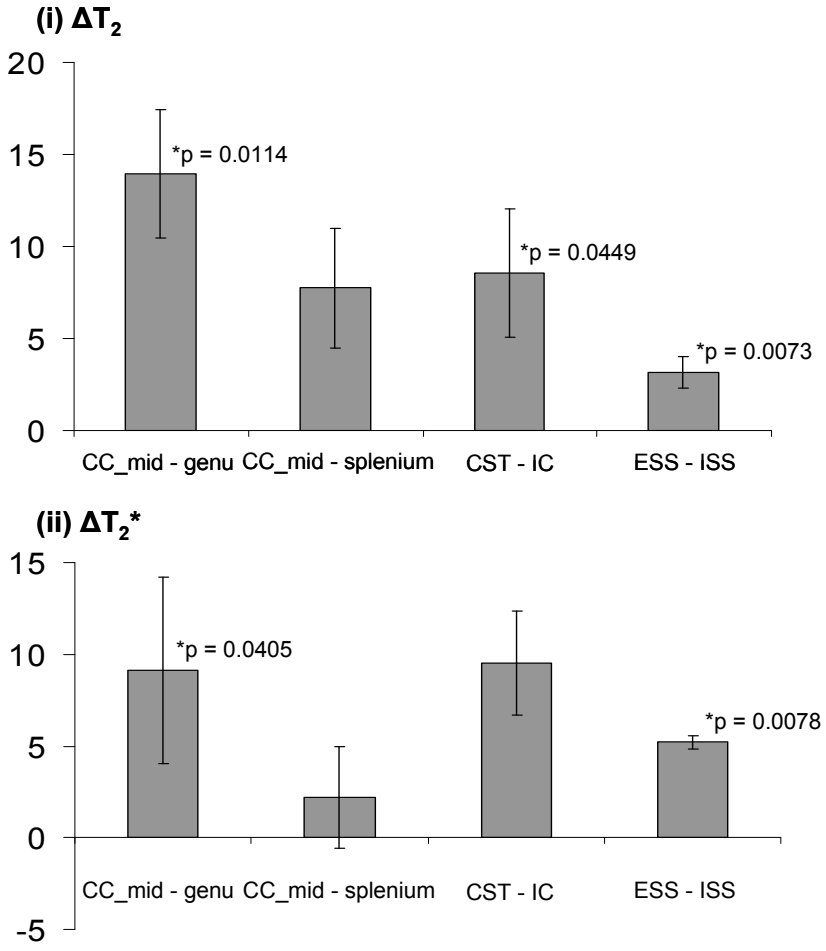

Figure 7-18: (mean ± SEM, in ms) Differences in (i) T_2 and (ii) T_2* relaxation times between neighbouring white matter tracts. Significant differences are highlighted. (abbreviations: IC = internal capsule, CST = corticospinal tract, CC_mid = central corpus callosum, ISS = internal sagittal stratum, ESS = external sagittal stratum)

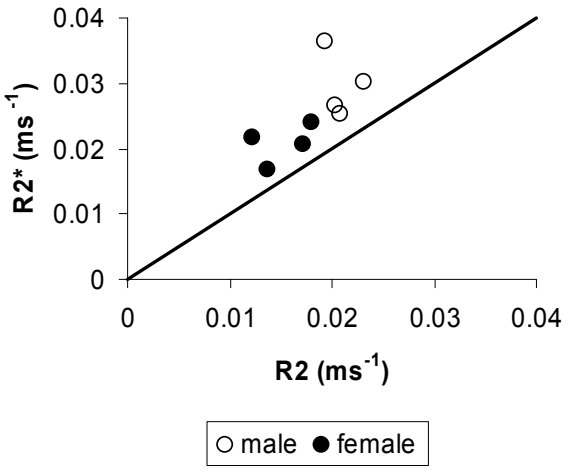

Figure 7-19: Individual subject R_2 and R_2* comparison in the middle of the corpus callosum (CC_mid) for male and female subjects. The line of identity is shown; the deviation from this line will give R_2'.

7.4.5 Discussion

The variation in white matter T_2* between tracts that has recently been reported [33, 34] is also visible in T_2 data presented here, in agreement with the neuroradiological literature [32]. In fact the T_2 maps (Figure 7-15) are strikingly similar to myelin stain images [32]. The precise origin of the variation of T_2 and T_2* is not known. Theoretically, white matter T_2 could depend on myelin content, fibre structure (axonal calibre/surface area), and iron content. Also, the magic angle effect [35] associated with fibre direction relative to the main magnetic field could be a potential factor affecting T_2 and T_2*.

Myelin is known to vary across cerebral white matter regions. Water bound to myelin has a shortened T_2 and T_2* so in heavily myelinated fibres there will be a reduction in signal intensity. The corticospinal tract and external sagittal stratum are heavily myelinated tracts [36] but have long T_2*s, which suggests that myelin content may not be the primary determinant of T_2/T_2* in these particular tracts.

Myelin and axonal staining studies [36] demonstrated small axons, thin myelin sheaths and narrow spaces between axons within the internal sagittal stratum (short T_2 and T_2* in our data) and large axons, thick myelin sheaths and wide spaces between axons within the external sagittal stratum (long T_2 and T_2* in our data).

The differences in the corpus callosum relaxation parameters could relate to known variations in fibre composition in the different regions [37]. The largest fibres are found in the middle and splenium of the corpus callosum (longer T_2 and T_2*), while the genu (short T_2 and T_2*) of the corpus callosum mostly consists of small diameter fibres. This indicates that T_2 could be related to fibre diameter.

Peters *et al*. [38] measured T_2* in grey and white matter at 7.0 T and their white matter T_2* results are very similar to those obtained for white matter here. Li *et al*. [34] have previously measured T_2* in white matter at 7.0 T, but the only region common with this study was the splenium. However, they did show that highly myelinated regions (e.g. splenium) had low T_2* values. Li *et al*. [33] have shown correlations between T_2*-weighted images at 7.0 T and diffusion tensor imaging (DTI) tractography at 3.0 T. Wakana et al. [39] give an extensive fibre tract atlas obtained by DTI at 1.5 T showing variations between tracts.

7.4.6 Conclusions

There is considerable variation in T_2 and T_2* between white matter tracts at 7.0 T, which may be related to fibre diameter, or possibly iron content. Correlation of these differences with histological data, MRI phase data or DTI may allow the relaxation mechanisms in white matter tracts to be clarified fully. Also, effects of orientation should be investigated to determine if there is any dependence in the measured T_2 and T_2* values.

7.5 STUDY 3. Investigating differences in T_2 of deep grey structures of healthy controls and in patients with Parkinson's Disease

7.5.1 Introduction

Brain iron and its role in brain function and disease has been of great physiological interest to many researchers over the last century. A review was completed by Haacke *et al*. [9] in 2005 of the attempts to measure brain iron and the potential to do so using MRI.

In certain regions of the brain, in particular deep grey matter structures, there are disproportionately large amounts of iron. Some MRI studies [40, 41] have

shown that some neurodegenerative disorders such as Parkinson's disease show excess iron deposition in specific areas of the brain (e.g. substantia nigra). By measuring brain iron deposition in normal individuals, this could help to understand the pathology of such disorders. MRI investigations have not always been consistent with post-mortem findings. Therefore, improved accuracy is required to assess iron deposition in the brain using MRI techniques. Although T_2 falls with increasing field strength and there is therefore less range in tissue T_2 variation at 7.0 T compared with 1.5 T or 3.0 T, it was anticipated that the ultra high field would provide an increase in sensitivity to the paramagnetic effects of iron.

7.5.2 Aims

To measure T_2, T_2* and T_2' in order to indicate iron levels at 7.0 T in the substantia nigra and other sub-cortical regions in patients with Parkinson's disease using the GESSE sequence.

7.5.3 Methods

Ten patients with Parkinson's disease (mean age 61 y, range 34 – 81 y) and nine healthy volunteers (mean age 54 y, range 34 – 69 y) were scanned on a Philips Achieva 7.0 T scanner using the GESSE sequence. Measurements were made using either a T/R head or a SENSE coil.

GESSE was implemented as a multislice sequence (number of slices = 9, slice thickness = 3 mm, slice gap = 1.5 mm, slice order descending). The imaging parameters were 256 x 256 matrix, 0.81 x 0.81 mm^2 pixel size. Timing parameters were TR = 1000 ms, TE = 55 ms, gradient echo spacing (ΔT) = 1.43 ms and number of gradient echoes (M) = 31. NSA = 3 was used to improve SNR giving a total imaging time < 9 minutes.

Five regions of interest were drawn manually using Analyze6® (Mayo Foundation, USA) as shown in Figure 7-20. Data was then fitted for relaxation times using the Powell algorithm (method B) as described previously. This included two regions for the substantia nigra: one including the total substantia nigra including the pars reticulata (SN*tot*), and a more refined region in the laterodorsal substantia nigra centered on the pars compacta (SN*ldi*). Also regions were drawn for the dorsolateral putamen (dPUT), medial globus pallidus (Pall*med*) and the red nuclei (RN).

Statistical analysis was performed to compare regions between healthy volunteers and Parkinson's patients. A Shapiro-Wilk normality test was performed and then either an unpaired t-test (normal) or a Mann-Whitney test (not normal) to check for significant differences ($p < 0.05$).

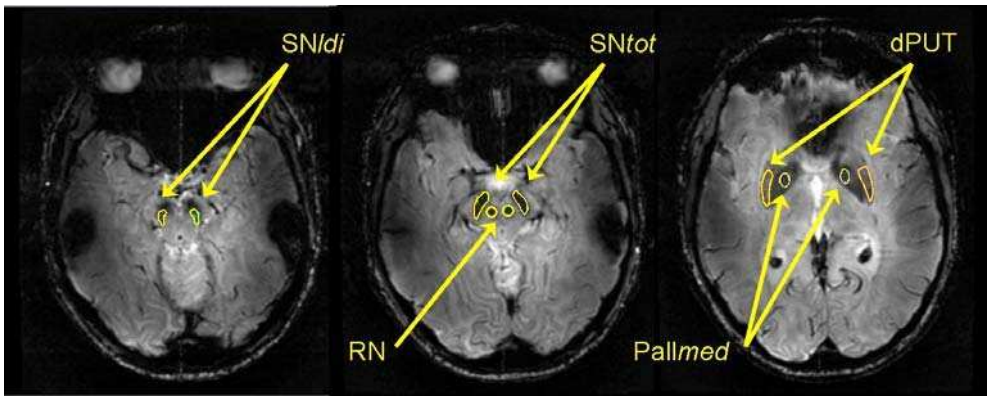

Figure 7-20: ROIs drawn to calculate T_2, T_2* and T_2'. (abbreviations: SN*ldi* = laterodorsal substantia nigra, SN*tot* = total substantia nigra, RN = red nucleus, Pall*med* = medial globus pallidus, dPUT = dorsolateral putamen)

7.5.4 Results

Figure 7-21 and Figure 7-22 show the values of T_2, T_2* and T_2' calculated in Parkinson's disease and in healthy volunteers measured from the ROIs shown in Figure 7-20. There were no significant differences between the patients and the healthy volunteers (Table 7-5), but there is a tendency to measure a longer T_2 in healthy volunteers compared with patients. There was a trend towards

significance for T_2 measured in the medial globus pallidus (Pall med) where p = 0.0831 (see Table 7-5 †). Figure 7-21ii shows some signal data for Parkinsons's patients for the laterodorsal substantia nigra. The two shortest and two longest T_2 values are shown. The decay curves for the longest T_2 are quite flat, whereas the shorter T_2 have a much higher initial signal and then decay to approximately the same signal as the long T_2 curves. It is interesting that for the short T_2 values, the refocusing of the spin echo does not occur at the centre of the acquisition as expected. Figure 7-23 shows correlations between R_2 and R_2* for healthy volunteers and Parkinson's patients; there was no significant difference. There were no trends between relaxation times and age in either the healthy volunteers or the Parkinson's patients.

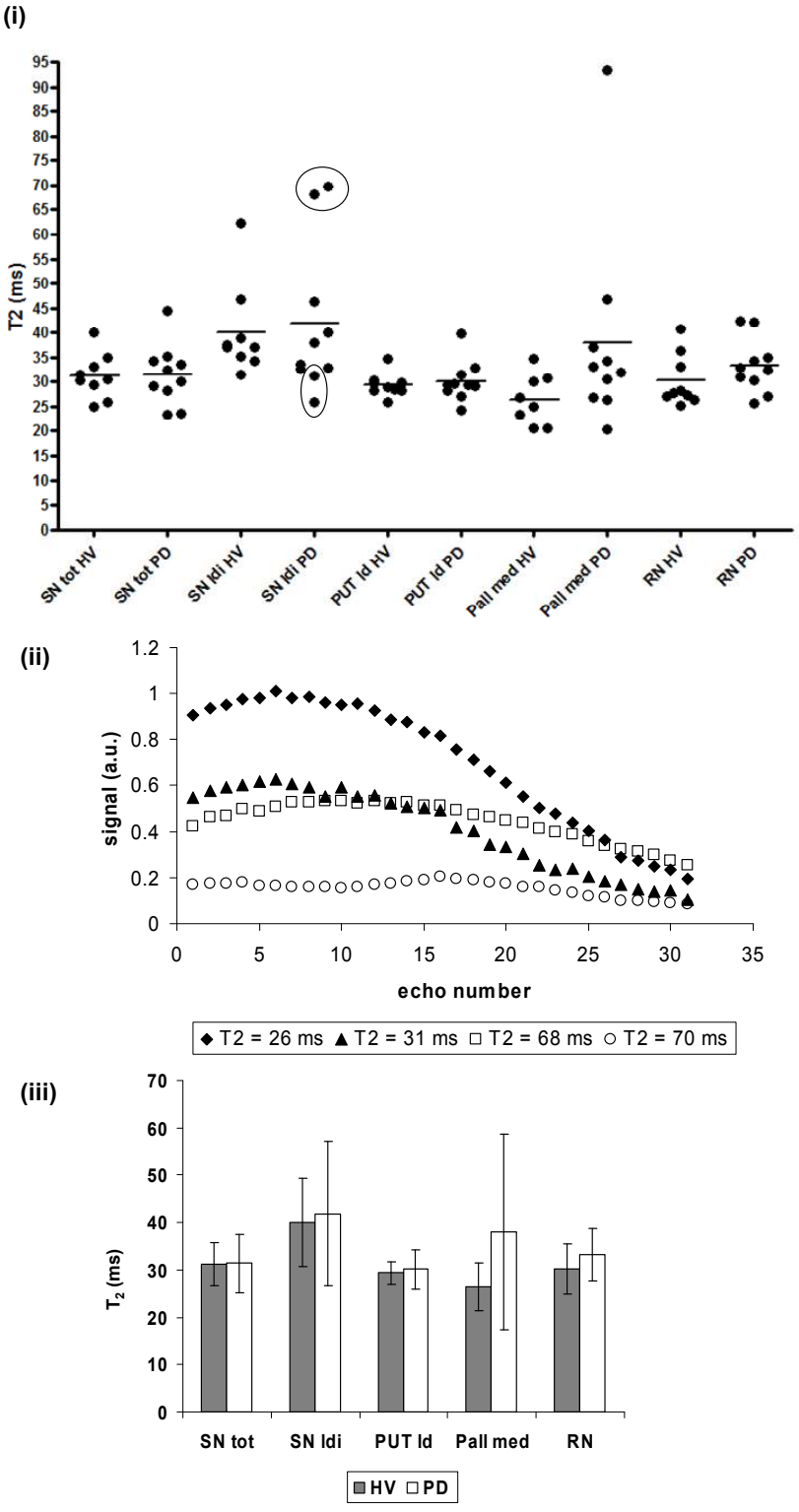

Figure 7-21: (i) Individual subject T_2 relaxation times calculated for ROIs in Parkinson's disease (PD) and healthy volunteers (HV), (ii) Signal decay for T_2s highlighted in individual subject data for SN ldi PD, (iii) Mean ± std. dev. relaxation times for T_2. (abbreviations: SN tot = total substantia nigra, SN ldi = laterodorsal substantia nigra, dPUT = dorsolateral putamen, Pallmed = medial globus pallidus, RN = red nucleus)

(i) T_2*

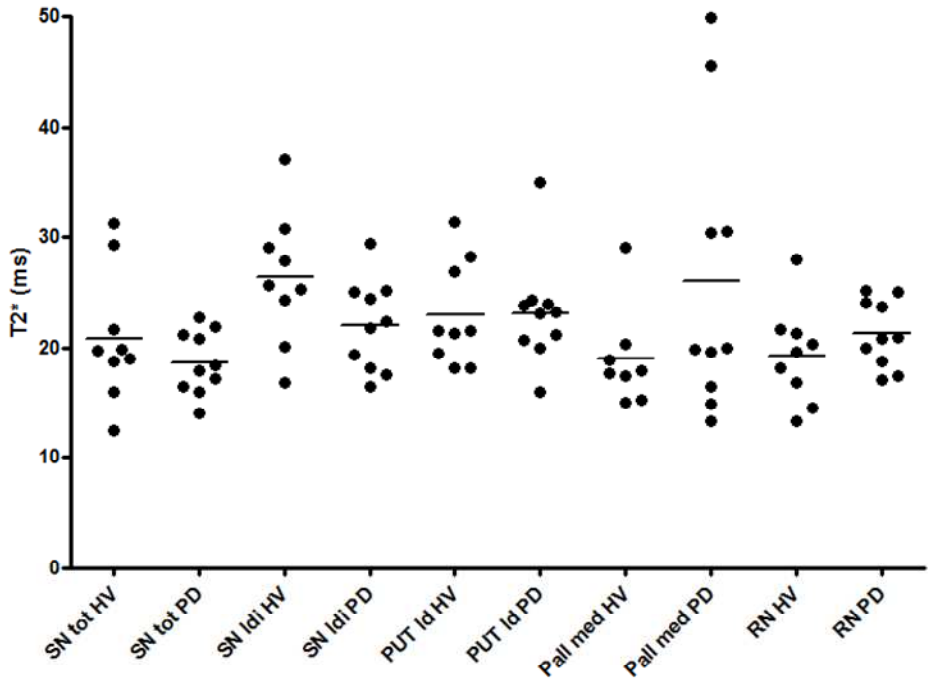
50
40
30
20
10
0
T2* (ms)
SN tot HV
SN tot PD
SN ldi HV
SN ldi PD
PUT ld HV
PUT ld PD
Pall med HV
Pall med PD
RN HV
RN PD

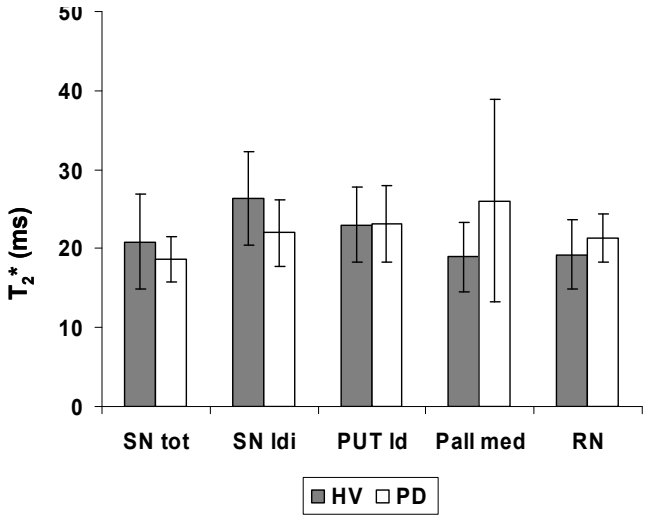
50
40
30
20
10
0
T2* (ms)
SN tot
SN ldi
PUT ld
Pall med
RN
HV
PD

(ii) T_2'

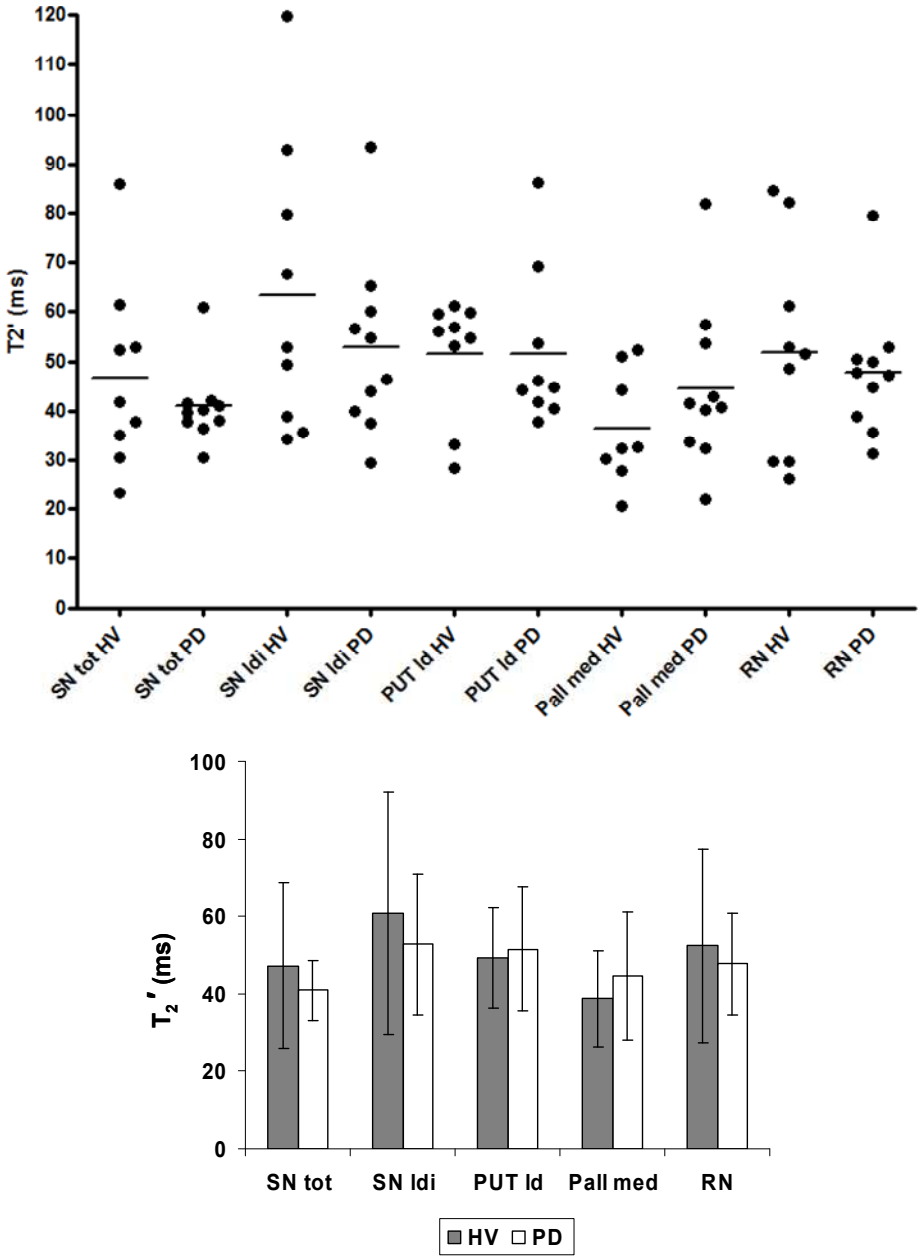

Figure 7-22: Individual subject and mean ± std. dev. relaxation times for (i) T_2* and (ii) T_2' calculated for ROIs in Parkinson's disease (PD) and healthy volunteers (HV). (abbreviations: SN tot = total substantia nigra, SN ldi = laterodorsal substantia nigra, dPUT = dorsolateral putamen, Pallmed = medial globus pallidus, RN = red nucleus)

ROI	T_2		T_2*		T_2'	
	Normal?	p value	Normal?	p value	Normal?	p value
SN tot	Y	0.9443	Y	0.3082	N	0.6607
SN ldi	N	0.7802	Y	0.0781	Y	0.3463
PUT ld	Y	0.6450	N	0.8421	N	0.5457
Pall med	N	0.0831 †	N	0.3154	Y	0.2479
RN	N	0.2775	Y	0.2539	Y	0.6252

Table 7-5: Statistical p-values comparing T_2, T_2* and T_2' in healthy volunteers and patients with Parkinson's disease. (abbreviations: SN tot = total substantia nigra, SN ldi = laterodorsal substantia nigra, dPUT = dorsolateral putamen, Pallmed = medial globus pallidus, RN = red nucleus)

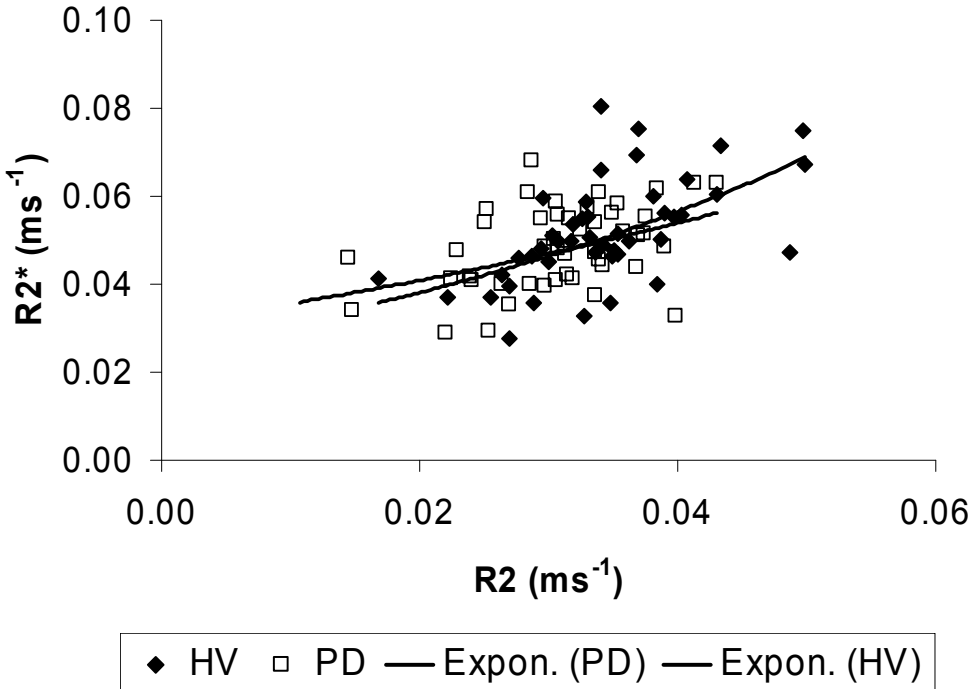

Figure 7-23: R_2 and R_2* correlation between healthy volunteers and Parkinson's patients. The Parkinson's data correlated linearly (r^2 = 0.3805) and the healthy volunteers correlated exponentially (r^2 = 0.2077). The line of identity (dotted) is shown and the deviation from this line indicates R_2'.

7.5.5 Discussion

There were no significant changes in T_2, T_2* or T_2' in the substantia nigra, or any other region, of patients with Parkinson's disease at 7.0 T. This was

surprising since the ultra-high field should have provided a high sensitivity to the iron content.

Other groups have studied differences in relaxation times at 1.5 T [42], 3.0 T [43] and 7.0 T [44] between healthy controls and Parkinson's patients. Graham *et al*. [42] and Wallis *et al*. [43] found that R_2* and R_2' were significantly higher in the substantia nigra in Parkinson's patients compared with the healthy controls. However, at 1.5 T, the putamen was found to have a shorter R_2' in the Parkinson's patients, but at 3.0 T R_2' was longer in the Parkinson's patients. At 7.0 T [44] there were no differences in R_2* between the two groups, except for a trend indicating shorter R_2* values in Parkinson's patients in the red nucleus, again suggesting that T_2* only partially represents tissue iron and that there must be other factors, such as magnetic susceptibility effects, which may contribute to the T_2*. There is a major difference in the numbers of patients and healthy volunteers scanned in this work and in the other studies. The 7.0 T studies (this work and [44]), have much fewer subjects than the studies at lower fields, which have 25 patients/14 controls at 1.5 T and 70 patients/10 controls at 3.0 T. This suggests that by increasing the number of subjects, and therefore increasing the power of the study, it would be possible to ascertain whether there actually are significant differences in T_2 or T_2* at 7.0 T between the two groups. The standard errors in the mean of the relaxation times measured in this work are comparable with the studies at lower fields. In fact, the errors are apparently highest for the 3.0 T study which had the highest number of subjects, indicating that there is a large variability between subjects.

The increase iron content seen post mortem and in transcranial sonography [45] may not translate into enhanced relaxation as assumed and maybe MRI of *in vitro* brains should be investigated. It is possible that the iron showing up in the post mortem studies could be in a non-paramagnetic state and therefore the change in iron levels has no effect on the MRI data and the measured T_2. To infer that tissue iron affects relaxation time is difficult since

two assumptions must be made: tissue iron is mainly stored as ferritin and that iron concentration is the dominant factor governing relaxation behaviour. In addition to this, reduced nigral ferritin levels have been reported in Parkinson's brains [46], which means these assumptions may be wrong.

7.5.6 Conclusions

In conclusion, despite the expected increased iron sensitivity of ultra-high field MRI, there were no significant changes in relaxation times in any of the regions. The results support the notion that iron concentrations cannot be directly inferred from relaxation time measurements of diseased tissue, even at ultra-high field.

7.6 FUTURE WORK

It was interesting to see that in some data, the spin echo did not always refocus in the centre of the acquisition window. This could be due to static dephasing and should be investigated using simulations.

The preliminary liver T_2 maps obtained using the GESSE sequence were very promising, but further development is required to improve the signal to noise ratio without significantly increasing scanning time. It is particularly challenging to apply this sequence in the abdomen since breathing artifacts degrade the images, so determining the optimum method for scanning during the breath cycle should be investigated.

The variations between white matter tracts could be combined with phase data obtained using MRI in order to further our understanding of the relationship between myelin density and relaxation mechanisms. This could also be combined with post mortem brain MRI scanning using the GESSE sequence at 7.0 T. Similarly, MRI phase data was also acquired for the

Parkinson's disease study and so this data should be compared with the relaxation data in order to determine if any further conclusions can be made.

There is some evidence to suggest that T_2 varies with age [47, 48], so as part of an attempt to achieve an understanding of how relaxation times vary in healthy volunteers, it would be interesting to measure T_2 in various different regions of the brain, in particular deep grey matter. The difference between male and female relaxation times is also worth pursuing.

7.7 References

1. Tropres, I., et al., *Vessel Size Imaging.* Mag. Res. Med, 2001. **45**: p. 397-408.
2. Prinster, A., et al., *Simultaneous Measurement of ΔR2 and ΔR2* in Cat Brain during Hypoxia and Hypercapnia.* Neuroimage, 1997. **6**: p. 191-200.
3. Kjolby, B.F., L. Ostergaard, and V.G. Kiselev, *Theoretical Model of Intravascular Paramagnetic Tracers Effect on Tissue Relaxation.* Mag. Res. Med, 2006. **56**: p. 187-197.
4. Kiselev, V.G. and S. Posse, *Analytical Model of Susceptibility-Induced MR Signal Dephasing: Effect of Diffusion in a Microvascular Network.* Mag. Res. Med, 1999. **41**: p. 499-509.
5. Yablonskiy, D.A. and E.M. Haacke, *Theory of NMR Signal Behaviour in Magnetically Inhomogeneous Tissues: The Static Dephasing Regime.* Mag. Res. Med, 1994. **32**: p. 749-763.
6. Tropres, I., et al., *Vessel size imaging using low intravascular contrast agent concentrations.* MAGMA, 2004. **17**: p. 313-316.
7. Tropres, I., et al., *In Vivo Assessment of Tumoral Angiogenesis.* Mag. Res. Med, 2004. **51**: p. 533-541.
8. Dennie, J., et al., *NMR Imaging of Changes in Vascular Morphology Due to Tumour Angiogenesis.* Mag. Res. Med, 1998. **40**: p. 793-799.

9. Haacke, E.M., et al., *Imaging iron stores in the brain using magnetic resonance imaging.* Mag. Res. Im., 2005. **23**: p. 1-25.
10. Schenck, J.F., *Magnetic Resonance imaging of brain iron.* J. Neurol. Sci., 2003. **207**(1-2): p. 99-102.
11. An, H. and W. Lin, *Impact of intravascular signal on quantitative measures of cerebral oxygen extraction and blood volume under normo- and hypocapnic conditions using an asymmetric spin echo approach.* Mag. Res. Med., 2003. **50**: p. 708-716.
12. Gossuin, Y., et al., *Nuclear magnetic relaxation dispersion of ferritin and ferritin like magnetic particle solutions: a pH-effect study.* Mag. Res. Med., 2001. **46**: p. 476-481.
13. Flynn, S.W., et al., *Abnormalities of myelination in schizophrenia detected in vivo with MRI, and post-mortem with analysis of oligodendrocyte proteins.* Mol. Psychiatry, 2003. **8**: p. 811-820.
14. Mueller, B.A., et al., *Comparison of in vivo MRI Methods for Examining White Matter Abnormalities in Schizophrenia.* Proc. 15th Annual Meeting of ISMRM, 2007: p. P2216.
15. Oakden, W., et al., *Quantitative T_2 Relaxation of White Matter Hyperintensities in Probable Alzheimer Patients.* Proc. 15th Annual Meeting of ISMRM, 2007: p. P2146.
16. Laule, C., et al., *Water content and myelin water fraction in multiple sclerosis. A T_2 relaxation study.* J. Neurol., 2004. **251**: p. 284-293.
17. Mackay, A., et al., *In vivo visualisation of myelin water in brain by magnetic resonance.* Mag. Res. Med, 1994. **31**(6): p. 673-677.
18. Vavasour, I.M., et al., *A comparison between magnetisation transfer ratios and myelin water percentages in normals and multiple sclerosis patients.* Mag. Res. Med, 1998. **40**(5): p. 763-768.
19. Laule, C., et al., *Myelin water imaging of multiple sclerosis at 7.0T: Correlations with histopathology.* Neuroimage, 2008. **40**: p. 1575-1580.

20. Talwalkar, J.A., et al., *Magnetic Resonance Imaging of Hepatic Fibrosis: Emerging Clinical Applications.* Hepatology, 2008. **47**: p. 332-342.
21. Yablonskiy, D.A. and E.M. Haacke, *An MRI Method for Measuring T2 in the Presence of Static and RF Magnetic Field Inhomogeneities.* Mag. Res. Med, 1997. **37**: p. 872-876.
22. An, H. and W. Lin, *Quantitative Measurements of Cerebral Blood Oxygen Saturation Using Magnetic Resonance Imaging.* J. Ce. Blood Flow Met., 2000. **20**: p. 1225-1236.
23. Powell, M.J.D., *Efficient method for finding minimum of function of several variables without calculating derivatives.* Computer Journal, 1964. **7**(2): p. 155-162.
24. Press, W.H., et al., *Numerical Recipes in C (Second Edition).* 1996: p. 412-420.
25. Taylor, J.R., *An Introduction to Error Analysis (Second Edition).* 1982: p. 181-226.
26. Press, W.H., et al., *Numerical Recipes in C (Second Edition).* 1996: p. 695-698.
27. Stanisz, G.J., et al., *T1, T2 Relaxation and Magnetisation Transfer in Tissue at 3T.* Mag. Res. Med, 2005. **54**: p. 507-512.
28. Gelman, N., et al., *MR Imaging of Human Brain at 3.0T: Preliminary Report on Transverse Relaxation Rates and Relation to Estimated Iron Content.* Radiology, 1999. **210**: p. 759-767.
29. Bartha, R., et al., *In Vivo $^{1}H_2O$ T_2^{+} Measurement in the Human Occipital Lobe at 4T and 7T by Carr-Purcell MRI: Detection of Microscopic Susceptibility Contrast.* Mag. Res. Med., 2002. **47**: p. 742-750.
30. Zhou, J., et al., *Inverse T_2 Contrast at 1.5 Tesla Betwen Gray Matter and White Matter in the Occipital Lobe of Normal Adult Human Brain.* Mag. Res. Med., 2001. **46**: p. 401-406.
31. Gowland, P.A. and R. Bowtell, *Theoretical optimization of multi-echo fMRI data acquisition.* Phys. Med. Biol., 2007. **52**: p. 1801-1813.

32. Curnes, J.T., et al., *MR imaging of compact white matter pathways.* AJNR, 1988. **9**(6): p. 1061-1068.
33. Li, T.Q., et al., *Mapping White Matter Fiber Tracts Using T2*-Weighted MRI at 7T.* ISMRM High Field Workshop Rome, 2008.
34. Li, T.-Q., et al., *Extensive heterogeneityin white matter intensity in high resolution T_2*-weighted MRI of the human brain at 7.0 T.* Neuroimage, 2006. **32**: p. 1032-1040.
35. Chappell, K.E., et al., *Magic Angle Effects in MR Neurography.* AJNR, 2004. **25**: p. 431-440.
36. Kitajima, M., et al., *MR Signal Intensity of the Optic Radiation.* AJNR, 1996. **17**: p. 1379-1383.
37. Aboitz, F. and J. Montiel, *One hundred million years of interhemispheric communication: the history of the corpus callosum.* Brazilian. J. Med. Biol. Res., 2003. **36**: p. 409-420.
38. Peters, A.M., et al., *T_2* measurements in human brain at 1.5, 3 and 7 T.* Mag. Res. Im., 2007. **25**: p. 748-753.
39. Wakana, S., et al., *Fiber Tract-based Atlas of Human White Matter Anatomy.* Radiology, 2004. **230**: p. 77-87.
40. Kosta, P., et al., *MRI evaluation of the basal ganglia size and iron content in patients with Parkinson's disease.* J. Neurol., 2006. **253**: p. 26-32.
41. Atasoy, H.T., et al., *T_2-weighted MRI in Parkinson's disease; Substantia nigra pars compacta hypointensity correlates with the clinical scores.* 2004. **52**(3): p. 332-337.
42. Graham, J.M., et al., *Brain iron deposition in Parkinson's disease imaged using the PRIME magnetic resonance sequence.* Brain, 2000. **123**(12): p. 2423-2431.
43. Wallis, L.I., et al., *MRI Assessment of Basal Ganglia Iron Deposition in Parkinson's Disease.* J. Mag. Res. Im., 2008. **28**: p. 1061-1067.
44. Reader Cuson, B., et al., *Initial Study of Parkinson's Disease at 7T: Can Differences Between Parkinson's Patients and Healthy Controls Be Depicted?* Proc. 16th Annual Meeting of ISMRM, 2008: p. P2280.

45. Berg, D., et al., *Disturbance of iron metabolism in Parkinson's disease - ultrasonography as a biomarker.* Neurotox. Res., 1996. **9**(1): p. 1-13.
46. Dexter, D., et al., *Alterations in the levels of iron, ferritin and other trace metals in Parkinson's disease and other neurodegenerative diseases affecting the basal ganglia.* Brain, 1991. **114**: p. 1953-1975.
47. Agartz, I., et al., *T_1 and T_2 Relaxation Time Estimates in the Normal Human Brain.* Radiology, 1991. **181**: p. 537-543.
48. Breger, R.K., et al., *T1 and T2 in the Cerebrum: Correlation with Age, Gender, and Demographic Factors.* Radiology, 1991. **181**: p. 545-547.

CHAPTER 8

CONCLUSIONS

This thesis has described the development of techniques for quantitative whole body imaging. The initial aim of this work was to develop methods for investigating the fate of food within the gastrointestinal tract at 3.0 T. Small bowel water content (SBWC) was measured and a T_2-prepared balanced turbo field echo (T_2-prep bTFE) sequence was used to measure T_2 of contents in the stomach and colon. These techniques were both optimised and validated for use at 3.0 T. With the arrival of the 7.0 T scanner, it seemed logical to investigate the possibility of using the T_2-prep bTFE sequence in the brain at 7.0 T but the challenges of scanning at ultra-high field were high for this sequence. However, this prompted interest in developing another sequence that would be able to measure T_2 at ultra-high field. A hybrid gradient echo-spin echo (GESSE) sequence was, validated and optimised to measure T_2 in the brain at 7.0 T and with the gradient echo component, had the advantage of measuring T_2* simultaneously.

Chapter 4 described and validated a technique, based on Hoad *et al*. [1] for measuring small bowel water volumes at 3.0 T. An intubation method was used where known volumes of a mannitol solution were infused and scanned using a turbo spin echo (TSE) sequence. A threshold technique was used to eliminate unwanted signal from the images; a conversion factor was required to calculate this threshold based on the signal from the cerebral spinal fluid (CSF). The calculation of the conversion factor was optimised using data from six subjects and then validated by measuring small bowel water volumes on a further 11 subjects using the calculated conversion factor.

Chapter 5 introduced the T_2-prep bTFE sequence which is capable of accurately measuring T_2. It is also possible to use this sequence to

simultaneously measure T_1 in addition to T_2 by using echo times optimised for the tissues of interest. After optimisation of the echo times used in the T_2-preparation phase, the T_2-prep bTFE sequence was validated using phantoms against gold standard spin echo-echo planar imaging (SE-EPI) sequence. In vivo measurements of different abdominal tissues were made and correlated well with those reported in the literature [2] using other techniques. The benefit of the technique presented here, compared with other techniques used to measure abdominal relaxation times, is the application within the gastrointestinal tract where motion artifacts (breathing and peristalsis) are a problem.

Chapter 6 combined the techniques developed in chapters 4 and 5 to study the fate of food in the gastrointestinal tract. First the effect of alginate beads on the stomach was studied; gastric emptying and T_2 measurements were made in the stomach. Different strength beads were investigated; gastric sieving of the water through the beads occurred and it was possible to infer gelation of the beads in the stomach from the measured T_2 values. Secondly the effects of fasting and feeding on the gastrointestinal tract were investigated. The effects of fibre and fasting on SBWC and colonic T_2 and T_1 values were observed; it was found that dietary fibre had no effect on fasting SBWC or colonic T_2 and T_1 values. After a rice pudding meal was consumed, there was a drop in SBWC, but no significant changes in the colonic relaxation times. However, there was a significant difference in colonic T_1; the ascending colon had a much lower T_1 than the descending colon. Gastric emptying was found to be slower with increased calorie content. Mannitol was found to induce intestinal secretions suggesting that it could be used as a model for diarrhoea.

Chapter 7 described the gradient echo-spin echo (GESSE) sequence which is capable of simultaneously measuring T_2 and T_2* in a reasonable scanning time. It was found from simulations, that the spin echo time should be approximately equal to the T_2 of the region of interest to reduce errors in the measured T_2. The sequence was validated at 7.0 T using phantoms against

gold standard SE-EPI and the first deep grey matter T_2 values were measured at 7.0 T. Preliminary results showed that this sequence was applicable when measuring T_2 and T_2* in the liver, which is of particular interest due to the high iron content within the liver. The advantage of this sequence compared with similar hybrid gradient echo spin echo sequences is that no errors arise due to pulse imperfections. Fitting methods capable of using all the acquired data were implemented in this work unlike the method used by Yablonskiy *et al*. [3]. Three experiments were performed using the GESE sequence. Initially a cross field comparison of T_2 and T_2' in the brain was carried out at 1.5 T, 3.0 T and 7.0 T. It was found that T_2 decreased approximately linearly with increasing field strength. Secondly, differences in T_2 and T_2* were measured in adjacent white matter tracts to determine if there was any relationship between myelin density and axonal structure. The results indicated that the T_2 could be related to fibre diameter, but the iron content may also be a consideration. Finally, comparisons were made of T_2, T_2* and T_2' in deep grey matter structures between healthy volunteers and patients with Parkinson's disease since it was expected that there would be an elevated iron level in Parkinsonian patients, particularly in the substantia nigra, but no significant differences were found.

References

1. Hoad, C.L., et al., *Non-invasive quantification of small bowel water content by MRI: a validation study.* Phys. Med. Biol., 2007. **52**: p. 6909-6922.
2. de Bazelaire, C., et al., *MR Imaging Relaxation Times of Abdominal and Pelvic Tissues Measured in Vivo at 3.0 T: Preliminary Results.* Radiology, 2004. **230**(3): p. 652-659.
3. Yablonskiy, D.A. and E.M. Haacke, *An MRI Method for Measuring T2 in the Presence of Static and RF Magnetic Field Inhomogeneities.* Mag. Res. Med, 1997. **37**: p. 872-876.